Three Grains, Two Photons and a Colourful Diamond

Tales of optical physics from the macroscale to quanta

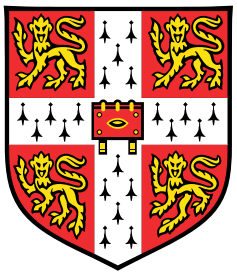

Camille Stavrakas

Department of Physics
University of Cambridge

This dissertation is submitted for the degree of
Doctor of Philosophy

Selwyn College

May 2019

Au Petit Prince,
A ma grand-mère qui habite une étoile voisine en forme de Corse,
A tous ceux qui croient en la magie.

To the Little Prince,
To my grand-mother who has moved to a neighbouring star in the shape of Corsica,
To all those who believe in magic.

Declaration

I hereby declare that except where specific reference is made to the work of others, the contents of this dissertation are original and have not been submitted in whole or in part for consideration for any other degree or qualification in this, or any other university. This dissertation is my own work and contains nothing which is the outcome of work done in collaboration with others, except as specified in the text and Acknowledgements. This dissertation contains fewer than 65,000 words including appendices, bibliography, footnotes, tables and equations and has fewer than 150 figures.

Camille Stavrakas
May 2019

Acknowledgements

First of all, I would like to thank my supervisor Sam Stranks for welcoming me in his group and giving my PhD a second beginning in May 2017. Had it not been for Sam Stranks, I would have never written this thesis. I also thank my lab- and college-mates: Mayami *and the cakes*, Ed and his MT-07, Alan and his travelling tips for Scotland (and for our physics discussions), Lucio for looking after Selwyn college's beehive with me, Xiaoya for all the delicious chinese food, Jhal, Young-Ik and many more who have left Cambridge already and are scattered around the globe - I'll keep travelling!

I also want to thank my college tutor Gavin Jarvis, Samantha Carr, Gina Vivian-Neal and the porters of Selwyn college for their precious support and for believing in me from the beginning to the end of this adventure, especially in times of turmoil.

Thank you to the Cambridge Violin Makers: Juliet, Kit, Nicky, Bob, Malcolm and more, for teaching me the art of violin making during three wonderful years. I also want to acknowledge the student societies that I joined, and in particular the MagSoc choir of Queen's college and the University Gliding Club - Cambridge looks even nicer from the sky.

I am also very grateful to everyone at the Molecular Foundry - Lawrence Berkeley National Lab and in particular Edward Barnard who worked alongside me. Thanks Ed for making robots work for me at night!

Thank you to all at Outsmart Insight (London) for your trust and for taking me onboard with all the fun (though intense!) consulting projects that we've done together in the last two years. It has been (and shall be!) a very valuable and enjoyable experience.

Finally, my thoughts go of course to my family and friends, to Monia and Olivier, to Nicolas and Pauline and their guitars, to Bernard and his Belgian waffles, to Claire Le Gall and her generous cooking(!), and for being both a friend and a scientific mentor (food for thoughts?).

Three Grains, Two Photons and a Colourful Diamond

Camille Stavrakas

Abstract

Exploring how light interacts with physical systems is an elegant and powerful way to unravel processes occurring at different scales, from bulk materials to single atoms. In this thesis, we employ several microscopy and spectroscopy techniques to investigate the local optoelectronic properties of metal halide perovskites, from thin films to large crystals, as well as to elucidate the physics of single-photon emitters in diamond.

First, the influence of the grain size on the low-temperature phase transition in methylammonium lead iodide perovskite polycrystalline thin films is assessed by means of temperature-dependent macro- and micro-photoluminescence measurements coupled with complementary X-ray diffraction and absorption measurements. The results suggest that local strain plays a role in inhibiting the low-temperature tetragonal-to-orthorhombic phase transition, and in the extreme case of very small grains, can almost entirely suppress it.

We then unveil buried charge-carrier recombination pathways in both thin film and micro-crystal methylammonium lead halide perovskite structures through 3D photoluminescence tomography acquired using two-photon confocal microscopy. These measurements reveal that light-induced passivation approaches are primarily surface-sensitive and that even nominal single crystals still contain heterogeneous defects that impact charge-carrier recombination.

We build on the two-photon mapping by developing a technique to monitor the carrier diffusion at different depths in a semiconductor by monitoring the photoluminescence as a function of distance from the two-photon-excitation spot. The technique was applied to methylammonium lead bromide crystals, revealing a spatial heterogeneity in diffusion that is not captured in macroscopic diffusion measurements. We outline a model to explain the observations by distinguishing the influences of carrier diffusion and photon reabsorption at different depths in the sample.

Finally, a series of optical studies on the Silicon-Vacancy (SiV) colour-centre in diamond are reported. Coherent Population Trapping (CPT) experiments performed using electrically actuated diamond micro-cantilevers show that the ground state splitting, and therefore the strength of the electron-photon coupling limiting the coherence time in this system, depends upon mechanical strain. A route to the all-optical control of such single electron spins in diamond is then outlined.

The thesis overall introduces a number of powerful techniques to shed light on the intimate relationships between carrier recombination, defects, strain and other physical properties of novel light absorbing and light emitting materials.

Table of contents

List of figures

List of tables

Chapter 1

Once upon a time...

No better words can, through a deliberate lack of specificity, transcend the *here and now*. No time, no place, no fetters but expanding horizons, enabled by the human capacity for mental abstraction[1]. *Once upon a time* is an invitation for creativity and imagination, a freedom of fantasy and reflection that we rarely give ourselves as we grow older. This ability to look beyond appearance with imagination is nonetheless crucial to comprehend the microscopic world. "*What is essential is invisible to the eye*". I learned this lesson from someone I encountered many years ago: the Little Prince.

If I first met him through the eyes of Antoine de Saint-Exupéry[2], the glider pilot that I am had the privilege to receive his visit. One summer day, as I was thermalling under a cloud as fluffy as sheep wool, I heard an odd little voice. It said: "S'il vous plaît... raconte-moi l'Univers !" (*"If you please... tell me about the Universe!"*). The temperature under the canopy was reaching figures only measured in the Sahara desert. I turned my head and saw him sitting on the wing, his yellow hair rippling in the wind. "Raconte-moi l'Univers...", the little man insisted. So I did, and the story that I wrote for him is dispersed throughout this thesis. If it does not unify the laws of physics in a *Theory of Everything*, it does try to give a poetic account of science. Famous French poets liked to evoke the close relationship between poetry and magic: they talked about incantation, enchantments, "*evocative sorcery*" (Baudelaire), "*alchemy of the word*" (Rimbaud); and after all, the ancient Mesopotamians had no distinction between "rational science" and magic[3–5].

As every story, my PhD followed the dramatic arc[6]: *exposition*, *rising action and conflict*, *climax*, *falling action* and *resolution*. In order to recount my journey as faithfully as possible, I have tried to incorporate in this thesis all the elements of narrative tension: anticipation (there is something interesting on the next page), uncertainty (feeling of doubt or lack of resolution) and, hopefully, investment (the reader also feels invested in the outcome).

In this introductory chapter, I will set the scene and introduce the topics that I have investigated as well as set the context for my work. I will provide a brief background for my research, while a more thorough account will be given within each individual chapter. I shall establish the link between my projects and position them in the broader scope of Physics.

1.1 Context for my work

I started my research in April 2015 in quantum optics within the Atomic, Mesoscopic and Optical Physics (AMOP) group at the Cavendish Laboratory, studying Silicon-Vacancy centres in diamond. Facing difficulties with my project and supervisor, I transferred to the Optoelectronics (OE) group in May 2017, and then started to work on perovskites, novel photovoltaic materials. This thesis is mostly based on the work done during my time in the OE group, but the last chapter is dedicated to my original PhD project.

1.2 A brief history of light and matter

Near the beginning was a very hot and extremely dense soup of elementary particles called quarks and leptons, which soon coalesced into subatomic protons, neutrons and electrons. This is how modern cosmology describes the very early Universe, as it was right after the Big Bang. During 17 minutes it had the temperature and pressure to fuse 25% of protons and neutrons into helium and heavier elements (*nucleosynthesis*), creating photons of gamma radiation immediately scattered by charged particles in the primordial opaque plasma.

As the Universe slowly cooled down, matter gradually took over radiation until about 380,000 years after the Big Bang where nuclei could start to combine with electrons to create neutral atoms. As a result, photons no longer interacted frequently with matter and the Universe became transparent. This is the oldest light that we still detect today, referred to as the *Cosmic Microwave Background*.

Light and matter went from strongly interacting in a very dense plasma to disregarding each other completely. This period, known as the *Dark Ages*, ended with the formation of the earliest generations of stars and galaxies 400 to 700 million years after the Big Bang. For the billion years to come, the rich and subtle interplay between light and matter in the midst of all the laws and forces of Nature was to give rise to the physical world as we observe it today, and nourish primitive cosmogonies just as much as our construction of modern Science.

From Mesopotamia to Greece and China, from the Neolithic to the Enlightenment and recent times, technique and empiricism slowly developed into scientific thinking. Calculation

differs from mathematics just as technology differs from science. Deeply tied to philosophy and existentialism, the construction of science and the birth of human societies are indivisible. They are anchored in an endless quest for emancipation, a search for progress, free thought and democracy as a way out of obscurantism. Science is built on the extraordinary ability of mankind: consciousness. The capacity to question where we come from, what we and the world around us are made of. Of the latter, practical knowledge is only a consequence.

As a theoretical physicist and cosmologist by training, it is in this continuity and with the urge to take fundamental knowledge further that I decided to pursue doctoral studies. Against all expectations this long and winding road led me to the vast territory of applied science. In the short time that I had, I could only touch on different topics and I regret not having the possibility to explore them in greater depth. In this world of ruthless competition where everything has to be fast and sell well, I have witnessed a growing confusion between science and technique, accompanied by a taking up of power and leadership of private success and profit at the cost of universality. I have seen people being used and exploited. All of that done, hypocritically and misleadingly, in the name of *progress*.

1.3 Downscaling the physical world... with uncertainty

The legend says that here, in Cambridge, sometime in the 1660s, an apple fell on Isaac Newton's head. In a stroke of brilliant insight, he worked out his theory of gravity and a set of laws describing the motion of physical objects[7]. Thanks to these, we know the orbits of the planets, we fly planes and we can predict the trajectory of cannon balls.

With the progress of experimental physics in the late 19th century and more recently with the ability to interrogate smaller and smaller objects, the observation was made that there is a limit beyond which the deterministic laws of classical mechanics cannot be downscaled. The evidence arose that around the atomic scale matter stops to obey such rules. In order to explain this behaviour, a new theory had to be developed. That sealed the advent of a new field of physics: *quantum mechanics*.

The novel and unsettling postulates of quantum mechanics were then to revolutionise our understanding of the physical world. It was different in nature, in essence. Starting with the quantisation of light and energy, it then introduced the wave-particle duality, entanglement, the uncertainty principle and the concept of inherently probabilistic measurement. Beyond the physical objects themselves, their interactions had to be revisited in the framework of this new theory.

My PhD was at the interplay between the macro and quantum worlds, interrogating quantum objects using classical light sources, and classical materials using quantum optical phenomena. This thesis investigates the interaction between light and matter in photovoltaic and elementary quantum systems. The following sections will introduce the projects that I worked on, each of which constitute a separate chapter of my thesis. The experimental and numerical methods used throughout this work are introduced in Chapter 2

1.4 Photoelectric alchemy

The transfer of energy from the quantised light to an electron, also called *photoelectric effect*, was first theorised by Albert Einstein in 1905. Efficient ways of turning light into electricity, and electricity into light, have since then been eagerly pursued. Since the end of the 20th Century and the mastery of silicon manufacturing, *sunlight harvesting* has become one of the potentially sustainable alternatives to fossil energy consumption.

In the quest for a cheaper though versatile and high-performance alternative to silicon-based optoelectronics, metal halide perovskites hold promise[8, 9]. Perovskites belong to a class of inorganic crystals with chemical formula ABX_3, sharing the same structure with calcium titanate $CaTiO_3$. In this structure, A and B are inorganic cations coordinated by 12 and 6 anions X, respectively. The first hybrid organic-inorganic perovskites (HOIPs), namely *methylammonium lead halide* or $CH_3NH_3PbX_3$ (X=Cl, Br, I) were synthesised and characterised in 1978[10] in which methylammonium (CH_3NH_3+), an organic cation, occupies the A site. HOIPs remained largely unnoticed until the first successful application of $CH_3NH_3PbX_3$ (X=Cl, Br) as photovoltaic absorbers with a power conversion efficiency of 3.8% in 2009[11]. The sites A, B, and X in a HOIP can be occupied by a wide range of different elements and compounds[12, 13]. For this work, the organic cation used at the A site will always be methylammonium. Inorganic cations B will be Pb while the smaller halogens Br and I will be used for at X sites ($MAPbBr_3$ and $MAPbI_3$). Figure 1.1 illustrates the hybrid structure used throughout this thesis.

Since a key breakthrough in 2012[15, 16] the power conversion efficiency of perovskite photovoltaic (PV) solar cells and light-emission devices (LED) has risen dramatically to over 24%[17] and 8-12%[18–20] respectively, with the efficiency of laboratory PV cells now surpassing the commercial thin film PV technology cadmium telluride (CdTe)[21]. Such rapid progress combined with low-cost fabrication from simple precursors[22], scalability[23] and band-gap tunability[24], has motivated the use of these materials in the fabrication of high-performance devices - including tandem cells[25, 26], placing them on the verge of

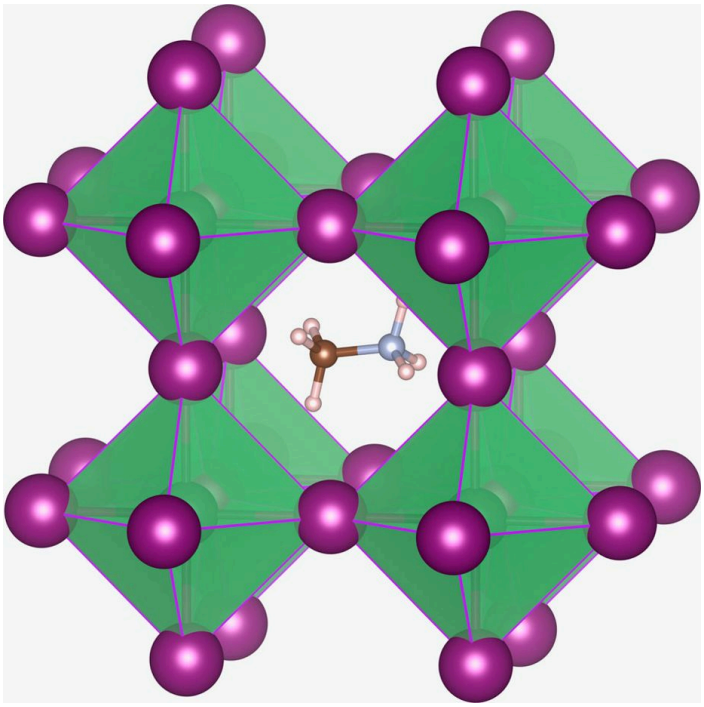

Fig. 1.1 **Methylammonium lead halide perovskite structure.** Methylammonium cation (CH_3NH_3+) occupies the central site surrounded by 12 nearest-neighbour halide ions in corner-sharing PbX_6 octahedra (X=I or Br). Figure taken from [14].

commercialisation[27–30]. Bulk halide perovskites are known to possess large dielectric constants leading to low exciton binding energies[31, 32], meaning excitons dissociate into free charges at room temperature[33, 34]. An unexpectedly efficient free charge-carrier recombination is thought to dominate radiative recombination in these materials[35, 36]. Nevertheless, a better understanding of what influences their crystalline structure along with efforts to unravel the mechanisms underpinning and limiting their radiative efficiency[37, 38] are needed in order to achieve phase purity, manage defects and ultimately achieve optimal device performances. .

1.4.1 Creation and recombination of charges in perovskites

In photovoltaic materials, the absorption of a photon leads in the most favourable case to the generation of a pair of charge-carriers (*photogeneration*): an electron promoted to the conduction band, and a hole forms in the valence band. Excitons, electron-hole pairs bound by Coulomb interaction, can also be created by photons of energy smaller than the band-gap, but the difference between the latter and their binding energy being usually less than k_BT most of them dissociate at room temperature[33, 34]. Over the first few hundreds

of femtoseconds, these "hot" carriers relax via elastic carrier-carrier scattering into a self equilibrium at a temperature higher than the ambient temperature, before loosing kinetic energy over the next few picoseconds through collisions with phonons (lattice vibrations). When the temperature of the distribution is reduced to the lattice temperature, the global thermal equilibrium is not yet restored. Although they have relaxed to a lower energy state, the photo-generated free electrons and holes are still overpopulating the conduction and valence band, respectively.

Photogeneration rate

Macroscopically, the photogeneration rate is a function of the photon flux and the material's propensity to absorb light: the absorption coefficient α. As a beam of photons of energy E travels through a slab, the light intensity $I(x)$ at a depth x is given by[33]:

$$I(x) = I(0)e^{-\int_0^x \alpha(E,x')dx'}, \tag{1.1}$$

where $I(0)$ is the intensity at the surface (after accounting for reflection). The coefficient α depends on the wavelength λ of the light as:

$$\alpha = \frac{4\pi Im(n)}{\lambda}, \tag{1.2}$$

where $Im(n)$ is the imaginary part of the refractive index of the material. For a monochromatic light source, this reduces to Beer-Lambert's law:

$$I(x) = I(0)e^{-\alpha x}. \tag{1.3}$$

Due to the partial overlap between the absorbance and emission spectra in perovskites, a fraction of the photons emitted during recombination events are reabsorbed. The intensity of the PL as a function of the distance from the emitter follows Equation 1.3. Re-emission events can then occur, commonly referred to as *photon recycling*. The efficiency of this process depends upon the material's PL and absorption spectra and upon its internal PL quantum yield[39, 40].

Evidence for strong re-absorption in $MAPbI_3$ and $MAPbBr_3$ single crystals has been reported[41, 40].The photon recycling efficiencies have been experimentally found to be less than 0.5% in $MAPbI_3$ and $MAPbBr_3$ single crystals (with an excitation intensity close to one sun), attributing the long carrier diffusion length[42–44] in these materials to an intrinsically long carrier recombination lifetime instead of the photon-recycling-induced photon propagation[41]. The low photon recycling efficiency might be caused by a low PL

quantum yield, which is thought to be highly dependent on excitation light intensity and below 20% under one sun illumination at room temperature[45].

Charge-carrier diffusion

Following a laser pulse, free electrons and holes are generated locally. Their concentration spreads spatially as the excitation profile, creating a local charge-carrier concentration gradient in the material. By virtue of the thermodynamic identity, adding particles to a system causes a change in energy. In order to reduce their statistical potential energy[33] and relax to thermal equilibrium, electron and hole populations diffuse as illustrated in Figure 1.2. The time-dependent concentration $c(t)$ of carriers can be described using Fick's second law:

$$\frac{\partial c(t)}{\partial t} = D\Delta c(t), \tag{1.4}$$

where D is the diffusion coefficient. If the electron and hole gradients are similar, the electron and hole diffusion currents tend to cancel each other out. As charge carriers diffuse, recombination events start to occur at a distance from where the charges were first generated. The speed at which they diffuse, or *diffusion coefficient*, is related to their velocity as well as their mean free path in the material (the distance between scattering events), and therefore to their interactions with the lattice.

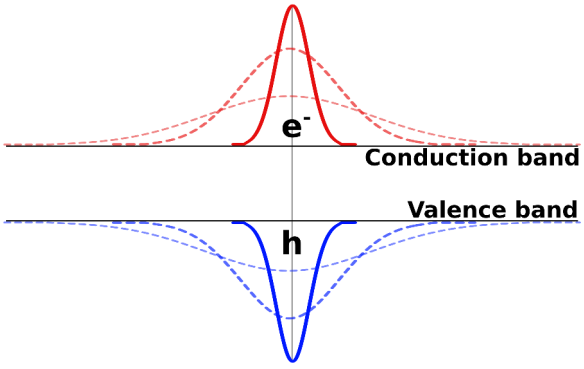

Fig. 1.2 **Diffusion of charge-carriers**, electrons (red) and holes (blue), in a concentration gradient generated by a laser pulse.

Charge-carriers photogenerated in the thin-film absorber layer of a perovskite-based solar cell then travel to reach an electron-collection and a hole-collection layer on either side of the absorber. The fraction of charge-carriers extracted from the cell, and therefore its efficiency, increases with increasing diffusion length.

Recombination rate

To reinstate the thermal equilibrium, the carriers recombine over a longer time scale: the generation of photocurrent in solar cells is governed by a balance between light absorption, current generation and charge recombination. The energy released as electron-hole pairs recombine can be given up as a photon (*radiative recombination*), as heat through phonon emission or as kinetic energy to another free carrier (*Auger recombination*). In the theoretical framework proposed by Shockley and Queisser[37] in 1961, the efficiency of a solar-cell is limited by the radiative recombination rate inside the active material. Any non-radiative recombination then further limits this efficiency. In perovskites, non-radiative and radiative recombination processes compete according to the rate equation[46, 47, 34]:

$$\frac{dn}{dt} = -A_{trap}n - B_{rad}n^2 - C_{Auger}n^3, \tag{1.5}$$

where n is the photocarrier density, A_{trap} the single-carrier trapping rate, B_{rad} the bi-molecular recombination rate constant for radiative electron–hole recombination, and C_{Auger} the Auger recombination rate constant. A_{trap} and C_{Auger} lead to non-radiative recombination. In perovskites, the impact of local environment such as lattice defects and strain on the formation of traps that can alter the generation mechanism (introduced earlier) is not fully known. This is what some of the work presented in this thesis attempts to elucidate. In the presence of traps, an electron can be promoted to or from a localised "trap" state in the band gap, generating a single free charge-carrier (respectively a hole or an electron)[33]. At low fluences the charge-trapping pathways limit the PL quantum efficiency, whereas at high fluences the traps are predominantly filled and recombination of the photogenerated species is dominated by efficient radiative processes. The recombination rate through a single trap state is described by the Shockley Read Hall expression[33]. Exceptionally low trap-state densities of the order of 10^9-10^{10} cm^{-3} were reported in $MAPbX_3$ single crystals[43], comparable to the best photovoltaic-quality silicon. In solution-processed polycrystalline thin films, however, the trap density rises to $\sim 10^{16}$-10^{17} cm^{-3}[48].

The nature of defects in perovskites, how they affect surfaces and interfaces between different crystal regions in a polycrystalline film, is still an open question. Localised states at surfaces and interfaces could include crystal defects due to broken bonds and extrinsic impurities[33]. There has been evidence for photo-induced degradation, and ion migration and oxidation play a major role[14, 49]. Interface passivation is one of the most commonly used and efficient strategies to improve the photovoltaic performance of perovskite solar cells[50]. It aims at reducing the defect trap states and at mitigating ion migration in order to optimise the charge transfer between various interfaces. Among the strategies that can be

drawn on in order to passivate perovskite devices are light and atmospheric treatments[51–54] as well as the decoration of surfaces and grain boundaries with potassium halide layers[55].

In Chapter 3, temperature-dependent X-Ray Diffraction (XRD) crystallography is used in conjunction with macro- and micro-photoluminescence (PL) microscopy to explore the influence of grain-size and local environment on the structural, mechanical and optoelectronic properties of polycrystalline $MAPbI_3$ perovskite films. The results suggest that local strain plays a role in inhibiting the low-temperature tetragonal-to-orthorhombic phase transition, and in the extreme case of very small grains, can almost entirely suppress it.

1.5 Probing light emission inside out

> In the book it said: "Boa constrictors swallow their prey whole, without chewing it. After that they are not able to move, and they sleep through the six months that they need for digestion."
>
> I pondered deeply, then, over the adventures of the jungle. And after some work with a coloured pencil I succeeded in making my first drawing. My Drawing Number One. It looked something like this:
>
> 
>
> **My Drawing Number One**
>
> I showed my masterpiece to the grown-ups, and asked them if the drawing frightened them. But they answered: "Frighten? Why should any one be frightened by a hat?"
>
> My drawing was not a picture of a hat. It was a picture of a boa constrictor digesting an elephant. But since the grown-ups were not able to understand it, I made another drawing: I drew the inside of a boa constrictor, so that the grown-ups could see it clearly. They always need to have things explained. My Drawing Number Two looked like this:
>
> 
>
> **My Drawing Number Two**
>
> *The Little Prince*, Chapter 1 - Antoine de Saint-Exupéry

Photoluminescence (PL) microscopy and spectroscopy are commonly used to characterise the light emitted by a semiconductor following radiative charge-recombination events. However, photovoltaic materials such as perovskite structures are very absorptive and any light with an energy above the band-gap is absorbed in the first few hundreds of nanometres[56]. For this reason, conventional microscopy is only suited to the exploration of phenomena occurring near the sample surface, which, as introduced earlier in this chapter, exhibit peculiar properties due to the interface with air and the propensity for a higher density of defects. In order to explore the bulk material, we need to call on a more complex, non-linear technique called *two-photon photoluminescence spectroscopy*.

Two-photon absorption (2PA) is one of the most fundamental non-linear processes which can be used to produce squeezed light with fluctuations below the standard quantum limit and thus reveals the quantum nature of light[57, 58]. The process involves the excitation of an atom or molecule from a lower quantum state $|1\rangle$ to an excited state $|2\rangle$ of the same parity, which cannot be connected through an electric dipole transition, in a single step. Thus parity conservation implies that two photons must be absorbed simultaneously. The theory of 2PA was first developed by Maria Göppert-Mayer in 1931[59]. As a brief introduction to this phenomenon, let us describe the interaction of light and an otherwise isolated system in quantum mechanical terms. The time-dependent Hamiltonian $\widehat{H}(t)$ is as follows:

$$\widehat{H}(t) = \widehat{H}_0 + V(t), \tag{1.6}$$

where $\widehat{H}_0$ is the Hamiltonian of the isolated system and all time dependence enters through the potential $V(t)$. In the interaction picture, both the operators and the state vector $|\psi_I\rangle$ carry part of the time-dependence:

$$|\psi_I(t)\rangle = e^{i\widehat{H}_0 t/\hbar}\,|\psi_S(t)\rangle\,, \tag{1.7}$$

where $\hbar$ is the reduced Planck's constant and $|\psi_S(t)\rangle$ is the state vector expressed in Schrödinger's picture. The wave function then obeys the following equation of motion (Schrödinger equation):

$$\begin{aligned} i\hbar\partial_t\,|\psi_I(t)\rangle &= e^{i\widehat{H}_0 t/\hbar}(i\hbar\partial_t - \widehat{H}_0)\,|\psi_S(t)\rangle \\ &= e^{i\widehat{H}_0 t/\hbar}(\widehat{H} - \widehat{H}_0)\,|\psi_S(t)\rangle \\ &= e^{i\widehat{H}_0 t/\hbar}V(t)e^{-i\widehat{H}_0 t/\hbar}\,|\psi_I(t)\rangle \\ i\hbar\partial_t\,|\psi_I(t)\rangle &= V_I(t)\,|\psi_I(t)\rangle\,. \end{aligned} \tag{1.8}$$

For a general time-dependent Hamiltonian, an analytical solution is usually infeasible. However, as for the time-independent Schrödinger equation, we can develop to a perturbative expansion (in powers of interaction):

$$|\psi_I(t)\rangle = \sum_n c_n(t)\,|n\rangle\,, \tag{1.9}$$

where $\widehat{H}_0\,|n\rangle = E_n\,|n\rangle$ and with:

$$c_n(t) = c_n^{(0)} + c_n^{(1)}(t) + c_n^{(2)}(t) + \ldots + c_n^{(m)}(t) \tag{1.10}$$

In this development, $c_n^{(m)} \sim \mathscr{O}(V^m)$ where $|m\rangle$ is a general state, and $c_n^{(0)}$ represents some (time-independent) initial state of the system. As with the Schrödinger picture, in the interaction representation, $|\psi_I(t)\rangle$ is related to an initial state $|\psi_I(t_0)\rangle$, at time t_0, through a time-evolution operator $\widehat{U}_I(t,t_0)$:

$$|\psi_I(t)\rangle = \widehat{U}_I(t,t_0)\,|\psi_I(t_0)\rangle\,. \tag{1.11}$$

Substituting Equation 1.11 into Equation 1.8, and using the boundary condition $U_I(t_0,t_0) = \mathbb{I}$, it can be shown that[57, 60]:

$$\widehat{U}_I(t,t_0) = \sum_{n=0}^{\infty}\left(-\frac{i}{\hbar}\right)^n \int_{t_0}^{t} dt_1 \ldots \int_{t_0}^{t_{n-1}} dt_n V_I(t_1)V_I(t_2)\ldots V_I(t_n). \tag{1.12}$$

If a system is prepared in an initial state $|i\rangle$ at $t = t_0$, at a subsequent time t it will be in a final state $\widehat{U}_I(t,t_0)\,|i\rangle$. Using the resolution of identity $\sum_n |n\rangle\langle n| = \mathbb{I}$, we therefore have:

$$\begin{aligned} \widehat{U}_I(t,t_0)\,|i\rangle &= \sum_n |n\rangle\langle n|\,\widehat{U}_I(t,t_0)\,|i\rangle \\ \widehat{U}_I(t,t_0)\,|i\rangle &= \sum_n |n\rangle\, c_n(t). \end{aligned} \tag{1.13}$$

From Equation 1.12 and 1.13, the coefficients $c_n(t)$ in the expansion can be expressed as:

$$\begin{aligned} c_n(t) = \delta_{ni} &- \frac{1}{\hbar}\int_{t_0}^{t} dt'\,\langle n|\,V_I(t')\,|i\rangle \\ &- \frac{1}{\hbar}^2 \int_{t_0}^{t} dt' \int_{t_0}^{t'} dt'' \sum_m \langle n|\,V_I(t')\,|m\rangle\langle m|\,V_I(t'')\,|i\rangle \\ &+ \ldots \end{aligned} \tag{1.14}$$

Recalling the definition $V_I(t)\,|\psi_I(t)\rangle = e^{i\widehat{H}_0 t/\hbar}V(t)e^{-i\widehat{H}_0 t/\hbar}\,|\psi_I(t)\rangle$ from Equation 1.8, the matrix elements entering the coefficients are then given by:

$$\begin{aligned}\langle n|\,V_I(t)\,|m\rangle &= \langle n|\,e^{i\widehat{H}_0 t/\hbar}V(t)e^{-i\widehat{H}_0 t/\hbar}\,|m\rangle \\ &= \langle n|\,V(t)\,|m\rangle\, exp\left[\frac{i}{\hbar}(E_n - E_m)\right] \\ \langle n|\,V_I(t)\,|m\rangle &= V_{nm}e^{i\omega_{nm}t},\end{aligned} \tag{1.15}$$

where $V_{nm}(t) = \langle n|\,V(t)\,|m\rangle$ denote matrix elements between the basis states of $\widehat{H}_0$ on the perturbation and $\omega_{nm} = (E_n - E_m)/\hbar$.

Using the relation 1.15 into Equation 1.14 finally gives:

$$c_n^{(1)}(t) = -\frac{i}{\hbar}\int_{t_0}^{t} dt' e^{i\omega_{ni}t'}V_{ni}t'c_n^{(2)}(t) \quad = -\frac{1}{\hbar^2}\sum_m \int_{t_0}^{t} dt' \int_{t_0}^{t'} e^{i\omega_{nm}t'+i\omega_{mi}t''}V_{nm}t'V_{mi}t''. \tag{1.16}$$

As a result, the transition probability $P_{i\to n}$ from the state $|i\rangle$ to a state $|n \neq i\rangle$ reads:

$$P_{i\to n} = |c_n(t)|^2 = |c_n^{(1)}(t) + c_n^{(2)}(t) + ...|^2. \tag{1.17}$$

Let us now consider a system prepared in initial state $|i\rangle$ and perturbed by a periodic harmonic potential $V(t) = Ee^{-i\omega t}$ abruptly switched on at time $t = 0$, such as an atom perturbed by an external oscillating electric field of amplitude E (light, in a semi-classical approach). The probability that, at some later time t, the system is in state $|f\rangle$ is, to first order in perturbation theory $P_{i\to f} \approx |c_f^{(1)}(t)|^2$ with:

$$c_f^{(1)}(t) = -\frac{i}{\hbar}\int_0^t dt' \,\langle f|\,E\,|i\rangle\, e^{i(\omega_{fi}-\omega)t'} \quad = -\frac{i}{\hbar}\,\langle f|\,E\,|i\rangle\,\frac{e^{i(\omega_{fi}-\omega)t}-1}{i(\omega_{fi}-\omega)}, \tag{1.18}$$

giving the transition probability $P_{i\to f}(t)$:

$$P_{i\to f}(t) \approx \frac{1}{\hbar^2}|\langle f|\,E\,|i\rangle|^2\left(\frac{\sin((\omega_{fi}-\omega)t/2)}{(\omega_{fi}-\omega)/2}\right)^2. \tag{1.19}$$

In the limit where t is large, we obtain the transition rate $R_{i\to f}$ or *Fermi's Golden rule*:

$$R_{i\to f} = \lim_{t\to\infty}\frac{P_{i\to f}(t)}{t} = \frac{2\pi}{\hbar^2}|\langle f|\,E\,|i\rangle|^2\delta(\omega_{fi}-\omega). \tag{1.20}$$

Although first order perturbation theory is often sufficient, sometimes $\langle f|\,E\,|i\rangle = 0$ by symmetry (e.g. parity, selection rules, etc...). In such cases, the transition may be accomplished by an indirect route through other non-zero matrix elements. To be more realistic, if we consider that the harmonic potential perturbation is gradually switched on, we have

$V(t) = e^{\varepsilon t} E e^{-i\omega t}$. Using second order perturbation theory as expressed in Equation 1.16 with this potential and with the initial time $t \to -\infty$, we obtain:

$$c_n^{(2)}(t) = -\frac{1}{\hbar^2} e^{i(\omega_{fi} - 2\omega)t} \frac{e^{2\varepsilon t}}{\omega_{fi} - 2\omega - 2i\varepsilon} \sum_m \frac{\langle f|E|m\rangle \langle m|E|i\rangle}{\omega_{mi} - \omega - i\varepsilon}. \tag{1.21}$$

In the limit where $\varepsilon \to 0$, the transition rate $R_{i\to f}$ becomes:

$$R_{i\to f} = \frac{2\pi}{\hbar^4} \left| \sum_m \frac{\langle f|E|m\rangle \langle m|V|i\rangle}{\omega_{mi} - \omega - i\varepsilon} \right|^2 \delta(\omega_{fi} - 2\omega). \tag{1.22}$$

This translates to a transition in which the system gains an energy $2\hbar\omega$ from harmonic perturbation, i.e. two photons are absorbed. Physically, this absorption occurs via a short-lived intermediate virtual state with energy ω_m. From Equations 1.20 and 1.22, it also comes that the absorption rate scales as E^2 (I) and E^4 (I^2) for one- and two-photon absorption, respectively. In 2PA, the power absorbed is then proportional to the square of the intensity I of the incoming field, if both photons have the same energy, and thus higher excitation power is required[61].

Owing to the quantum nature of the interaction between light and matter, it becomes then possible to excite transitions in a material using low energy photons that would not be absorbed individually. Different approaches and a full quantum treatment of two-photon absorption can be found in the literature[58, 62]. In Chapter 4, we investigate buried recombination pathways in perovskite structures by probing the light emitted below the surface, in the bulk, using 3D photoluminescence tomography acquired using two-photon confocal microscopy. These measurements reveal that light-induced passivation approaches are primarily surface-sensitive and that even nominal single crystals still contain heterogeneous defects that impact charge-carrier recombination.

In Chapter 5, we monitor the carrier diffusion at different depths in methylammonium lead bromide crystals by measuring the photoluminescence as a function of distance from the two-photon-excitation spot. Our results reveal a spatial heterogeneity in diffusion that is not captured in macroscopic diffusion measurements. We propose a model to explain the observations by distinguishing the influences of carrier diffusion and photon reabsorption at different depths in the sample.

1.6 Schrödinger's cat lives in a colourful diamond.

In previous sections we have seen how exploring the absorption and emission of light in a semiconductor could allow one to study the mechanisms underlying the generation and recombination of charge-carriers. We were able to probe recombination pathways in the bulk of single crystals, thanks to the quantum nature of light. In bulk materials, billions of atoms and electrons contribute to create macroscopically observable phenomena. Due to the complexity of their interactions with one another, it is very difficult to understand their intricate behaviour at a fundamental level.

There exist simpler systems, however, on which the laws of quantum mechanics can be directly tested. Extensive research in quantum optics from cold atoms to solid-state single photon emitters has provided us with very advanced tools and the ability to observe and control quantum states of matter [63, 64].

I spent the first two years of my PhD studying a particular impurity of diamond which interacts with light, making it colourful. My early work in quantum optics is reported in Chapter 6. This *colour centre* is based on a silicon atom trapped in the carbon lattice, attracting an electron at its vicinity in such a way that it is negatively charged[65]. This extra electron is a quantum system, which can be driven optically (or using microwaves) from the ground state to excited states, defined by interactions with neighbouring atoms and the electron's spin degree of freedom[66]. By carefully tuning the energy of the photons used to drive the quantum system, it becomes possible to put it in a state where it is on more than one level, in more than one state, at the same time[67].

This powerful though disturbing quantum superposition principle was illustrated in 1935 by Erwin Schrödinger[68], who compared it to a cat being alive and dead at the same time. If we think in terms of computation power, a classical computer can only perform a single operation at a time on a single binary bit, 0 or 1. A quantum computer, on the other hand, could use a quantum bit that would be a superposition of 0 and 1, and hence perform operations simultaneously on two bits in a single system at a single point in time.

Quantum information research promises more than computers. From cryptography to metrology and sensing, data acquisition and treatment could be made exponentially faster, safer (with security guaranteed by the laws of physics) and with higher precision than is possible otherwise [69, 70]. At the dawn of nanotechnology, joining forces to delve into the physics of very small objects and systems, obeying the rules of quantum mechanics, could provide us with advances in fundamental science together with novel technological applications. My work was at the interface between nanoscience and quantum optics, aiming at providing a deeper understanding of the interactions between photons and

electron spins together with novel ways of controlling them. I tried to address the need for quantum information hardware, the development of materials and control setups that make the manipulation of quantum states possible.

Manipulation of photon-spin interactions is a transferable technique that can be applied to many systems. Since diamond has a unique combination of properties that is not found in any other material [71, 72] (it has the largest optical bandgap which provides it with many potential electronic, optical and thermal applications, it is biocompatible and chemically robust), my work focused on diamond. More specifically, silicon atoms artificially implanted in pure diamond crystals to form *Silicon-Vacancy* (SiV) centres. The SiV centre is formed by replacing two neighbouring carbon atoms in the lattice with one silicon atom, which places itself between the two vacant lattice sites, as shown in Figure 1.3 **a**. In the presence of a high density of SiVs, diamonds turn orange (Figure 1.3 **b**).

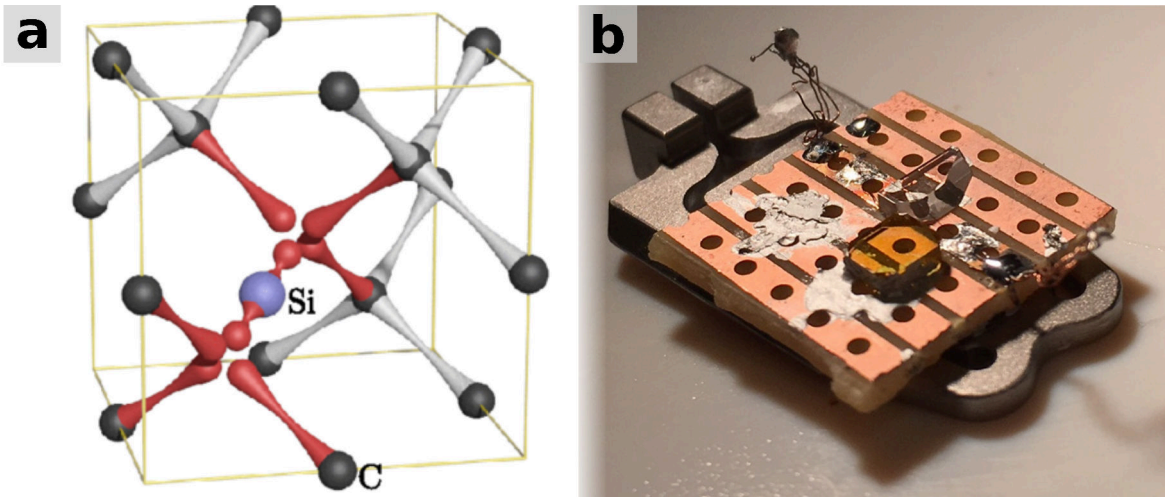

Fig. 1.3 **The SiV centre in diamond.** (a) The SiV is aligned along a [111] axis of the diamond host crystal, with the silicon atom (Si) located in the middle of two empty lattice sites. The system has D_{3d} (including inversion) symmetry (taken from [73]). (b) Diamond samples containing respectively a low (transparent) and high (orange) density of SiVs.

At the time, the SiV centre was a new system and little was known about its properties. Yet, the spectrally narrow lines in its light emission spectrum strongly suggested a low electron-phonon coupling, and therefore a large fraction (80%) of the emitted photons were thought to be indistinguishable at cryogenic temperatures (4 K)[73]. In this respect, its optical properties were significantly different from the *Nitrogen-Vacancy* (NV) centre, the most studied colour-centre in diamond, emitting less than 5% of such photons at 4 K[74].

However small, the electron-phonon coupling was thought to be the cause of the comparatively short coherence time measured for SiVs, the time during which a quantum superposition

can be maintained [67, 75, 76]. One hypothesis proposed by C. Hepp[77, 65] was that the strength of this coupling depended upon the mechanical strain experienced by the SiV centre. This explanation was yet to be demonstrated experimentally, and doing these experiments with our collaborators at Harvard was part of my project. Together, with electrically actuated diamond micro-cantilevers that they had fabricated, we performed strain-dependent optical measurements that validated these speculations[78, 79].

Allowing fast calculations to be performed, the SiV's short coherence time could also be seen as an advantage in the development of quantum nodes and universal quantum gates, a necessary step to fulfil the requirements for the physical implementation of quantum computation [80]. Towards this goal, correspondingly fast manipulation techniques and strategies needed to be developed. At the time, my efforts then converged towards designing and building an ultrafast optical setup, and laying the first stone on a path to the ultrafast optical control of the SiV spin.

1.7 Thesis outline

In this thesis, several microscopy and spectroscopy techniques are used to explore how light interacts with novel photovoltaic materials: hybrid perovskites, and single-photon emitters: silicon-vacancy (SiV) centres in diamond. The work reported herein investigated the impact of local environment on the optoelectronic properties, charge-carrier diffusion and recombination in perovskites. It interrogates the role of strain in the coherence time of single spin qubits in SiV centres, and discusses how such qubits could be manipulated optically to create quantum gates for quantum information. The outline is as follows:

1. Chapter 1: Introduction (current chapter)
2. Chapter 2: Methodological framework and tools for data acquisition and analysis
3. Chapter 3: Influence of grain size on phase-transitions in perovskite films
4. Chapter 4: Probing buried recombination in perovskite structures with 3D time-resolved tomography
5. Chapter 5: Visualising carrier diffusion in halide perovskite crystals
6. Chapter 6: Towards the optical control of single spins in diamond
7. Chapter 7: General conclusion and outlook

1.8 S'il vous plaît, raconte-moi l'Univers. (If you please, tell me about the Universe.) 1

Le petit prince était rentré chez lui, heureux de retrouver ses trois volcans dont un toujours éteint, de contempler sa fleur-soleil désormais si spéciale et précieuse à ses yeux. Son voyage l'avait changé, il avait grandi. L'enfant qu'il était avait gagné en sagesse, et ce qu'il avait appris rendait son regard plus sensible encore aux merveilles de la vie. Il était donc de retour, sur son île au milieu de l'espace et du temps, parmi la multitude d'astres dont certains lui ayant offert l'hospitalité le temps d'une visite en étaient devenus familiers. Lui qui était auparavant si triste, se sentant si seul, était maintenant empli de la joie d'avoir ouvert les portes du monde et vu briller sous bien d'autres soleils des vertus de sagesse. Il prenait dès lors soin de ses souvenirs comme l'on protègerait un inestimable trésor.

Il avait libéré son mouton, et lui avait présenté sa fleur. En sortant la muselière et avant même de constater l'absence de la courroie de cuir, il se demanda comment son nouvel ami jardinier l'aiderait à s'occuper des baobabs s'il ne pouvait les croquer. Peut-être risquait-il aussi de lui faire de la peine en le privant de cette liberté. Il s'agenouilla, et entourant le cou du mouton de ses bras lui expliqua doucement : « Ecoute mon ami, cette fleur est unique et elle m'est chère. Promets-moi d'en prendre soin et de ne jamais la manger ». Et le mouton comprit. Il s'approcha de la fleur pour en mieux apprécier le parfum, puis retourna auprès du petit prince.

Le temps coulait, passait, et se lassant du quotidien il cédait parfois à l'envie d'essayer de voir plus loin, d'explorer et de découvrir. Il avait pris pour coutume de laisser divaguer son imaginaire en contemplant l'horizon, inventant mille et une histoires fabuleuses.

Un beau jour, alors qu'il s'était assis pour regarder se succéder quelques-uns des quarante- quatre couchers de soleils journaliers, il vit apparaître à quelques mètres de lui une bien étrange planète. Elle avait un cœur gros comme une orange autour duquel gravitaient plein de petits grains de poussière. Un petit homme assis en tailleur semblait flotter à quelques centimètres de sa surface, observant le ciel dans l'oculaire d'un télescope. Stupéfait de cette apparition, le petit prince l'interpela.

The little prince who had returned home was delighted to find his three volcanoes again - one of which was still extinct -, to contemplate his flower-flame that had become so special and precious in his eyes. His trip had changed him, he had grown up. The child had gained in wisdom and learnt so much that he had become even more sensitive to the wonders of life. He was then back, on his island in the middle of space and time, among the multitude of stars - some of which had become familiar along the way. He who used to be so sad and feel so lonely was now serene, having opened up himself to the World and seen shining beneath many other Suns virtues of wisdom. He had been taking the greatest care of his memories, as one could protect the most precious of all treasures.

He had released his sheep, and introduced him to his flower. Grasping the muzzle without even realising that I had forgotten to draw the leather strap, he found himself wondering how his new friend, this little gardener, could help him to get rid of the baobabs if he was not able to crunch them. Moreover, this lack of freedom could upset the sheep, and he did not want to take that risk. He kneeled down, took his friend in his arms and told him gently: "Listen, little friend. This flower is unique and so dear to me. Promise me to take care of her and never ever attempt to eat her." And the sheep understood. He stepped up to the flower, smelled it, and joined the little prince.

Time was flying by, and tired of the daily routine he had got into the habit of yielding sometimes to the urge to explore and discover, allowing his imagination to ramble while contemplating the horizon, dreaming up one thousand and one fabulous stories.

One day, while watching a few of the forty-four daily sunsets, he saw a very odd planet appear in from of him. Its heart was the size of an orange, and hundreds of dust grains seemed to be gravitating around it. A little man was sitting cross-legged, floating a few centimetres above its surface observing the sky through a telescope. Astounded by this apparition, the little prince hailed him.

Chapter 2

Methodological framework and tools for data acquisition and analysis

In this chapter, I will explain the methodology developed and used to perform the experiments reported in this thesis. A methodological framework was developed in order to analyse accurately large spectral maps as well as time-resolved 3D tomography and diffusion data. It will be described and discussed herein.

2.1 Experimental methods

The basic principles of confocal laser scanning microscopy (CLSM) and time-resolved CLSM will be introduced first, along with the implementation of these experimental techniques for the present work. Although the core of this work was based on optical microscopy and spectroscopy, a range of characterisation techniques was used. The structural analysis presented in Chapter 3 was done by means of X-Ray Diffraction (XRD) measurements, and scanning electron microscopy (SEM) is used in most of the chapters. They will be presented as well.

2.1.1 Confocal Laser Scanning Microscopy (CLSM)

Originally developed by Marvin Minsky in the mid-1950s (patented in 1957[81]) but first realised in the late 1960s and early 1970s with the advent of laser light, confocal scanning microscopy is one of a series of methods to generate slices from microscopic samples by means of optics[82, 83]. Only a single, diffraction limited spot is illuminated and observed at a time, and the benefit of confocal imaging is a dramatically increased contrast by removal

of out-of-focus haze. Such filtering is achieved by placing pinholes at confocal points in the excitation and collection arms, as illustrated in Figure 2.1.

During the late 1980s, advances in computer, electronics and laser technology coupled to new algorithms for digital manipulation of images enabled the commercialisation of different types of laser scanning confocal microscopes[84], and the dawn of 3D image stacks as sources for subsequent rendering as depth-coded maps or 3D movies. Confocal microscopy is also very well compatible with multi-photon imaging[85, 86]. The first field of science to benefit from confocal microscopy was biology[87, 88], but applications in material science and technology soon arose[89, 90].

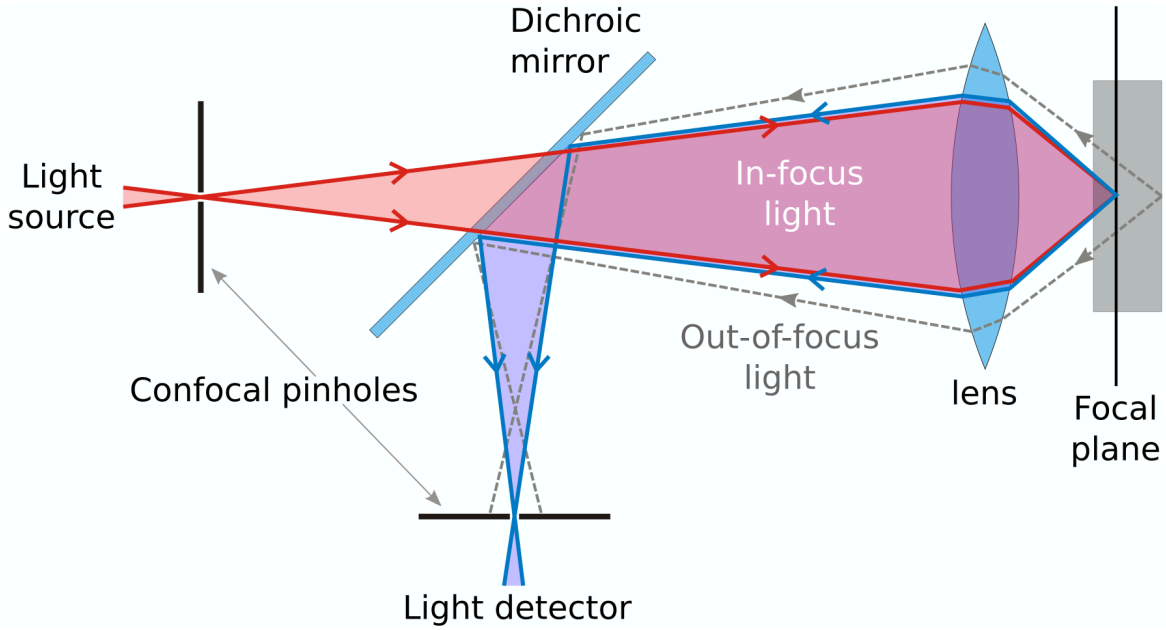

Fig. 2.1 **Excitation (red) and emission (blue) light pathways in a basic confocal microscope configuration.** Two pinholes are placed at confocal points in the excitation and collection arms to remove out-of-focus haze (grey dotted rays). θ is the half-angle of the light-cone formed between the objective lens and the sample

Field of view, contrast and resolution

As in every microscope, the objective lens is the critical element. It determines magnification, field of view (through its *numerical aperture*) and resolution, and its quality determines light transmission and the contrast and aberrations of the image. These parameters and qualities are also critical in confocal microscopy, so a good objective lens is always necessary[91]. The two components of image quality are contrast and resolution. Resolution can be derived

from the geometry of the system. Contrast, on the other hand, is what limits the available resolution by introducing noise into the image.

Numerical aperture: The angular behaviour of the cone of light converging to an illuminated spot or diverging from one depends on the *numerical aperture* (*NA*) of the objective lens as[91]:

$$NA = n \sin \theta, \tag{2.1}$$

where n is the index of refraction of the medium separating the objective from the sample and θ is the half-angle of the cone (see Figure 2.1). The numerical aperture of the objective lens determines the field of view of the microscope.

Resolution and contrast The amplitude of the field at the sample, rather than being uniform, is given by the *point-spread function* (PSF) of the objective. For a circular aperture, the PSF or resolution is usually defined by the Airy disc[92]. However this is in principle an approximation for small *NA*s (paraxial optics). As the *NA* becomes large, dark fringes never quite go to zero and the width of the PSF is a bit more than the approximation predicts. The radius r of the first dark fringe depends on the illumination wavelength λ as[91]:

$$r \approx 1.22 \frac{\lambda}{2NA}. \tag{2.2}$$

If a Gaussian beam (typical laser profile) under-fills the lens pupil it will be focused to a beam waist that is Gaussian in cross section. A partially filled pupil will produce a mixture of the Gaussian and diffraction patterns. Then by underfilling the pupil we can avoid all the complexity of the diffraction pattern and get much more light through, at the cost of a slight decrease in resolution. Finally, in a confocal microscope both the illumination and observation volumes are described by PSF, representing respectively the probability that photons will reach a given point on the sample and that photons will be received from that point. If the illumination and fluorescence emission wavelengths are approximately the same, their product is then the total point-spread function giving a slightly different r than for a wide-field microscope (Equation 2.2):

$$r_{conf} \approx 0.88 \frac{\lambda}{2NA}, \tag{2.3}$$

therefore increasing the resolution. These are all, however, theoretical limits. In practice, especially when imaging the photoluminescence (PL) of a sample, the image intensity at any point (x,y) in the image is determined by squaring a convolution of the amplitude PSF

(which gives the amplitude of the field) with the PL amplitude profile: the response of the material[93, 94]. This profile itself depends on the excitation energy and intensity, on the charge-carriers' diffusion length, and when the light is emitted from within a crystal the change in refractive index and the outcoupling efficiency also contribute to the shape of the imaged PL profile. In some cases and particularly when performing multi-photon imaging, the excitation and emission wavelengths are different, which implies that the resolution is different in excitation and collection. The PSF can be calculated for a particular objective lens, and images can then in principle be deconvoluted[95].

In principle, if two features on a sample are separated by a distance larger than r_{conf} they can be resolved, if the noise level is low enough. The signal-to-noise ratio being inversely proportional to the square-root of the stray light intensity[91], stray light is usually the main cause of any loss in contrast. But since in a confocal microscope the out-of-focus light (and therefore background light as well) is not detected, this effect is reduced and the contrast is higher than with a wide-field microscope. Finally, the axial resolution r_{ax} (in depth) is defined as[91]:

$$r_{ax} = \frac{1.5n\lambda}{NA^2}, \tag{2.4}$$

which is close to r_{conf} in the limit where NA is close to 1. Again, this is valid only with conventional one-photon excitation and linear absorption. Multi-photon absorption (in our case, two-photon absorption) is non-linear and therefore the excitation volume (resolution in depth) is more difficult to define. This will be discussed later in this chapter.

In order to build an image with a confocal microscope, the focused spot of light must be scanned across the sample. In Minsky's original microscope the beam was stationary and the specimen itself was moved. This optical arrangement is also used for the work reported in this thesis, as it has the advantage of always scanning on the optical axis, which can eliminate any lens defects. The 4th dimension, time, was made accessible by the development and use of pulsed lasers.Chapter 4 presents such 3D tomography experiments performed on perovskite structures.

2.1.2 Time-Resolved CLSM

Ultrafast pulsed light sources, single-photon-detectors and fast electronics have made it possible to excite and probe materials precisely both in space and in time. Sub-nanosecond dynamical processes, such as the PL emission and decay following a very short and localised excitation pulse can be imaged and investigated. Short optical pulses are also a means of achieving high peak powers, which is necessary to take advantage of non-linear processes such as two-photon absorption.

The time-resolved measurement window is divided into time bins (according to a sampling rate reflecting the precision of the hardware), and for every photon detected one count is added to the bin corresponding to its delay with respect to the last laser pulse ("start" trigger)[96]. The same measurement is repeated many times. Provided that the probability of registering more than one photon per cycle is low (i.e, that the light level at the sample has been attenuated), a histogramme is built that gives the statistical distribution of detected photons per time bin across the time window. This histogramme represents the time decay one would have obtained from a "single-shot" time-resolved analog recording). Detector and electronics have a *dead time* for at least some nanoseconds after a photon event, during which they cannot process another event. If the number of photons following one laser pulse is more than one, the system would very often register the first photon but miss the following ones, leading to an over-representation of early photons in the histogramme.

As an example, Figure 2.2 shows the decay of the photoluminescence from a perovskite single crystal measured with the setup used in Chapters 4 and 5. The red marker highlights the position of the trigger (laser pulse) and therefore time t_0. In order to determine t_0, the programme looks for the time at which the gradient is maximum.

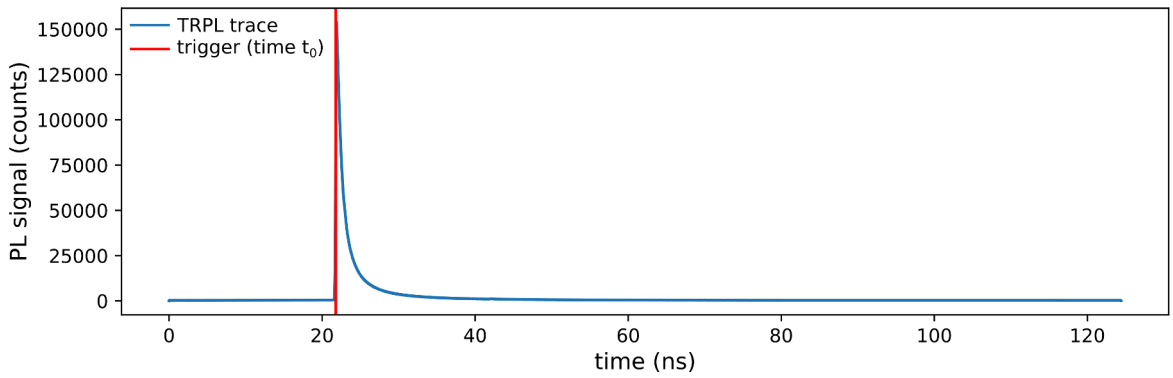

Fig. 2.2 **Time-resolved PL (TRPL) example trace.** The red marker highlights the position of the trigger (laser pulse) at time t_0.

Short (picosecond range) and ultrashort (femtosecond range) pulses generated by a mode-locked laser are in the form of a pulse train with a repetition rate of the order of few MHz to few GHz for the fastest device available. The lasers used for this work have a repetition rate of 76 MHz. Although that allows for fast manipulation of physical systems, some processes occur on a time scale longer than the distance between consecutive pulses. It is the case of the PL decay imaged in Chapter 4 and 5. Furthermore, to perform particular experiments one may want to prepare specific pulse sequences, with a controlled spacing, as in Chapter 6. Finally, time-correlated-single-photon-counting (TCSPC) as introduced above requires the delay between consecutive laser pulses to be grater than the dead time of the detector and electronics. For all these reasons, it is often necessary to pick certain pulses from such a pulse train, i.e., to transmit only certain pulses and block all the others. This can be done with a *pulse-picker*, which is essentially an electrically controlled optical switch. In this subsection, a description of the hardware needed to prepare the excitation beam is given.

Introduction to pulsed lasers and optical switches

The operation of a laser is divided in three main steps corresponding to three building blocks: a pump triggering an inversion of population in a gain medium by supplying energy to it, and an optical resonator in which the amplified light and bounce back and forth. When more than half the atoms in the gain medium are excited, stimulated emission occurs. The coherent photons travel then back and forth in the cavity between a highly reflective mirror and a partially transmitting one called *output coupler* through which the coherent beam partially escapes. The laser radiation is generated at one or several frequencies corresponding to modes of the resonator [97]. The first laser system ever made by Theodore Maiman [98] in 1960 used a ruby crystal as gain medium: it was the first pulsed solid-state laser. In fact, the word "ruby" hides a more complex compound: sapphire (Al_2O_3) doped with a small amount of chromium. The lasers used for the present work is based on a similar crystal, the difference being that titanium ions were incorporated instead of chromium as impurities into sapphire.

Ti:Sapphire lasers : Twenty-six years after Maiman's first prototype, P. F. Moulton [99] demonstrated at the Lincoln Laboratory (MIT) that titanium-doped sapphire (Ti^{3+}:sapphire or Ti:Al_2O_3) has the largest tuning range of any known laser: from 670 nm to 1000 nm (Figure 2.3), a property that still holds today. It also provides high peak-power and short pulses (picosecond to femtosecond range). Such crystals have a broad band absorption centred around 500 nm, and are therefore usually pumped by high power continuous-wave (CW) 532 nm diode lasers.

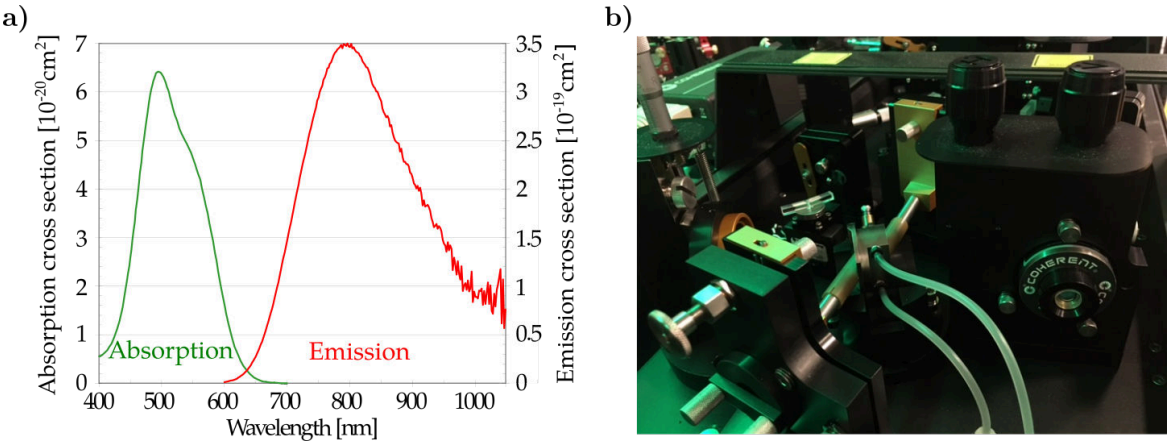

Fig. 2.3 **Absorption and emission of a Ti:Sapphire laser. a**) Although the fluorescence band extends from wavelengths as short as 600 nm to wavelengths greater than 1000 nm, the lasing action is only possible at wavelengths longer than 670 nm because the long wavelength side of the absorption band overlaps the short wavelength end of the emission spectrum. **b**) Water-cooled Ti:Sapphire crystal inside our Mira laser.

In any laser, the allowed oscillating wavelengths (or frequencies) are also determined by the longitudinal modes and therefore the length of the cavity. In the cavity, the electric field of the oscillating optical frequencies must repeat itself after one round-trip. Just as a guitar string should have the right tension to give the right note, the oscillating light must have the right energy and satisfy a standing wave condition in the laser cavity: an integral number of half wavelengths must exactly fit between the end mirrors [97]. The small group of frequencies that satisfy this condition are the longitudinal modes of the laser, depending on the cavity length which can be tuned. A birefringent filter in the cavity, allows to select the spectral window within the broadband emission. This is depicted in Figure 2.4.

In order to have a repetition rate around 76 MHz, the cavity has to be about 2 m long (the time between pulses is equal to the time it takes for light to make one round trip from the output coupler to the high reflector at the other end of the cavity and back to the output coupler). To produce short picosecond or femtosecond pulses, the cavity needs to be mode-locked: there needs to be a single pulse in the cavity at a time created by constructive interference of multiple longitudinal modes. One common way of achieving mode-locking (ML) is to add in the cavity an absorbent material (passive ML) or AOM (active ML) introducing periodic losses (before and after each pulse) strong enough to stop the lasing process until the next pulse, as illustrated in Figure 2.5 . Indeed, to achieve lasing the gain provided by the crystal should be greater than the losses inflicted to the light travelling in the cavity. With an AOM, for example, one can trigger or inhibit emission of light. The central

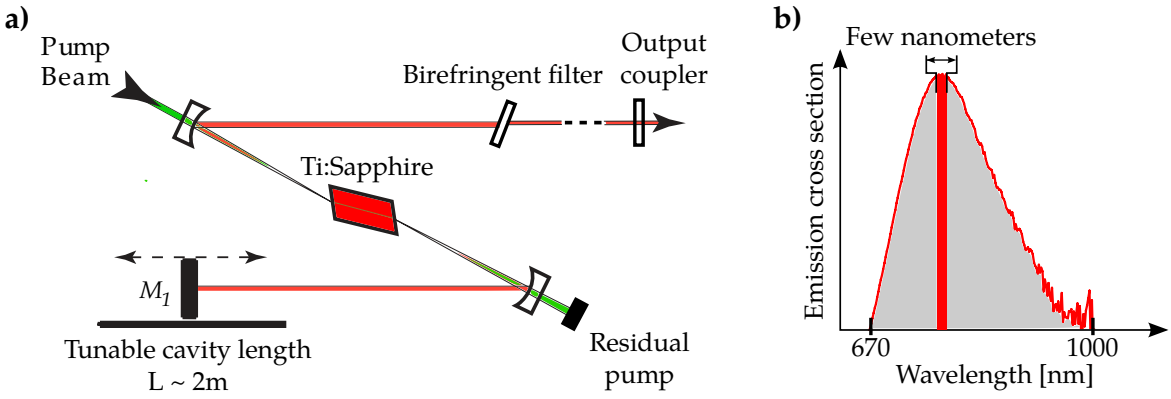

Fig. 2.4 **Tunability of the Ti:Sapphire laser.** **a**) The main cavity length can be tuned by moving the end mirror M_1. **b**) Within the emission range of the crystal, the centre wavelength is tuned by rotating a birefringent filter located in the cavity).

part of the pulse can go through the 'open gate' while its tail is diffracted, shortening it. The repetition rate is the speed of light c divided by twice the cavity length L.

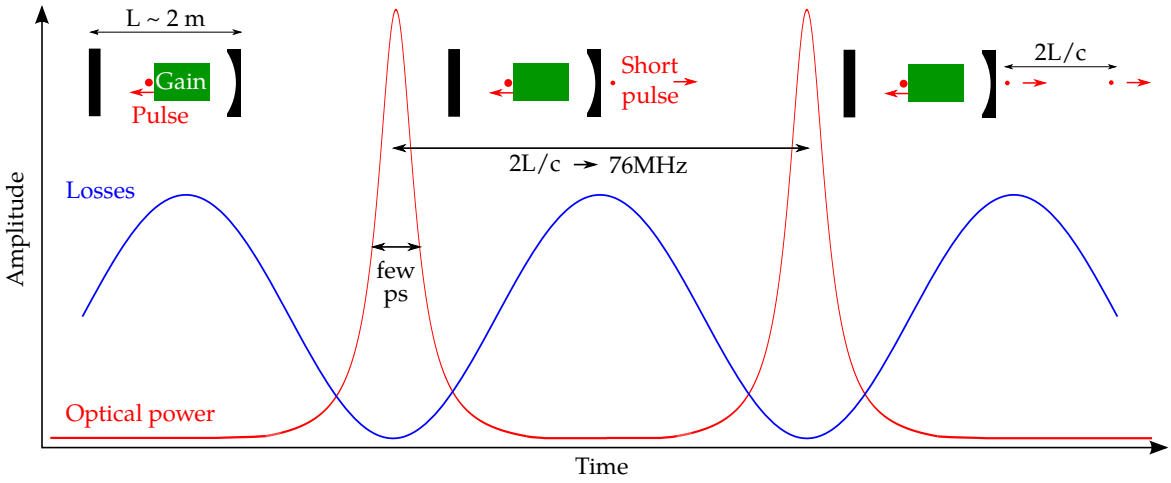

Fig. 2.5 **Mode-locking of a Ti:Sapphire laser.** Only pulses of the right frequency are transmitted in the cavity.

The Coherent lasers used for this work employ a different means to produce the same result: the Kerr effect [100]. The Ti:Sapphire crystal shows a non-linear response with the passage of light, and its refractive index is dependent on the field strength. The centre of a Gaussian pulse will then experience a greater refractive index than its tail, and the crystal will act as a focusing lens. The diameter of a pulsed beam is then narrower than a continuous wave (CW). In order to promote the pulsed mode, we need to call upon the balance between gain and losses again and ensure that the CW beam is subject to too much loss to exist in the cavity. This mode selection is achieved by placing a slit with adjustable width after the

crystal, so the large diameter laser beam associated with CW operation is interrupted at its edges while a high-intensity pulse will pass uninterrupted 2.6. Since it does not require the use of electronic devices nor absorptive materials, Kerr-lens mode-locking is a passive and lasting solution. Once the laser is mode-locked, the small loss introduced by the slit is enough to completely extinguish the CW beam.

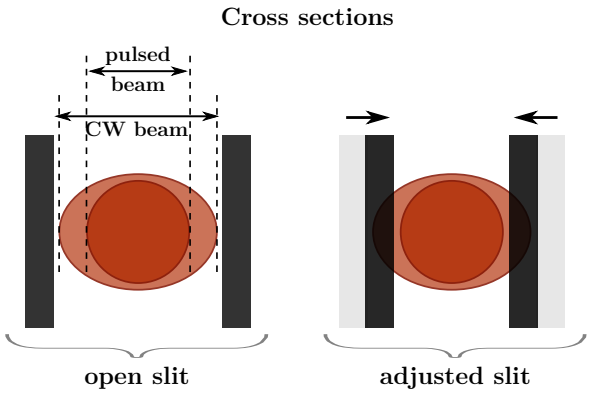

Fig. 2.6 **Kerr-lens mode-locking of a Ti:Sapphire laser.** Pulses are more tightly focused through the crystal than the CW beam. Adjusting the width of the slit interrupts the latter at its edges, extinguishing it.

The peak power of a pulsed laser can be estimated from the average power measured at the output [101]. Assuming that the energy E, contained in every pulse, is constant, we can define the peak power P_{peak} and the average power P_{avg} as follows:

$$P_{peak} = \frac{E}{\Delta t} \quad \text{and} \quad P_{avg} = \frac{E}{T}, \tag{2.5}$$

where T is the inverse of the repetition rate and Δt is the duration of a pulse. From these two expressions, it comes:

$$P_{peak} = P_{avg}\frac{T}{\Delta t}. \tag{2.6}$$

In our case, the measured average power is about 4 W, the repetition rate is 76 MHz and the duration of a pulse few picoseconds (about 3 ps), which means a peak power close to 25 kW. Knowing that the energy of a photon is defined as:

$$E_{photon} = h\frac{c}{\lambda}, \tag{2.7}$$

at our operating wavelengths (mainly around 1200 nm and 737 nm), this energy is $\sim 2\text{x}10^{-19}$ J.The energy contained in a laser pulse is $E_{laser} = P_{peak}\Delta t$, giving $\sim 8\text{x}10^{-8}$ J. The number of photons per pulse is therefore E_{laser}/E_{photon} which is of the order of 10^{11}.

Pulse-picking: With a repetition rate around 76 MHz, the lasers used for this work produce a light pulse every 13 ns. To transmit only certain pulses and block all the others (*pulse-picking*), two devices are commonly alternatively used: the *acousto-optic modulator* (AOM) (used in Chapter 6) and the *electro-optic modulator* (EOM) (used in Chapters 4 and 5). In the following I will briefly explain how these work, and as an example I shall detail how pulse-picking was achieved using AOMs for the experiments reported in Chapter 6.

Acousto-optic modulator (AOM): Just like ripples on the surface of a lake, sound propagates as mechanical waves carried by the medium's molecules and atoms. Acoustic waves travelling through a crystal can be modelled as crests of increased refractive index alternating with troughs of decreased refractive index. Light incident on such acoustic wavefronts will experience Brillouin scattering [102]. It can be shown that, for an optical wave scattering from sound with a frequency of order 10^8 Hz (Bragg regime), the condition for constructive interference of the scattered light can be approximated as Bragg's law[103, 104]:

$$n\lambda_L = 2\Lambda \sin\theta_d, \tag{2.8}$$

where λ_L and Λ are respectively the optical and acoustic wavelengths, n is an integer and θ_d is the angle of the incident and scattered light.

AOMs can be used as optical switches by turning on and off the radio-frequency (RF) signal sent into the crystal, for example using a TTL signal generator (such as the delay generator depicted in Figure 2.10 and 6.23): the zeroth diffraction order will still be transmitted, but the beam will no longer be scattered and there won't be any light in the first order. When the RF is on, the two beams (zeroth and first order) can be separated using an optical aperture. Then can hence be used to select individual pulses (while suppressing the others) from a beam coming out of a pulsed laser. This is how pulse-picking is achieved.

Electro-optic modulator (EOM): Electro-optic modulators are based on the Pockels effect: the linear electro-optic effect where the birefringence of a non-centrosymmetric crystal is modified in proportion to the applied electric field strength (as opposed to the Kerr effect, where the change is proportional to the square of the field). In a birefringent medium, the refractive index depends on the polarisation and propagation direction of incident light. In the case where that light propagates orthogonal to the optic axis, the polarisation components

perpendicular (*ordinary*) and parallel (*extraordinary*) to the optic axis see different refractive indices n_0 and n_e respectively. Travelling with a velocity $v_e = c/n_e$ (where c is the speed of light in vacuum) different from $v_0 = c/n_0$, the *extraordinary* component gradually builds up a phase difference with its *ordinary* counterpart, rotating the overall polarisation as illustrated in Figure 2.7. In a nutshell, a Pockels cell behaves like a tunable waveplate.

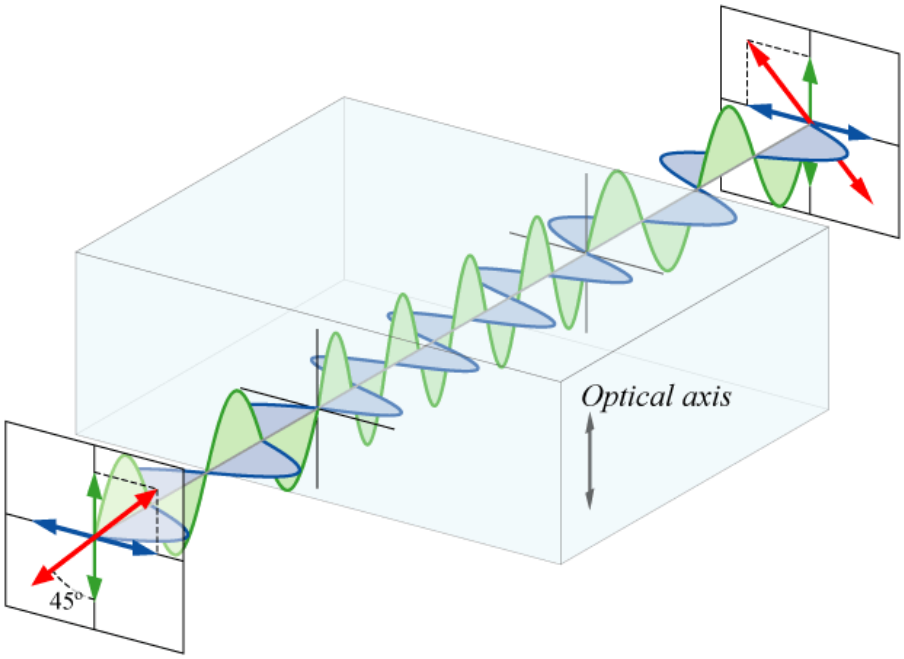

Fig. 2.7 **Rotation of the polarisation of light through a birefringent crystal.** Linearly polarised light (red arrow) propagating perpendicularly to the crystal's optic axis can be decomposed into a parallel (green) and a perpendicular (blue) components travelling with different velocities. A phase difference gradually builds up, rotating the polarisation. In this particular case, the delay after the crystal is exactly half of a wavelength. Figure copied from the english Wikipedia.

The EOM-based pulse-picker used for the work reported in Chapter 4 and 5 (ConOptics 350-50 Potassium Dideuterium Phosphate (KD*P) Crystal Series and a power supply with a 8 ns rise-time) consists of a Pockels cell, which manipulates the polarisation state according to a modulated electrical signal or pulse sequence (Figure 2.8 **a**), and some polarising optics transmitting or blocking each pulse depending on its polarisation (Figure 2.8 **b**). In general, the transmitted light is elliptically polarised. For the special case when the retardation Γ is $\pi/2$ (quarter-wave value) it is circularly polarised, and for $\Gamma = \pi$ (half-wave value) it is rotated by 90deg (as in Figure 2.7). The retardation Γ depends on the wavelength λ, the birefringence Δn and the crystal's length I as follows:

$$\Gamma = 2\pi\Delta n I/\lambda, \tag{2.9}$$

while Δn is proportional to the electric field experienced by the crystal[105]. The polarisation changes are described by the tensor properties of the crystal's susceptibility (second order). These relate the polarisation state of the input and output beams to the structure and orientation of the crystal.

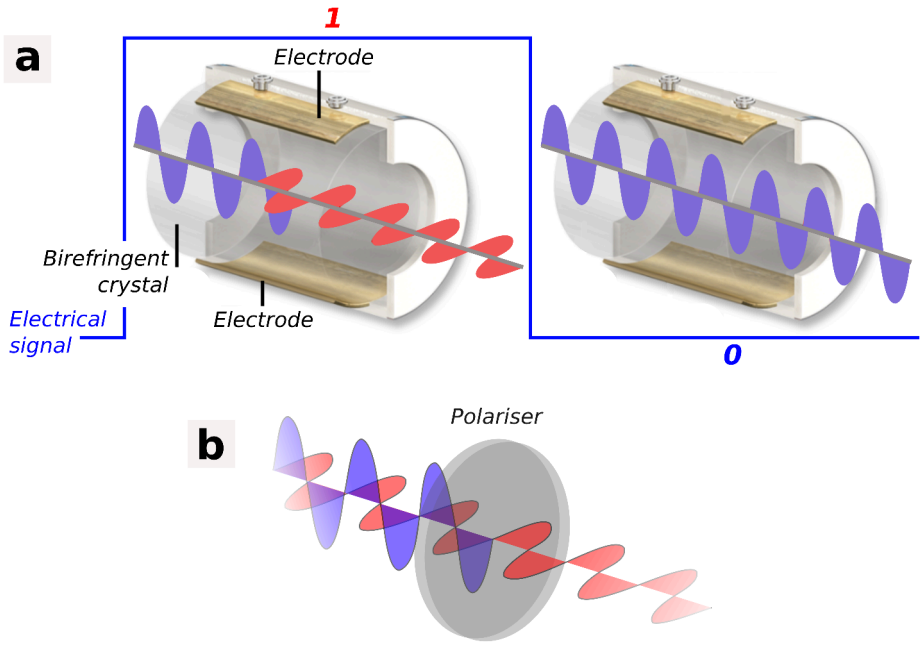

Fig. 2.8 **Optical switching with an EOM.** (**a**) When an electrical pulse is sent to the EOM, the polarisation of the incoming light (blue) is rotated (red). (**a**) Placed after the EOM, a polarising optics transmit or block the light depending on its polarisation.

Main differences between AOMs and EOMs: Both AOMs and EOMs can be used for pulse-picking. The choice of the pulse-picker is then dependent on the setup in addition of which it needs to be implemented. When doing time-resolved measurements, the most important consideration is the rise-time (or response time) of the device. On this territory, while EOMs are only limited by the response time of the electronics (signal generator), modulation frequency in AOMs is limited by the time that the acoustic wave takes to propagate through the complete cross-section of the input beam. In typical AOM crystals, the acoustic velocity ranges from 110 to 1600 ns/mm[106], and the rise-time therefore depends on the beam's diameter. However, because electro-optic media are very often piezoelectric, for some driving frequencies close to the acoustic resonance of the crystal (generally in the 1-100MHz range) unwanted amplitude modulation and beam deflection can occur. Another

difference between AOMs and EOMs is the (theoretical) extinction ratio: generally around 300-700:1 for an EOM[107], and above 2000:1 for an AOM[108], making AOMs more suitable for very sensitive studies such as quantum optics experiments. AOMs also conserve the polarisation of the incident light. However, they need to be specifically designed for narrow bandwidths, while EOMs are generally broadband (see Equation 2.9). Indeed, the operating wavelength λ, modulation frequency f and optical power density dictate the AOM design parameters in such a way that they must satisfy Bragg's law. A measure of the Bragg condition is given by the *Q-factor*:

$$Q = 2\pi \frac{\lambda L f^2}{nV}, \tag{2.10}$$

where V is the acoustic velocity, L is the interaction length and n is the refractive index. Ideally, Q should be greater than 10 for strong Bragg diffraction. However if the *Q-factor* is too high, the device will be very sensitive to angular alignment and intolerant of input beam divergence (or convergence)[109]. EOMs and AOMs have a comparable laser damage threshold: around 5W/mm^2 (in CW).

Pulse-picking with acousto-optic modulators (AOM): Pulse-picking with AOMs and EOMs is analogous. As an example, I will now explain how the AOMs used for pulse picking in Chapter 6.4 were set up. The ultrafast Ti:Sapphire laser used in Chapter 6 (Coherent Mira HP) produces pulses of light with a temporal width of about 3 ps, and a repetition rate of 76 MHz meaning that individual pulses are about 13 ns and nearly 4 m apart, in the temporal and spatial pictures respectively. In order to pick individual pulses, the response of the AOM must be faster than this delay. The rise time, also called 'access time' T_a of such devices is strongly dependent upon the nature of the crystal (material) and the diameter of the light beam passing through it [110]:

$$T_a = \frac{\phi}{V}, \tag{2.11}$$

where ϕ is the light beam diameter inside the AOM and V is the acoustic velocity in the crystal. In order to obtain as sharp a rise time as possible, the diameter D of the laser beam before the lens and the focal length f of the lens used to focus it into the device should be carefully chosen. For a Gaussian profile (which is approximated to be the case here), the beam diameter inside the AOM is defined as twice its waist ω_0 which depends upon the two aforementioned parameters as follows [111]:

$$2\omega_0 = \left(\frac{4\lambda}{\pi}\right)\left(\frac{f}{D}\right) = \phi, \tag{2.12}$$

where λ is the wavelength of the light. Combining equations 2.11 and 2.12 gives the access time T_a as a function of the beam diameter D before the lens and the focal length f:

$$T_a = \frac{1}{D}\left(\frac{4\lambda f}{V}\right). \tag{2.13}$$

Our device, a fast 350 MHz AOM optimised for 700-950 nm (AA Opto-Electronic MT350-A0.2-800), uses a TeO_2 crystal in which the sound velocity is 4200 ms^{-1} and a rise-time up to 5 ns (according to the manufacturer [112]). The wavelength needed to perform the experiment is 737 nm, and in order to focus tightly into the crystal, the choice was made to use a lens with a short focal length: f=50 mm. Knowing this, the dependency of the rise time on the beam diameter can be calculated. The calibration graph plotted in Figure 2.9 shows that a beam diameter of 2 mm (before the lens) would give a fast enough response of the AOM.

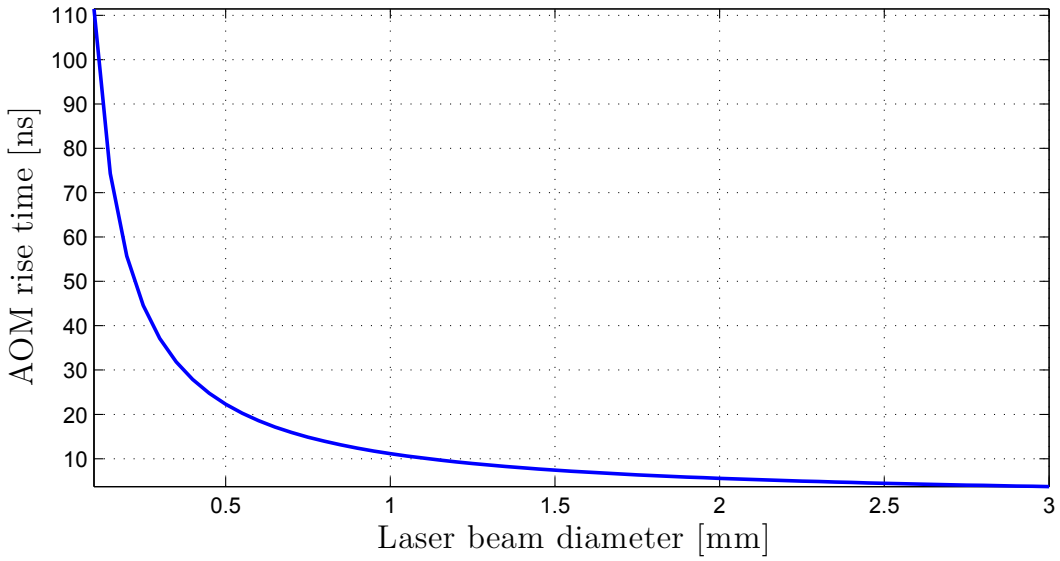

Fig. 2.9 AOM rise time depending on the beam diameter before the focusing lens.

In order to increase the diameter of the beam, we implemented a telescope before the first beam splitter consisting of a concave lens (f_1 = -50 mm) and a convex lens (f_2 = 200 mm) for collimation. Going through the AOM should not have any noticeable impact on the shape and profile of the laser pulses, apart from a 350 MHz shift in frequency.

To measure the extinction ratio achieved with the pulse picking, we used a single-photon counting module, a single-photon avalanche diode (SPAD) coupled to a time-to-amplitude converter (TAC) or a time-to-digital single-photon-counting module as depicted in Figure 2.10 (TAC - Ortec 567 in Chapter 6.4 and Picoharp in Chapter 4 and 5). To the start channel we connected the delay generator's output (identical to the signal sent to the AOM). The

beam coming from one of the AOMs, attenuated very strongly by neutral density filters, was coupled into a fibre to the SPAD. The measured signal-to-dark-count was $\sim$1000. In order to test the setup, a pre-scaling factor was set on the delay generator in order to reduce the repetition rate of the laser by 20 through the AOM. After each 'start' trigger, the TAC was set to look for a 'stop' trigger in a time window of 200 ns. During that time interval, any 'start' pulse would be ignored (although in our case the 'start' channel was triggered every 260 ns only). Figure 2.11 shows the response of the system measured through a fast photo-diode for an AOM pulse width of 10 and 30 nanoseconds. The delay visible between the two pulses is due to the length of the BNC cables between the devices and the oscilloscope. The bad shape of the AOM pulse is attributed to electronic noise and reflections in the BNC cables (also visible on the right side of the optical pulse). The number of counts as a function of the time elapsed is shown in Figure 2.12 using a logarithmic scale, after an integration time of 37 minutes. The extinction ratio in dB can be estimated for each laser pulse:

$$\text{extinction ratio} = -10\log_{10}\left(\frac{A_p}{A_{max}}\right), \tag{2.14}$$

where A_p is the number of counts contained in the pulse under consideration and A_{max} the area of the pulse intentionally selected with the AOM. Figure 2.12 shows that the extinction ratio is 22.7 dB for the adjacent pulse, and about 32 dB on average for the other pulses.

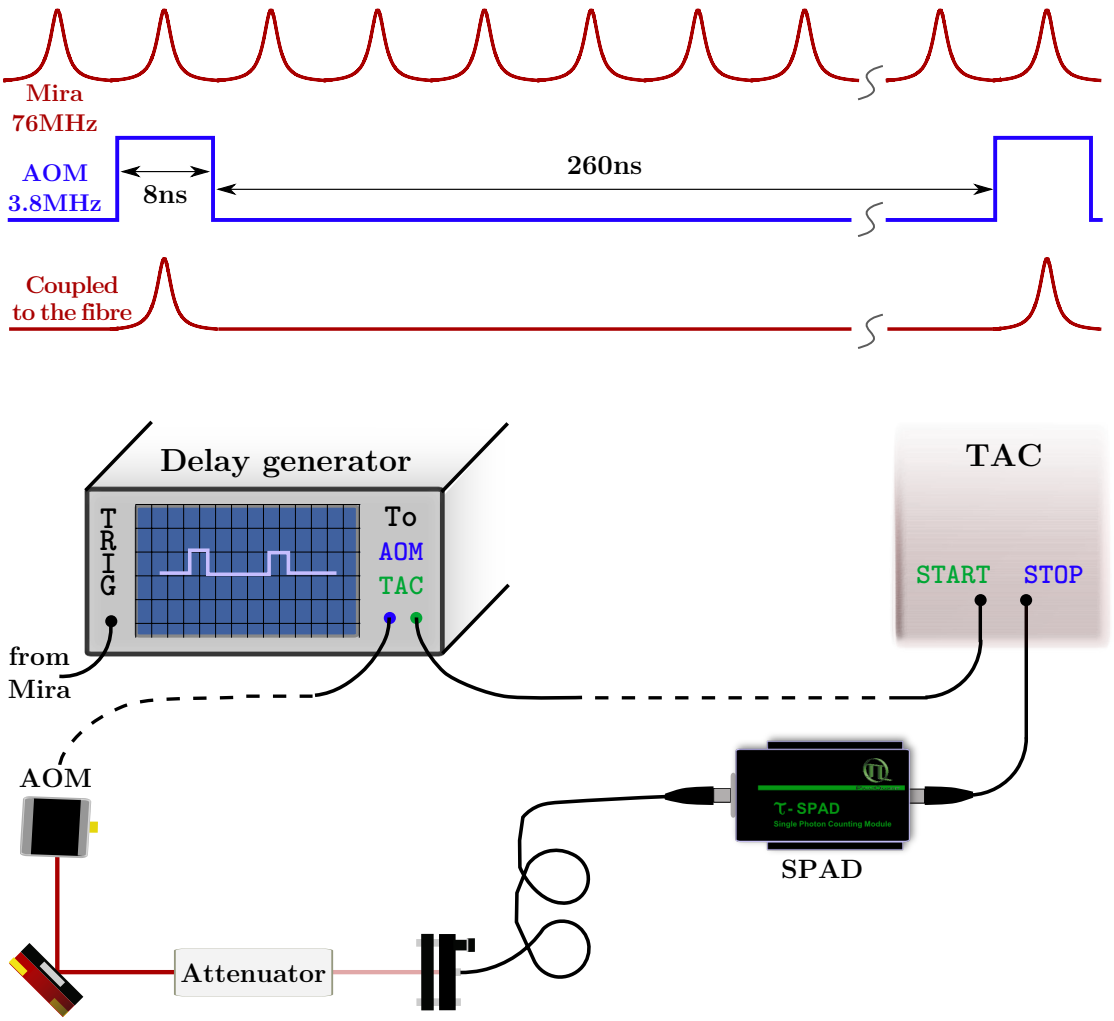

Fig. 2.10 Layout for the time-resolved measurement with a TAC of the number of photons collected by the SPAD, as the AOM is picking one every 20 laser pulses.

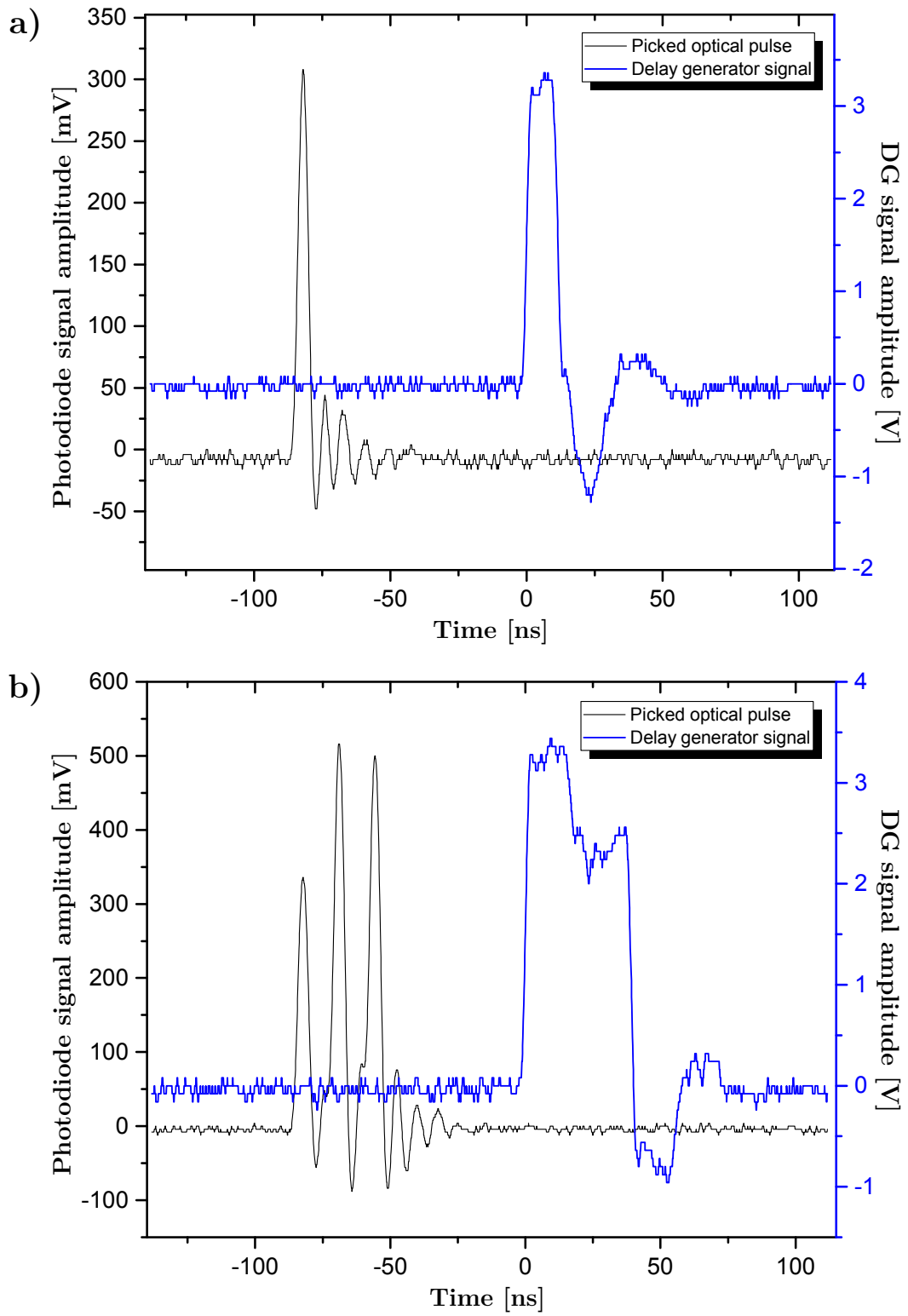

Fig. 2.11 **Selection of single optical pulses with an AOM.** An AOM pulse width of **a**) 10ns and **b**) 30ns allows to pick one or multiple pulses, respectively.

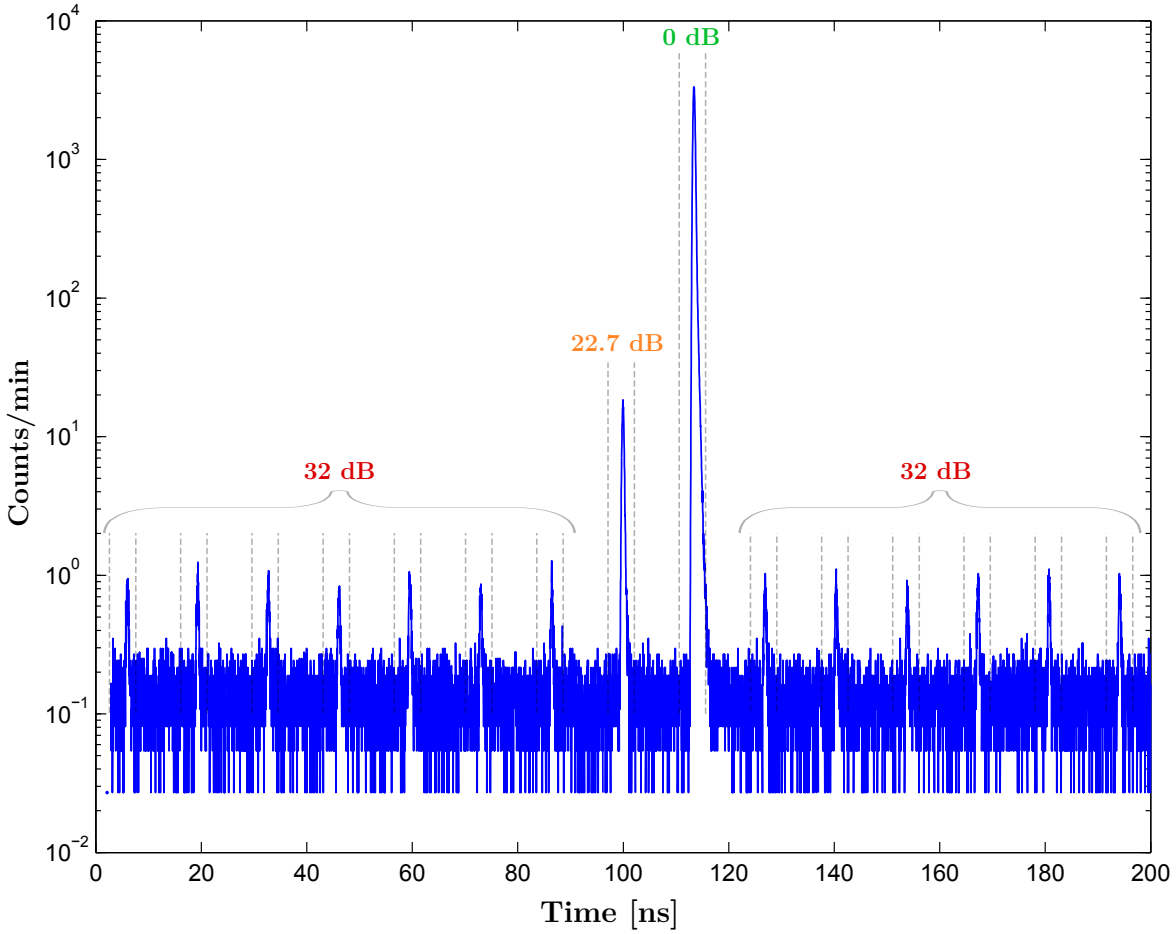

Fig. 2.12 **Number of counts as a function of the time elapsed after each 'start' trigger**, integrated over 37 minutes. The extinction ratio is indicated for each pulse.

2.1.3 Optical setup for two-photon measurements

For two-photon (2P) experiments, a Coherent Ultra II Ti:Sapphire excitation laser (700-1100 nm tunable, 150 fs pulse duration, 80 MHz) pumps a Coherent / APE OPO which in-turn is optically coupled to the input of a confocal microscope through a 950 nm short-pass dichroic to block any light with an energy higher than the material's band-gap. The sample is mounted on a three-axis stage, which allows the excitation volume to be moved both laterally across and into the depth of the film, thus permitting tomographic mapping of optoelectronic properties. A schematic of the setup is shown in Figure 2.13

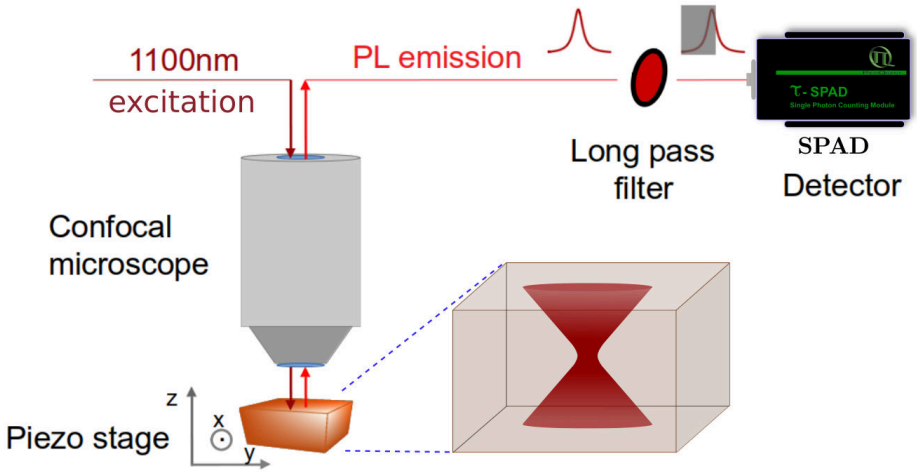

Fig. 2.13 **2P-PL microscope**: a pulsed near-infrared Ti:Sapphire laser is coupled to a confocal microscope with a dichroic beam splitter and an objective lens that focuses the light onto the sample, mounted on a three-axis stage. The photoluminescence from the sample is collected confocally through the objective lens by an avalanche photodetector (SPAD).

In the collection path, photoluminescence (PL) from the sample was filtered with a long-pass filter to only collect photons in the longest wavelength tail of the emission to minimise the impact of reabsorption and photon-recycling effects, which may otherwise cause us to probe different emitting species at different depths[113]. The PL was then collected through a 100 µm pinhole and into detection optics: a SPAD (Micro Photon Devices PDM series). For spectral collection we used an Acton 2300i spectrometer with 150 groves/mm grating and an Andor iXon electron-multiplied CCD.

We used a pulse-picker (EOM) to bring the repetition rate of our laser down to 5 MHz and 1.25 MHz for TRPL measurements. A PicoQuant PicoHarp 300 time-correlated single-photon counting (fully digital alternative to a TAC) system was used to record the timing data. This time-resolved part of the setup is schematised in Figure 2.14.

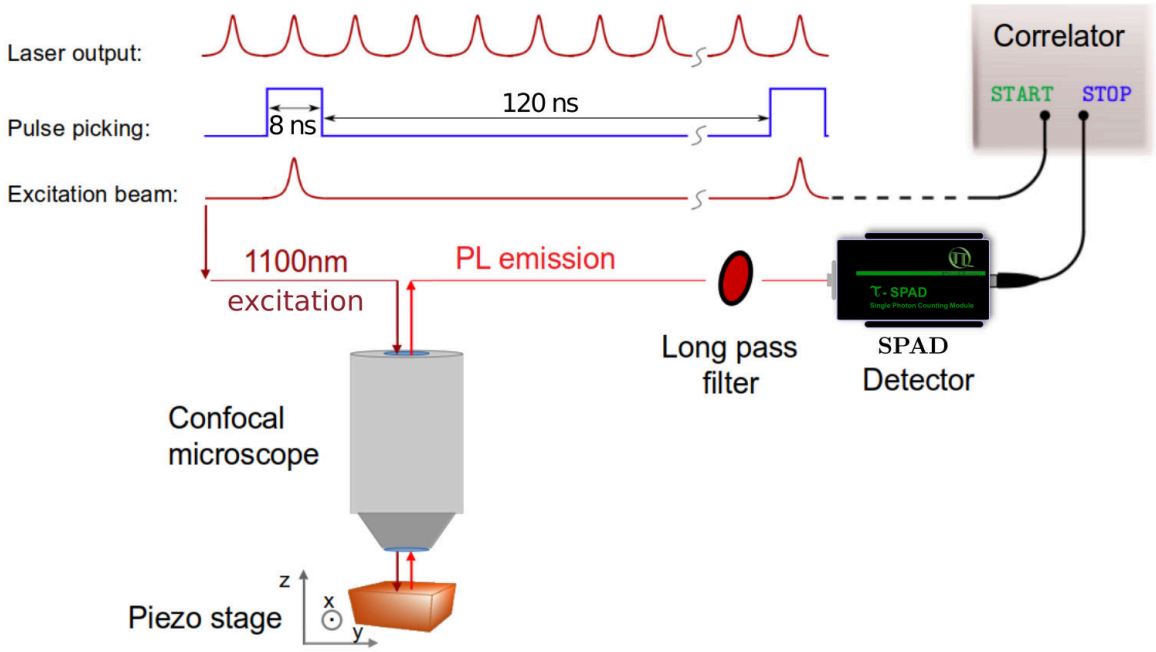

Fig. 2.14 **2P-TRPL setup**: the repetition rate of the laser is reduced by a pulse picker, such that only a pulse every 120 ns is sent on the sample. PL emission is then collected confocally by a SPAD and recorded by time-correlated single-photon counting electronics.

Resolution and depth-of-focus in two-photon microscopy

The lateral resolution of the excitation is diffraction limited, with a full width at half maximum (FWHM) of ∼626 nm at 1100 nm in our case. The derivation for the axial resolution limit taking into account the convolution between the spatial distribution of the fluorescence generation and the product of the PSF of the lens operating at the two wavelengths (excitation and photoluminescence)[94], can be adapted for two-photon excitation[114, 115]. It can be shown that the intensity $I_{2p}(z)$ as a function of depth depends upon the ratio $\beta = \lambda_{em}/\lambda_{ex}$ of the PL and excitation wavelengths λ_{em} and λ_{ex}[115]. The diffraction limited depth response of a two-photon (2P) fluorescence confocal microscope, if the 2P excitation wavelength and photoluminescence wavelengths are the same ($\beta = 1$), is given by[115]:

$$\Delta z_{2p,FWHM} = \frac{0.53\lambda_{ex}}{n(1-\cos\theta)} \approx \frac{1.06n\lambda_{ex}}{NA^2}, \tag{2.15}$$

where λ_{ex} is the excitation wavelength in vacuum, n is the index of refraction of the imaged medium and $NA = n\sin\theta$ is the numerical aperture of the objective lens as introduced earlier in this chapter. This formula slightly overestimates the resolution (FWHM) for the typical two-photon situation where the emission wavelength is shorter than the excitation wavelength. Since the depth response increases with excitation wavelength, the smallest

resolution is obtained when the excitation wavelength is slightly longer than the fluorescence. However the wavelength should be sufficiently long to avoid any one-photon processes such as excitation of defect states in the material.

In practice, the depth-of-focus increases as the focal volume is focused deeper into the sample due to aberrations caused by refraction at the surface of the sample[116]. To obtain the actual depth-of-focus (DOF), a correction has to be applied to the position of the focal point Δ set experimentally. This correction is as follows[116]:

$$DOF = \Delta\left[\left(\frac{NA^2(n^2-1)}{(1-NA^2)}+n^2\right)^{1/2}-n\right], \tag{2.16}$$

where n is the refractive index of the medium and NA is the numerical aperture of the objective lens. In the case of $MAPbBr_3$ perovskite, $n \sim 2.5$[117] and $DOF \sim 4\Delta$.

The PL intensity first increases as the whole focal volume is pushed into the sample and then declines due to both reabsorption of the emitted light and optical aberrations, practically limiting the maximum depth in our system to less than 10 µm[115]. This could be improved significantly with the use of immersion optics. In our case, we estimate the axial resolution to be around 1.5 µm. The two-photon absorption (TPA) cross-section in perovskites has not been well characterised, but we estimate that TPA occurs within a diffraction limited focal volume of approximately 1 μm^3[115].

Temporal resolution of the TR-PL microscope

Traditional single-photon-counting is based on a TAC (as introduced earlier and used in Chapter 6.4), which is essentially a highly linear ramp generator that is started by one signal and stopped by the other. The result is a voltage proportional to the time difference between the two signals, which is then digitised. This design has limitations in the time range that it can cover and the maximum data rate that it can handle. In order to achieve a better resolution, the single-photon-counting module used for time-resolved PL measurements in Chapters 4 and 5 is not based on a TAC design but fully digital (Time-to-Digital Converter or TDC). Such detectors typically have a shorter dead time, hence reducing the distortion effects in time-resolved measurements[118].

The timing precision of a TR-PL setup, defined as its *Instrument response function* (IRF), depends on the temporal uncertainties of all components involved. These are typically the laser pulse width, the laser timing jitter, the detector jitter, and the timing uncertainty of the TCSPC electronics, summarised in Table 2.1 for the setup used in Chapters 4 and 5. The

Hardware	SPAD	TCSPC electronics	Laser	OPO	Trigger diode
Temporal resolution	50 ps	4 ps	150 fs	150 fs	250 ps
Timing jitter	-	<12 ps	<150 fs	<150 fs	<100 ps
Dead time	77 ns	<95 ns	-	-	-

Table 2.1 Temporal resolution of the light sources (laser and OPO), detectors (SPAD an trigger diode) and TCSPC electronics used in our 2P-TRPL setup.

total IRF is a convolution of all component IRFs, but an estimate can be obtained from their geometric sum[96]. According to statistical errors propagation laws[96]:

$$e_{IRF\,system} > \sqrt{\sum e^2_{component}}. \tag{2.17}$$

The achievable temporal resolution of a TCSPC setup is therefore dominated by the slowest component. In our case, that is probably the trigger photodiode used to derive a sync signal from the optical pulse train: a fraction of the excitation beam is picked-off and fed into the TCSPC electronics as "start" signal. The timing jitter for this diode is not provided by the manufacturer, but we estimate that 100 ps is a reasonable upper bound. According to Equation 2.17, the temporal resolution of our setup is then ∼100 ps, and it could be improved by the use of a faster photodiode for pick-off. The timing resolution of the EOM used for pulse-picking should also, in principle, be taken into account.

Two-photon absorption coefficient in perovskite

The proportionality factor β between the absorption coefficient α and the light intensity was recently measured for $MAPbBr_3$ perovskite single crystals using different methods and found to be ∼9 cm per GW at 800 nm[119] and 1100 nm[120]. With a photon wavelength of 1100 nm, the absorption coefficient at the focal point is expected to be two orders of magnitude smaller than for one-photon absorption[56]. To obtain the same order of magnitude of photoluminescence intensity, we used a few nanowatts of one-photon (1P) excitation and an average power between 23 µW and 27 µW (peak power between 125 W and 145 W) for two-photon (2P) excitation. This suggests that the absorption coefficient is 3-4 orders of magnitude lower with 2P than with 1P at 1100 nm, hence somewhere around 100 cm^{-1}. By looking at the parameter space in Figure 2.15, β could be around 5 cm per GW, which is consistent with the value of 9 cm per GW at 800 nm reported in [119] assuming that it should be smaller at 1100 nm than at 800 nm.

At 23-27 µW (around 2000 µJ/pulse/cm^2) with a repetition rate of 1.25 MHz, a laser pulse energy of ∼20 pJ/pulse was used to excite (with 2P) the untreated and treated perovskite films in Chapter 4. This corresponds to a maximum pulse energy density (fluence) of 5 mJ.cm^{-2}, a time-averaged power density of 6.3 kW·cm^{-2}, and a peak power of approximately 16 GW.cm^{-2}. From the pulse energy density and the energy of a 1100 nm photon, the density of photons was ∼2.8×10^{16} cm^{-2} . Assuming a β coefficient of 5 cm.GW^{-1}, the absorption coefficient α at an average power of 23-27 µW is ∼100 cm^{-1} giving a maximum number of absorbed photons per unit excitation volume of 2.8×10^{18} cm^{-3}. Given the uncertainty in the 2P absorption coefficient and through careful comparison with the 1P excitation densities, we estimate photo-generated carrier concentrations in our measurements to be ∼10^{16} -10^{17} cm^{-3}. The pulse energy used for 1P-PL with an average power of a few nanowatts is of the order of ∼2 fJ/pulse, giving a fluence of about 0.1 µJ.cm^{-2} (and a carrier concentration of ∼10^{16} cm^{-3}).

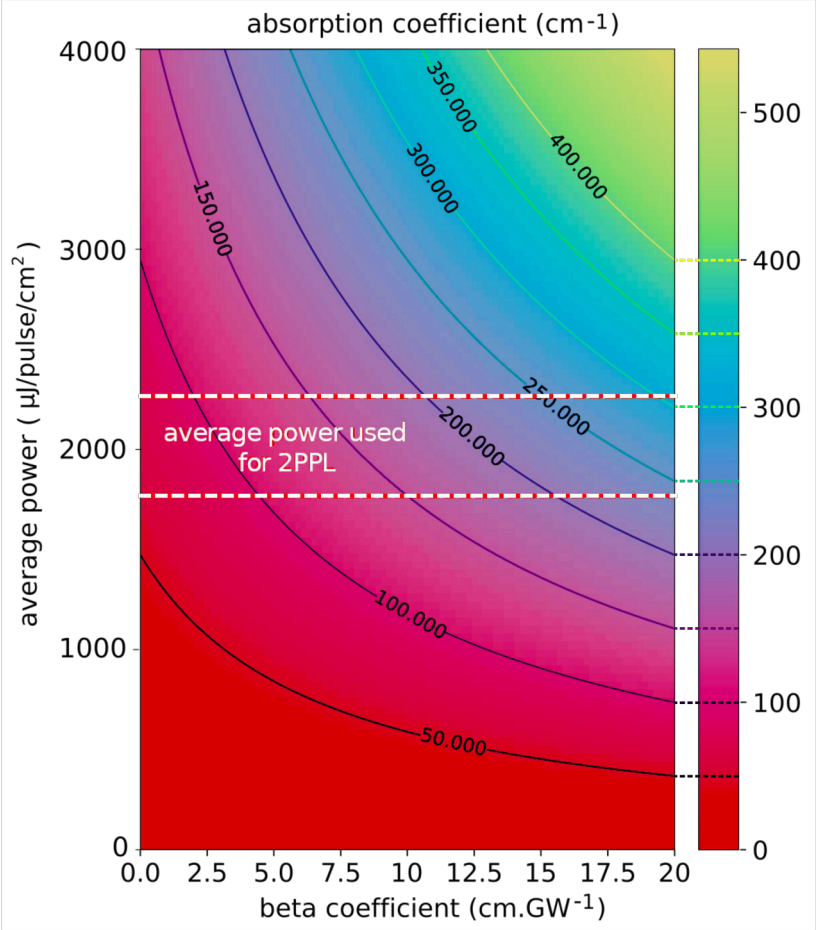

Fig. 2.15 **Parameter space for the 2-photon absorption coefficient** depending on the excitation power used and the value of the proportionality factor β.

2.1.4 Temperature-dependent PL and optical absorption

Photoluminescence (PL) and optical absorption spectroscopy are complementary techniques. Combined, they allow one to explore both the excitation pathways (band-to-band or via molecular vibrations and rotations, for example) and the optical transitions resulting from radiative recombination. Comparing the absorption and PL spectra can help to assess the interactions between charge carriers and their environment, such as the coupling to thermal phonons (vibrations). Moreover, while PL is affected by broadening and is prone to enhancing low-energy inter-band transitions, optical absorption can help to pin down excitonic emission and observe the existence of multiple phases of the material giving rise to different excitation energies. For the experiments presented in Chapter 3, temperature-dependent PL and optical absorption were performed on $MAPbI_3$ perovskite thin films of varying grain size.

Temperature-dependent confocal PL microscopy

Samples were mounted in an Oxford Instruments flow cryostat and cooled down with liquid helium. The temperature was controlled using a digital PID temperature controller from Oxford Instruments. A 532 nm continuous wave diode-pumped solid-state laser (Roithner Lasertechnik GmbH, model RLTMGL-532-100) spectrally cleaned with a bandpass filter was fed into a home-built confocal microscope placed on top of the cryostat. Excitation as well as light collection to and from the samples were performed through a Mitutoyo 50x objective lens (numerical aperture of 0.55, working distance 13 mm) and separated using a longpass filter (dedicated Semrock RazorEdge). The photoluminescence from the sample was then sent to a 500 mm Princeton Acton SP-2500 spectrometer equipped with a liquid nitrogen cooled Si CCD (Princeton PyLoN). Each macro-PL spectrum was obtained with an illumination spot of $\sim$1 mm, using an integration time of 0.5 s and 10 accumulations. We used an excitation density of 0.6 mW.cm^{-2}. During macro-PL series, the illumination dose on the sample was $\sim$18 mJ.cm^{-2} per measurement.

Temperature-dependent optical absorption

A broadband light from a halogen lamp was dispersed with a grating monochromator and focused on the sample to a spot of 1 mm x 3 mm. The transmitted light intensity was measured with a single channel Si amplified photodiode. To obtain high signal dynamics and sensitivity, the measurement was done using the lock-in technique (Stanford Research Systems SR830), with the probing beam as the modulated medium. The sample was cooled with a Janis Research dry cryocooler system (sample in vacuum configuration), steered with a PID temperature controller (Lake Shore 335).

2.1.5 X-ray Diffraction for structural analysis

Bragg diffraction occurs when radiation, with a wavelength comparable to atomic spacings in a crystal, is scattered by the atoms in the lattice. Waves scattered off different lattice planes at a different angle θ travel accumulate a path difference given by $2d\sin\theta$, where d (or *d-spacing*) is the interplanar distance, and interfere. The condition on θ for the constructive interference to be at its strongest is given by Bragg's law:

$$2d\sin\theta = n\lambda, \tag{2.18}$$

where n is a positive integer and λ is the wavelength of the incident wave. X-ray diffraction (XRD) crystallography was used to monitor the temperature-dependent crystal structure of $MAPbI_3$ perovskite films with different grain sizes in Chapter 3 as well as to characterise the samples prepared in Chapter 4. For the experiments in Chapter 3, XRD was performed on the spin-coated films using a Bruker X-ray D8 Advance diffractometer with Cu-Kα1,2 radiation (λ = 1.541 Angström). Low-temperature measurements were performed with a cooling and heating rate of 6K.min^{-1} and a dwell time of 30 min using an Oxford Cryosytem PheniX stage. Spectra were collected with an angular range of $5 < 2\theta < 60°$ with the angular resolution $\Delta\theta = 0.02°$ over 60 minutes.

2.1.6 Scanning electron microscopy

When a beam of electrons with high kinetic energy interacts with a sample, some are backscattered after elastic interactions, and some undergo inelastic interactions where they transfer some of their energy to the sample. *Secondary electrons* originating from the atoms near the surface of the sample following inelastic scattering events are usually used as a signal to image the topography of a surface. Depending on the scanning electron microscope (SEM), the quality and accuracy of the correction of aberrations and the sensitivity of the detector, the resolution can fall between 1 nm and 20 nm.

Unlike optical microscopy, SEM imaging on perovskite films is a destructive measurement. The samples on which SEM was preformed were then discarded and not used for further measurements. The SEM image of the $MAPbBr_3$ in Chapter 4 micro-crystal film was taken on FEI Quanta 600. The surface morphology of the films prepared in Chapter 3 was examined using a Leo Gemini 1530VP FEG-SEM, shown in Figure 3.2 **a**.

2.2 Data analysis

The first framework, designed initially for the analysis of large sets of spectral data, has proven easily transferable to other types of data. I shall start by detailing the algorithm created to serve that purpose, before showing how it can be applied to the analysis of TRPL maps and diffusion data, composed of dozens, hundreds of sometimes thousands of TRPL traces. Global information is extracted through the individual analysis of each trace.

Part of what differentiates the human brain from a computer programme, is the ability to interpret a situation subjectively. But one's subjectivity depends also upon one's experience and own expectations (for example, how many peaks we expect and would like to see on a given spectrum). This leads to a subjective judgement, which could be perfectly valid, but could also be biased. A computer, on the other end, establishes purely objective judgements, based on a well-defined finite set of criteria and assumptions. Both human-made and machine-made judgements can be wrong, but a systematic machine error (or in this case a wrong interpretation) reveals an invalidity of a least one of the hypotheses used to construct the methodology. Poor interpretations can occur for a limited number of reasons, setting the designed framework's limitations. Once these have been delimited, the developed methodology can become a standard, with its known assumptions and limitations.

Large datasets become really useful if we can exploit their size and the number of repeated measurements to build statistics, and this progressively stood out as my main motivation to develop these tools. This framework for spectral analysis is used in Chapter 3 on confocal maps, and a demonstration of statistical analysis on actual data can be found in Chapter 3 section 3.7. Adopting an object-oriented treatment throughout makes complex data analysis and visualisation possible, in a neater way than procedural codes. More importantly, it sets up strong foundations on which to build and implement consecutive layers of increasing complexity. I hope that the methodology described herein will enable more scientists to go beyond single-spectrum analysis, and set out new standards for data treatment. The complete methodology that could be used to understand and reproduce this analysis will be detailed in this chapter.

2.3 General framework for spectral analysis

The general framework that I have developed for spectral analysis is structured around the algorithm schematised in Figure 2.16, using a combination of user-defined and hardcoded parameters (listed in Figure 2.17). These parameters contain most of the assumptions as mentioned in introduction. They can be adjusted to suit a specific type of analysis.

The programme takes in a spectrum and subtracts a background using a model function given by the user (Fig. 2.16 block **A** and parameter **UP.1** in Fig. 2.17). A peak-finding routine is then applied, that identifies all peaks in the spectrum even when they overlap (Fig. 2.16 block **B**). Once all peaks have been detected, initial parameters extracted from the raw data are passed on to a fitting procedure (Fig. 2.16 block **C**).

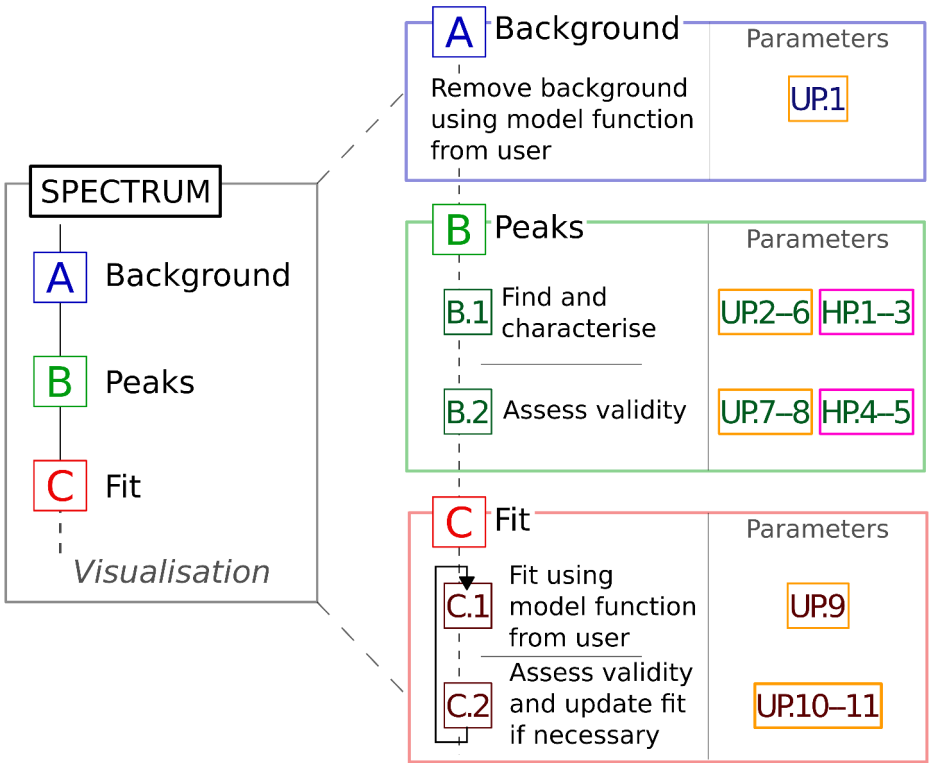

Fig. 2.16 **Overview of the algorithm used for spectral analysis.** It is composed of background subtraction (**A**), peak-finding (**B**) and peak-fitting (**C**) routines. It is divided in subroutines detailed in Fig. 2.27 and 2.28, using parameters given in Fig. 2.26

Each routine uses a set of parameters, summarised in Figure 2.26. In order to make the code as general as possible, the number of hardcoded parameters has been kept low. Each of these will be explained and detailed in the following sections.

2.3.1 Peak-finder

Developing a reliable and resilient peak-finder was probably the most arduous task of all. In order to create a programme able to analyse a spectrum even in the presence of overlapping peaks, I had to work out a robust definition of "a peak". This definition had to enclose a set of self-contained, objective and sufficient criteria and assumptions on which to base the following judgement: "this is a peak". The key elements will be discussed here.

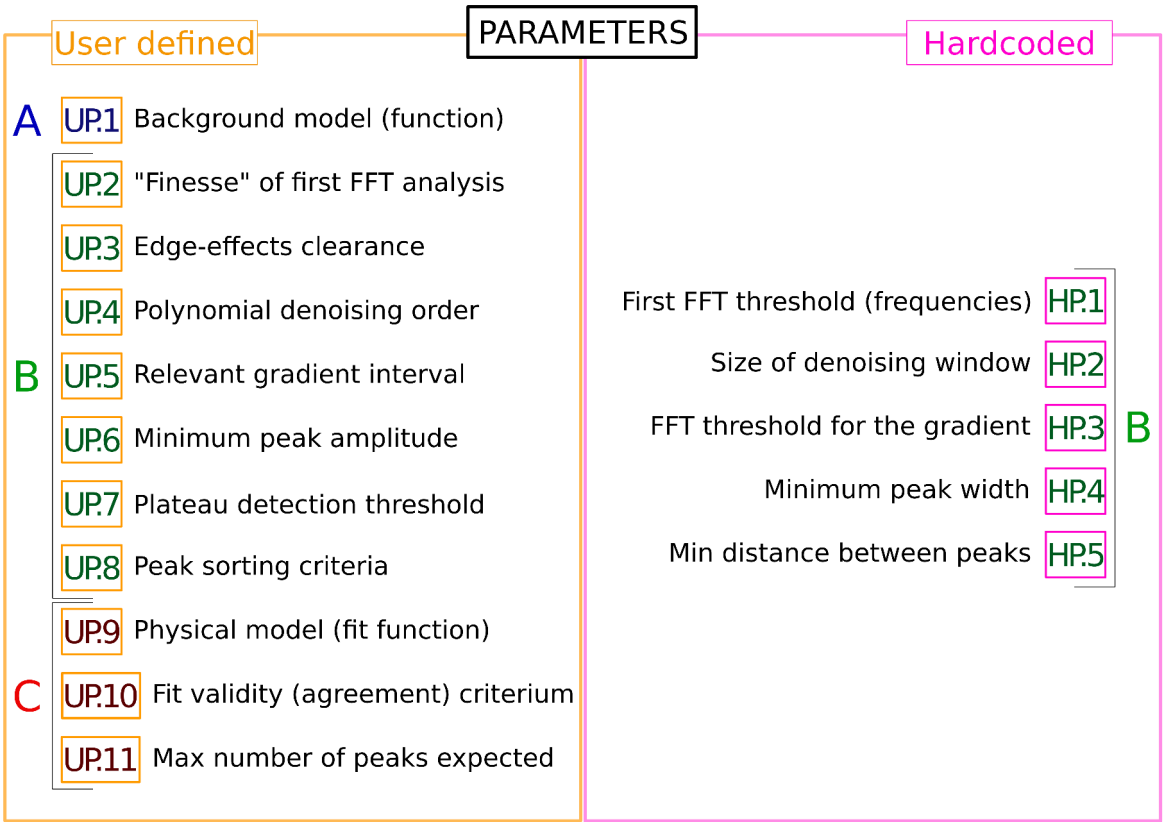

Fig. 2.17 **List of parameters used for spectral analysis.** They enclose the main assumptions and hypotheses used for the analysis. In order to make the code as general as possible, the number of hardcoded parameters has been kept low.

The peak-finder block (block **B** in Figure 2.16) is divided in two subroutines: one finds and characterises peaks on a spectrum, and the other assesses their validity (sub-blocks **B.1** and **B.2**, respectively, in Figure 2.16 and Figure 2.27). Block **B.1** starts with the detection of main peaks, before searching for overlapping or "hidden" peaks.

Detection of main peaks

Main peaks are defined as local maxima. By definition, it's then a maximum located between two minima. However, this only works on ideal signals that are not affected by measurement noise. On a real signal, depending on the sampling rate and the sensitivity of the experimental setup, a very high number of such local maxima can be found on a spectrum, that do not correspond to real peaks (see black curve in Figure 2.18). The first step to take then before analysing a signal is to filter out these high-frequency fluctuations. One common way to do so, is to decompose the signal into periodic sinusoidal components using a Fast Fourier Transform (FFT), apply a low-pass filter, and inverse-transform the result back to

real space. An example of this procedure, indexed as **B.1.a** (Fig. 2.27) is shown in Figure 2.18. Choosing the appropriate cutoff frequency is an important part of the analysis, and it warrants a dedicated user-defined parameter (**UP.2**). To help apprehend this cutoff parameter, I have linked it implicitly to the width **w** of a peak relative to a spectrum of size **L** through the hardcoded parameter **HP.1**. The required user input becomes a simple estimate of this relative width in percent of spectrum, herein called *finesse* and illustrated in Figure 2.19). The latter is then converted by **HP.1** to a number of frequencies that should be kept for the inverse FFT. A table of optimised harcoded parameters including **HP.1** is given in Figure 2.26.

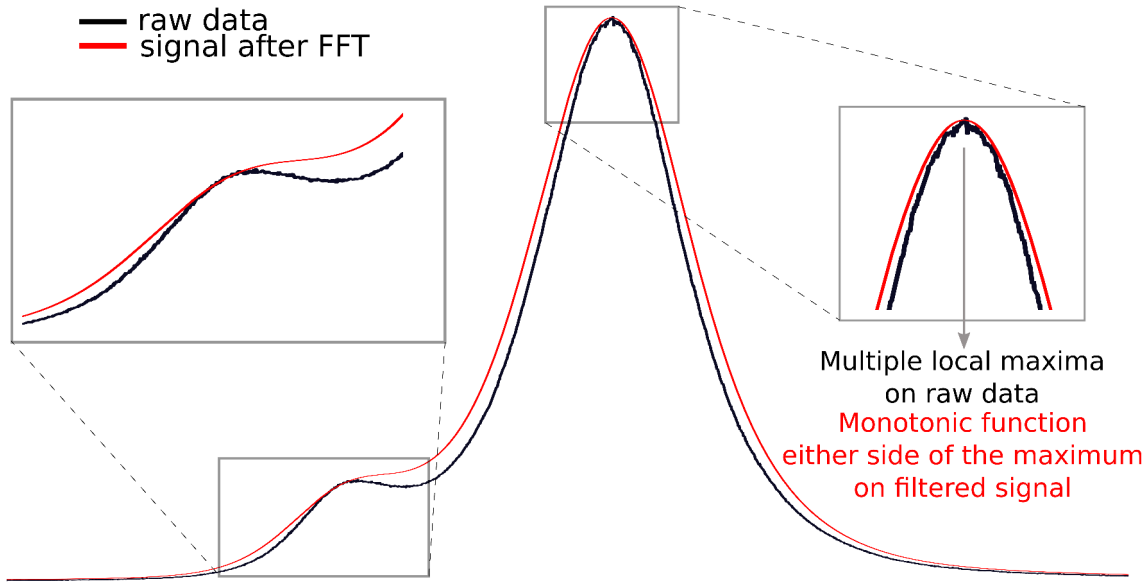

Fig. 2.18 **Signal de-noising with FFT.** After performing an FFT analysis on the raw data, a low-pass filter is applied. The signal is then tranformed back to real space, effectively de-noised.

Great care must be taken when applying a low-pass filter after the FFT. Indeed, filtering the desired frequencies using a step-function (pink curve in Figure 2.20 **a**) induces oscillations in real space, such as the ones visible on the pink curve in Figure 2.20 **b** and **c**. Applying a Gaussian filter, however, with a σ corresponding to the number of frequencies to keep (red curve in Figure 2.20 **a**), gives the much smoother signal shown in red (Figure 2.20 (Figure 2.20 **b**) and (Figure 2.20 **c**)). Indeed, this comes from the mathematical fact that the Fourier Transform of a Gaussian preserves its shape. By virtue of the Uncertainty Principle, functions that are localised in the time domain have Fourier transforms that are spread out across the frequency domain and vice versa, the critical case for this being the Gaussian function (the Fourier transform of a Gaussian function is a Gaussian function).

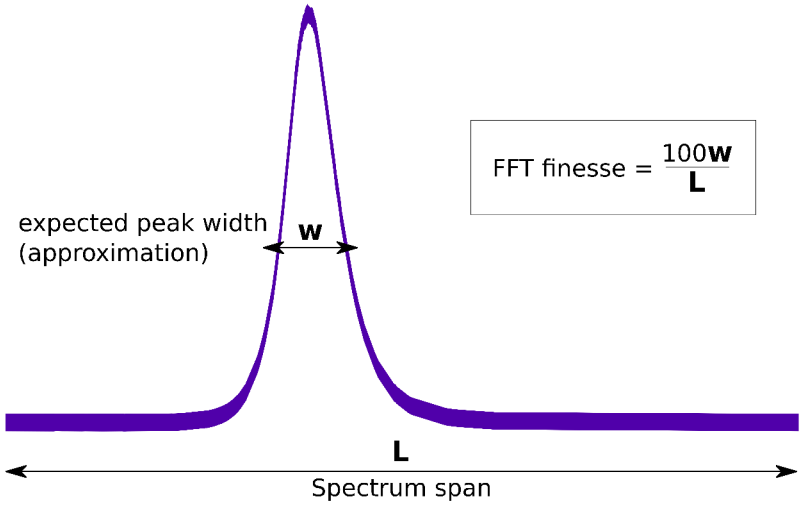

Fig. 2.19 **Finesse of the FFT filtering.** The number of frequencies kept after the FFT analysis is determined by the FFT finesse.

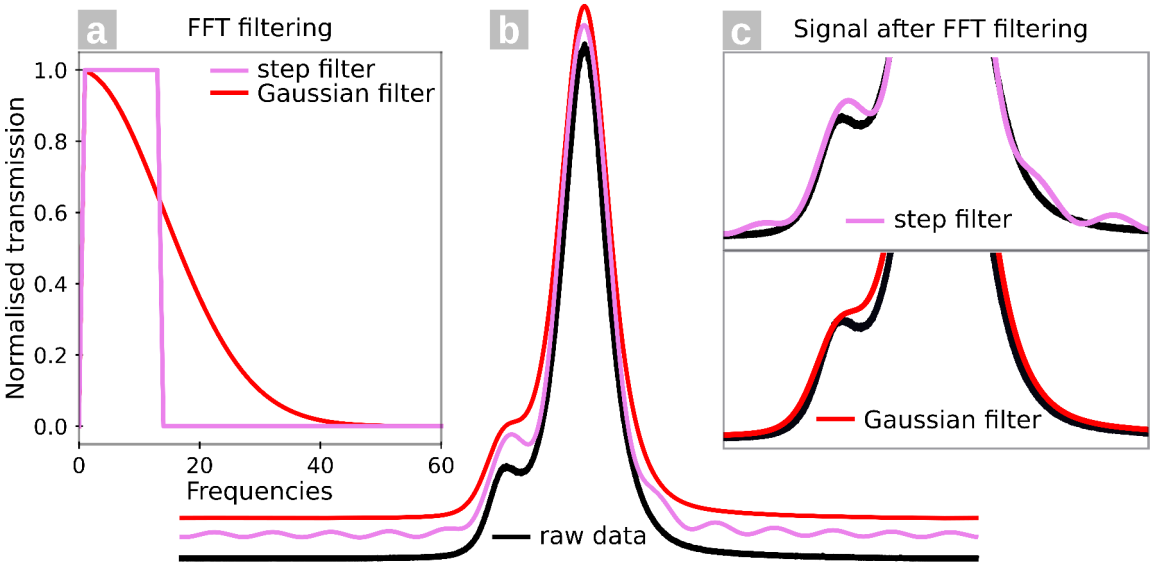

Fig. 2.20 **Gaussian vs step low-pass FFT filter.** (a) low-pass filters used after FFT, giving the red and pink curves in (b) shown with the raw data (black). A close-up is displayed in (c).

Once the FFT analysis is complete, the signal can be used as an input for the routine detecting local maxima. Edge-effects are avoided by ignoring the first and last x% of the spectrum, x being set by the user parameter **UP.3** (Fig. 2.17). Main peaks are then clearly identified, as illustrated in Figure 2.21 **a**. Before characterising these peaks and extracting the initial fitting parameters, a *Savitzky–Golay filter* is applied on the raw data. This is done for the purpose of smoothing the data by fitting successive sub-sets of adjacent data points

(defined as parameter **HP.2** in Fig. 2.17 and Fig. 2.26) with a low-order polynomial by the method of linear least squares. The order of the polynomial is set by the user (parameter **UP.4** in Fig. 2.17) By doing so, the precision of the data is increased without distorting the signal tendency, and the extraction of initial fitting parameters (such as the full-width-half-maximum, the central position and the amplitude) becomes more accurate. Other denoising methods, such as algorithms based on the *Anscombe transformation*[121] can equally be used. The span of a peak is defined as the interval between local minima located on each side of the peak (Figure 2.21).

When there is an overlap between two (or more) peaks, however, there is often no local minimum between the peaks. In such a case, the routine fails to detect the "hidden" peaks (as illustrated in Figure 2.21 **b**), and the need for a different strategy arises.

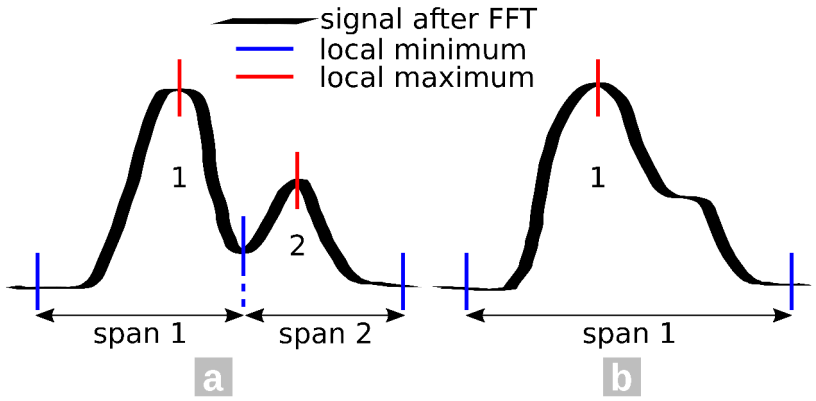

Fig. 2.21 **Detection of main peaks using local maxima of the Fourier-filtered signal.** (a) Spectrum with two main peaks identified as local maxima. (b) Spectrum with two overlapping peaks, where only one corresponding to a local maximum is detected.

Detection of "hidden" peaks

"Hidden" peaks do not correspond to local maxima, but to changes in the slope on either side of a main peak. Easily seen by the human eye, they are more difficult to find for a computer. However, changes in the slope translate into local extrema of the signal's gradient, that our peak detection routine can detect. Just as we made sure to clean the signal from high frequency noise before running the peak detection, we now need to make sure that the gradient does not contain too many artefacts arising from small undulations of the Fourier-filtered data. A simple way to achieve that is to perform a second FFT analysis with a lower frequency cutoff as shown in Figure 2.22, in order to start with a smoother signal. The *finesse* of this second FFT filter is defined as the parameter **HP.3** (Fig. 2.17). Empirically, it was

found on several datasets that lowering the threshold (or cutoff) to 75% of the one used for the first FFT analysis lead to reasonable and reproducible results (Fig. 2.26). Because of this consistency, it was saved as a hardcoded parameter.

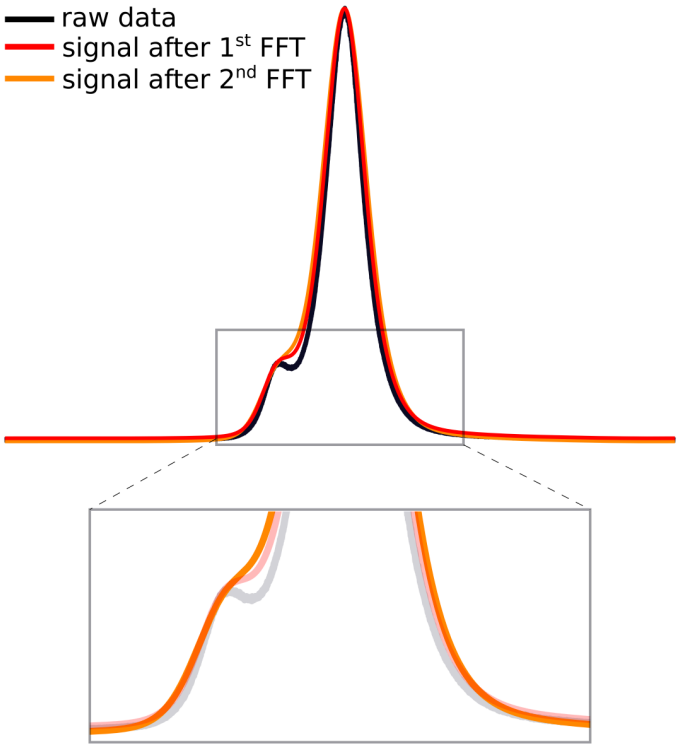

Fig. 2.22 **Further de-noising before detection of "hidden" peaks.** The number of frequencies kept for the 2nd FFT filtering depends directly upon the *finesse* used for the 1st FFT. The second cutoff is at a lower frequency than the first one, giving a smoother filtered signal.

Once the raw data has been filtered a second time, the search for local extrema can begin. Previously in the analysis procedure, we asked the programme to look for main peaks. These correspond to points in the signal where the gradient is zero (Figure 2.23 **a**). "Hidden" peaks are in fact characterised by negative maxima and positive minima of the gradient, that are close but not equal to zero (Figure 2.23 **b** and **c** respectively). Local extrema located in regions where the absolute value of the gradient is too high, however, usually correspond to artefacts or peak broadening that are not caused by the presence of an extra peak (Figure 2.23 **d** and **e**). Therefore, the analysis should concentrate on local extrema of the gradient located in an interval close to zero. This is noted as $grad \in [a,b]U[c,d]$ and illustrated in Figure 2.23. The values of a, b, c and d can be set by the user; they are contained in **UP.5** (Fig. 2.17)

While the span of a main peak was easily determined as the interval between the local minima located on each side of it (Figure 2.21 and 2.24 **a**), a "hidden" peak is associated

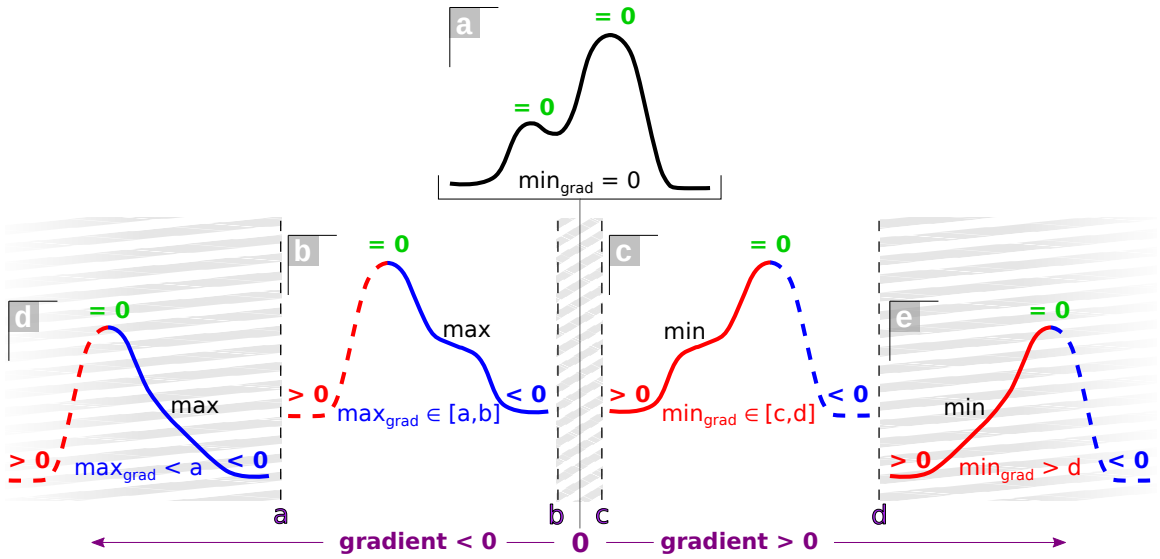

Fig. 2.23 **Detection of "hidden" peaks using local maxima of the gradient of the Fourier-filtered signal.** Red and blue curves represent intervals where the gradient is positive and negative, respectively. In the case of main peaks, the gradient is zero (a). "Hidden" peaks are located on local extrema of the gradient, negative maxima and positive minima (b and c respectively). Outside of the interval [a,b]U[c,d] around zero, local extrema are unlikely to represent extra peaks (d,e).

with only one local minimum. The other limit of the span is set as the adjacent main peak's central position(Figure 2.24 **b**). The "hidden" peaks thus identified are then characterised in the same way as for main peaks, after applying a Savitzky–Golay filter. If the full-width-half-maximum can't be extracted, the peak's span will be used instead as initial fitting parameter.

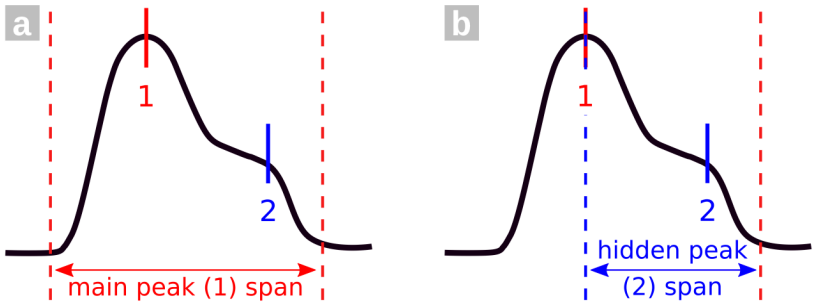

Fig. 2.24 **"Hidden" peak span.** (a) Main peak's span determined as the interval between the local minima located on each side of it. (b) "hidden" peak span, using the adjacent peak's position as lower limit.

The last but not least task for the peak-finder is to assess the detected peaks' validity (see block **B.2** in Figure 2.16). Peaks that are too small (according to the user-parameter

UP.6 in Fig. 2.17) or too narrow (according to the harcoded parameter **HP.4** in Fig. 2.17 and Fig. 2.26) are discarded. Then, a subroutine is used to detect plateaux and discard any peak detected on any of them.

Detection of plateaux

A perfect plateau would have a gradient equal to zero, and any small variation would fall in the $[b,c]$ interval(Figure 2.23) and be ignored by the peak finder. However, real data often contain a linear background with a non-null slope. Small oscillations of that background would be registered as peaks, unless we managed to identify the underlying plateau.

The approach used here is a systematic measurement of the angle α formed by the left and right limits of a peak's span and its maximum (Figure 2.25 **a**).

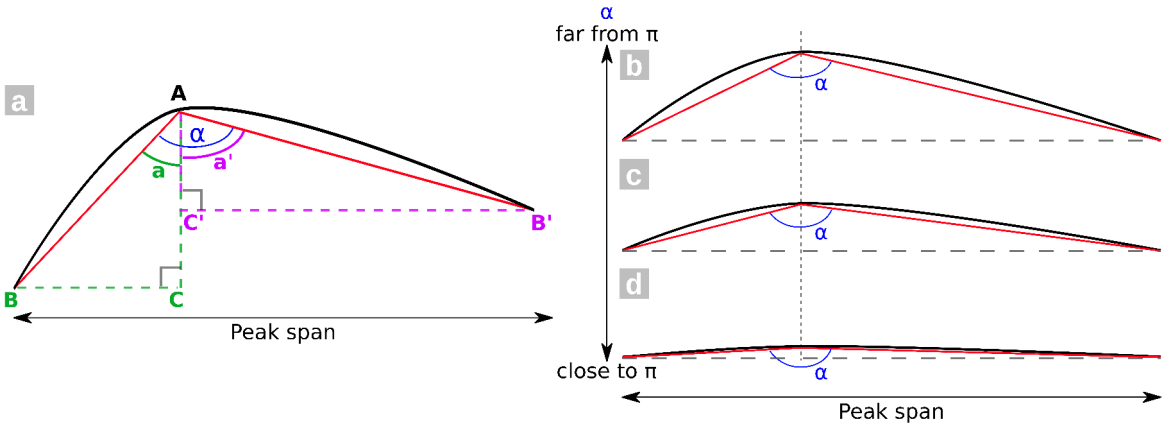

Fig. 2.25 **Plateau detection method.** (a) Geometrical construction used to assess the flatness of a peak. (b,c,d) Evolution of the shape of a peak as α gets close to π.

The value of α is easily calculated using basic trigonometry in each right-triangle ABC and $AB'C'$ formed by the peak's maximum A and its distance from the left and right limits of the span B and B' (Figure 2.25 **a**). To do so, the left and right distances are normalised over the entire spectrum. Let BC and $B'C'$ be the distances from the central position to the left and right limits respectively, in number of sampling bins. We define l and r as follows:

$$\begin{aligned} l &= \frac{BC}{length_{spectrum}}, \\ r &= \frac{B'C'}{length_{spectrum}}, \end{aligned} \tag{2.19}$$

where $length_{spectrum}$ is the total length of the spectrum expressed in sampling bins. The angles a and a' are calculated using the following relations:

$$\begin{aligned} a &= \arctan\frac{l}{AC}, \\ a' &= \arctan\frac{r}{AC'}, \\ \alpha &= a + a', \end{aligned} \tag{2.20}$$

where AC and AC' are normalised to the maximum of the spectrum.

Figure 2.25 **b**, **c** and **d** illustrate how the shape of a peak changes as α gets close to π. A threshold angle beyond which the peak is judged too flat is defined by the user as parameter **UP.7** (Fig. 2.17). Such peaks are then ignored in the analysis.

The programme finally assesses the distance between adjacent peaks. In the case where it is found to be smaller than the minimum value set as parameter **HP.5** (Fig. 2.17 and Fig. 2.26), the affected peaks are merged into one according to the following priority rules:

- Priority to main peaks: If a main and a "hidden" peaks are too close, the latter is discarded.
- If two peaks of the same type (both main or both "hidden") are too close, the peak with the largest span is kept.

Once all valid peaks have ben registered, the list is passed on to the peak-fitting routine.

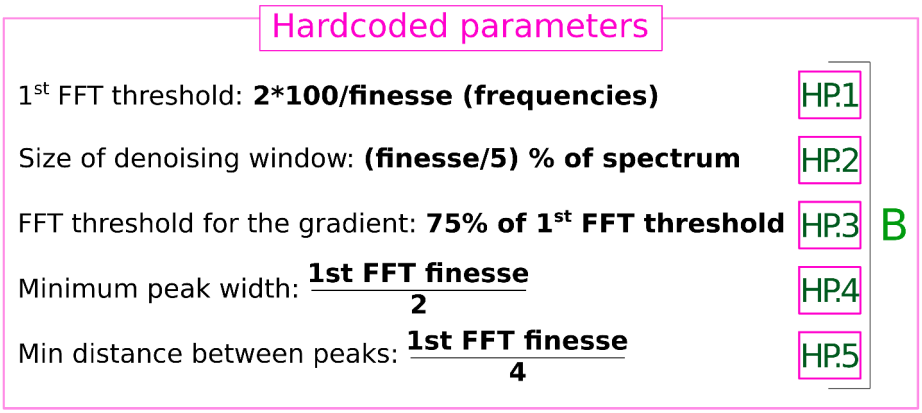

Fig. 2.26 **Optimised hardcoded parameters for the peak-finder.**

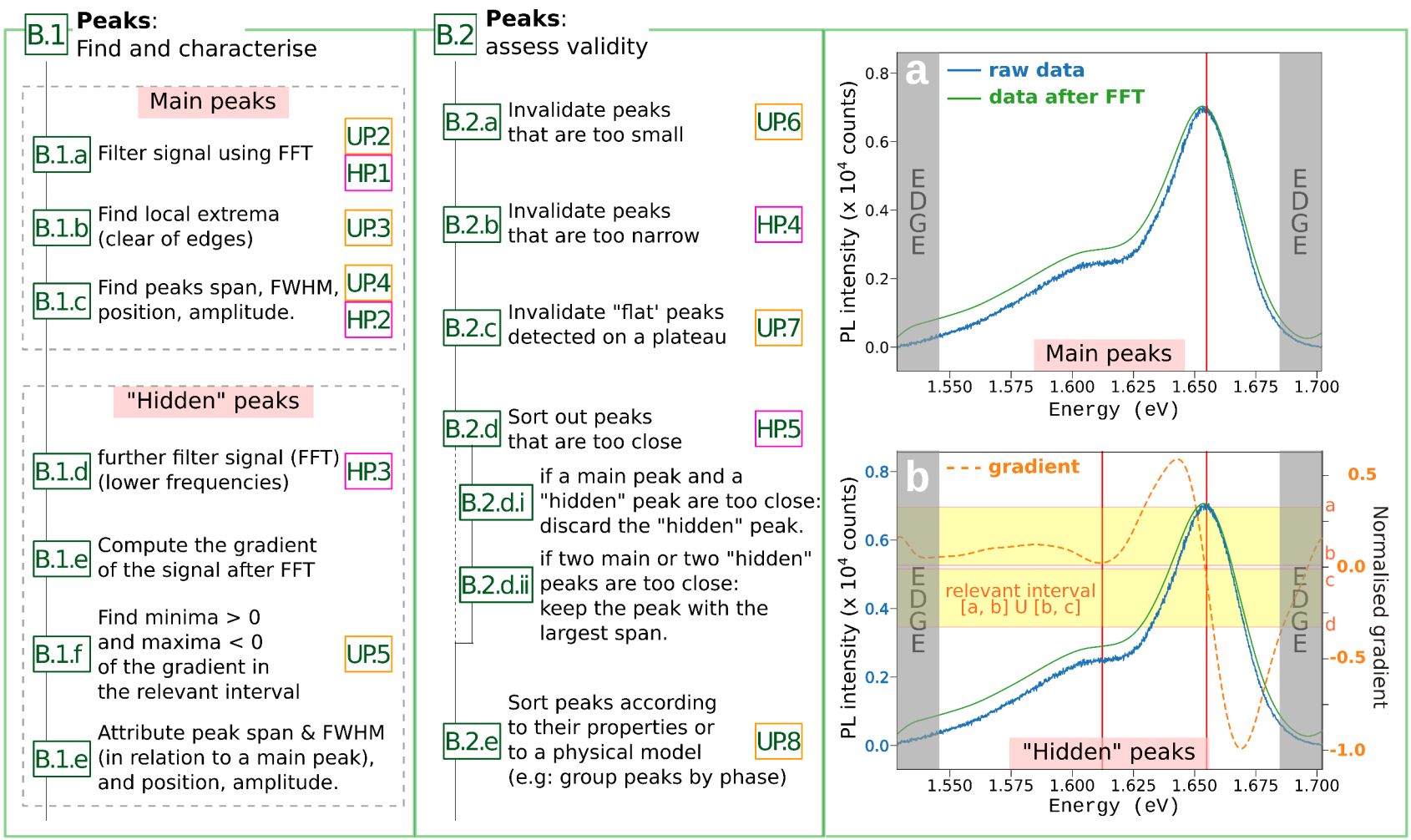

Fig. 2.27 **Peak-finding algorithm.** (a) shows the detection of a main peak as a local maximum in the Fourier-filtered signal. (b) shows the detection of "hidden" peaks as local extrema of the signal's gradient within a relevant interval.

2.3.2 Peak-fitting

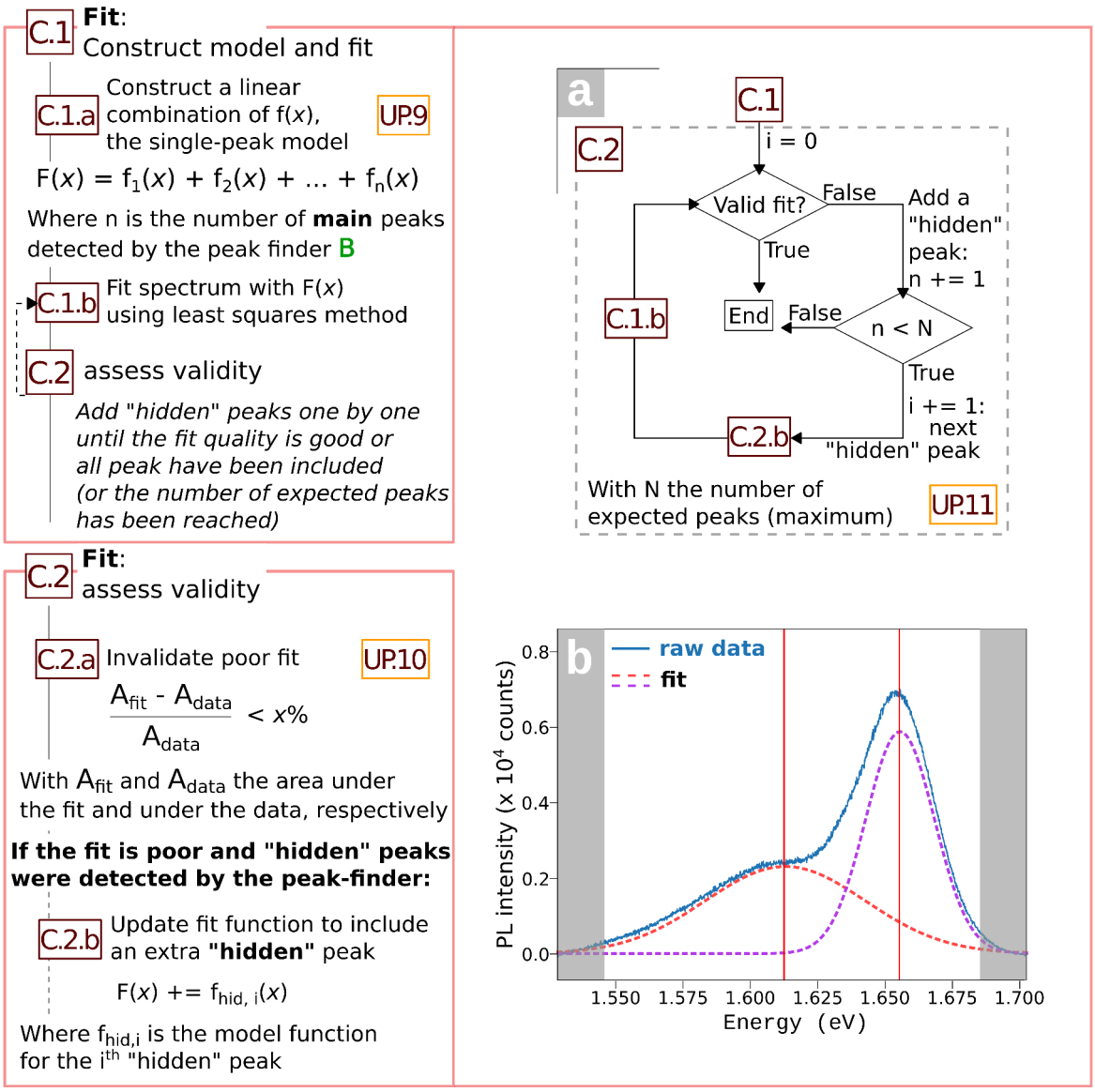

Fig. 2.28 **Peak-fitting algorithm.** The programme gets a physical model from the user and constructs a linear combination of this function with as many elements as the number of main peaks on a spectrum. A fit is calculated and its quality assessed. If the agreement is lower than a user-defined threshold, a new fitting function is created including the largest "hidden" peak detected, if any. A new fit is calculated using this function and its quality is assessed. This loop continues until all hidden peaks have been included, or the total number of expected peaks has been reached, or the quality of the fit is good enough.

A list of peak objects reaches the peak-fitting part of the analysis algorithm displayed in Figure 2.28. These peaks may have been sorted according to some criteria inputted by the

user (**UP.8** Fig. 2.17), such as an arrangement by physical phase or size. Each peak object contains as attributes initial parameters extracted by the peak-finder.

The programme gets a physical model or fitting function from the user (parameter **UP.9**, Fig. 2.17), and constructs a linear combination of this function with as many elements as the number of main peaks on the list (block **C.1.a** in Fig. 2.28). It then uses this function to fit the spectrum a first time using the least squares method (block **C.1.b** in Fig. 2.28). The quality of this fit is evaluated by comparing its integral to the area under the data (block **C.2.a** in Fig. 2.28). If the agreement is lower than a user-defined threshold (parameter **UP.10**, Fig. 2.17), a new fitting function is created including the largest "hidden" peak detected, if any (block **C.2.b** in Fig. 2.28). This new function is used to fit the data, before the fit's quality is assessed again. This loop continues until all hidden peaks have been included, or the total number of expected peaks has been reached (user-parameter **UP.11**, Fig. 2.17), or the quality of the fit is good enough.

The fitting algorithm is described in Figure 2.28 **a**, and an example spectrum is displayed in Figure 2.28 **b**. Each peak object previously created by the peak finder is now augmented with a new set of parameters extracted from the fit. Both sets of parameters are stored and can be accessed easily at all times.

2.4 Analysis of time-resolved and diffusion data.

Generalities

The use of pulsed laser sources and fast electronics makes it possible to probe dynamic processes at the sub-nanosecond level. This section will focus on the numerical methods developed to analyse time-resolved PL (TRPL) data. TRPL traces are acquired using a single-photon counter or correlator, as introduced earlier in this chapter (see 2.1.2). This experimental technique is used in Chapter 4 and Chapter 5.

Static TRPL traces can be turned back into dynamical information. Dividing the signal into time bins (with a width at least as large as the hardware's resolution) allows to extract time-dependent information for further analysis. Figure 2.29 shows an example with 1 ns bins starting 1 ns before the laser pulse (as printed by the software, which allows to check the binning visually prior to any analysis). This is particularly interesting when it comes to analysing TRPL maps, as time-dependent images or snapshots can be extracted.

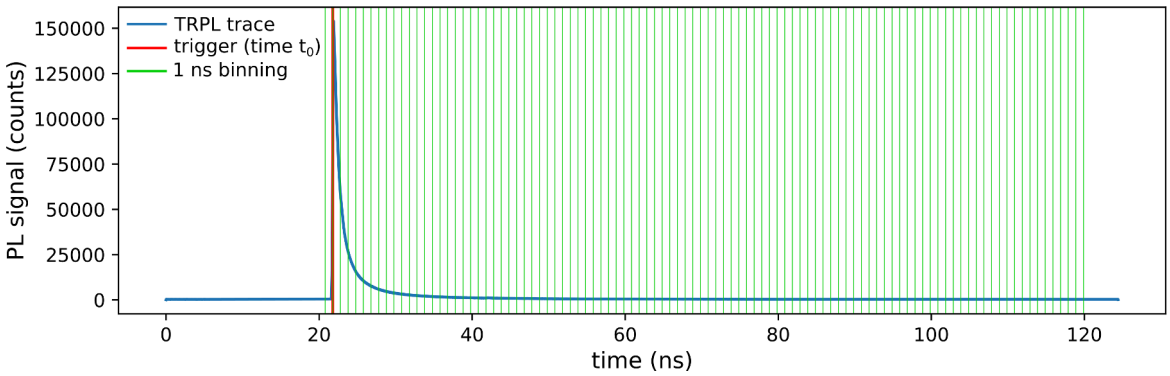

Fig. 2.29 **Binning of TRPL example trace.** The red marker highlights the position of the trigger (laser pulse) at time t_0. Green vertical lines show the time bins (1 ns per bin starting 1 ns before the trigger).

Long PL decays are always difficult to analyse, whether we fit them or extract figures from the raw data, the noise floor introduces artefacts. In particular, the PL emission can appear to be longer-lived than it actually is, and great care has to be taken.

Noisy signals originating from poorly emissive samples can be de-noised using a Savitzky–Golay filter, as introduced earlier in this chapter. Figure 2.30 displays two TRPL traces with (**a**) good and (**b**) poor SNR, as well and the de-noised traces. Blue and orange markers highlight the time (extracted from the raw and de-noised data respectively) at which the PL has dropped below $1/e^2$ ($\sim$13%) of its maximum value (intensity threshold). While the agreement is good in Figure 2.30 **a**, Figure 2.30 **b** demonstrates how noise can impede our

evaluation of the lifetime. The error on the extracted value is defined either as the size of the smoothing window (in this case, ∼0.4 ns) or the time-interval across which the signal oscillates around the intensity threshold, whichever is the largest.

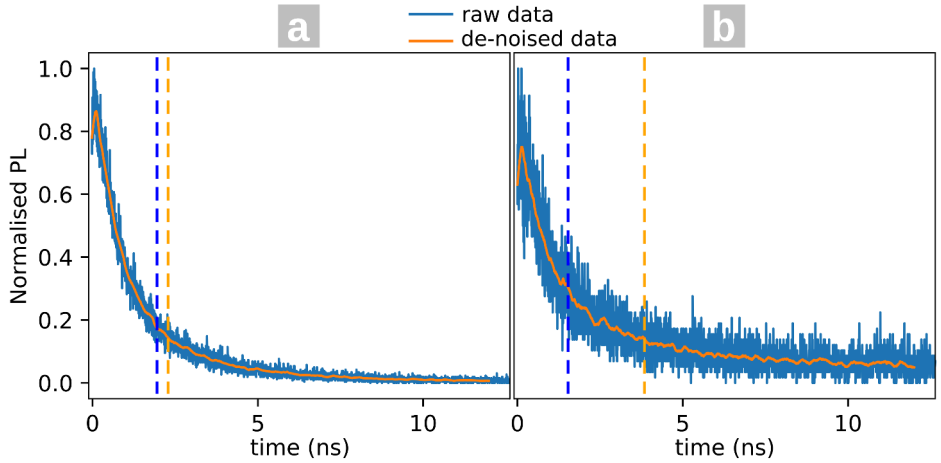

Fig. 2.30 **De-noising of TRPL example traces** with good (a) and poor (b) SNR. The blue and orange dotted lines indicate the time (extracted from the raw and de-noised data respectively) at which the PL has dropped below $1/e^2$ of its maximum value.

Looking at the first and fast part of a decay trace, however, can be more trust-worthy, although the information extracted is only partial. One may want to extract the time at which the PL intensity has dropped to 1/2 or $1/e^2$ of its maximum, as in Figure 2.30. Another route to the extraction of the lifetime is to look for the time at which a particular fraction of the total number of photons was detected. This second method is advantageous as no smoothing is done and no assumption is made regarding the physical model underlying the data. The drawback of method, which is used in Chapter 4, is that background and noise counts will be taken into account in the total number of photon detected. Therefore, the signal-to-noise ratio (SNR) can potentially have a large impact on the result, especially when looking at long-lived emission or large time-measurement windows.

Analysis of 3D tomography

To obtain the 3D tomography data in Chapter 4, the laser is rastered across the sample and PL maps acquired at different depths. The image stack is then filtered to remove any background noise. 3D images are then reconstructed from the stacks in two steps. First, the topography of the sample is rendered using a PL isosurface. For each pixel of the image within this isosurface, the integrated PL and lifetime information are extracted from the TR-PL trace. The pre-treatment and 3D rendering are obtained using the Mayavi environment (Python).

Analysis of diffusion maps

Diffusion is the process of particles (in our case, charge carriers) distributing themselves from regions of high concentration to regions of low concentration. If this process is left unperturbed, there will eventually be a uniform distribution of particles. Upon illumination and excitation, a high density of charge carriers are generated locally which then diffuse in the material. A more detailed introduction to this topic is given in Chapter 5.

Diffusion maps are specific types of TRPL maps, where the collection is scanned across the excitation spot. Figure 2.31 is an example map, showing radial diffusion from a central excitation at different depths inside a $MAPbBr_3$ single crystal.

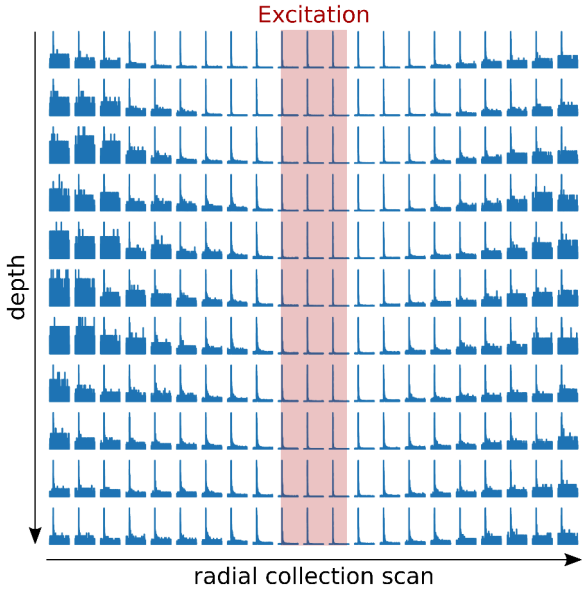

Fig. 2.31 **A diffusion map** showing radial diffusion from a central excitation at different depths inside a MAPbBr3 single crystal. Each pixel is a TRPL trace.

To each pixel corresponds a TRPL trace. In order to compare all TRPL traces to the same time reference, t_0 is determined as explained in section 2.4 from the brightest pixel (assumed to be directly under the laser's illumination). After binning (as in Figure 2.29), time-dependent PL is extracted at each position. A time-dependent luminescence profile across the excitation spot can then be reconstructed. Figure 2.32 shows an example of diffusion profile at a certain time t.

One-photon optical absorption is proportional to the intensity of the light used to excite a material. Assuming Gaussian laser pulses, the initial carrier distribution is therefore expected to be Gaussian. With two-photon excitation, however, the absorption is non-linear and depends upon the square of the intensity. As a result, a Gaussian laser pulse will create a

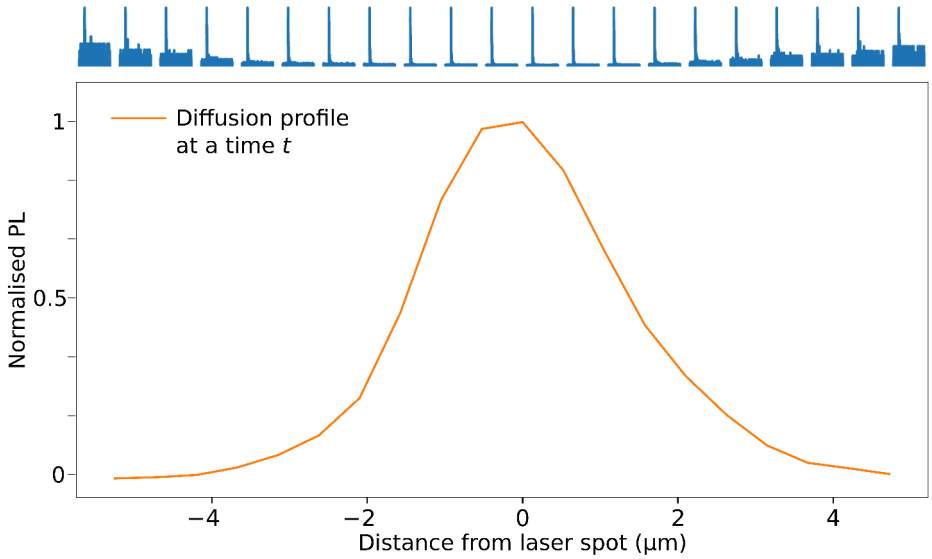

Fig. 2.32 **Example of diffusion profile** at a certain time t, extracted from a radial TRPL measurement across the excitation spot.

Gaussian squared distribution. However, any light emitted by the sample is collected through a diffraction-limited objective lens, and the shape of the PL emission is then convoluted with a Gaussian as explained in Chapter 1. As a result, and to simplify the analysis, a Gaussian fit can be applied on the data.

This is where the spectral analysis methodology developed earlier and described in 2.3 is useful again. The diffusion profile is first characterised by the peak-finder, and its central position and FWHM are extracted. As diffusion profiles can be asymmetrical due to anisotropies and defects in the material, it is not possible to fit them accurately with a simple function (here, a Gaussian function) and special precautions have to be taken.

Since the fitting routine uses a user-defined function, it is possible to input an asymmetrical Gaussian equation, with different standard deviations for the left and right side of the peak (respectively). The drawback of using an asymmetrical function is that all the parameters will evolve at once to converge on the data, and a compromise will be found that may not fit either side as well as we would hope. Another route to fitting asymmetrical data is simply to symmetrise them first. In this scenario, left- and right-hand diffusion can be mirrored individually with respect to the peak's central position. It becomes then possible to fit each of them with a Gaussian function. This procedure is illustrated in Figure 2.33.

The left and right standard deviations can then be extracted from the fit. An example is shown in Figure 2.34, where both methods are compared. The main drawback of the second method is that when the sampling rate is low, the central position of the distribution may

be difficult to identify, in which case the symmetrised shape could be distorted and give inaccurate diffusion lengths. Using this method, time-dependent diffusion can be captured and turned into useful data for further analysis. Moreover, fitting allows one to extrapolate data acquired with a low sampling rate, and thus increases the spatial resolution. This method is used in Chapter 5 to analyse time- and depth-dependent diffusion in $MAPbBr_3$ perovskites.

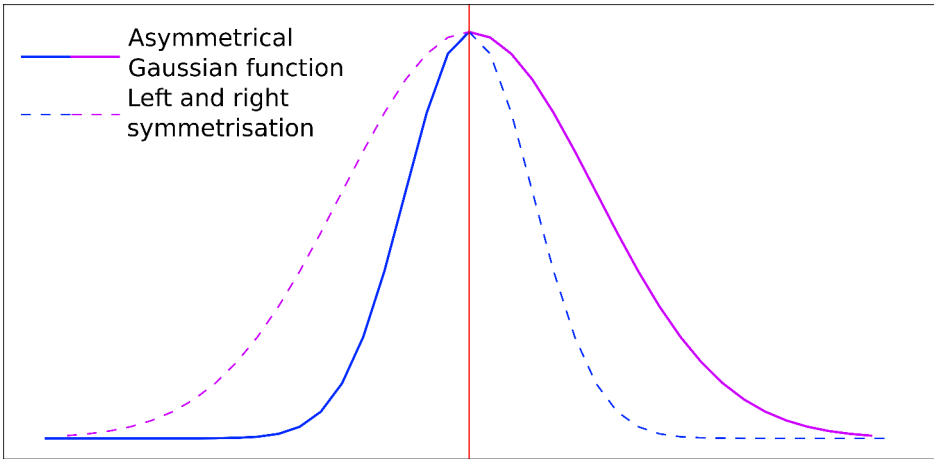

Fig. 2.33 **Symmetrisation of asymmetrical data.** Left- and right-hand tails can be mirrored individually with respect to the peak's central position

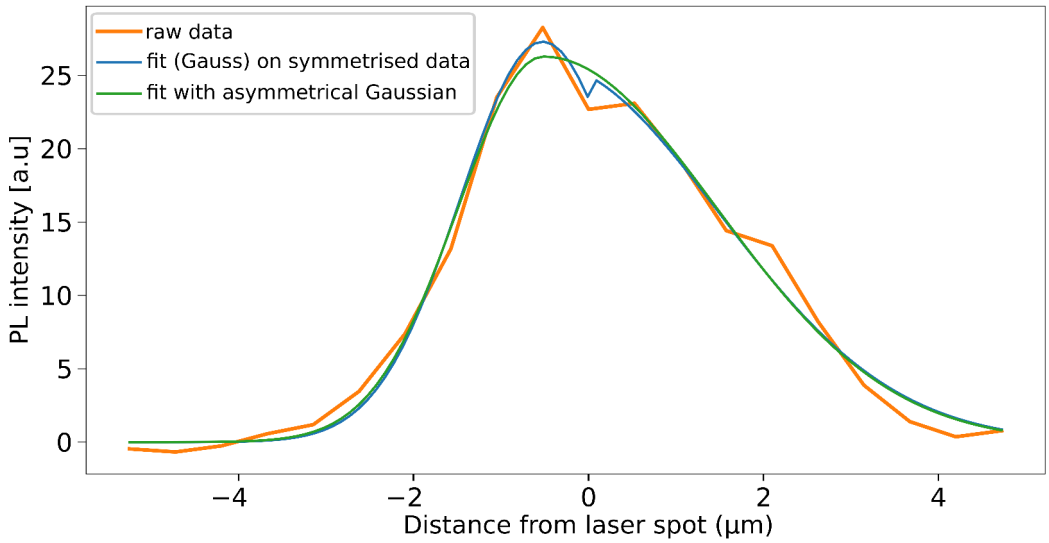

Fig. 2.34 **Asymmetrical data and fit.** The blue fit was obtained in two steps after symmetrisation while for the green one an asymmetrical Gaussian function was made to converge directly on the data.

2.5 Summary

In this chapter, the main experimental techniques used for the work presented herein were introduced and their respective resolutions were discussed. The core technique used for each project (and therefore each chapter) is confocal microscopy, which is distinguished from conventional microscopy by a dramatically increased contrast by removal of out-of-focus haze. It is used in Chapter 3 to perform micro-PL maps on perovskite films, and in Chapter 6.4 to address single SiV centres in diamond. In Chapters 4 and 5, it is complemented by a time-correlated-photon-counting (TCSPC) module in order to perform time-resolved PL (TR-PL) measurements. In both of these chapters, a two-photon excitation beam is coupled to the microscope (2P-TRPL) for 3D tomography and diffusion measurements in the bulk of perovskite structures. X-ray Diffraction (XRD) and Scanning Electron Microscopy (SEM) were also introduced as techniques used in this work to characterise the crystal structure and the topography of samples.

The main methodological framework developed and used for data analysis throughout this thesis was described and explained. It was designed to facilitate the treatment of large data sets: large spectral maps with a number of peaks that varies from pixel to pixel, 3D tomography and diffusion maps. It was designed and implemented using object programming, in order for the code to be more structured and for consecutive layers of complexity to be added in a more sustainable way than with procedural programming.

In the following chapter, the first result chapter, we will discuss the influence of grain size on the low-temperature phase transition in $MAPbI_3$ thin films.

2.6 S'il vous plaît, raconte-moi l'Univers. (If you please, tell me about the Universe.) 2

— Je ne t'ai encore jamais vu, comment es-tu arrivé là ?

Surpris, comme tiré prématurément d'un rêve profond, l'homme le regarda à travers de petites lunettes:

— Comment ? M'as-tu bien demandé « Comment » ?

Gêné, le garçon répondit :

— Je n'avais encore jamais vu de planète apparaitre, et je me demandais comment...

Il n'eut pas le temps de finir sa phrase que le voyageur, esquissant un sourire, s'exclama :

— Alors tu dois être un curieux, toi aussi ! Bonjour l'ami, tu as de la chance de te trouver sur ma route : Cet astéroïde s'appelle Quantique et il est un peu farceur. Je ne peux jamais prévoir où il m'emmène ! D'ailleurs, je ne sais jamais non plus quand il repart... Vite, rejoins-moi avant qu'il ne soit trop tard !

— Je voudrais bien, mais j'habite ici, j'ai une fleur et un mouton sur lesquels veiller. Si ton astéroïde repartait je ne saurais comment rentrer, ...

— Ne t'inquiètes pas, je te montrerai comment retrouver ta planète. Je t'en prie, saute !

A peine le petit prince se fut-il assis auprès de son mystérieux hôte que tous deux furent transportés aux confins de la galaxie.

— Il était moins une ! As-tu une idée de l'endroit où nous avons atterri ?, s'enthousiasma l'homme.

— Qui es-tu pour vivre sur un astéroïde aussi étrange ?, interrogea le petit prince qui comme à son habitude ne répondit pas à la question posée.

— Oh, pardonne-moi, j'ai oublié de me présenter. Je suis physicien. Vois-tu ce carnet ?, dit-il en feuilletant un bloc de feuilles noircies de symboles incompréhensibles. J'imagine et y inscris à chaque voyage un des chapitres d'une bien longue histoire...

— I have never seen you before, how did you get here?

Surprised, as pulled prematurely from a deep dream, the man looked at him through his tiny glasses and said:

— How? Have you just asked me "how"?

Embarrassed, the little prince replied:

— Well, it is the first time that I see a planet appear under my nose, and I wonder how...

Raising a smile, the passenger interrupted him:

— So you must be curious too! Hello my little friend, you are lucky to meet me on my journey, because the asteroid I'm sitting on, Quantum, is a bit of a prankster. I cannot foresee where it will take me next! Neither do I know when it will leave this place for another... Quick! Join me before it's too late!

— I wish I could, but I live here, I have a flower and a sheep to look after... If your asteroid moved again, I would not find my way back, ...

— Don't worry, I shall show you how to find and reach your planet. Please, jump!

The little prince sat next to his mysterious host, and all in a sudden both of them were transported to the far reaches of the galaxy.

— You got on by the skin of your teeth! Where are we now? Do you have a clue?, asked the man with enthusiasm.

— Who are you to live on such a weird asteroid?, questioned the little prince who, as usual, did not answer the question he was asked.

— Oh, excuse-me, I forgot to introduce myself. I am a physicist. Can you see this note pad?, said he while looking through a heap of paper full of cabbalistic symbols. Along my journey I imagine and write the chapters of a long story...

Chapter 3

Influence of grain size on phase-transitions in perovskite films

Grain size in polycrystalline halide perovskite films is known to have an impact on the optoelectronic properties of the films, but its influence on their soft structural properties and phase transitions is unclear. The material is known to adopt 3 different phases of the crystal structure[122] namely orthorhombic (OP, below 150 K), tetragonal (TP) and cubic (CP, above 330 K), as illustrated in Figure 3.1. We investigated the influence of the grain size on the nature of the TP to OP phase transition in $MAPbI_3$ perovskite polycrystalline thin films, with grains sizes ranging across two orders of magnitude from tens of nanometres to micrometer-scale. We characterised the changes in structural and optoelectronic properties of these films by means of temperature-dependent X-ray diffraction (XRD), optical absorption, as well as macro- and micro-photoluminescence (PL) measurements.

Our results revealed that the phase transition is increasingly suppressed with decreasing grain size. We also find that the temperature range of the hysteresis of the phase transition between the heating and cooling cycles increases with decreasing grain size. These results provide strong evidence that the phase transition and optoelectronic properties are significantly influenced by the local grain environment of the material, and reveal new insights to control the phase and optoelectronic behaviour in these mechanically "soft" semiconductors.

This work was published in Advanced Energy Materials[123]. I am the first author of the article. It is the result of a collaboration between the Cavendish Laboratory, the LNCMI in Toulouse (France) and the Wroclaw University of Science and Technology (Poland). The samples were made in Cambridge by Kyle Frohna, Kangyu Ji and myself. XRD measurements were performed in Cambridge by Edward Booker. Macro and micro-PL measurements were performed in Toulouse by Krzysztof Galkowski, Szymon Zelewski and

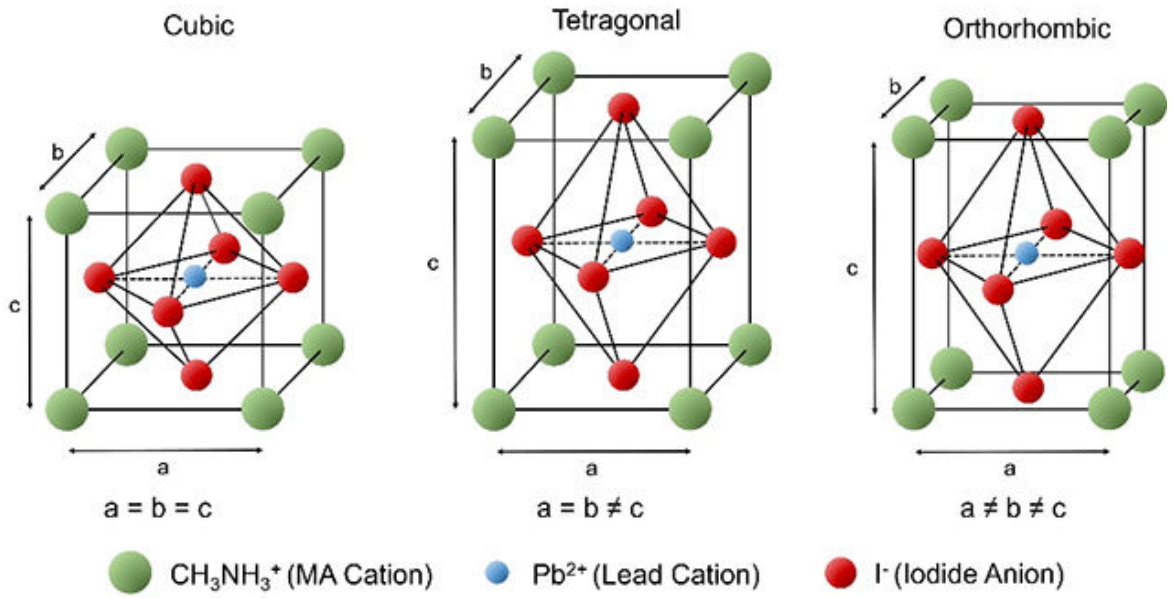

Fig. 3.1 **Different phases of $MAPbI_3$ perovskite structure.** Figure taken from [122].

myself, and I performed the data analysis. Absorption measurements were carried out in Wroclaw by Szymon Zelewski, who also analysed them.

3.1 Introduction

The dramatic gain in solar cell device efficiency since 2012 is only one of the features making perovskites stand out among other photovoltaic (PV) materials. With a Young's modulus around 20 GPa[124–127], perovskites are mechanically softer than most other PV materials such as Silicon (>160 GPa)[128, 129], GaAs (∼85 GPa)[130], CIGS (∼80 GPa)[131, 132] and CdTe (∼40 GPa)[133, 134], and their structure has been reported to be prone to light-induced, electric-field-induced and temperature-dependent rearrangements[51, 135, 14, 136–138]. The workhorse system studied to date, methylammonium lead iodide ($MAPbI_3$), is in a tetragonal phase (TP) at room temperature, but undergoes a transition to a cubic phase at high temperature (∼330 K) and an orthorhombic phase (OP) at low temperature (∼150 K).

Recently, we and others[139–141] have reported that the structural rearrangement from TP to OP causes a distinct hysteretic change in optical and transport properties as well as device behaviour between heating and cooling cycles. This hysteresis could be reduced by scraping the film from the substrate and instead measuring randomly oriented powder samples[139]. This suggests that the thermal stability and phase transition can be influenced

by the local environment of the film due to interactions between the material and substrate as well as within the bulk film itself, both interactions of which may depend on grain size.

State-of-the-art perovskite films are polycrystalline, which leads to microscale inhomogeneities in a number of properties such as morphology and defect distributions[48, 142–145] and, in turn, to local variations in the electronic environment for charge carriers. Generally, increasing grain sizes in $MAPbI_3$ films has resulted in improvements in critical performance parameters, such as an increase in carrier mobility and charge collection efficiency[146, 147], along with smaller band gaps, longer lifetimes and higher absorption coefficients[148]. Nevertheless, an understanding of the underpinning differences in structural and mechanical properties of bulk films with different grain sizes, and how grain size influences their crystal phase heterogeneity, is still lacking.

3.2 Sample preparation

Glass substrates were washed sequentially with soap, de-ionized water, acetone, and isopropanol, and finally treated under oxygen plasma for 10 minutes. All samples are based on a solution processed methylammonium iodide (MAI) and lead acetate $Pb(Ac)_2{\cdot}3H_2O$ precursor mixture in dimethylformamide (DMF). The standard recipe used is based on the stoichiometry:

$$n_{MAI} = 3n_{Pb(Ac)_2 3H_2O}, \tag{3.1}$$

where n is the number of moles.

In order to prepare small grain samples for the experiments to follow, films with a grain size on the order of tens of nanometres (small grain) were obtained by confining the perovskite, deposited with a lead acetate recipe, within a mesoporous scaffold of Al_2O_3 nanoparticles ($\sim$50 nm in size). The recipe had to be optimised first to obtain a good coverage (or filling) of the scaffold. A low perovskite concentration would lead to a partly filled scaffold and a poorly emissive material, while a high concentration would overfill it and create a capping layer of medium-sized grains.

To find the appropriate concentration, four solutions were prepared containing respectively 24 wt%, 26 wt%, 28 wt% and 30 wt% of perovskite, with x [wt%] defined as:

$$x[wt\%] = \frac{m_{solute}}{(m_{solute} + m_{solvent})}, \tag{3.2}$$

where m_{solute} is the precursors' mass ($m_{MAI} + m_{Pb(Ac)_2 3H_2O}$) and $m_{solvent}$ that of DMF.

A 30 wt% stock solution was first prepared. From this stock solution, lower concentrations were obtained by dilution as follows. Let $m_{s-dilution}$ be the solvent mass after dilution from a stock solution obtained using a mass $m_{s-stock}$ of that solvent. Let x' [wt%] be the desired concentration after dilution, we have:

$$\begin{aligned} x'[wt\%] &= \frac{m_{solute}}{m_{solute}+m_{s-dilution}} \\ \iff m_{s-dilution} &= m_{solute}\left[\frac{1}{x'[wt\%]}-1\right]. \end{aligned} \tag{3.3}$$

The volume of solvent V' to add to the initial volume V corresponding to $m_{s-stock}$ is then:

$$V' = V\left(\frac{m_{s-dilution}}{m_{s-stock}}-1\right), \tag{3.4}$$

using $m_{s-dilution}$ as defined in Eq 3.3.

Table 3.1 gives the proportions of DMF to add to a stock solution of 30 wt% in order to obtain lower concentrations of perovskite.

x' perovskite concentration (wt%)	28	26	24
V' volume of DMF to add (% of V)	10	22	36

Table 3.1 Dilutions from a 30 wt% perovskite stock solution prepared using a volume V of DMF. The volume V', given in percentage of V, is added to the stock.

Test samples were prepared by spin-coating a first layer of alumina nanoparticles (annealed at 150°C for 10 min) and then the precursor solution (as described in Table 3.2). The surface morphology of the films was then examined using an SEM, shown in Figure 3.2 **a**. An electron beam from a field emission source accelerated to 5 kV was used with an Inlens detector. Optical and SEM images of the test samples are shown in Figure 3.2 **b** to **e**, in order of increasing perovskite concentration from 24 wt% to 30 wt%.

In Figure 3.2 **b** (24 wt%), we observe a lightly-coloured film and a poor filling of the scaffold. The film becomes increasingly darker with increasing perovskite concentration, and a capping layer is clearly visible in Figure 3.2 **e** (30 wt%). A good compromise is found around 26-28 wt%, and all our experiments on small grain films there after were conducted on samples prepared with a perovskite concentration of 26 wt%.

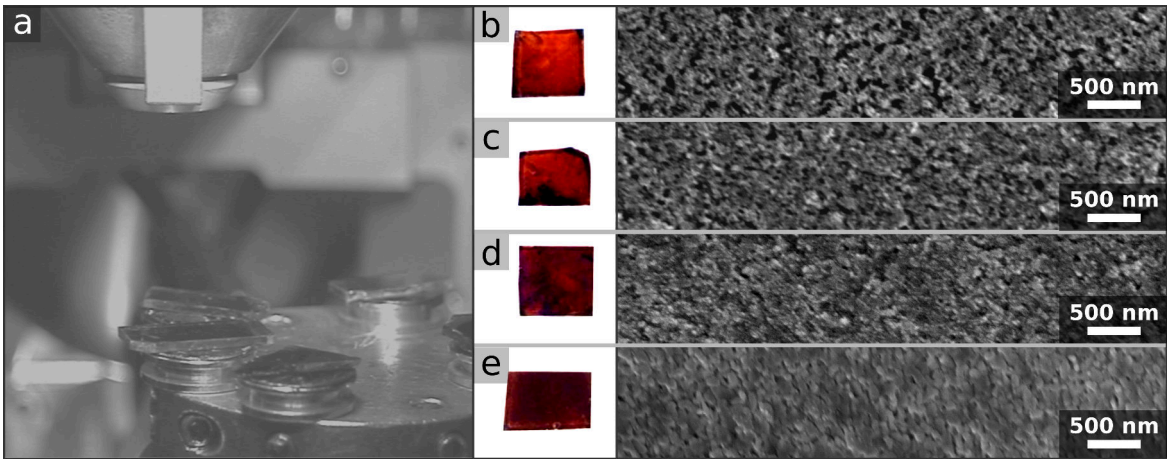

Fig. 3.2 **Optical and SEM images of test samples for the fabrication of small grain $MAPbI_3$ films.** The SEM chamber showing the objective lens and the test samples is displayed (a), together with optical and SEM images of films with increasing perovskite concentration from 24 wt% to 30 wt% in steps of 2 wt% (b-e).

For the following experiments, we solution-processed thin films of $MAPbI_3$ of varying grain size on glass substrates by modifying recipes involving lead acetate and methylammonium iodide precursors. Specific steps or alterations required to obtain the different grain size films are summarised in Table 3.2. Medium grain (∼100 nm) films were fabricated as planar films with the same lead acetate recipe, and large grain films (∼0.5-1 µm) were made in the same way but by adding hypophosphorous acid to the lead-acetate-based precursor solution following previous methods[149]. Scanning electron microscope (SEM) images of these films are shown in Figure 3.3 **a** (small grain), **b** (medium grain) and **c** (large grain).

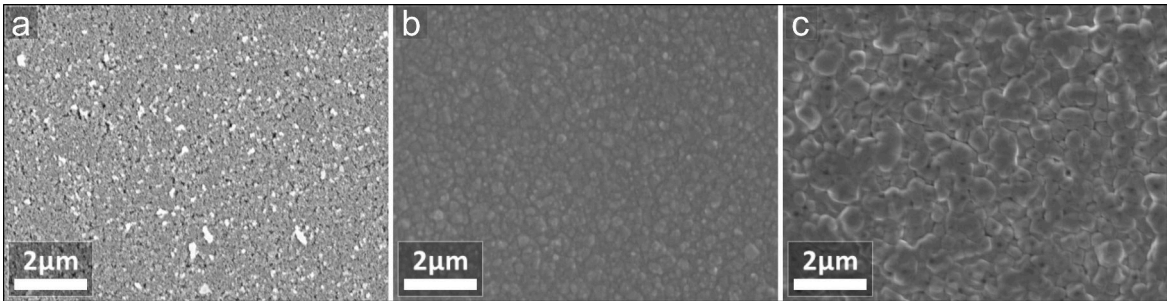

Fig. 3.3 **SEM images of $MAPbI_3$ thin films of varying grain size.** Less than 50 nm: "small" (a), 100 nm: "medium" (b) and 0.5-1 µm: "large" (c).

Grain size:	**Small** (<50 nm)	**Medium** (∼100 nm)	**Large** (∼0.5-1 µm)
Specific substrate preparation (other than cleaning and 0_2 plasma):	Mesoporous layer spin coated (at 2500 rpm for 60 seconds) from a solution of alumina nanoparticles (<50 nm) dispersed in IPA with a concentration of 1:2 Al_20_3:IPA and annealed at 150°C for 10 minutes.	None	None
Alteration of the standard precursor mixture:	None	None	Addition of 11% molar ratio of Hypophosphorous acid (HPA)[149]
Perovskite concentration:	26 wt%	37 wt%	37 wt%

Table 3.2 Summary of the key fabrication steps of $MAPbI_3$ films of varying grain size.

3.3 Temperature cycles

We followed the same temperature cycles for all measurements: Starting at 300 K, we cooled down each sample to 200 K with a 20 K step, then to 170 K with a 10 K step and finally to 100 K in steps of 5 K. We heated the samples back to room temperature (300 K) following the same protocol, as summarised in Table 3.3. The cooling rates are detailed in Table 3.4.

Temperature interval (K)	**Temperature step (K)**
300 - 180	20
180 - 160	10
160 - 100	5

Table 3.3 Temperature cycle steps used for all experiments when cooling and heating.

	Absolute cycle rate ($K.min^{-1}$)	**Dwell time (min)**	**Average effective cycle rate ($K.min^{-1}$)**
PL	2	5	0.25
Absorption	6	25	0.1
XRD	6	30	0.09

Table 3.4 Temperature cycle cooling rates used for all experiments when cooling and heating.

3.4 Analysis of hysteresis loops

A method was needed to compare the phase transition hysteresis between several experiments in spite of the different physical quantities measured (when comparing XRD, PL and absorption data). To illustrate this method, we use in Figure 3.4 the temperature-dependent *d*-spacing extracted from the XRD measurements performed on a large-grain $MAPbI_3$ perovskite thin film.) A linear regression (green dotted line in Figure 3.4 **a**) can be performed on the hysteresis loops. The linear component corresponding to the thermal dilatation of the material (its slope being the coefficient of dilatation) can then be subtracted, and the differential with respect to that line extracted as shown in Figure 3.4 **b**. The same method can be and will be applied later to the hysteresis loops measured in PL and optical absorption on $MAPbI_3$ thin films of varying grain size.

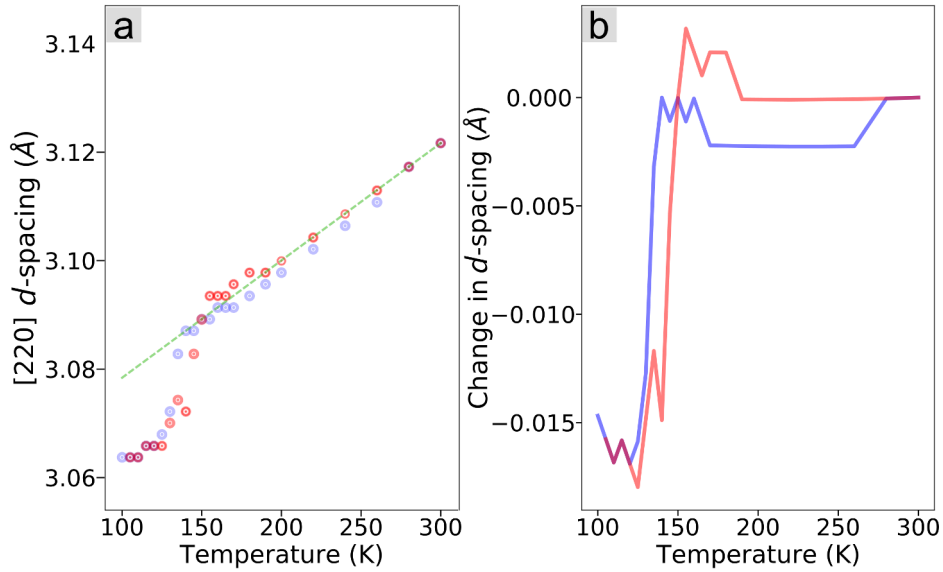

Fig. 3.4 **Hysteresis comparison method.** (a) Lattice spacing (*d*-spacing) as a function of temperature for the [220] XRD reflection on a large-grain $MAPbI_3$ thin film (taken as an example), measured while cooling (blue dots) and heating (red dots) the sample. The green dotted line shows the linear regression through the linear part of the temperature dependent, that is then subtracted to give the differential plot in (b).

3.5 Temperature-dependent structural characterisation

XRD was performed on the spin-coated films with Cu-Kα1,2 radiation (λ = 1.541 Angström). Low-temperature measurements were performed according to the aforementioned temperature cycles (Table 3.4)

In Figure 3.5, we show structural changes from temperature-dependent XRD measurements (normalised to their respective maximum) on large grain (Figure 3.5 **I.a**), medium grain (Figure 3.5 **I.b**) and small grain (Figure 3.5 **I.c**) films over the temperature range 100 – 300 K. A close-up around the phase transition (100 – 200 K) is displayed in Figure 3.5 **II. a-c**. The stated lattice spacing (d-spacing or d) was calculated from the measured 2θ diffraction angle of the [220] reflection using Bragg's law (3.5):

$$2d\sin\theta = n\lambda \Leftrightarrow d = \frac{n\lambda}{2\sin\theta}, \tag{3.5}$$

The distance between each diffractogram is proportional to the temperature step and blue and red arrows indicate the cooling and heating cycles, respectively. The phase transition onsets are highlighted in bold in Figure 3.5 **a** and **b**. We find that the first onset of a phase transition to the orthorhombic phase during the cooling cycle is at the highest temperature for the large grain sample (135 K), followed by the medium grain film at the slightly lower temperature of 130 K. Upon heating, both samples start the transition back to the tetragonal phase at a similar temperature (135 K). Surprisingly, although we observe a shift in d-spacing of the TP peak with temperature from ∼145 K (cooling) to 100 K and back to 145 K (heating), the d-spacing change between the end points of the hysteresis for the small grain sample is consistent with a suppression of the phase transition. We track the position of the [220] reflection, highlighted by dots in Figure 3.5 **I.a-c** and compare the hysteretic change in d-spacing for each sample in Figure 3.5 **II.d**. Around the phase transition, where both TP and OP peaks are present, we follow the average d-spacing d_{WA} weighted by the amplitudes A_{TP}, A_{OP} of both contributions as in Equation 3.6 :

$$\frac{A_{TP}X_{TP} + A_{OP}X_{OP}}{A_{TP} + A_{OP}}, \tag{3.6}$$

where X here is the d-spacing (d_{TP} and d_{OP}).

The hysteresis comparison in Figure 3.5 **II.d** suggests that the phase transition is increasingly suppressed and the width of the hysteresis between cooling and heating cycles increases as the grain size decreases. Indeed, we observe a hysteresis in structural properties between the two temperature cycles across a temperature range of ∼25 K for the large grain, ∼30 K for the medium grain and ∼45 K for the small grain samples. We propose that the suppression of the phase transition and widened hysteresis in the small grain samples is due to the grains being mechanically constrained in the mesopores and therefore cannot structurally rearrange as easily as in the other samples.

We also note that we observe a mixed phase of both TP and OP across a temperature span of 10 K during the cooling (from 130 K to 120 K) and heating (from 135 K to 145 K) cycles

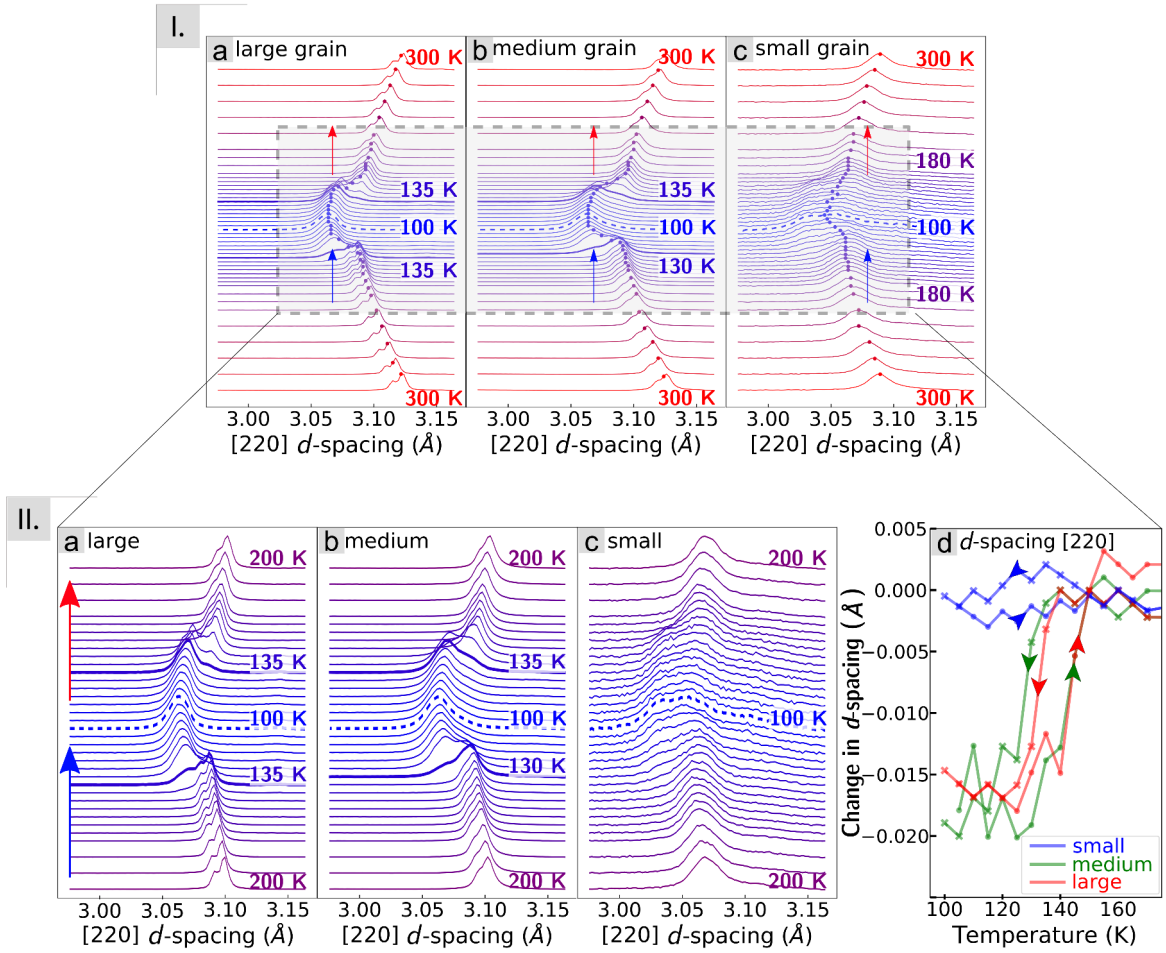

Fig. 3.5 **Temperature-dependent structural measurements (XRD).** Temperature-dependent X-ray diffractograms (normalised to their respective maximum) around the [220] reflection of MAPbI3 thin films of varying grain size: less than 50 nm (a), ∼100 nm (b) and 0.5-1 µm (c), where the lattice spacing was calculated from the measured 2θ angle. The blue and red arrows on each panel indicate the temperature cycle from room temperature to 100 K and back to room temperature respectively. The distance between each diffractogram is proportional to the temperature step, and the phase transition onsets are highlighted in bold. In d, we show a comparison of the hysteretic change in d-spacing for each film, with weighted averages used for mixed peaks (i.e. when both OP and TP peaks are present).

in the medium grain film, while in the large grain sample we observe this mixing across 10 K during the cooling cycle (from 135 K to 125 K) and 15 K during the heating cycle (from 135 K to 150 K), as displayed in Figure 3.6 **a,b**.

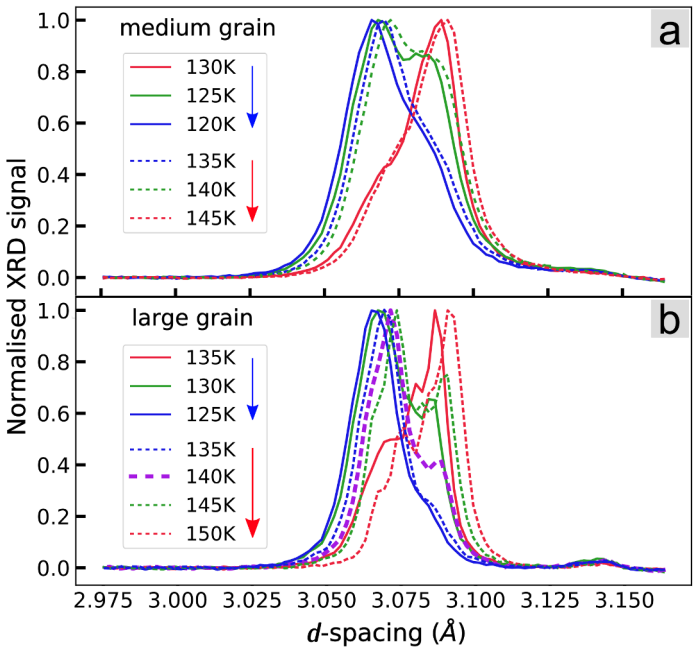

Fig. 3.6 **Temperature-dependent XRD patterns around the phase transition for the medium (a) and large (b) grain films** showing an asymmetry for the large grain sample.

3.6 Temperature-dependent optoelectronic changes characterised with PL and optical absorption

In order to investigate how the structural phase transition and hysteresis observations manifest themselves on optoelectronic properties, we performed temperature-dependent confocal PL and absorption measurements.

A fit was performed on each PL spectrum based on Gaussian functions, and used to extract parameters for each peak: energy, amplitude, area and full-width-half-maximum (FWHM). Around the phase transition temperature two peaks can be distinguished, corresponding to the orthorhombic and tetragonal phases, with respective energies E_{TP} and E_{OP}. The extracted peak amplitudes (A_{TP} and A_{OP}, respectively) serve as the weighing parameter for calculating the weighted average E_{WA} according to Equation 3.6 (with $X \equiv E$).

Optical density (OD) spectra were calculated from the absorption data using:

$$OD = \log_{10}(\frac{1}{T}), \tag{3.7}$$

with $T = A_S/A_R$, where A_S is the sample spectrum, and A_R is the reference spectrum taken with an empty sample holder. The band gap energy is extracted using a Tauc plot for direct allowed transition (an example is given in Figure 3.7), plotting $(\alpha h\nu)^2$ versus the

photon energy (assuming $OD \equiv \alpha$, the optical absorption coefficient) and extrapolating the linear part of the plot to zero. For the medium and large grain samples, excitonic absorption energies are determined by fitting a single Gaussian in the vicinity of the absorption peak.

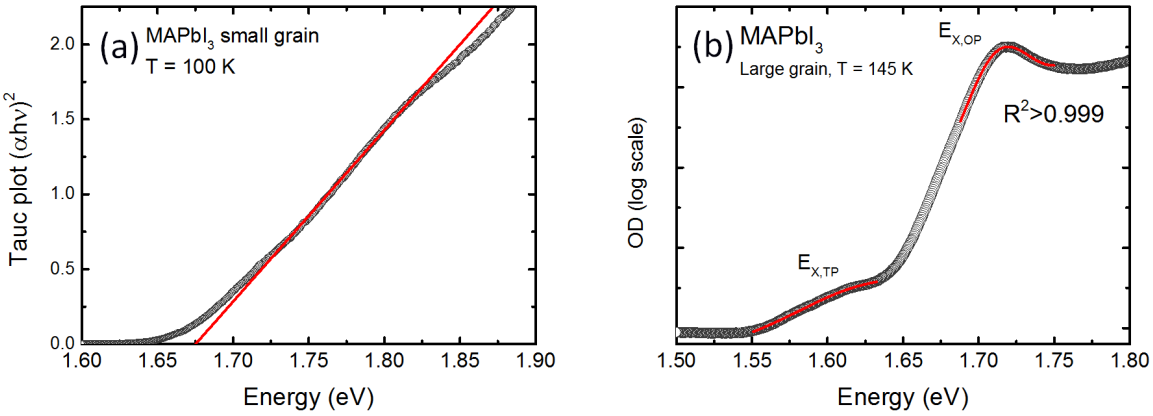

Fig. 3.7 **Band gap extraction method with a Tauc plot** for the small grain sample (a), exemplary fitting of excitonic absorption for the medium and large grain samples (b).

For the small grain sample no excitonic absorption is seen even at low temperatures, so the observed edge is treated as purely band-gap-related.

3.6.1 PL and absorption results and discussion

Temperature-dependent PL and absorption results are displayed in Figure 3.8 and Figure 3.9, respectively. At low temperature, a third peak appears on the low-energy side of the TP peak in the PL spectrum, predominantly in the medium and large grain samples. Power-dependent PL measurements reveal that the relative intensity of this peak decreases with fluence (Figure 3.10), which suggests that this emission may arise from defects in the films that can be saturated at higher fluences.

We compare the temperature-dependent absorption (Figure 3.11 **a**) and PL (Figure 3.11 **b**) of the two extreme cases: the small grain (top panels) and the large grain (bottom panels) films. These 2-dimensional colourmaps represent the spectra as measured in both absorption and PL, with a signal intensity ranging linearly from blue (low) to red (high). Yellow arrows indicate the temperature cycle from room temperature (300 K) to 100 K and back up to room temperature. The temperature steps as well as the cycle rate were close to the ones used for XRD measurements (see Table 3.3 and Table 3.4).

In the case of the small grain film, consistent with XRD measurements, we do not observe any clear indication of a phase transition in this temperature range despite a small shift in both

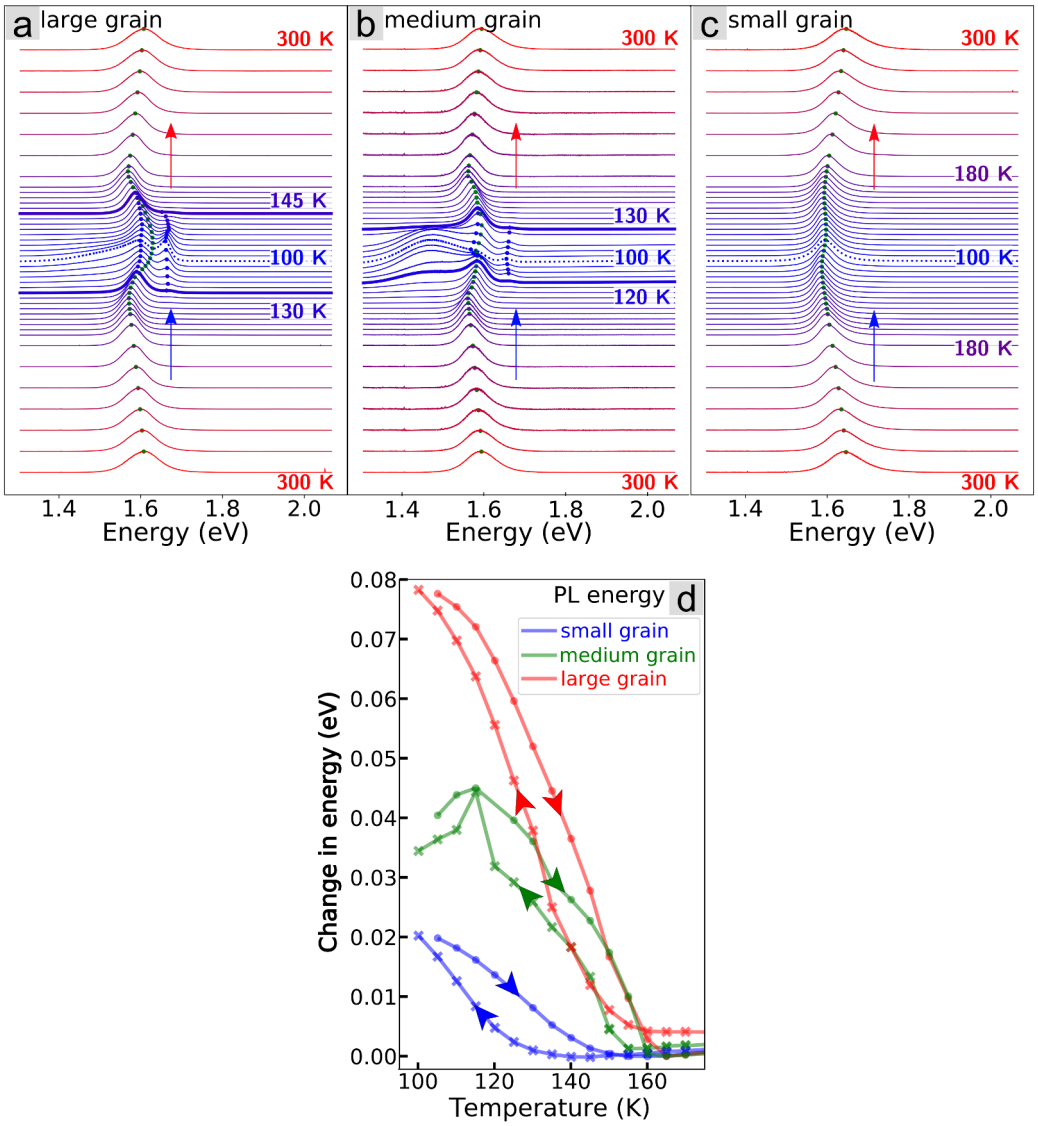

Fig. 3.8 **Temperature-dependent macro-PL spectra (normalised to their respective maximum) of $MAPbI_3$ thin films of varying grain size:** large (a), medium (b) and small (c). The blue and red arrows on each panel indicate the temperature cycle from room temperature to 100 K and back to room temperature respectively. The distance between each spectrum is proportional to the temperature step, and the phase transition onsets are highlighted in bold. As a guide to the eye, overlaid blue dots indicate the peak(s) position on each measurement, while green dots indicate the average energy weighted by the amplitude of the TP and OP peaks in the presence of both phases. In d, we show a comparison of the hysteretic change in PL energy for each film, with weighted averages used for mixed peaks.

absorption onset and PL energy (top panels in Figure 3.11 **a** and **b** respectively). However, further measurements carried out at lower temperatures (Figure 3.12 **a**) show slight PL peak

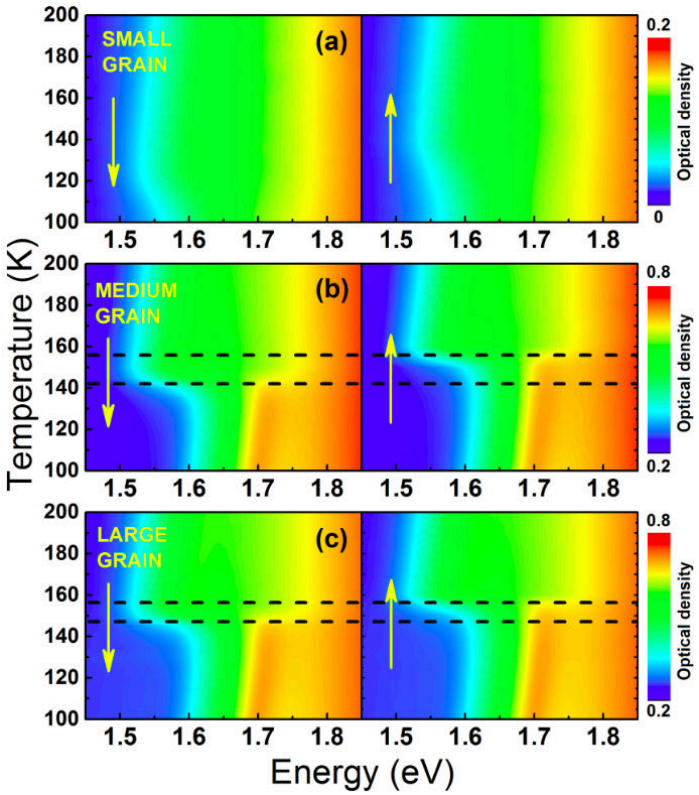

Fig. 3.9 **Temperature-dependent absorption maps of $MAPbI_3$ thin films of varying grain size:** large (a), medium (b) and small (c). The arrows indicate the temperature cycle (down for cooling, up for warming). Dashed lines represent the hysteresis width.

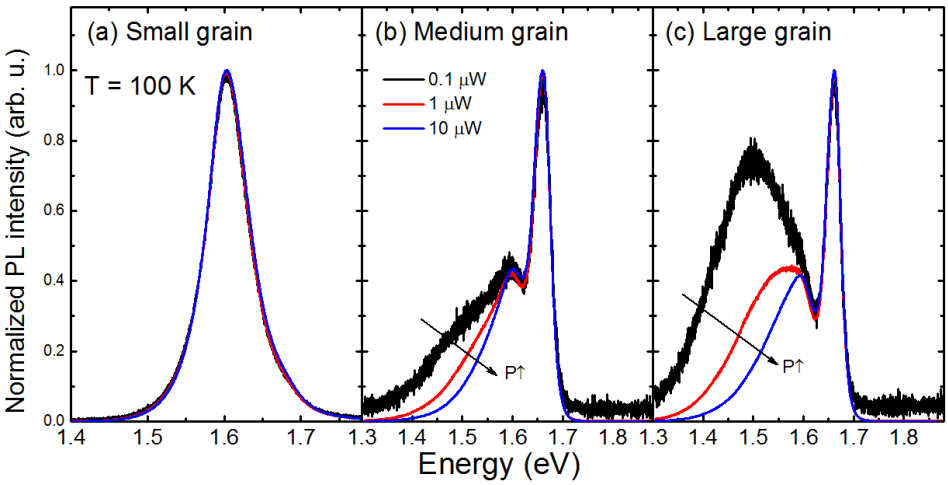

Fig. 3.10 **Power-dependent PL from $MAPbI_3$ thin films of varying grain size:** large (a), medium (b) and small (c). The arrows highlight the decrease in PL emission from defects with increasing excitation power (P) as more traps are saturated.

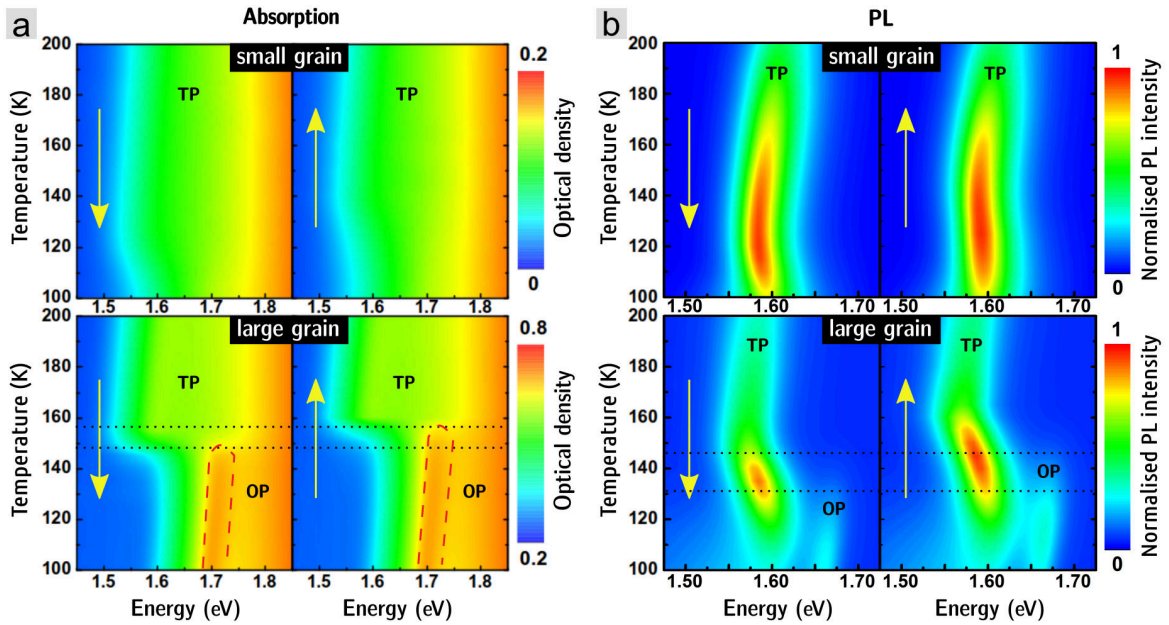

Fig. 3.11 **Temperature-dependent optical absorption and macro-PL measurements on small grain (top panels) and large grain (bottom panels) $MAPbI_3$ thin films.** Yellow arrows indicate the temperature cycle from 300 K down to 100 K and back up to 300 K with a rate of 2 K.min^{-1} and a dwell time of 5 min. Absorption spectra are displayed with a colour scale representing the measured optical density. PL maps for each sample are normalised to the maximum PL intensity measured during the temperature cycle. For all macro-PL measurements, the films were excited with a 532 nm diode laser with an excitation density of 0.6 mW.cm^{-2}. Black dotted lines show the phase transition onsets and red dashed lines highlight the excitonic emission.

broadening that may be the signature of the formation of the orthorhombic phase below 80 K (Figure 3.12 **b** and **d**). We also note a two-fold widening of the hysteresis, which is clearly visible between 150 K to 75 K (Figure 3.12 **c**) and therefore spreads over a larger temperature range (∼75 K) when compared to the large (∼60 K) and medium (∼50 K) grain films, with an overall trend consistent with the observed structural changes (XRD). This widening of the hysteresis, and the decrease in the overall amplitude of the energy changes between the two phases, again suggests that the phase transition is more suppressed in the small grain sample.

In contrast, the results obtained for the large grain sample (bottom panel of Figure 3.11 **a**) show a clear phase-transition hysteresis in absorption (shown by black dotted lines), coinciding with the apparition of an excitonic absorption peak around 1.7 eV (highlighted by a red dashed line). This phase transition is also observed in PL (bottom panel of Figure 3.11 **b**) with the emergence of a second peak blue-shifted by about 50 meV with respect to the TP emission peak. The coexistence of both phases is visible in PL from 130 K (when

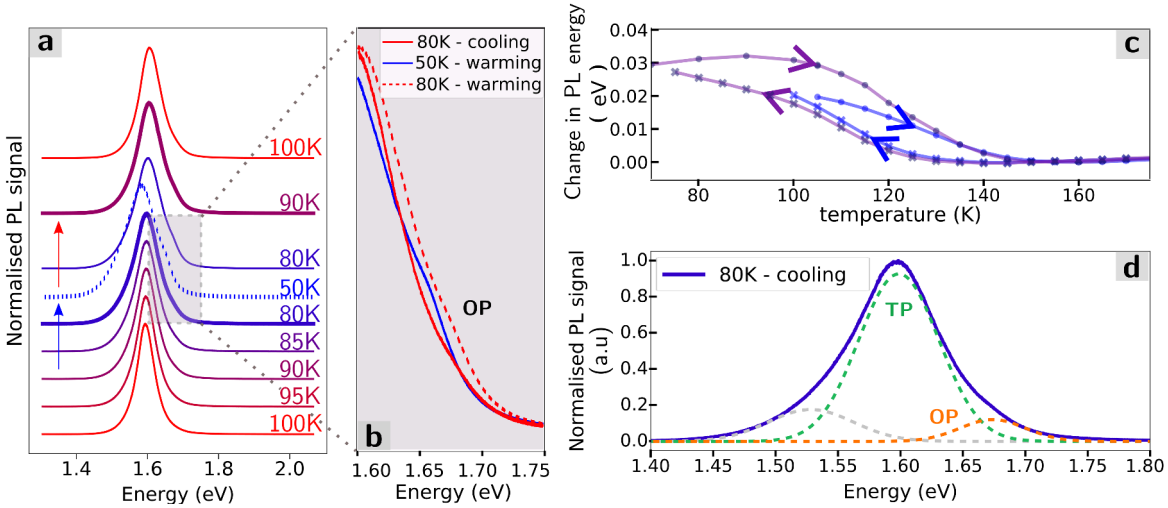

Fig. 3.12 **Temperature-dependent PL on small grain $MAPbI_3$ below 100 K.** Spectra series (a) with a close-up in showing hints for the presence of an OP peak (b). The widening of the hysteresis at low temperature shown in (c) is also a sign of a phase transition below 80K. (d) PL spectrum at 80K (during the cooling cycle) and a fit with 3 Gaussian functions (TP, OP, and potentially some emission from defect states at lower energy).

cooling down to 100 K) up to 145 K (when heating up to 300 K), which is overall in good agreement with XRD. We note a small shift in the temperature ranges between PL and XRD measurements, which we attribute to the fact that PL emphasises any TP components, even small fractions, due to energy funnelling of carriers from OP to TP[143].

In the large grain film, the phase transition asymmetry observed with XRD and mentioned earlier is followed by a positive shift (both in d-spacing and PL energy) remaining until ~275 K, indicating that the large grain structure does not transform back to its initial optoelectronic properties and lattice parameters (Figure 3.13 **a** and **b**, respectively) until room temperature, where the original d-spacing is recovered.

In Figure 3.14 we show absorption (green) and PL (black) spectra at 150 K when cooling and heating, respectively, for both the small (**a**,**b**) and large grain (**c**,**d**) films. Dotted lines mark the central position of the PL peak and absorption onset during the cooling phase as a reference point for comparison. While there is no clear sign of phase transition hysteresis between the cooling and heating cycles in the small grain film at 150 K (Figure 3.14 **a** and **b**), we observe clear differences in both PL and absorption in the large grain sample (Figure 3.14 **c** and **d**).

The emergence of the OP absorption edge upon cooling in the large grain sample shows that the phase transition has started at this temperature (Figure 3.14 **c**); this is not seen in the PL because the presence of any TP component will dominate the emission. In contrast,

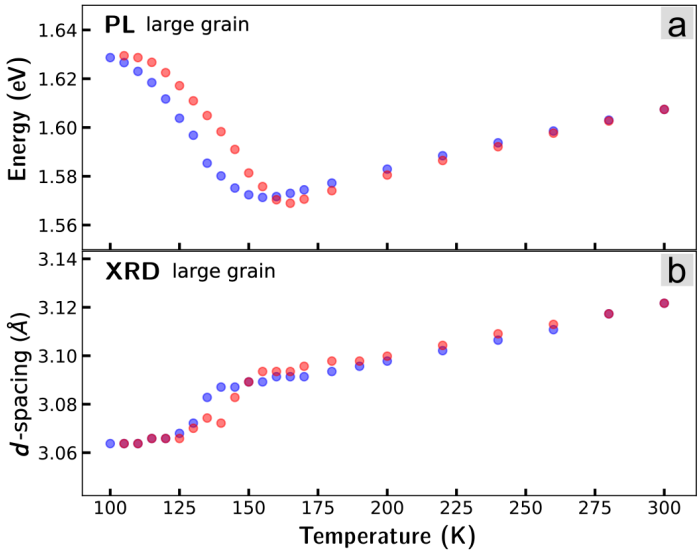

Fig. 3.13 **Asymmetry of the phase transition in the large grain $MAPbI_3$ thin film** which does not transition back to its initial structural configuration during the heating cycle until ∼275 K. The full temperature cycles both in PL (a) and XRD (b) highlight this remanence of the hysteresis until room temperature.

at that same temperature but upon the heating cycle (Figure 3.14 **d**), the TP absorption is diminished and the OP absorption peak dominates; the presence of a second PL peak (i.e. the OP emission) adds further evidence that the OP now constitutes a larger fraction of the film than it does at the same temperature during the cooling cycle. To further characterise this phase transition behaviour, we extract at each temperature the PL and absorption energy, and calculate the weighted average in the presence of any mixed OP and TP-related peaks. We summarise the results in Figure 3.14 **e** and **f** and compare the overall change in energy from before to after the phase transition for the PL and absorption spectra, respectively (see Figure 3.7). The amplitude of that change from both measurements is ∼5 times higher in the large grain (∼80-120 meV) than in the small grain sample (∼20 meV).

3.7 Temperature-dependent changes in local environment: micro-PL mapping

To understand how the PL properties change with temperature at the microscale, we performed micro-PL measurements. We scanned the laser in steps of 2 µm with an excitation density of 1512 $mW.cm^{-2}$, and recorded at each location a PL spectrum (using an integration time of 2 s and 2 accumulations) in order to create 2D maps at a range of temperatures while cooling down from room temperature to 100 K and heating back up to room temperature.

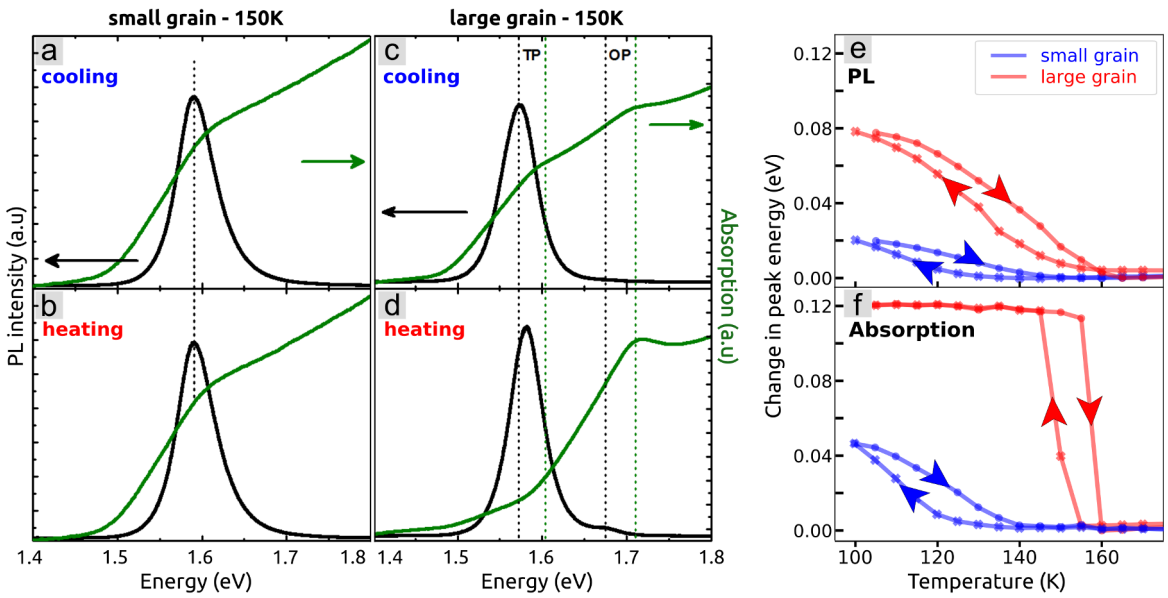

Fig. 3.14 **Comparison of absorption (green) and PL (black) spectra at 150 K while cooling and heating, respectively, for the small grain (a,b) and large grain (c,d) film.** Dotted lines mark the central position of the PL peak(s) during the cooling phase as a reference point, and arrows indicate that the energy difference between the absorption onset and the PL energy is larger during the cooling phase than the heating up phase. (e,f) Change in peak energy with temperature in PL and absorption, respectively. The energies were extracted from the spectra at each temperature, and the weighted average calculated in the presence of mixed peaks.

We performed a peak-detection and fitting routine on the data in each map in order to extract the statistically relevant peaks and relevant peak parameters. In order to analyse large spectral maps each containing over 50,000 spectra, a methodology is implemented based on a peak-finding and peak-fitting algorithm, described in Chapter 2.2. Figure 3.15 gives an overview of the algorithm used for the analysis, using the key parameters summarised in Figure 3.16. First, a linear background is subtracted from the spectrum (Figure 3.15 block A). To make the data smoother and remove high frequency noise, a Fast Fourier Transform (FFT) analysis is performed. The linear component is discarded and the first 4 frequencies are kept, consistently with a typical peak width expected around 25% of the spectrum's length. An inverse FFT is then computed and the resulting filtered signal is fed into the peak-finder routine (Figure 3.15 block B).

The peak detection happens in two steps. It starts with the search of local maxima of the smooth spectrum (main and well-defined peaks as in Figure 3.15 **a**), and moves on to analysing its variations (gradient, see Figure 3.15 **b**). This second step looks for local minima and maxima of the gradient in an interval ranging from 1% to 33% of its absolute maximum

(yellow regions in Figure 3.15 **b**). It allows for the detection of hidden peaks, for example shoulders appearing on the side of main peaks. A filter is then applied that discards peaks found within the first or last 10% of the spectrum in order to avoid edge effects (grey zones in Figure 3.15 **a**, **b** and **c**) and those judged as too narrow with regards to the expected peak width (parameter **UP.2**, set for the current analysis to 25% of the spectrum), as well as those corresponding to small variations of a plateau. Finally, only the peaks of amplitude greater than 5% of the largest one are kept for the next steps of the analysis.

Quantum theory states that atoms and molecules possess well defined energy levels, with transitions occurring at a single, well defined, frequency. At this level, the PL lineshape is usually well described by a Lorentzian. In a mesoscopic or macroscopic crystal, however, disorder as well as vibrations and the presence of impurities alter a material's optoelectronic properties. In a real semiconductor, photoconductivity excited below bandgap isn't negligible due to the presence of disorder forming localised defect-states in the bandgap. This appears in absorption spectra as an exponential band tail at lower energies called the Urbach tail, and makes the PL emission spectral shape asymmetrical as well. As a first approximation, a least-squares fit is performed in two steps using a Gaussian function and initial parameters extracted from the data by the peak-finder (Figure 3.15 block C and **c**). It is first applied to the main peaks (local maxima). The difference of the fit and the data is then evaluated, and the fit validated if the discrepancy is less than 10%. If that condition is not satisfied, hidden peaks (detected from the gradient) are added one by one (up to 3 peaks in total including the main peaks) until the agreement between fit and data is sufficient. If the discrepancy persists, then the spectrum is discarded from the analysis. Finally, a set of parameters (energy, FWHM, area, amplitude) is extracted from the fit for each peak.

For each sample, a scatter plot shows the amplitude and central position (energy) of each peak, at each temperature. Overlaid histogrammes show the distribution of peak energies per temperature. Of all peaks, only those with an energy within the FWHM of these histogrammes are kept for further analysis. Figures 3.17, 3.18 and 3.19 display these scatter plots for the large, medium and small grain films, respectively. Three panels show an overview of the full energy window and a close-up on the TP and OP regions, respectively, from top to bottom. All of these figures clearly show the separation between the TP phase at low energies, and the OP phase at high energies, which is absent in the small grain sample. In the large grain film, the coexistence of phases at 140 K (while heating back up to room temperature) is clearly observed, but the small size of the OP peak hidden within the high-energy tail of the TP peak introduces an uncertainty in the determination of its energy. In the medium grain film, all peak positions appear to be well defined.

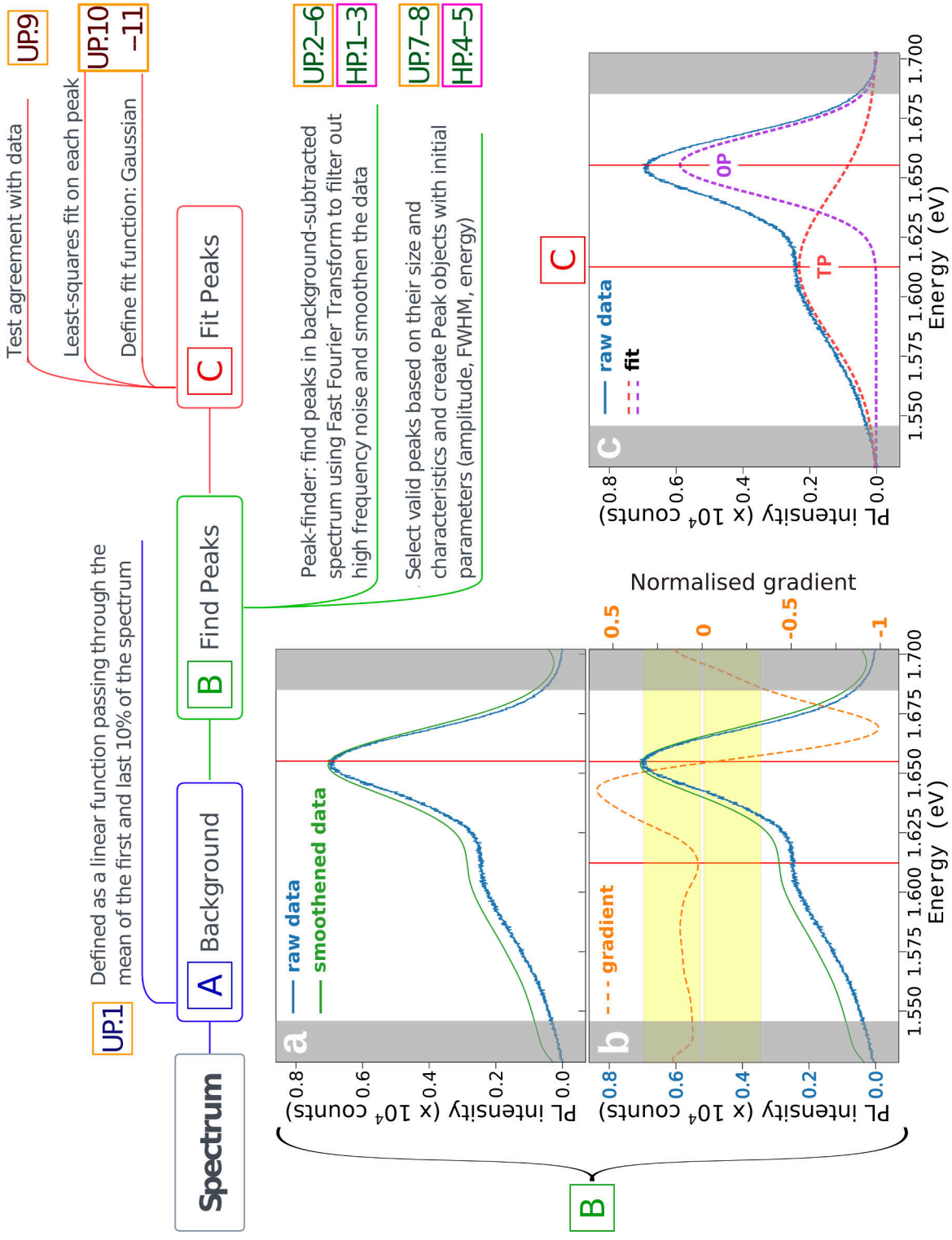

Fig. 3.15 **Backbone of the spectral analysis algorithm used to analyse micro-PL maps**, illustrated with a spectrum measured on the medium grain film at 100K. (a) and (b) show how the detection of main and hidden peaks is performed using extrema of the smooth data and its gradient (within the yellow region), respectively. (c) shows the final output of the analysis routine with a fit of the spectrum and the identification of the TP and OP peaks.

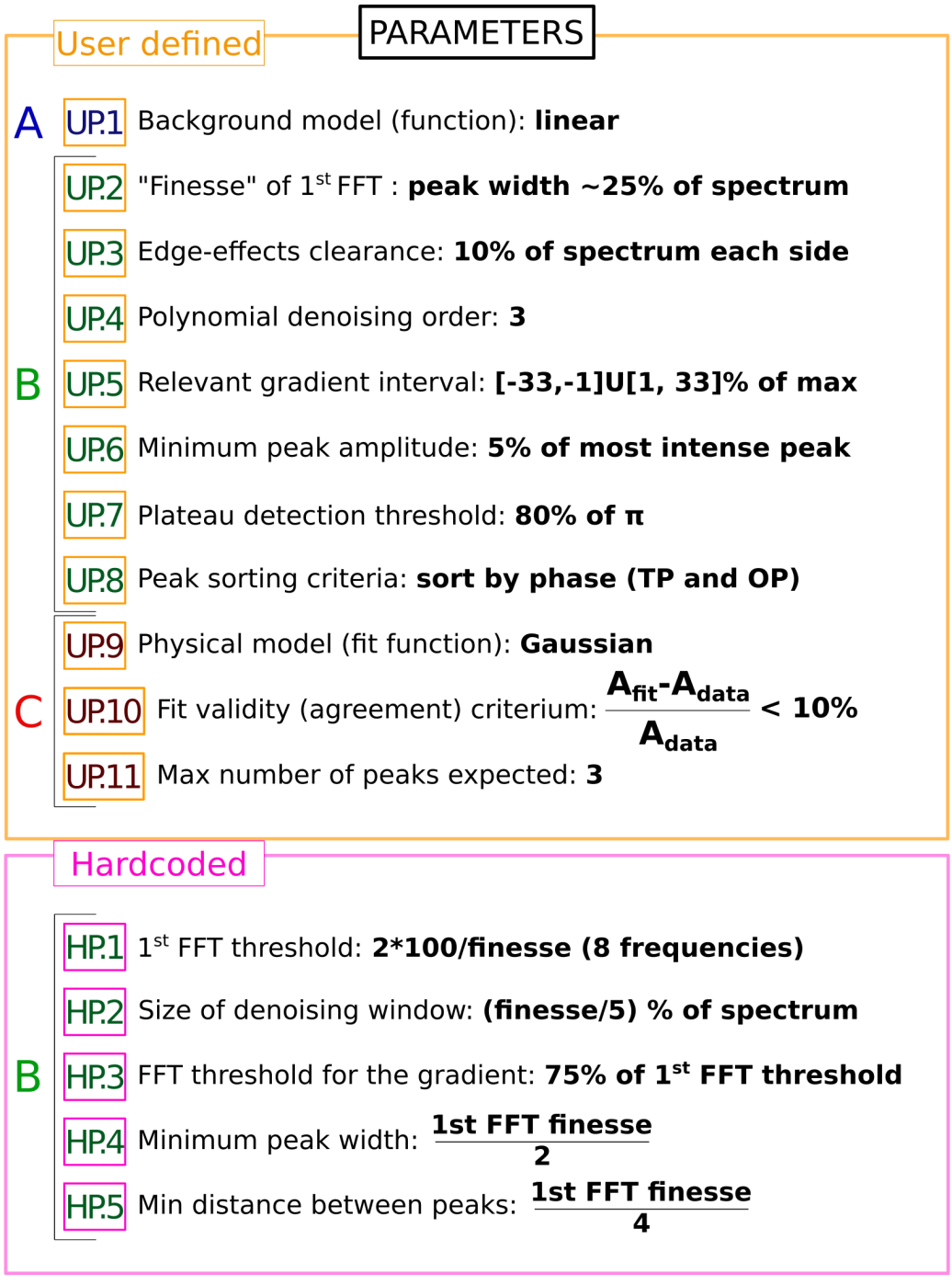

Fig. 3.16 **User-defines and hardcoded parameters fed into the spectral analysis programme for the current analysis.** These parameters reflect any assumptions made for the analysis, such as the expected peak width (parameter **UP.2**), the maximum number of peaks we expect to find (parameter **UP.11**) and the fit function (parameter **UP.9**).

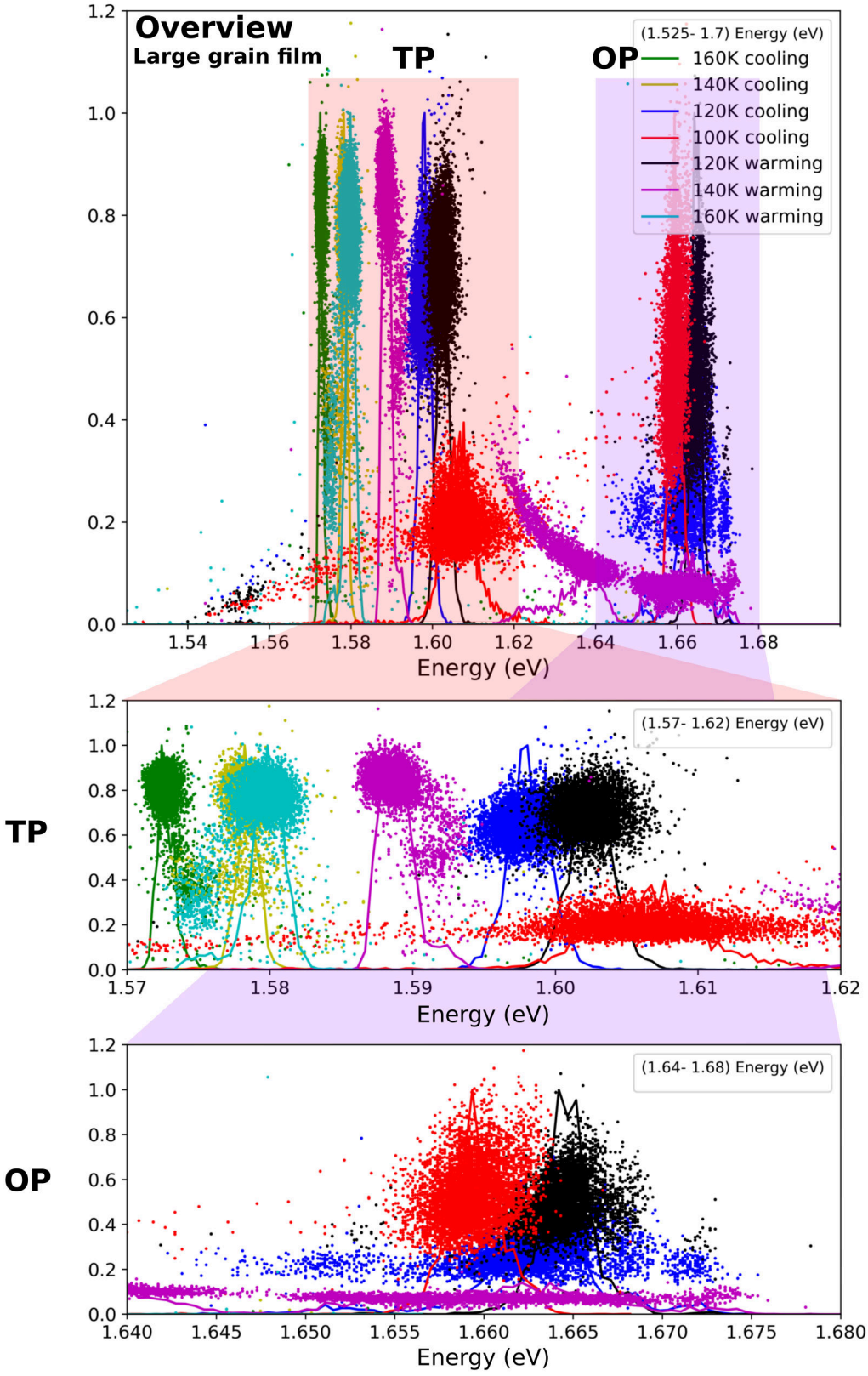

Fig. 3.17 **Statistical analysis on the micro-PL maps for large grain $MAPbI_3$.** On the overview (top), two phases are clearly visible, with the OP phase being present only between 120K (cooling) and 140K (heating). At 140K (heating), the OP peak is very small and hence difficult to locate precisely in energy. Two other panels show a close-up on the TP and OP regions, respectively, from top to bottom.

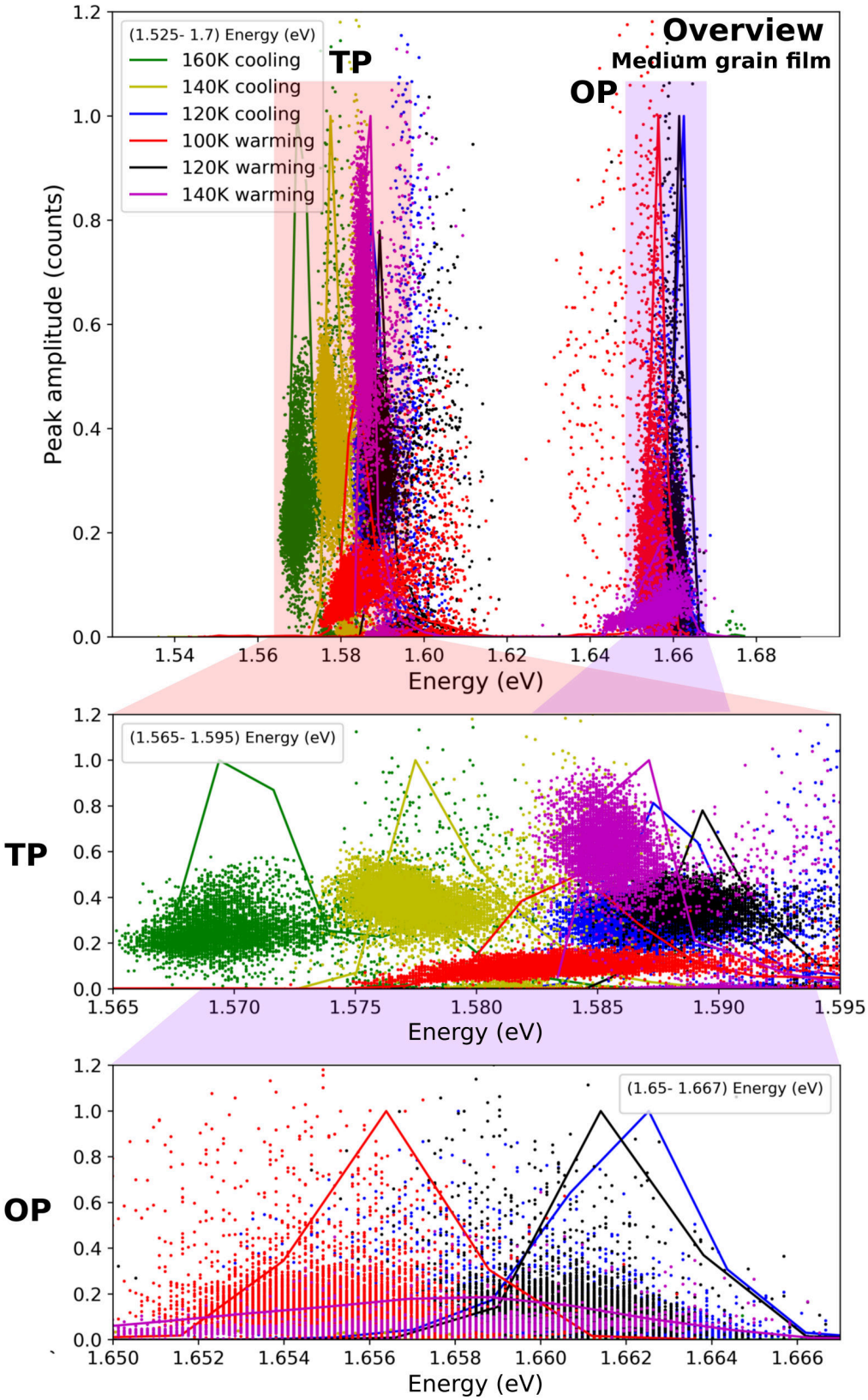

Fig. 3.18 **Statistical analysis on the micro-PL maps for medium grain $MAPbI_3$.** On the overview (top), two phases are clearly visible, with the OP phase being present only between 120K (cooling) and 140K (heating). Two other panels show a close-up on the TP and OP regions, respectively, from top to bottom.

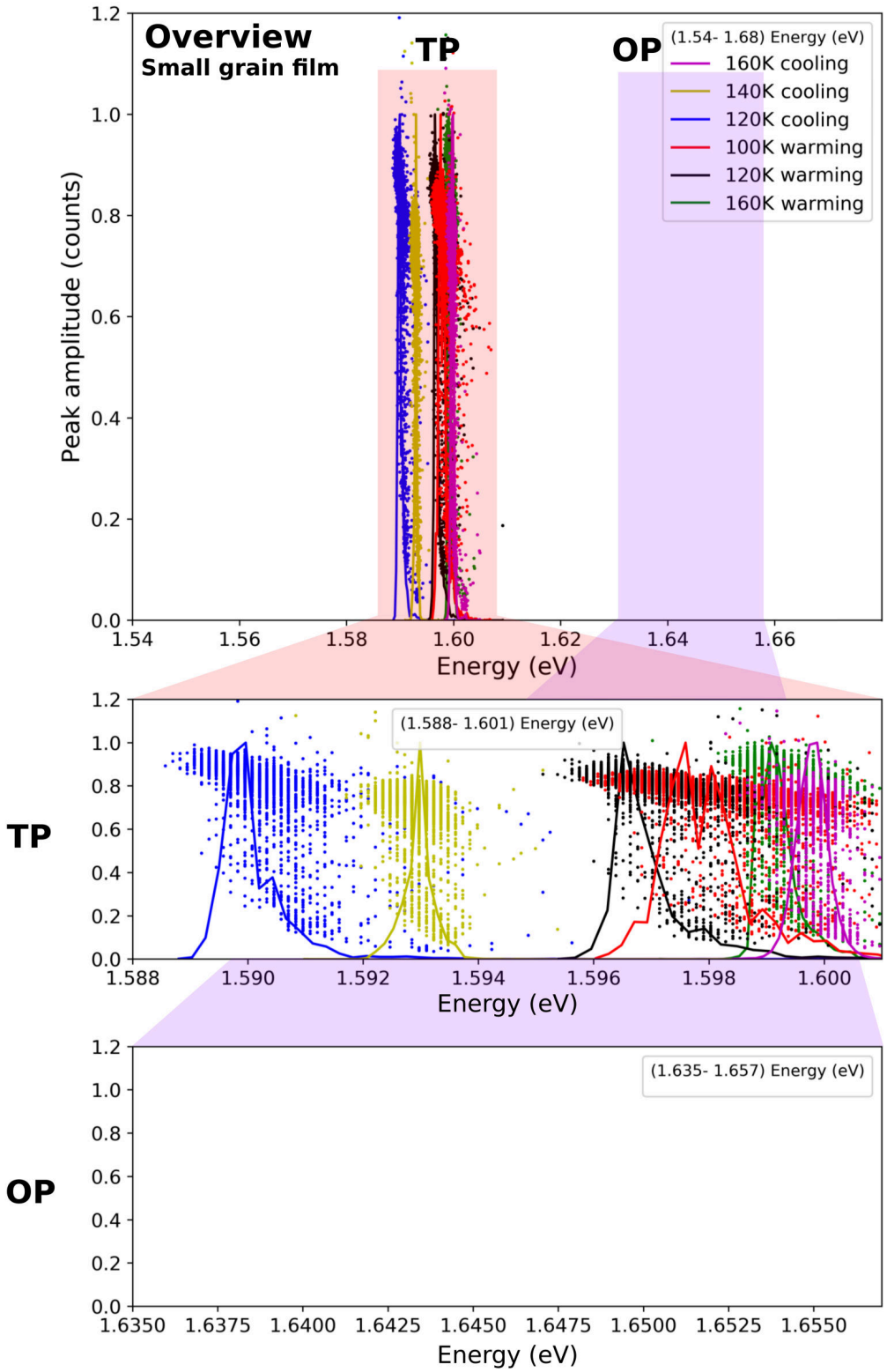

Fig. 3.19 **Statistical analysis on the micro-PL maps for small grain $MAPbI_3$.** On the overview (top), only the TP phase is visible. The close-up on the high energy region (bottom panel) does not show any sign of an OP phase.

Figures 3.20, 3.21 and 3.22 show the results obtained for the large, medium and small grain films respectively, after selection of the statistically relevant peaks. The pure TP phase is shown in blue. When both phases are present, the ratio of the OP peak area over the TP peak area is displayed with a linear colour scale ranging from red (TP peak dominates) to green (OP peak dominates).

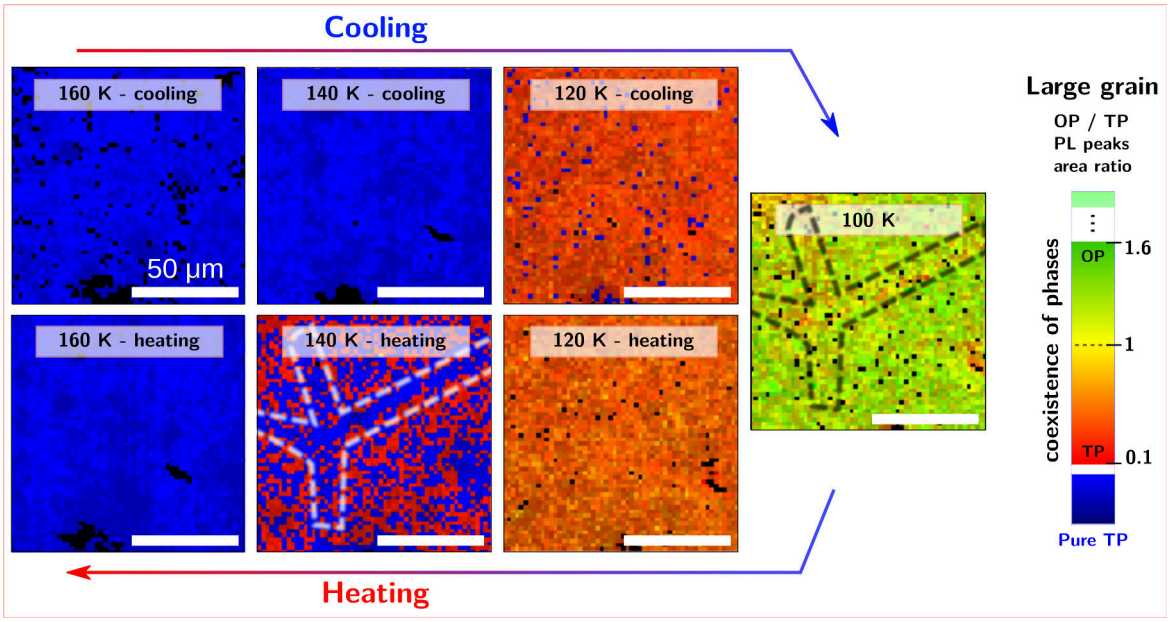

Fig. 3.20 **Temperature-dependent micro-PL measurements on the large grain $MAPbI_3$ thin film.** A tightly focused 532 nm laser was used with an excitation density of 1500 $mW.cm^{-2}$. We scanned the laser in steps of 2 µm and recorded at each location a PL spectrum in order to create 2D maps at 160 K, 140 K, 120 K and 100 K (while cooling down from room temperature to 100 K and heating back up to room temperature. Each spectrum was fitted with Gaussian functions, and the PL peak(s) area(s) extracted. Regions of pure TP phase are in blue, and the ratio of the OP peak area over the TP peak area displayed with a linear colour scale ranging from red to green when both phases coexist. The area circled by a dotted line highlights a region where the OP phase does not form very well even at 100 K and undergoes an early transition back to TP before 140 K (heating).

When cooling down the large grain sample (Figure 3.20), the PL arises only from the TP phase until 120 K, at which point mixed phases become interspersed throughout, with a larger proportion of emission from TP across the film. An increased heterogeneity in the area ratio of the OP and TP peaks in the presence of mixed phases appear at 100 K where the OP emission peak dominates overall (with a OP/TP ratio $\sim$1.6), apart from some features such as the one highlighted by dotted lines where it remains smaller than the TP peak. Interestingly, this heterogeneity is less visible at 120 K (heating), but it stands out again at 140 K (heating),

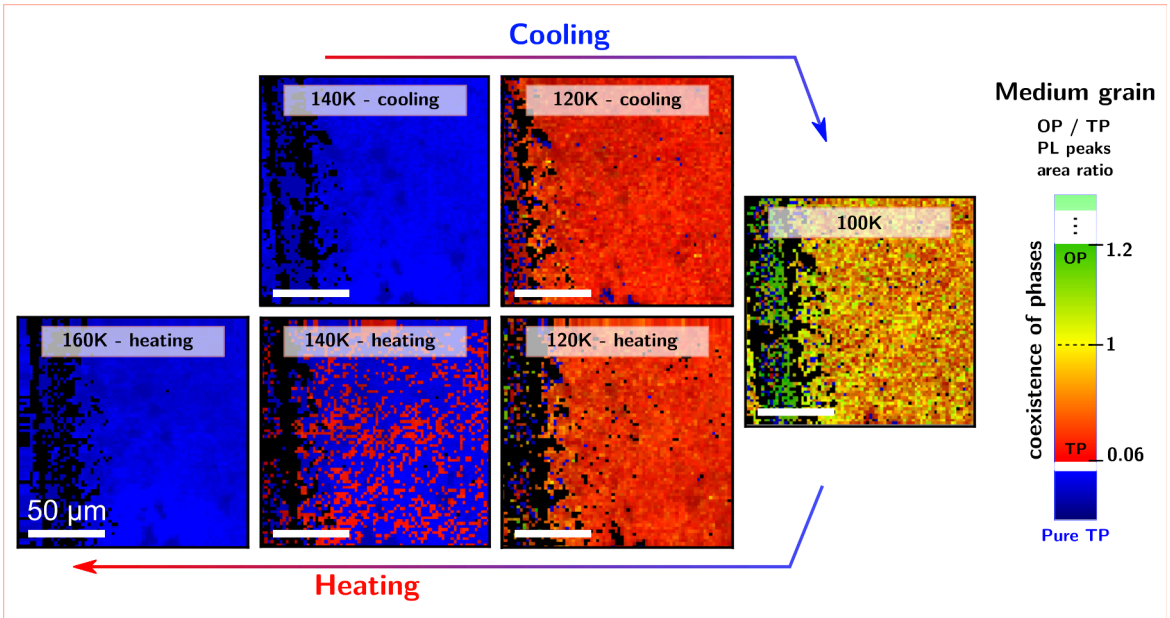

Fig. 3.21 **Temperature-dependent micro-PL measurements on the medium grain $MAPbI_3$ thin film.** Regions of pure TP phase are in blue, and the ratio of the OP peak area over the TP peak area displayed with a linear colour scale ranging from red to green when both phases coexist. On the left side, a scratch is visible that was used to track the laser and stepper drift across the temperature cycle.

the temperature at which the hysteresis is also the most noticeable when comparing with the 140 K (cooling) map.

The region highlighted by dashed lines in Figure 3.20 where the OP peak was still smaller than the TP peak at 100 K is also the first to transition back to the pure TP phase at 140 K (heating). These micro-PL maps reveal the micro-scale complexities of this phase transition behaviour and how sensitive the structure is to the local environment. Such pinning of the OP phase is not visible in the maps performed on the medium grain sample (3.21). We note as well that the fraction of OP phase at 100 K is less than in the large grain sample. This could result from a larger funneling of the OP emission to optically active defects, as suggested by Figure 3.8.

Again, no clear phase coexistence was seen on the small grain sample down to 100 K (Figure 3.22), which is consistent with these small grains being constrained and inhibited from freely undergoing phase transitions. However, the maps in Figure 3.23 show that the FWHM of the PL peak increases by ∼9 meV at 100 K across the film. This broadening suggests that the phase transition might be just starting, which corresponds to the macro-PL results in Figure 3.12. In contrast the phase transition is much more rapid and more easily performed in larger grain samples. This is consistent with our previous work, where we

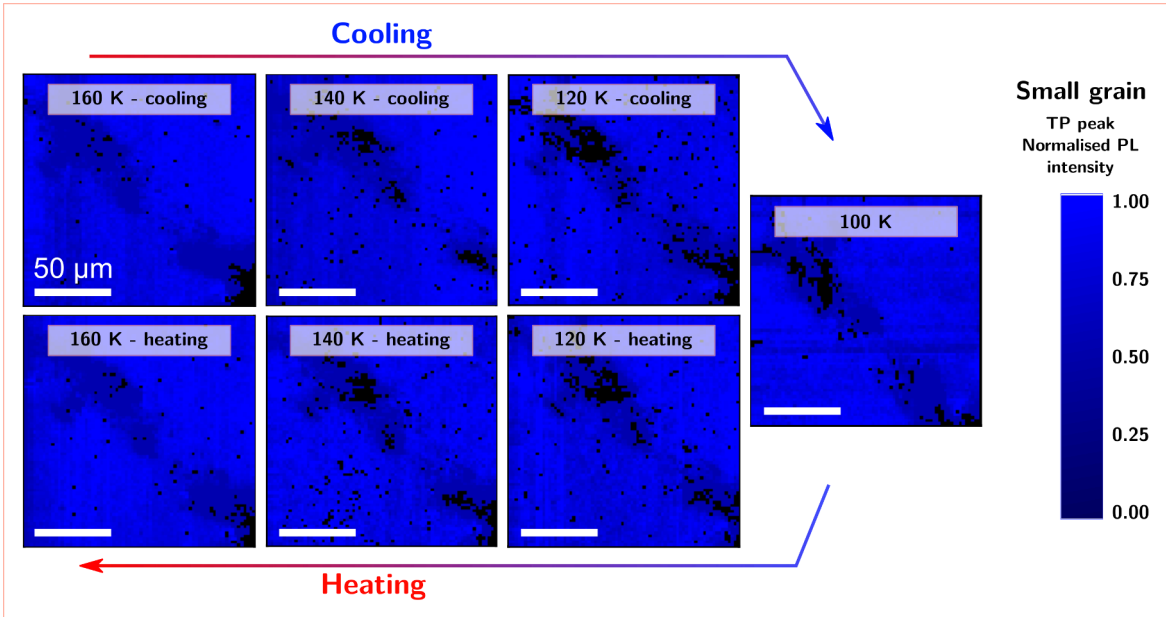

Fig. 3.22 **Temperature-dependent micro-PL measurements on the small grain $MAPbI_3$ thin film.** Regions of pure TP phase are in blue, and the ratio of the OP peak area over the TP peak area displayed with a linear colour scale ranging from red to green when both phases coexist. No phase transition is observed above 100K in this sample.

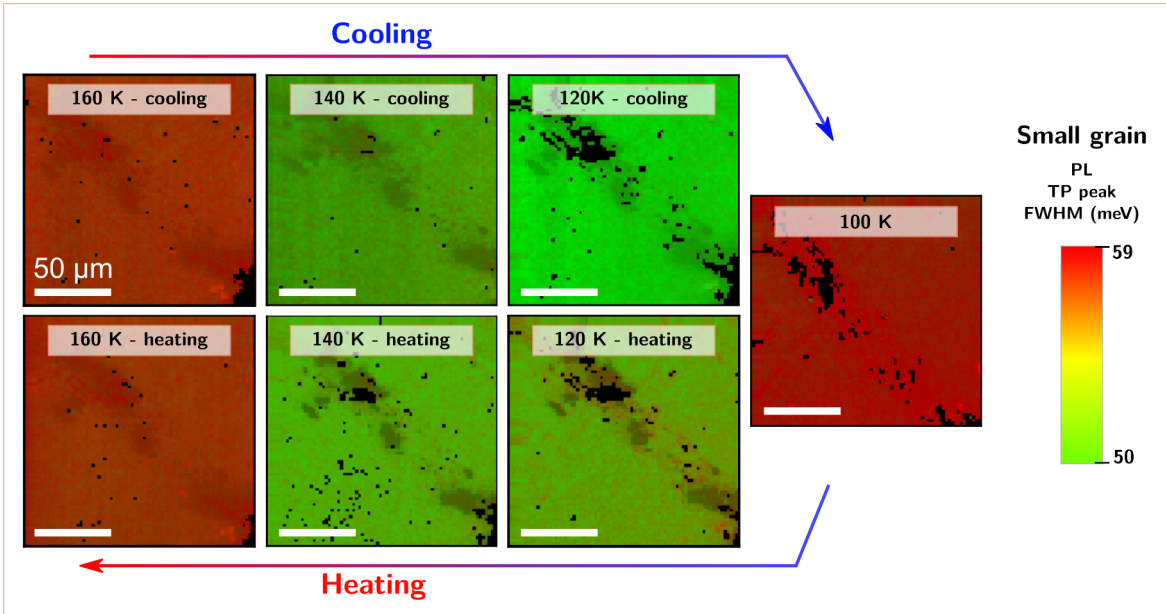

Fig. 3.23 **Temperature-dependent micro-PL FWHM on the small grain $MAPbI_3$ thin film.**

found that the hysteretic phase transition in a bulk film was reduced when the same film was scraped off into a powder form[139], allowing the system to more freely transition.

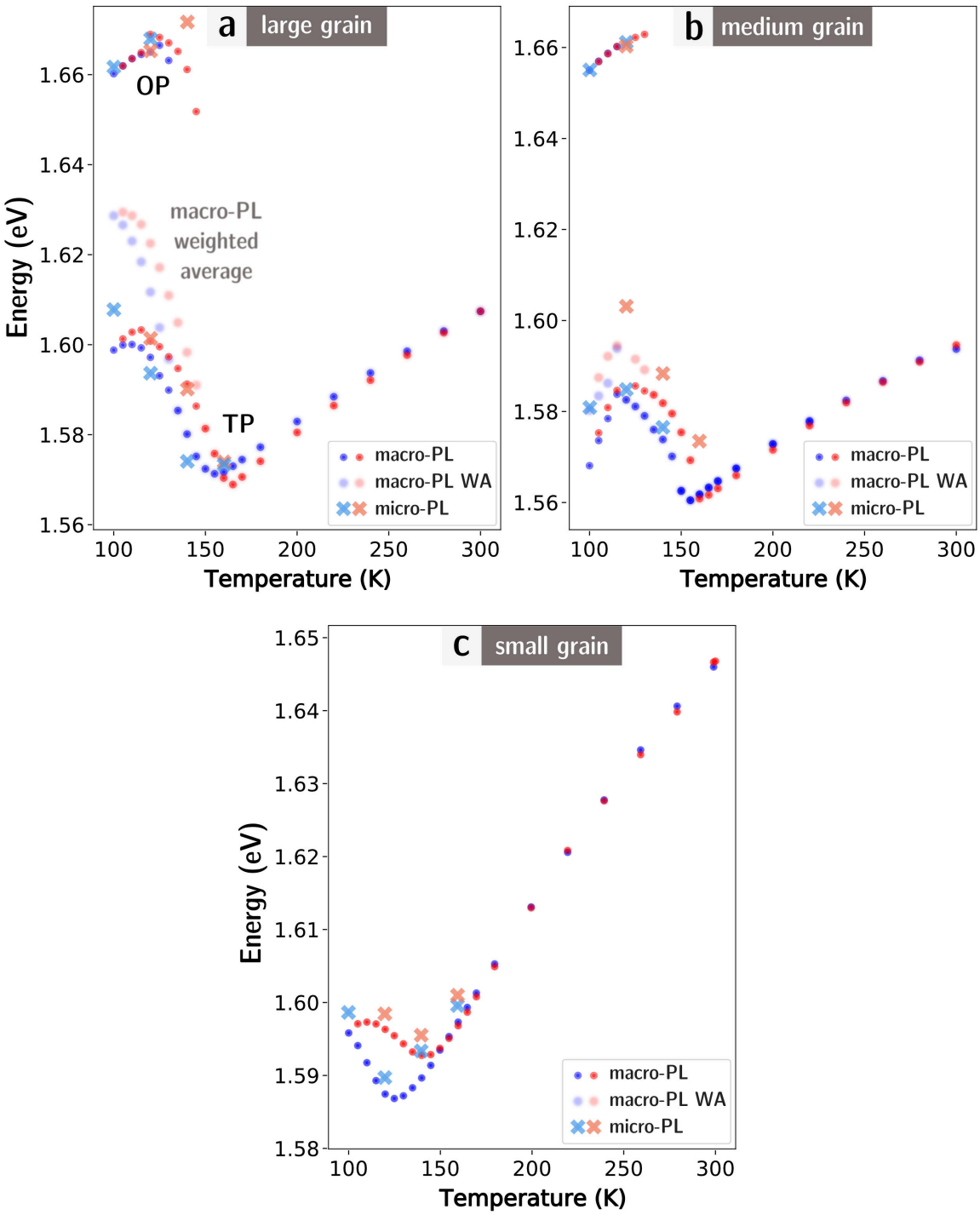

Fig. 3.24 **Temperature-dependent macro- vs micro-PL on $MAPbI_3$ thin films of varying grain size:** large grain (a), medium grain (b) and small grain (c). The positions in energy of the TP and OP peaks are displayed, as well as the weighted average of both phases (in macro-PL only). The agreement between macro- and micro-PL is good.

In Figure 3.24, the hysteresis loops extracted from the macro- and micro-PL measurements performed on each film are overlaid, showing a good agreement of both techniques. In the micro-PL case, each data point is an average over a map at a given temperature. For the medium grain film, the micro-PL spectra report a TP emission at higher energy than in macro-PL. Our interpretation is that micro-PL measurements being performed with a higher fluence, more traps are saturated and the emission is less funnelled to lower energies.

3.8 Conclusion

In this chapter, we investigated the TP to OP phase transition in $MAPbI_3$ perovskite thin films with grain sizes ranging across two orders of magnitude from tens of nanometres to micron-scale. By means of temperature-dependent X-ray diffraction, absorption, macro- and micro-photoluminescence measurements, we have shown that the phase transition was increasingly suppressed with decreasing grain size. We also reported that the hysteresis of both structural and optoelectronic properties widens across a larger temperature span with decreasing grain size. Micro-PL maps reveal a spatial heterogeneity in the presence of the mixed phase of the large grain film, providing a microscale visualisation of the findings. Our collective results provide insight into how sensitively the optoelectronic and phase transition properties depend on the local environment of the material. They strongly suggest that local strain plays a role in inhibiting the phase transition[150], and in the extreme case of very small grains, can almost entirely suppress the phase transition. This reveals strain as a lever for controlling phase behaviour, which could be exploited in future optoelectronic device structures[151, 148]. Further work would be required to elucidate the precise nature and magnitude of the strain involved in these phenomena.

We have established that local environment and mechanical constraints such as local strain can influence the optoelectronic properties of perovskite thin films. Yet, the optical techniques used in this chapter are surface sensitive and very little is known about sub-surface and bulk recombination pathways in these materials. In the next chapter, we use non-linear two-photon microscopy to map the photoluminescence at the micro-scale further into the depth of the samples, exploring the surface and bulk recombination properties in thin films and single crystals.

3.9 S'il vous plaît, raconte-moi l'Univers. (If you please, tell me about the Universe.) 3

— Mais je n'arrive pas à lire, ... pourquoi écrire une histoire que l'on ne peut pas lire ?, rétorqua le petit prince.

— Disons que je l'écris telle que ses personnages me la racontent !

— Moi aussi j'ai voyagé. J'ai rencontré un monarque, un businessman et un vaniteux, un buveur, un géographe et un allumeur de réverbère. J'ai aussi rencontré beaucoup d'animaux, mais aucun d'entre eux ne parlait un langage aussi étrange... De quoi parle ton histoire ?

— Cette histoire que j'essaie d'écrire, c'est celle de l'Univers. Le problème, c'est qu'il me la raconte sous forme d'énigmes.

— Il a l'air bien compliqué, ton Univers ! Il y a une chose que je ne comprends pas.

— Quelle est-elle ?, répondit le physicien, intéressé par la naïveté d'enfant du petit prince, cette capacité à questionner.

— C'est que je ne l'entends pas parler, l'Univers.

— Il parle tout doucement, et il faut tendre l'oreille... Tu aimes les animaux, m'as-tu dit. Je n'en ai pas, mais je voyage avec un ami qui ne me quitte jamais. Veux-tu que je te le présente ?

— J'en serais ravi, ... Mais je ne le vois pas ! S'exaspéra le petit prince.

— C'est qu'il est trop petit pour que nos yeux puissent le voir...

— Alors comment sais-tu qu'il est là ?

Le physicien sortit de sa poche une petite boite remplie de coton.

— Ouvre délicatement ta main, et laisse-moi te donner quelque chose.

Le petit prince s'exécuta, et le physicien retourna la petite boite au-dessus de ses doigts comme s'il voulut y déposer le contenu.

— C'est tout ? Je ne vois toujours rien !, s'impatienta le garçon.

— Détends-toi, tu vas lui faire peur ! Et surtout, tends bien l'oreille...

— But I cannot read it, ... why are you writing a story that cannot be read?, retorted the little prince.

— Let's say that I am writing it the way its characters tell it to me...!

— I have travelled as well. I have met a monarch, a businessman and a vain, a drinker, a geographer and a lamplighter. I have also encountered many animals, but none of them would speak such a weird language... What is your story about?

— Well, ... this story I am trying to write is that of the Universe. But he tells it through enigmas...

— Your Universe seems really complicated! There is something that I don't understand...

— What is it?, answered the physicist, interested in the naivety of the little prince, this ability to question that education seems to deprive us of.

— I do not hear the Universe speaking.

— He speaks very softly, you should prick up your ears... You like animals, don't you? Unfortunately, I don't have any pets. But I always travel with a friend who never leaves me. Would you like to meet him?

— I would love to, ... But I cannot see him!, the little prince was exasperated.

— That is because he is too small for our eyes to see him...

— Therefore how do you know that he is there?

The physicist took out of his pocket a tiny box full of cotton. He opened it, and said:

— Open your hand delicately, and let me give you something.

The little prince opened his hand, and the physicist flipped the box above his palm to drop off its content.

— Is that all? I still cannot see anything!, the boy was getting impatient.

— Relax, you will scare him! Now, listen carefully...

Chapter 4

Probing buried recombination in perovskite structures with 3D time-resolved tomography

Perovskite solar cells and light-emission devices are yet to achieve their full potential owing in part to microscale inhomogeneities and defects that act as non-radiative loss pathways. These sites have been revealed using local photoluminescence mapping techniques but the short absorption depth of photons with energies above the bandgap means that conventional one-photon excitation primarily probes the surface recombination.

Here, we use two-photon time-resolved confocal photoluminescence microscopy to explore the surface and bulk recombination properties of methylammonium lead halide perovskite structures. By acquiring 2D maps at different depths, we form 3D photoluminescence tomography images to visualise the charge carrier recombination kinetics.

The technique unveils buried recombination pathways in both thin film and micro-crystal structures that aren't captured in conventional one-photon mapping experiments. Specifically, we reveal that light-induced passivation approaches are primarily surface-sensitive and that nominal single crystals still contain heterogeneous defects that impact charge-carrier recombination.

Our work opens a new route to sensitively probe defects and associated non-radiative processes in perovskites, highlighting additional loss pathways in these materials that will need to be addressed through passivation treatments.

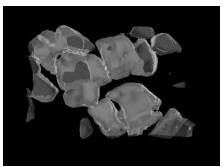

4.1 Introduction

Solution-processed perovskite films can be fabricated rapidly, showing great promise for large-scale manufacturing[152] and printable optoelectronic devices[153]. Single crystals can also be grown in millimetre size and as bulk films of interconnected micro-crystals[154, 155].

Despite high defect levels of the order of 10^{15} cm^{-3} in polycrystalline films, a million times higher than in gallium arsenide (GaAs) or silicon (Si), polycrystalline perovskite devices still operate remarkably well[9]. Nevertheless, these defects are yet not entirely benign, and lead to substantial fractions of non-radiative decay which still dominates recombination of charge carriers in perovskite structures under solar illumination conditions[156].

For example, recent reports of photoluminescence maps have revealed a grain-to-grain[157] heterogeneity in the emission from surfaces of metal-halide perovskite polycrystalline films, which leads to substantial losses in PV and LED devices[158, 48, 159]. However, these maps are dominated by photoluminescence from the surface of the films due to the finite absorption depth of the photons directly photo-exciting the material, and thus we do not gather information about important local recombination pathways buried beneath the surface.

Extensively used in biology for imaging over the past 20 years[160–162], two-photon photoluminescence (2P-PL) spectroscopy is based on the near-simultaneous absorption of two photons with an energy lower than the materials' band-gap. This is a non-linear optical process that only occurs in a measurable quantity at high excitation intensities compared with one-photon photoluminescence (1P-PL). As such, absorption only occurs at the focal point of the microscope where the local concentration of photons is sufficiently high. At lower intensities outside of the focal point, the material is transparent to these photons due to the sub-bandgap photon energy. This allows for 3D optical sectioning of the sample, while avoiding excitation of the sample out of the desired focal plane.

Time-resolved two-photon confocal photoluminescence (2P-TRPL) was recently developed to probe carrier lifetimes in semiconductors[115], and was used successfully to investigate the passivation of CdTe thin film solar cells[113]. Strong two-photon absorption in perovskites has been reported[163–165] and macroscopic 2PPL measurements revealed the existence of different recombination pathways in the bulk and at the surface of films[166, 167]. 2P-TRPL has also been used to investigate carrier recombination in perovskite single crystals[168, 169], quantum dots[170] and microplates[171].

Three-dimensional tomography has been performed on perovskite crystals using one-photon excitation but the strong absorption coefficient and finite absorption depth[56] means that optical effects such as those at the edges dominate and mask crucial information about the bulk[172].

In this chapter, 2P-TRPL microscopy measurements on methylammonium lead iodide ($MAPbI_3$) and bromide ($MAPbBr_3$) polycrystalline and micro-crystal films are reported, that compare local surface and bulk recombination properties. These measurements were performed using a home-built confocal microscope developed by Edward Barnard at the Molecular Foundry, Berkeley Lab. They reveal buried recombination pathways in both poly-crystalline and micro-crystal films. We also demonstrate the technique on photo-brightened (passivated) films to show that such approaches primarily passivate the surfaces and additional work will be required to passivate the non-radiative pathways below the surface.

For the first time, we demonstrate time-resolved 3D tomography on microcrystal films of $MAPbBr_3$ and $MAPbI_3$ and form 4D images of the PL with temporal and spatial resolution. We reveal buried, heterogeneous recombination pathways even in structures that have been previously considered as single crystals. Our work opens up 4D spectroscopy for the exploration of optical properties and recombination pathways in perovskites films, crystals and full device structures.

Alongside these main results, additional measurements performed on a triple-cation film are also reported. Today's best perovskite solar cells use a mixture of formamidinium and methylammonium as the monovalent cations. With the addition of inorganic cesium, the resulting triple cation perovskite compositions are thermally more stable, contain less phase impurities and are less sensitive to processing conditions[173]. Current-voltage (JV) measurements by Mojtaba Abdi-Jalebi on triple-cation full device stacks have shown very encouraging efficiencies and resilience, with a suppressed JV hysteresis. These results are summarised in the following section.

This work was published in the Energy and Environmental Science journal[145]. I am the first author of the article. It is the result of a collaboration between the Cavendish Laboratory, the Molecular Foundry in Berkeley (USA), MIT (USA) and KAUST (Saudi Arabia). $MAPbI_3$ thin films were made at MIT by Roberto Brenes while single crystals and micro-crystal-films were made and characterised at KAUST by Ayan Zhumekenov. The optical measurements were performed at the Molecular Foundry using the setup developed by Edward Barnard. The data analysis was carried out by myself.

4.2 Sample preparation

4.2.1 $MAPbI_3$ thin films

Similarly to what was reported in Chapter 4.2, we solution-processed thin films of $MAPbI_3$ on cover slip glass following previous methods[157, 51, 174]. Glass substrates were washed sequentially with soap, de-ionized water, acetone, and isopropanol, and finally treated under oxygen plasma for 10 min. Thin films of $MAPbI_3$ were solution processed by employing a methylammonium iodide (MAI) and lead acetate $Pb(Ac)_2{\cdot}3H_2O$ precursor mixture with a hypophosporous acid (HPA) additive[174]. MAI (Dyesol) and $Pb(Ac)_2{\cdot}3H_2O$ (Sigma-Aldrich) were dissolved in anhydrous N,N-dimethylformamide (DMF) at a 3:1 molar ratio with final concentration of 37 wt% and HPA added to an HPA:Pb molar ratio of $\sim$11%. The precursor solution was spin coated at 2,000 rpm for 45 s in a nitrogen-filled glove box, and the substrates were then dried at room temperature for 10 min before annealing at 100°C for 5 min. All samples were then stored in a nitrogen-filled glove box until used.

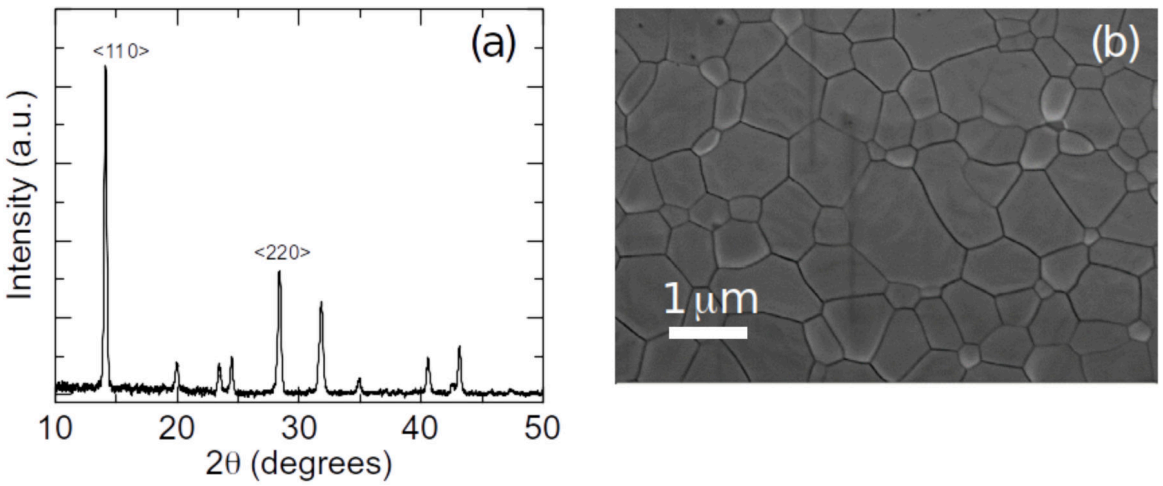

Fig. 4.1 **(a) X-Ray-Diffraction (XRD) pattern and (b) Scanning electron micrograph (SEM) of the $MAPbI_3$ films used in this work.** These materials were previously used to fabricate solar cell devices achieving $\geq$ 15% power conversion efficiency[157].

The light-soaking was performed on a few samples from the batch by photo-exciting perovskite films on coverslips enclosed in a custom-built flow chamber capable of flowing ultra-high purity gases in a controllably humidified form (40% - 50% relative humidity). The samples were photo-excited with a 532 nm CW laser at intensities approximately equivalent to the photon fluxes of 2 sun irradiation (150 mW/cm^2) for 30 minutes. They were then sealed and shipped for measurement the following day.

4.2.2 Triple Cation Samples and Devices

State-of-the-art triple-cation perovskites, yielding high-performing photovoltaic devices when prepared in a full device stack, were fabricated. The organic cations were purchased from Dyesol; the lead compounds from TCI; CsI from Alfa Aesar. The triple-cation perovskite thin films ($(Cs_{0.06}FA_{0.79}MA_{0.15})Pb(I_{0.85}Br_{0.15})_3$, where MA = methylammonium, $CH_3NH_3^+$ and FA = formamidinium, $NH_2CH{=}NH_2^+$), were deposited from a precursor solution containing FAI 1.0 M, PbI_2 1.1 M, MABr 0.2 M and $PbBr_2$ 0.22 M in anhydrous DMF:DMSO 4:1 (v:v). Then CsI, dissolved as a 1.5 M stock solution in DMSO, was added to the mixed perovskite precursor (5% volume) to make triple-cation perovskite. The perovskite solution was spin coated in a two-steps program at 1000 and 4000 rpm for 10 and 30 s respectively. During the second step, 150 µL of chlorobenzene was poured on the spinning substrate 5 s prior to the end of the program. The substrates were then annealed at 100°C for 45 min in a nitrogen-filled glove box.

The devices were fabricated following the same procedures for substrate preparation as well as deposition of both electron and hole transport layers (that is, TiO_2, spiro-OMeTAD) developed in earlier work[175]. Figure 4.2 displays current-voltage measurements and performance (**a**,**c**), as well as an SEM image of a typical triple-cation thin film (**b**).

4.2.3 Bulk micro-crystal films

Micro-crystal films of $MAPbX_3$ (where X = Br, I) were prepared following slightly modified protocol of that reported by Saidaminov et al.[155] Namely, 0.3 M solutions of MABr/$PbBr_2$ in DMF and 2MAI/PbI_2 in GBL were individually prepared and filtered through 0.22-µm pore-size filters. Each solution was mixed with 1,2-dicholorbenzene (DCB) in 5:4 volumetric ratio and then transferred into a crystallization dish (diameter 5 cm) containing pre-cleaned glass substrate. The crystallization dish was covered with a glass cover and then heated under continuous stirring at 500 rpm. After 30 mins of stirring at 40°C and 75°C, the micro-crystal films of $MAPbBr_3$ and $MAPbI_3$, respectively, were obtained on the glass substrates. An X-Ray diffraction (XRD) pattern is shown in Figure 4.3, whilst top and side view SEM images of both $MAPbBr_3$ (**a**, **c**) and $MAPbI_3$ (**b**, **d**) micro-crystal films are displayed in Figure 4.4. Finally, the substrates were extracted from the solutions and annealed on a hot plate at 110°C for 5 mins. All procedures were performed at ambient conditions with ∼55-57% relative humidity.

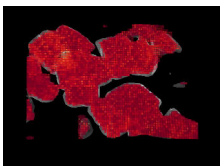

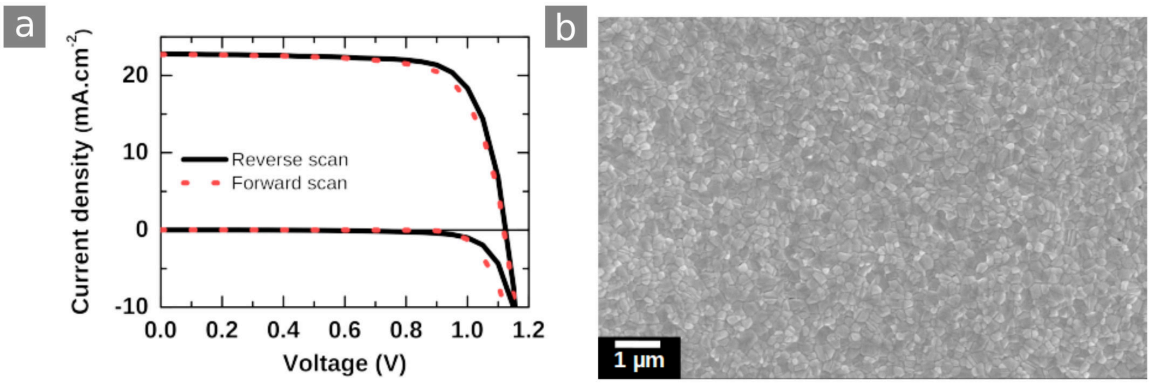

c

	J_{sc} [mA.cm^{-2}]	V_{oc} [V]	FF	PCE [%]
$(Cs,FA,MA)Pb(I_{0.85}Br_{0.15})_3$				
Reverse	22.8	1.124	0.76	19.4
Forward	22.7	1.118	0.73	18.5

Fig. 4.2 **Current-voltage (JV) curves measured on a triple-cation full device stack.** (a) Current-voltage curves measured under AM1.5 100mW/cm^2 simulated sunlight and in the dark for the alloyed triple cation sample $(Cs_{0.06}FA_{0.79}MA_{0.15})Pb(I_{0.85}Br_{0.15})_3$ films in the full device stack FTO (fluorinated tin oxide)/c-TiO_2/meso-TiO_2/Perovskite/Spiro-OMeTAD/Au. (b) Scanning electron micrograph (SEM) of a triple cation film characterised in this work. (c) Device parameters from a (FF is fill factor, PCE is power conversion efficiency). Data supplied by Mojtaba Abdi-Jalebi.

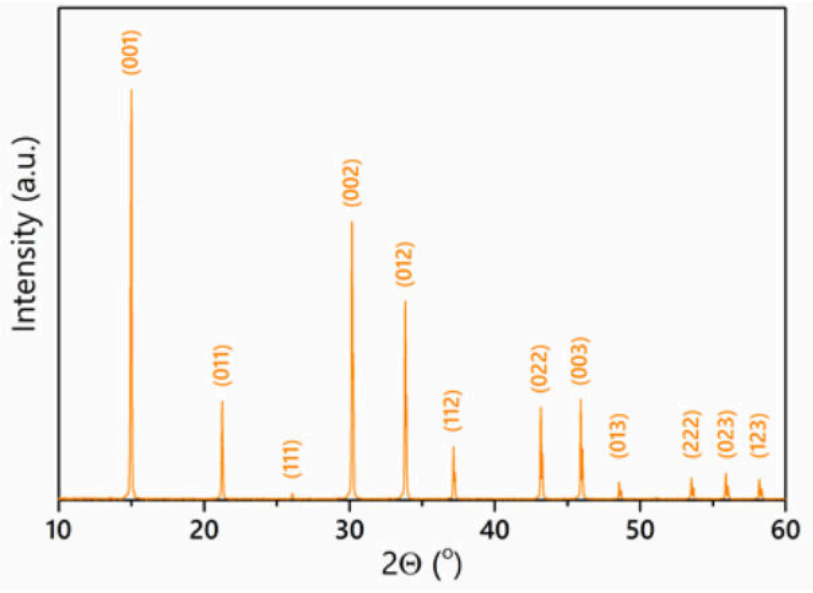

Fig. 4.3 **X-Ray Diffraction pattern measurement of a $MAPbBr_3$ micro-crystal film**, courtesy of Ayan A. Zhumekenov.

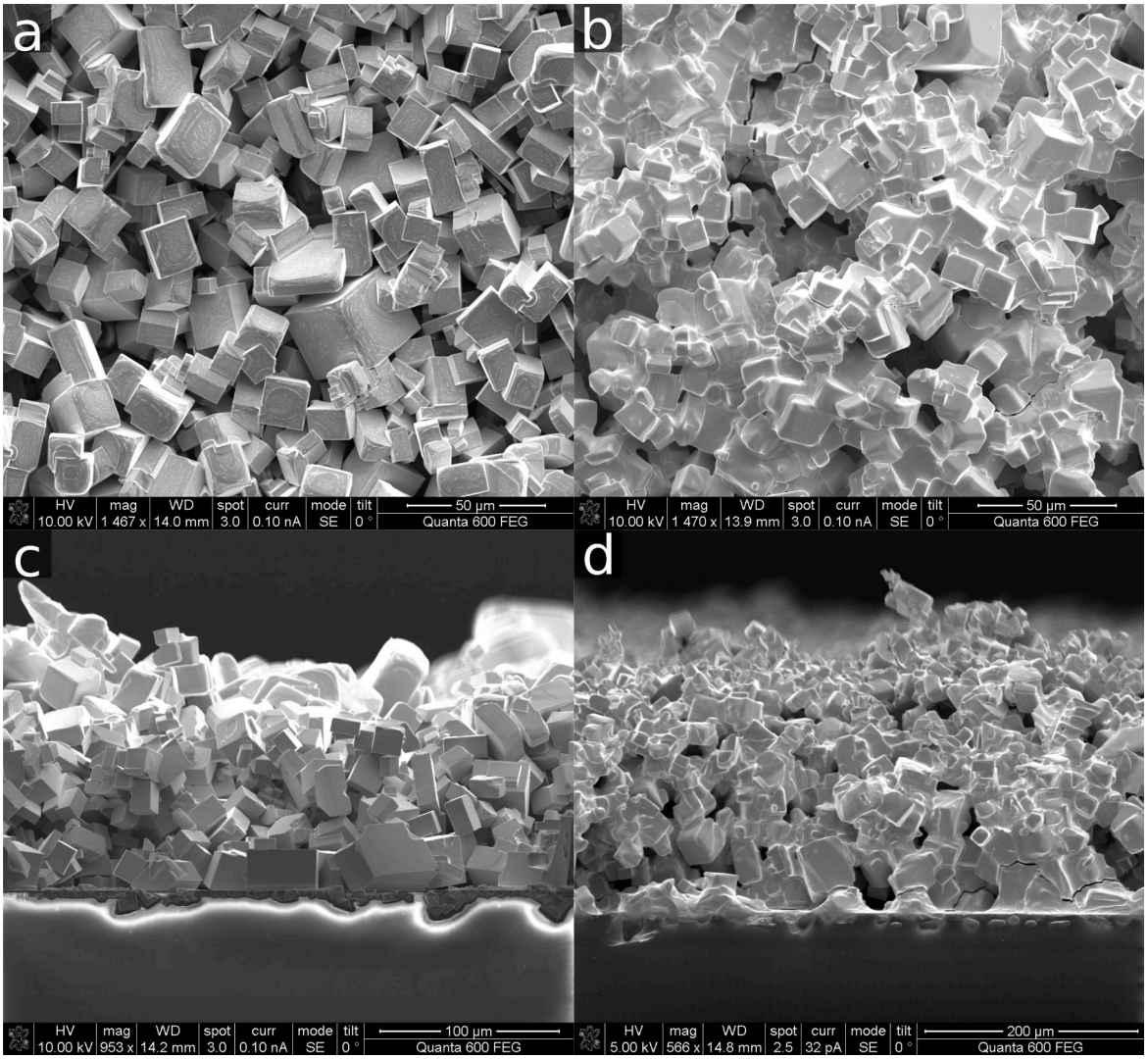

Fig. 4.4 **SEM images of micro-crystal films:** $MAPbBr_3$ (a, c) and $MAPbI_3$ (b, d), top and side view respectively. Courtesy of Ayan A. Zhumekenov.

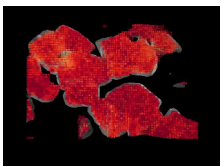

4.3 Two-photon TR-PL microscopy on $MAPbI_3$ and triple-cation thin films

In this section, we first compare conventional one-photon and two-photon confocal PL maps on $MAPbI_3$ perovskite thin films. Because of the high absorption coefficient of methylammonium lead halide perovskites, photons with energy above the band-gap are absorbed near the surface. In order for one-photon measurements to be as surface sensitive as possible, we used an excitation wavelength of 510 nm for which we estimate a penetration depth[56] of the order of 100 nm. Single photons with wavelengths longer than the absorption edge do not carry enough energy to promote electrons to the conduction band and travel therefore deep into the material. Measurements in the bulk were performed with a 1100 nm excitation beam tightly focused by the confocal system described in Figure 2.14.

In Figure 4.5 **a**, we show a confocal PL count rate map using direct (one-photon, 1P) excitation with pulsed illumination at 510 nm (2.43 eV, 150 fs pulse width) to selectively generate excitations nearer to the surface than the bulk. This reveals grain-to-grain heterogeneity in luminescence[157, 48, 159], which at the low excitation densities used here ($\sim 10^{16}$ cm^{-3}) have been shown to arise primarily from trap-limited heterogeneous recombination rather than local diffusion effects[159]. The difference in brightness between grains is then thought to be due to a local difference in trap density, rather than an anisotropic diffusion due to differences in intergrain connectivity.

In Figure 4.5 **b**, we show the PL count rate map of the same scan region but impinging on the sample sub-bandgap photon pulses (1.27 eV, wavelength 1100 nm, 150 fs pulse width) below the bandgap of the perovskite (1.6 eV), giving rise to two-photon (2P) excitation in the bulk of the film. The excitation fluences used were tuned to obtain similar total PL count rates for both 1P and 2P measurements, which yield comparable charge excitation densities in both cases. We note that a precise calculation of charge density would require complex optical modelling and knowledge of the 2P absorption cross-section, but this provides an approximate matching for comparison purposes.

We estimate the waist of the focused excitation beam to be such that 2-photon absorption occurs through the entire thickness ($\sim$350-nm) of the films, and hence we are comparing surface-dominated excitation (1P) with bulk-dominated excitation. We normalise the counts of both maps to the mean counts of each map to allow a relative comparison between the maps (see similar results when normalising to the maximum counts in Figure 4.6).

We find that some grains, such as those circled in red in Figure 4.5 **a** and **a**, are bright on the surface but relatively dimmer in the bulk. We observe the opposite trend for some

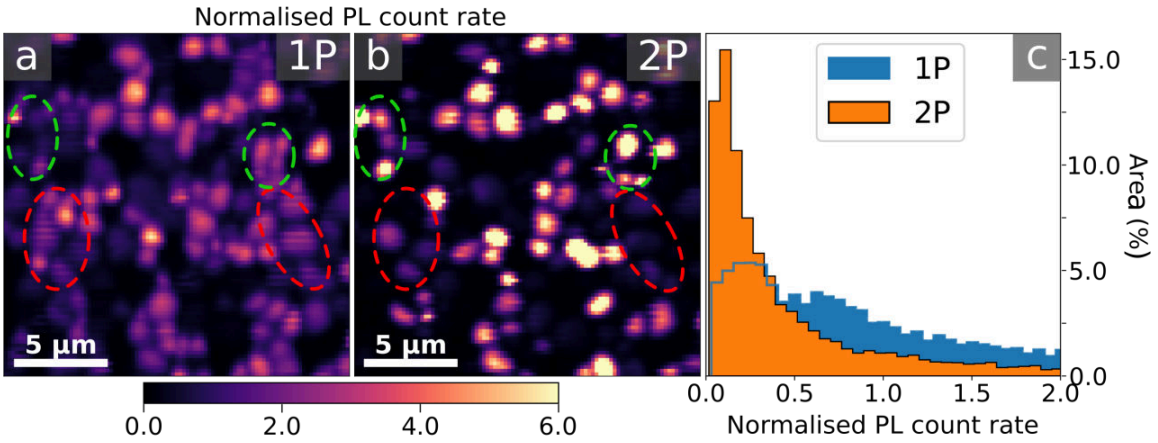

Fig. 4.5 **2D photoluminescence (PL) maps of a $MAPbI_3$ film normalised to their respective mean using (a) one-photon (1P-PL) and (b) two-photon (2P-PL) excitation** at 510 nm and 1100 nm respectively, with a pulsed (5 MHz, pulse width 150 fs) excitation density of $\sim 10^{16}$ cm^{-3}. (c) Comparison of the PL distributions from the two maps, normalised by the mean of each. The red dotted circles in (a) and (b) highlight grain clusters that are bright at the surface and dark in the bulk; the green dotted circles show the opposite trend.

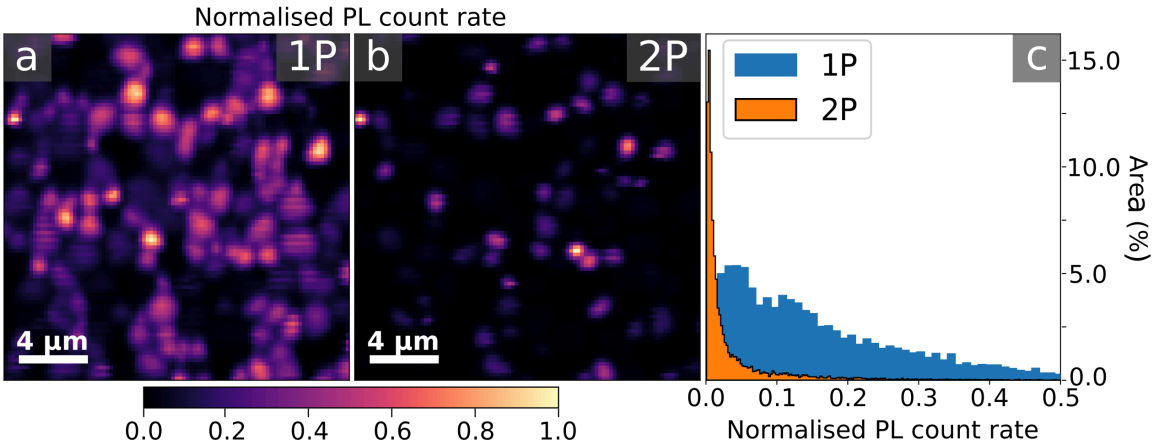

Fig. 4.6 **2D PL maps of the $MAPbI_3$ films from Figure 4.5 normalised to the total counts, using one-photon (1P) and two-photon (2P) excitation.** (c) Comparison of the count rate distributions again normalised to the total counts.

other grains (for example the clusters in green dotted circles), while many of the others are similarly bright or dark on the surface and in the bulk. From these maps, it is also clear that the contrast between dark and bright grains is greater when using 2P excitation.

This could be because local diffusion, which can act to homogenise the local emission heterogeneity, could potentially be more difficult through grain boundaries in the bulk compared to at the surface[159]. In Figure 4.5 **c**, we compare the relative luminescence for

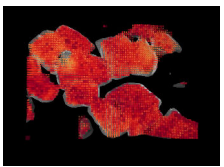

the 1P and 2P maps, with each again normalised to the mean counts for the maps. We find a tighter distribution of the 2P map with a long tail of brighter grains suggesting that the emission is closer to a normal (Gaussian) intensity distribution on the surface (1P) while being more localised below it (2P).

Figure 4.7 **a-d** compares the PL count rate to the spectral median in the same $MAPbI_3$ thin film. The difference in contrast and heterogeneity between bright and dark grains with 1P and 2P excitation, observed in PL, is not mirrored by a spectral heterogeneity (Figure 4.7 **e**). This suggests that the more localised PL emission observed below the surface is not due to a different nature of the traps (deep or shallow) present at the surface and below. We also note that bright grains exhibit a red-shifted emission compared with darker grains, which could indicate that in bright grains the trap-assisted recombination occurs via shallow trap states. It is then possible that charge carriers could be more easily thermally activated to the valence of conduction band from these trap states, hence mitigating non-radiative recombination and leading to brighter grains.

In contrast, the increased heterogeneity in 2P-PL versus 1P-PL count rate (Figure 4.8 **a, d** and **g**) in state-of-the-art alloyed triple cation samples $(Cs_{0.06}FA_{0.79}MA_{0.15})Pb(I_{0.85}Br_{0.15})_3$ is echoed by an increased heterogeneity in lifetime (Figure 4.8 **b, e**) and spectral median (Figure 4.8 **c, f**). The lifetime and spectral median distributions shown in Figure 4.8 **h, i** show that the more uniform and homogeneous PL at the surface is accompanied by longer lifetimes and a blueshift. Repeating the measurement on encapsulated samples could help to determine whether this clear difference between surface and bulk PL is intrinsic, or due to degradation of the material at the surface of the film. In the case where it would be due to degradation, it is interesting to note that the surface of triple-cation perovskite films would be more affected by environmental conditions than that of $MAPbI_3$ thin films.

These results collectively reveal new buried non-radiative recombination pathways that will need to be addressed to push even the highest performing devices to their radiative limits.

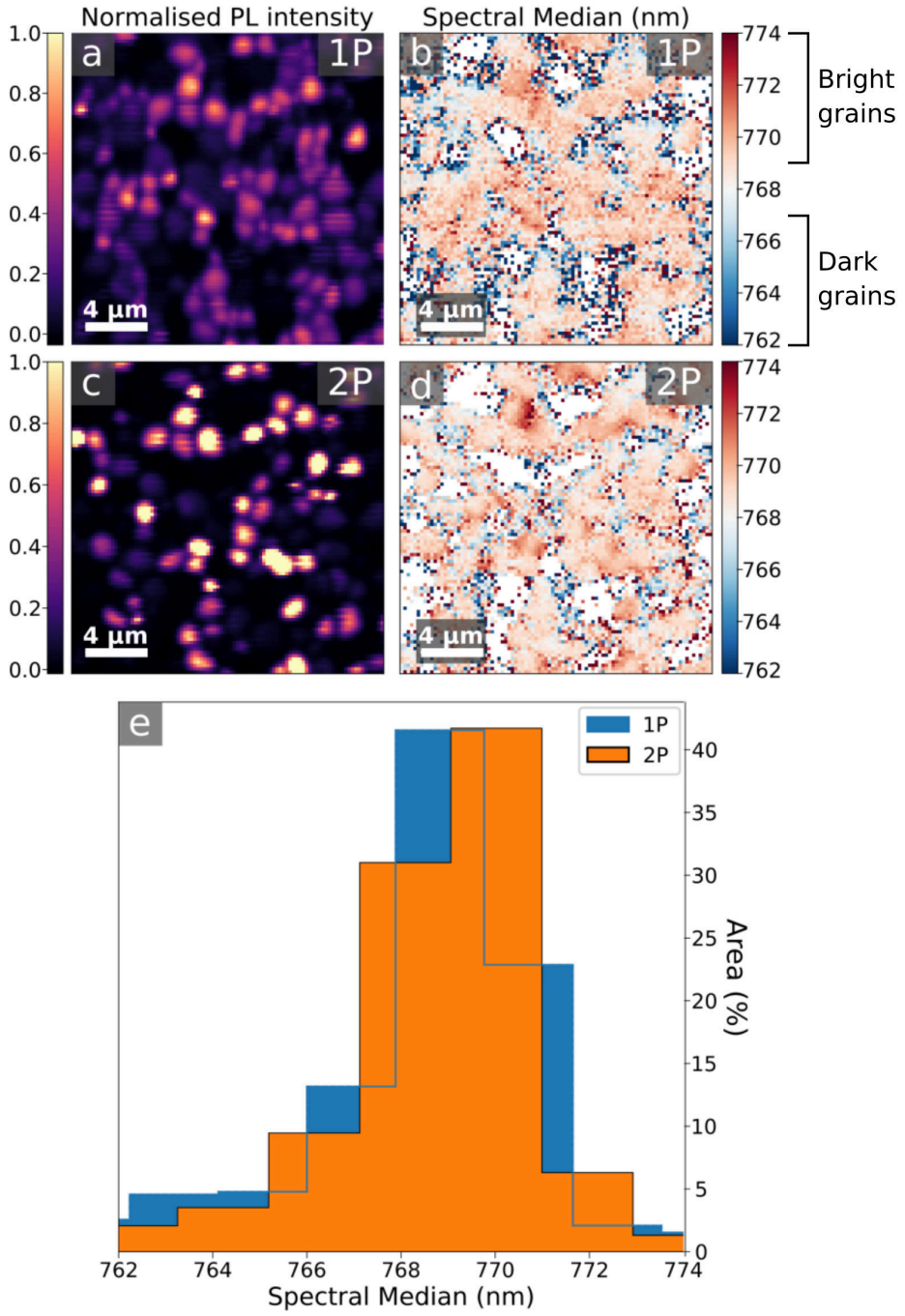

Fig. 4.7 **2D PL and spectral maps of $MAPbI_3$ films, using one-photon and two-photon excitation:** (a, b) 2D PL maps from Figure 4.5 normalised to their respective mean between 0 and 6, using one-photon (1P) and two-photon (2P) excitation. (b,d) spectral median maps extracted from 1P-PL and 2P-PL data. (e) Comparison of the spectral median distributions.

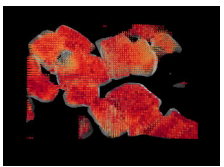

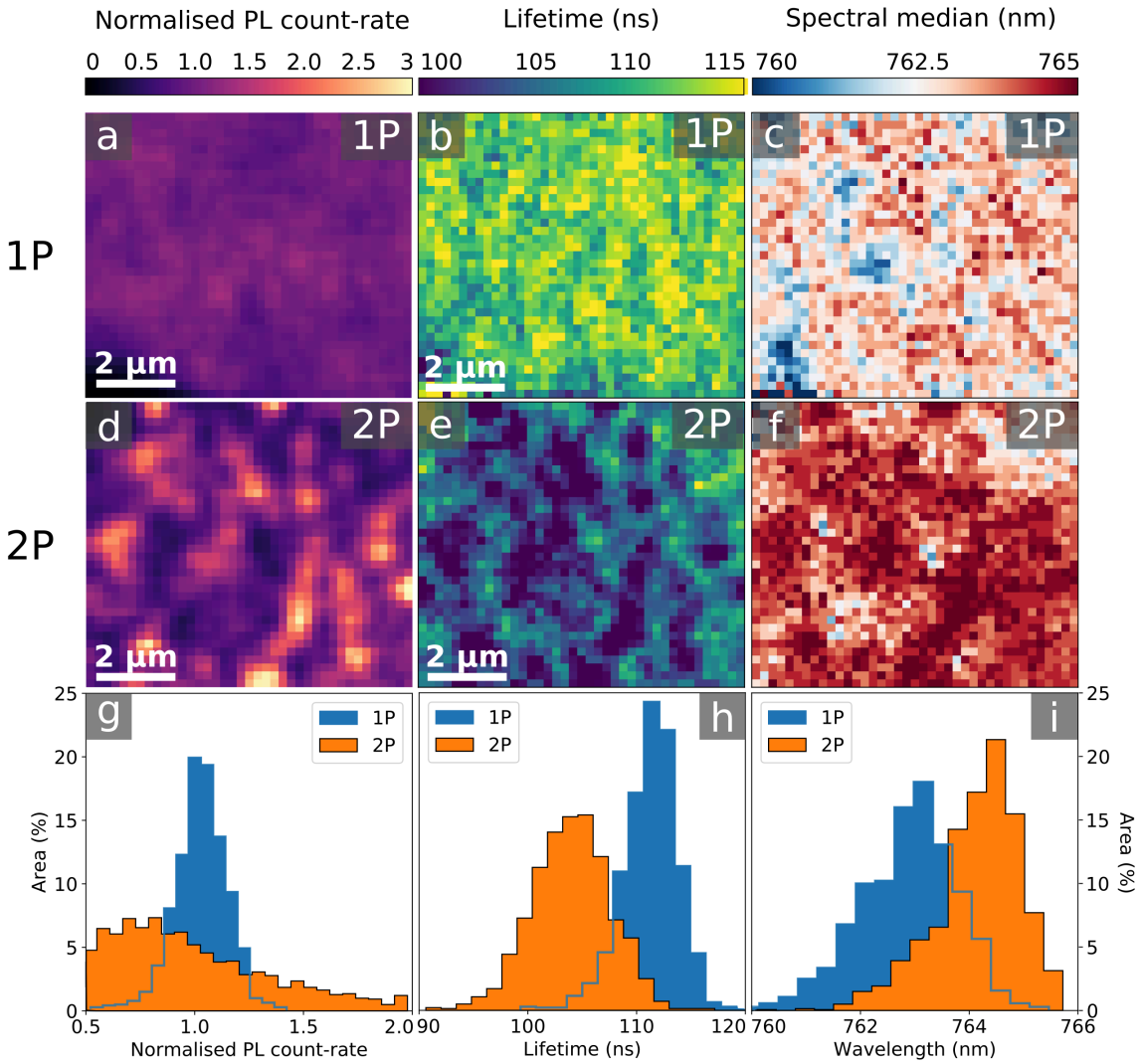

Fig. 4.8 **1P and 2P PL count rate (a, d, g), lifetime (b, e, h) and spectral median (c, f, i) maps and statistical distributions from a triple cation $(Cs_{0.06}FA_{0.79}MA_{0.15})Pb(I_{0.85}Br_{0.15})_3$ perovskite film.** The PL count rate maps are normalised to their respective mean, while in the PL count rate histogram (g) each distribution is normalised to its mean. The lifetime and spectral median maps (b, c, e and f) are respectively plotted on the same scale for direct visual comparison. The maps are recorded nominally on the same scan region, though there is some error in the precise alignment. The maps show that the PL is more uniform and homogeneous at the surface than below (a, d and g), and that this homogeneity is accompanied by longer lifetimes (b, e and h) and a blueshift (c, f and i).

4.4 Investigating the penetration of light-soaking and atmospheric treatments in $MAPbI_3$ thin films.

We and others recently found that light and atmospheric treatments[51–54] on polycrystalline $MAPbI_3$ perovskite thin films can result in large enhancements in the luminescence. These studies have proposed that the surfaces are selectively passivated though this has not yet been directly shown. Here, we use 1P- and 2P-TRPL to image the surface and the bulk of a $MAPbI_3$ film following an ex-situ light soaking treatment in humid air, with illumination from a 532-nm laser in 45% relative humidity for 30 minutes under intensities generating charge densities equivalent to ∼2 suns. In Figures 4.9 and 4.10, we show the maps obtained for an untreated and a treated film, respectively.

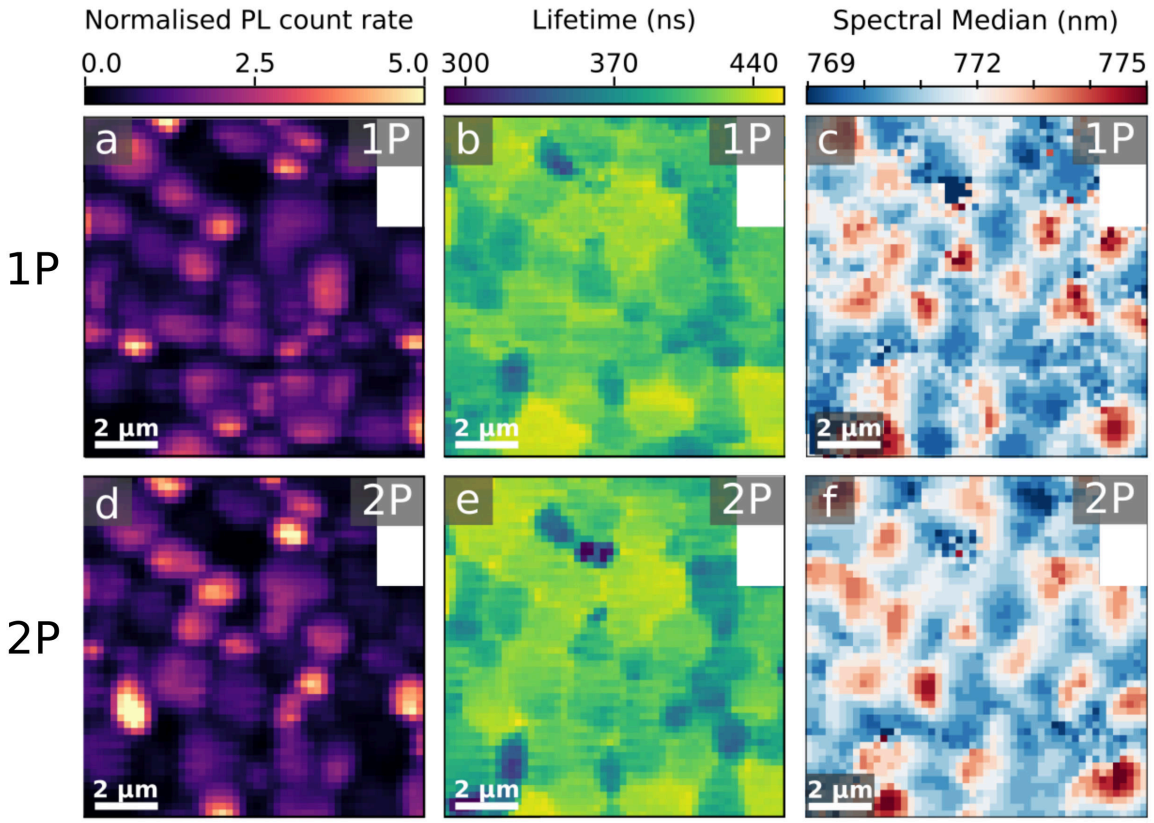

Fig. 4.9 **$MAPbI_3$ film: (a, d) PL count rate maps acquired using 1P and 2P excitation, normalised to their respective mean.** (b, e) Lifetime maps extracted from 1P- and 2P-TRPL measurements. (c, f) Spectral median maps extracted from 1P- and 2P-PL spectra. Regions denoted in white enclose marker particles on the surface of the film, which were excluded from the correlation analyses.

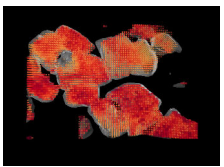

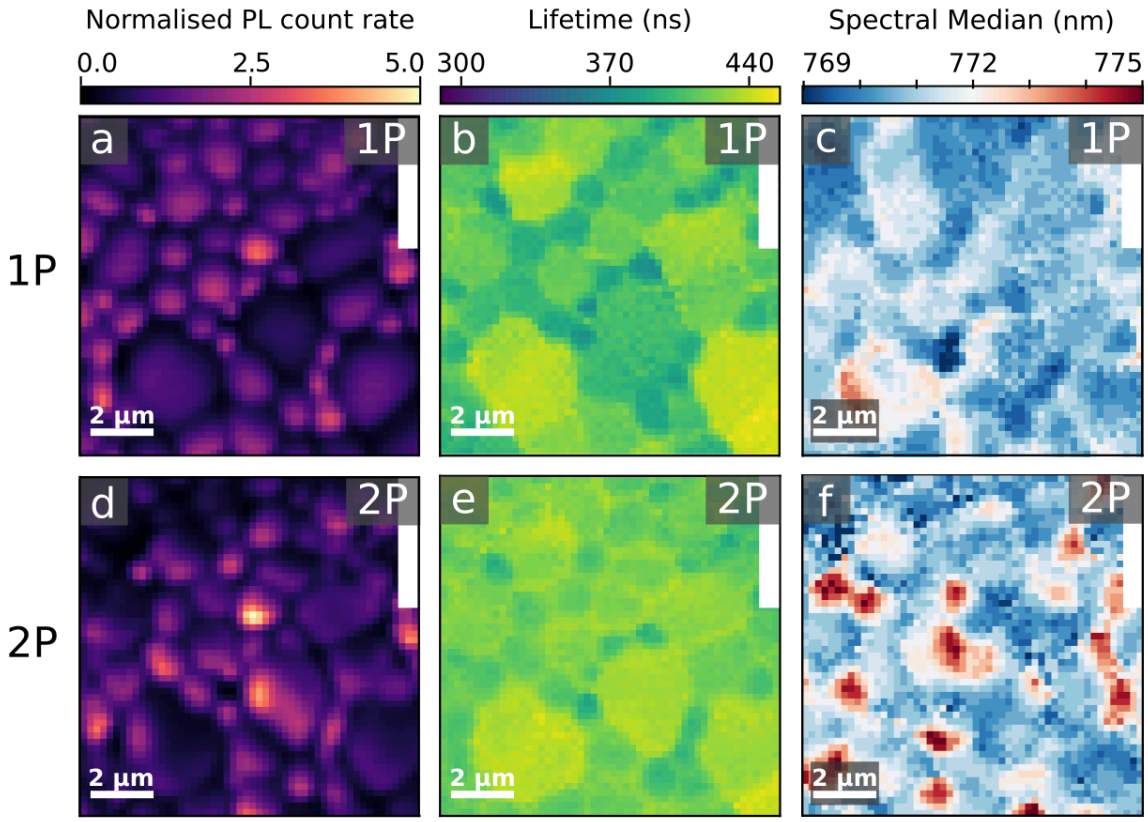

Fig. 4.10 **PL maps of a $MAPbI_3$ film after light soaking in humid air (30 minutes under 532 nm laser illumination at charge densities equivalent to ∼2 sun in air at 45% relative humidity).** (a,d) PL count rate maps (normalised to their respective mean) acquired using (a) 1P (510 nm) and (d) 2P (1100 nm) excitation with a pulsed (1.25 MHz, 150 fs pulse width) excitation density of $\sim 10^{17}$ cm^{-3}. (b,e) Lifetime maps extracted from (b) 1P- and (e) 2P-TRPL measurements. The lifetime is defined as the time at which 63% of the photons have been detected. (c,f) Spectral median maps extracted from 1P-PL and 2P-PL spectra. The regions marked in white denote marker particles on the surface of the film and were excluded from the analyses.

Figures 4.9 and 4.10 **a** and **d** display PL count rate maps obtained using 1P- and 2P-TRPL. As before, the 1P and 2P excitation fluences were chosen in order to obtain comparable PL count rates. Both 1P and 2P count rate maps, normalised to their mean, show that the PL is significantly more uniform in the treated sample. The 1P and 2P PL maps for the treated film displayed in Figure 4.11 **a** and **b**, respectively, were normalised to the maximum of their untreated counterpart. This normalisation allows for a direct comparison of the relative effect of the treatment on the the PL, with the greatest relative enhancement observed at the surface with 1P excitation (Figure 4.11 **a**). Overall, the normalised PL count rate distributions for 1P and 2P excitation in the treated film extend further towards lower values (Figure 4.11 **c**)

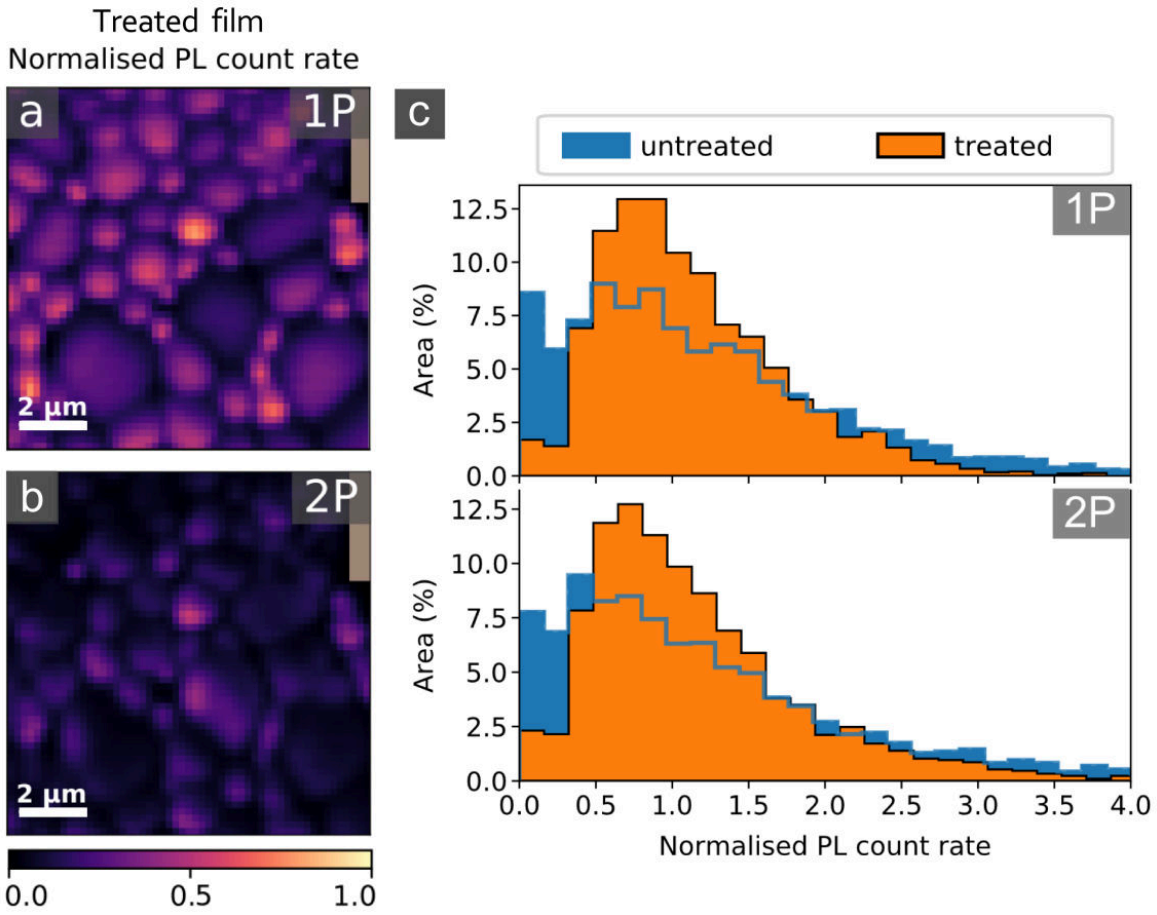

Fig. 4.11 **$MAPbI_3$ film after light soaking in humid air.** (a,b) PL count rate maps acquired using 1P and 2P excitation. The 1P map in (a) is normalised to the maximum of its untreated counterpart in Figure 4.9 (a). The 2P map in (d) is normalised to the maximum of Figure 4.9 (d). Shaded regions enclose marker particles on the surface of the film, excluded from the analysis. (c) Comparison between the PL count rates for 1P and 2P excitation on the untreated and treated films. Each distribution is normalised to its median value.

We plot the PL lifetime maps in Figure 4.10 **b** and **e** and compare the PL lifetimes for the treated and untreated samples in Figure 4.12 **a**. Here, we define lifetime as the time at which 1-1/e (∼63%) of the total photons have been detected following the excitation pulse, hence accounting for both the initial fast decay and the long-lived emission. Despite the increased homogeneity in emission in 1P-PL we observe a lengthening of the 2P-TRPL lifetime compared to the 1P-TRPL, which is particularly significant for the treated sample (Figure 4.12 **a**).

Interestingly, for both 1P- and 2P-TRPL we observe a positive correlation between the PL lifetime and count rate in the untreated film (Figure 4.13 **a** and **c**), but this turns into an anti-correlation in the treated film (Figure 4.13 **b** and **d**). We ascribe this observation to a decrease

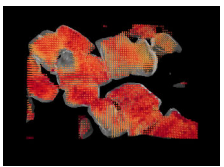

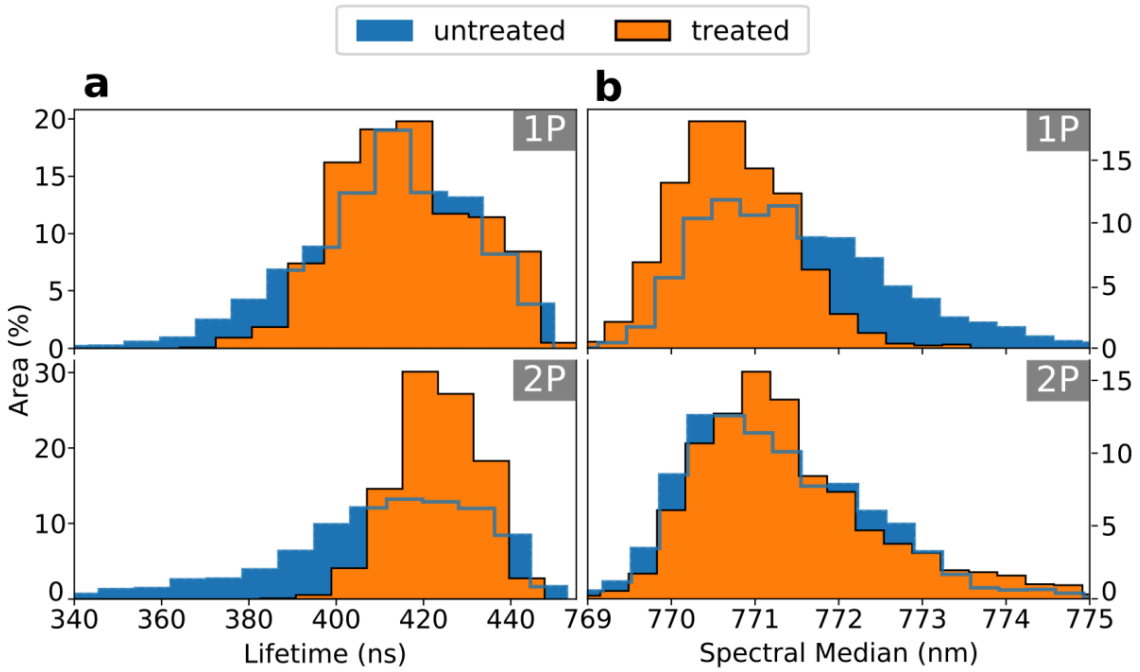

Fig. 4.12 **Comparison between (a) PL lifetime and (b) PL spectral median distributions in the untreated (blue) and treated (orange) films** extracted from the 2D maps in Figure 2 using one-photon (1P) and two-photon (2P) excitation.

in the trap density after treatment, particularly at the surface[157, 158], changing the nature of the primary recombination pathway for the same excitation fluence from trap-assisted (lifetime increases with decreasing trap density, i.e. with darker grains) to bimolecular (lifetime decreases with decreasing trap density, i.e. with brighter grains)[48, 47].

The longer 2P-TRPL lifetimes compared to the 1P-TRPL (Figure 4.12 **b**), particularly for the treated sample which follows bimolecular recombination kinetics, suggests that the treatment is most effective at the surface, leaving the bulk more defective than the surface. We note that the same grains appearing bright at the surface are also bright in the bulk (Figure 4.14). We also note that these observations on carrier lifetimes could be further complicated by any changes to local photon recycling due to increased luminescence yields[45], which would selectively increase the bulk lifetime more than the surface lifetime, or potential changes to local carrier diffusion[159] in the bulk and/or at the surface.

In Figure 4.10 **c** and 4.10 **f** we show the maps of the spectral median across the treated film, using 1P and 2P excitation, respectively (see Figure 4.9 for the untreated film). We show a direct comparison of the spectral median distributions for the treated (orange) and untreated (blue) films in Figure 4.12 **b**, unveiling a blueshift of the luminescence from the surface (1P) of the treated film. This could be consistent with the treatment leading to a reduction

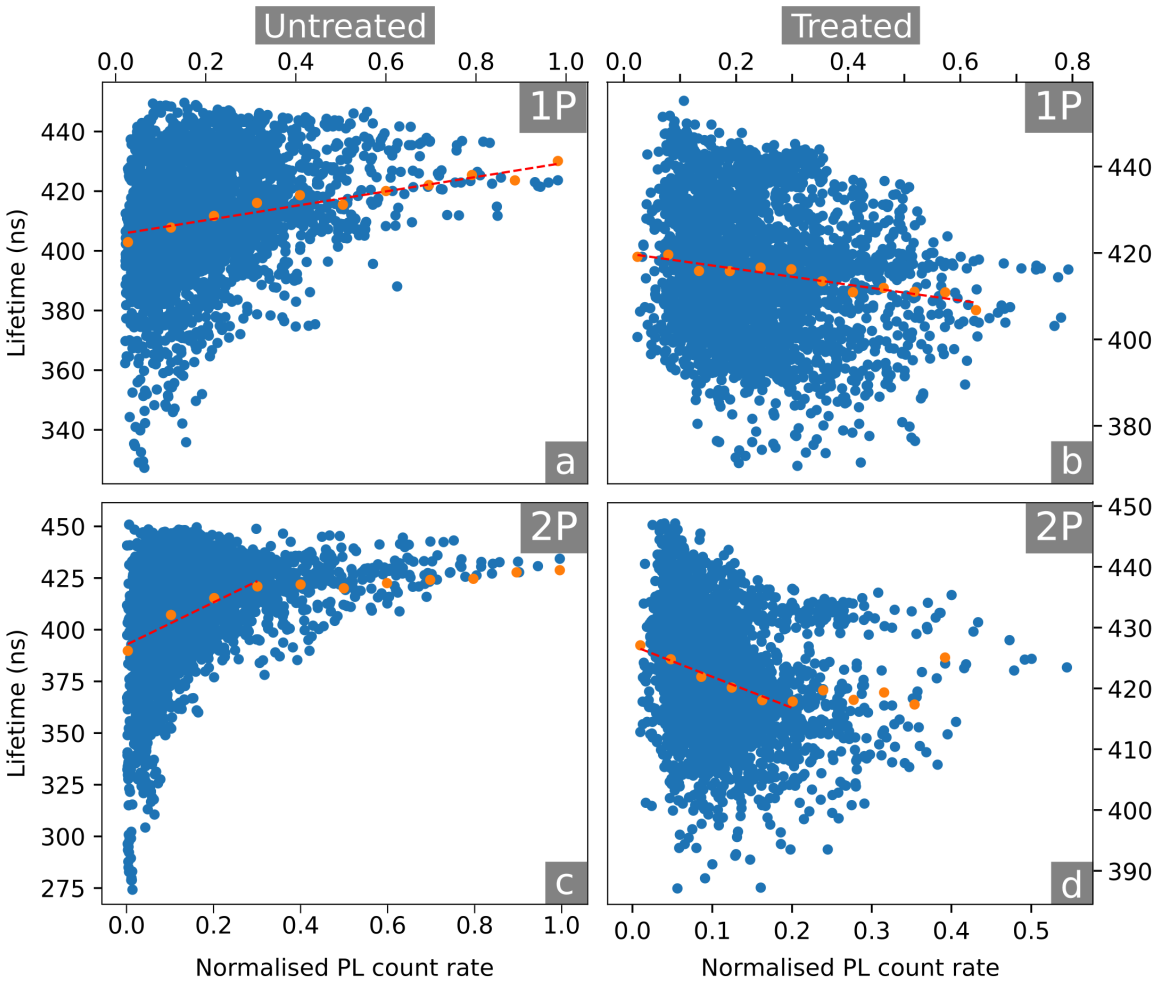

Fig. 4.13 **Spatial correlations between PL and lifetime in untreated (a, c) and treated (b, d) films**, using one-photon (1P) and two-photon (2P) excitation. Blue dots show the data point cloud and orange dots represent the same data after binning. In each quadrant, a linear fit (red dashed line) is applied to the binned data.

in shallow trap density (band-tail states)[157, 48, 176], leading to slightly higher energy emission. It may also be consistent with a greater fraction of the emission coming from a well-passivated surface than the bulk; emission from the latter would be red-shifted with respect to the surface through photon reabsorption and re-emission[45]. We note that some grains show red-shifted 2P-PL emission in both the treated (Figure 4.10 **f**) and untreated (Figure 4.9) samples, which do not correlate with PL count rate or lifetime on these specific grains; these could also be due to reabsorption events, although it is not yet clear why we observe them at sites that aren't necessarily more emissive than others.

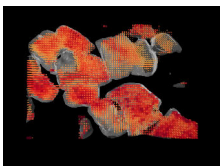

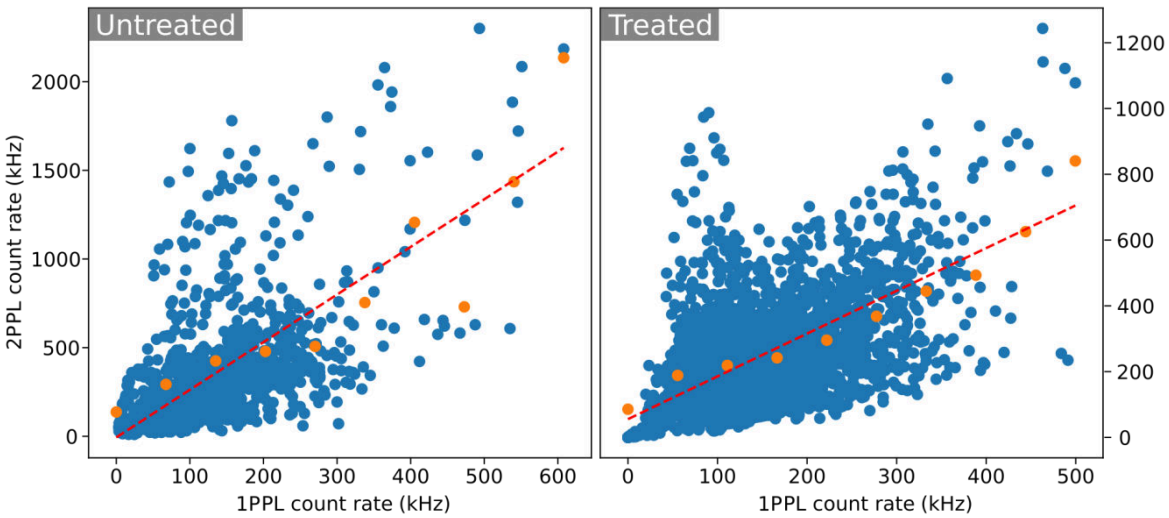

Fig. 4.14 **Spatial correlations between 1PPL and 2PPL in untreated (left) and treated (right) films**, using one-photon (1P) and two-photon (2P) excitation, respectively. Blue dots show the data point cloud and orange dots represent the same data after binning. In each panel, a linear fit (red dashed line) is applied to the binned data.

4.5 3D tomography on $MAPbBr_3$ micro-crystals

Two-photon photoluminescence microscopy can be powerful when it comes to constructing 3D PL tomography images. We applied this technique to micro-crystal films of $MAPbBr_3$ (Figure 4.15) shown in the SEM image in Figure 4.15 **d** and $MAPbI_3$ (Figure 4.16). We recorded a series of 2D 2P-TRPL maps, moving the focal point of the laser further into the bulk with a step of 1 µm between each map. In Figure 4.15 **a**, we show a time series of snapshots to visualise the PL decay over time after the excitation pulse. A flip-book animation is embedded in this (and the following) chapter, and a video of the 3D PL decay in a the micro-crystal film can be found online[1]. We note that for clarity we only show pixels with a relative PL count rate above 25% (see Figure 4.17 for a visualisation of the full dataset).

From the PL count rate data we plot isosurfaces, yielding the 3D image of the PL emission within single crystals shown in Figure 4b. In the same way, we display the 3D tomography of the lifetime in Figure 4.15 **c**.

In Figure 4.15 **b** and **c**, we compare the PL count rate and lifetime, and find that we again observe buried recombination and heterogeneity even within these structures which have been nominally reported as single crystals[154]. Interestingly, some pockets of strong

[1] https://pubs.rsc.org/en/content/articlelanding/2018/ee/c8ee00928g

luminescence intensity are associated with long lifetimes (blue circles in Figure 4.15 **b** and **c**) while some others are not (green circles).

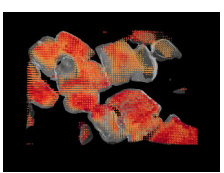

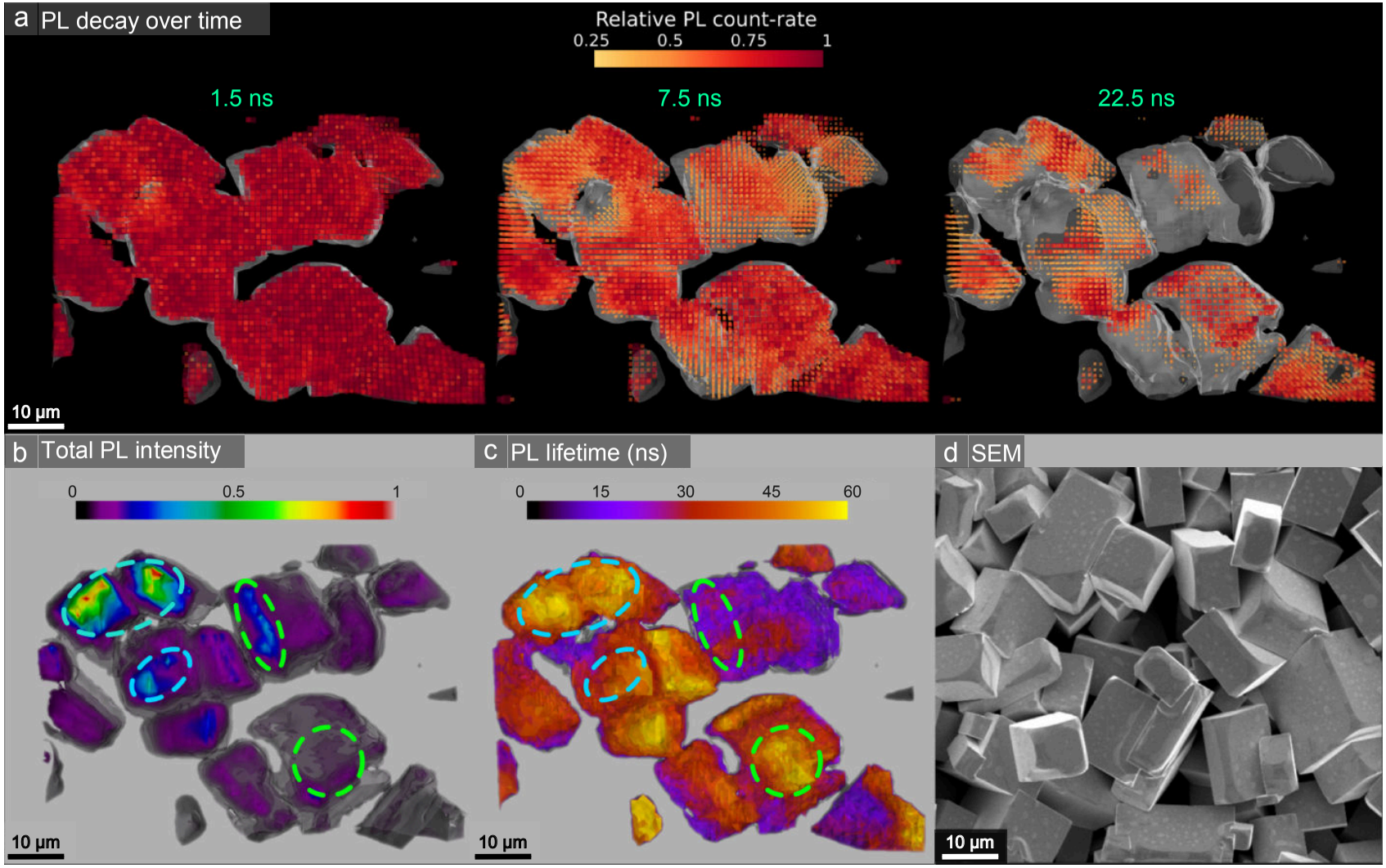

Fig. 4.15 **Time-resolved 3D tomography of a micro-crystal film of $MAPbBr_3$.** Images obtained using 2P-TRPL with a resolution of ∼1.5 µm in depth and 2P excitation fluence of ∼6000 µJ cm^{-2}. The greyscale topography background is a PL isosurface that represents the surface of the crystals. (**a**) Snapshots showing the relative spatial PL decay over time following the excitation pulse. For clarity, the lower quartile of the relative PL count rate is not shown. These images can be directly compared with the (**b**) total PL count rate and the (**c**) extracted lifetime, with both images showing some pockets of strong PL associated with long lifetime (blue circles) and some showing the opposite behaviour (green circles). (**d**) Representative SEM image of the crystal films.

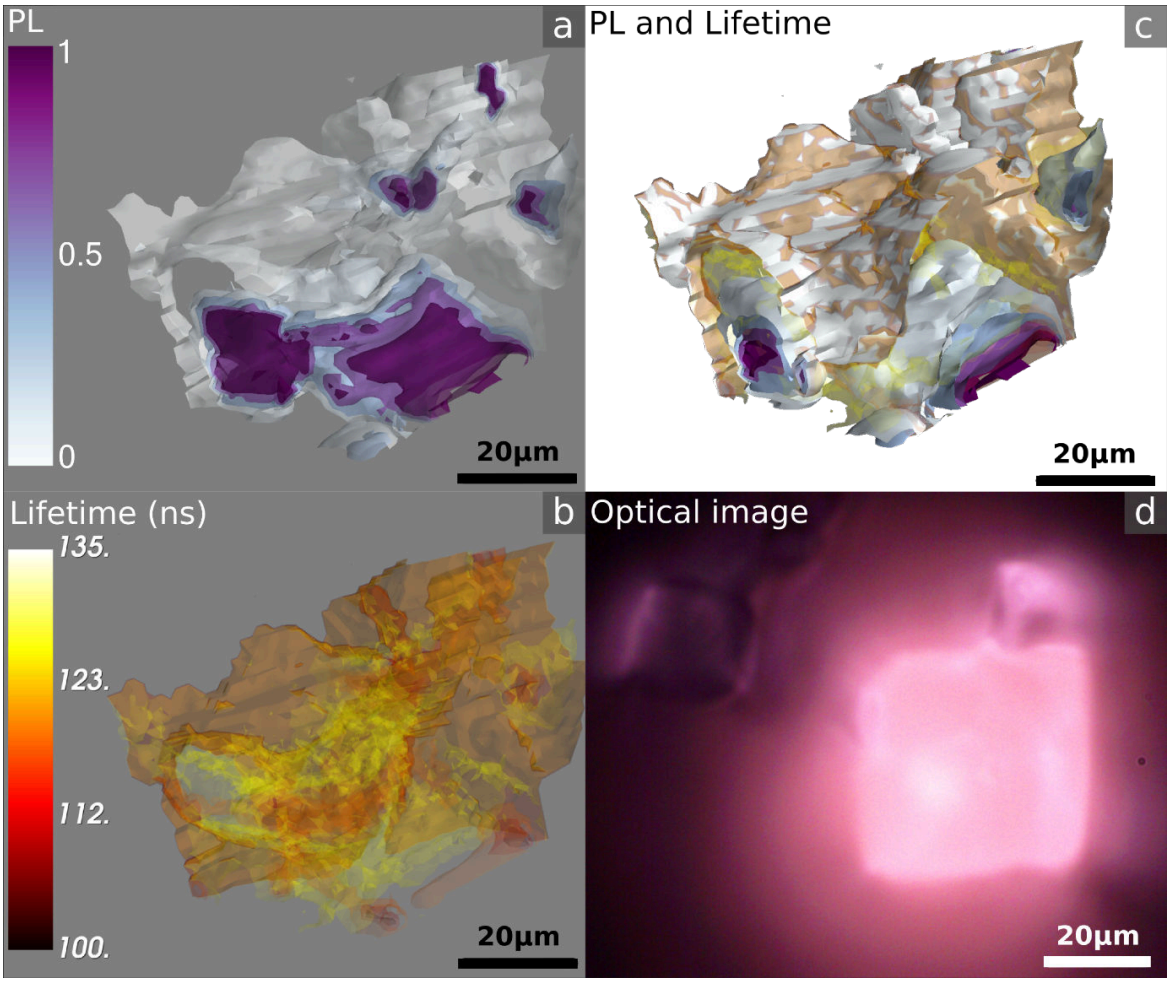

Fig. 4.16 **Time-resolved 3D tomography of a micro-crystal film of $MAPbI_3$ using 2P-TRPL** at 1100 nm with a resolution of ∼1.5 µm in depth. (a) The 3D count rate and (b) the extracted lifetime, which are both superimposed in (c). (d) Two-photon optical image of crystal from the top.

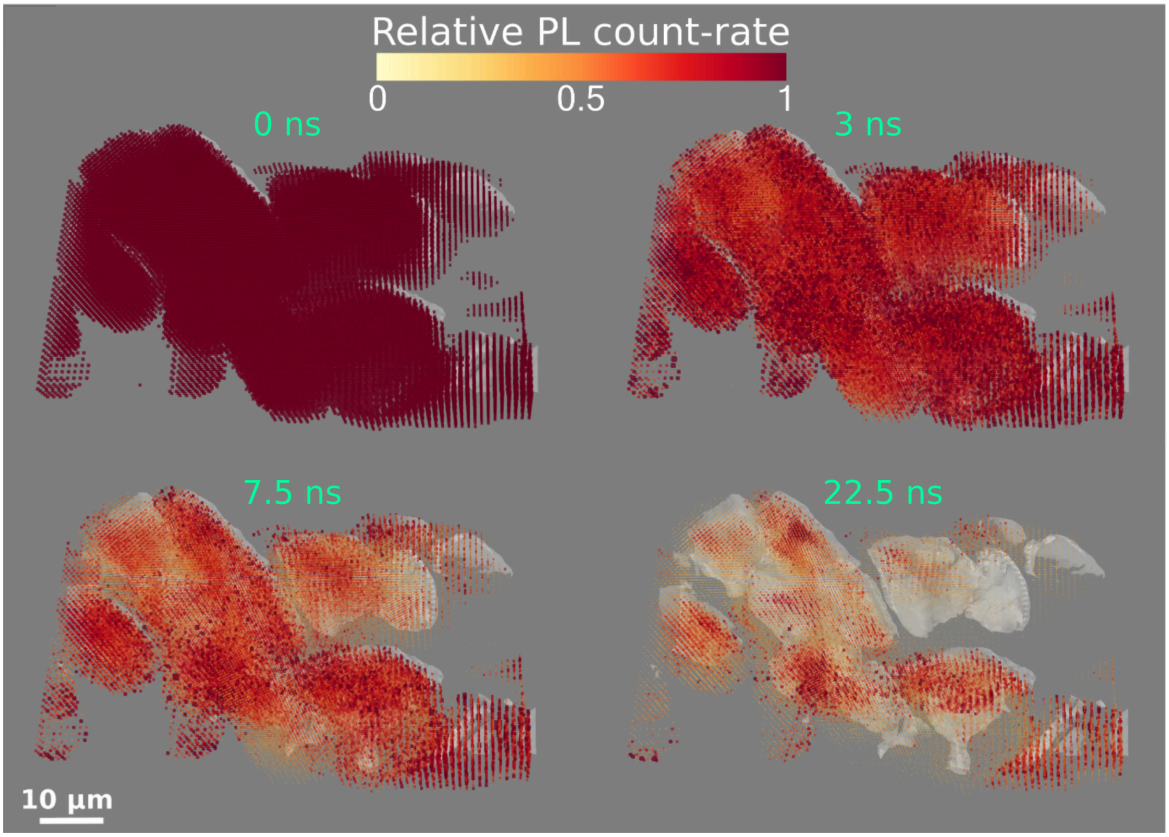

Fig. 4.17 **Full-scale time-resolved 3D tomography of a micro-crystal film of $MAPbI_3$ using 2P-TRPL** at 1100 nm with a step size of 1 µm in depth. The same data than in 4.15 is presented with only background pixels removed outside of the crystals.

By performing fluence-dependent measurements through a depth slice of one of the micro-crystals (Figure 4.18, we find that dark regions show an increasing lifetime with increasing excitation fluence, consistent with a trap-limited recombination regime in which a high density of traps become filled with carriers at higher charge density[36]. Statistics over the whole dataset (10 measurement points at each depth, >100 pixels in total) reveal that dark pixels (where the PL count rate is below 30% of the maximum PL measured) exhibit a trap-limited recombination behaviour. With a lifetime decreasing with increasing fluence, bright pixels (where the PL count rate is above 30% of the maximum PL measured), in contrast, exhibit bimolecular recombination (see Figure 4.19).

In fact, our results are consistent with these micro-crystal samples having a non-negligible density of defects that may have a large impact on device performance[177], and therefore will be crucial to understand and eliminate. Future work would be required to understand the recombination pathways within bright regions and to reconcile these trap densities with those reported previously using space-charge-limited current methods[178, 179]. This luminescence tomography approach will be particularly powerful because it is sensitive to even low densities of defects or low bandgap emission sites and therefore will detect inhomogeneities that might be beyond the resolution of conventional analytical techniques such as XRD, electroluminescence or wide field 1P-PL.

It is important to mention that several optical effects and physical phenomena have been excluded from our analysis of the 3D tomography data. We note that a quantitative trap density analysis would require complex optical modelling. Such a model would include a correction for the aberrations due to the refraction at the surface of the micro-crystals. Such corrections would impact the depth of focus, which is currently under-estimated (see Chapter 2.1.3). At every point on a sample, the fraction of the emitted PL that reaches the detector depends on the topography of the surface, it's angle with respect to the objective lens and more generally the out-coupling efficiency. As a first approximation, such effects could be simulated (through *Finite-difference time-domain simulations or a multi-physics simulation software*) based on SEM images or topographic measurements and deconvolved from the measured signal. To be more realistic, however, such a simulation would have to account for surface roughness, and local scattering off defects. Finally, a model of the reabsorption and photon recycling could be used to correct for any attenuation or amplification of the PL emitted at each point within the micro-crystals.

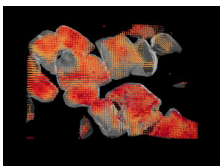

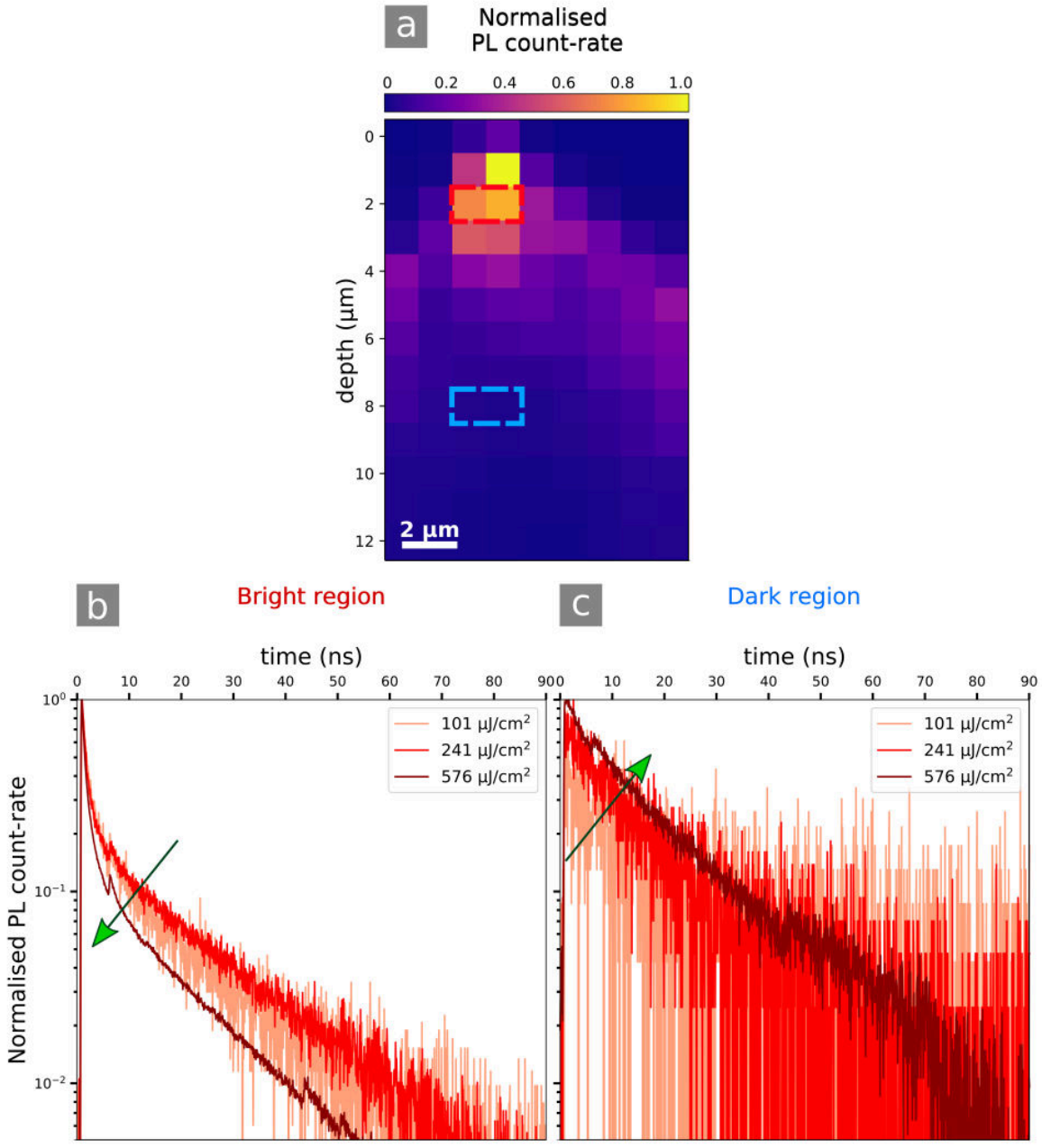

Fig. 4.18 **Fluence-dependent measurements on a micro-crystal film of $MAPbBr_3$ using 2P-TRPL** with a resolution of ∼1.5 µm in depth. The PL count rate map in (a) was performed at a fluence of 232 µJ/cm^2. The panels in (b) and (c) show respectively TRPL measurements averaged over two adjacent pixels of comparable brightness, at 2 µm (b) and 8 µm (c) below the surface. Green arrows indicate the dependence of the lifetime upon an increase in excitation power, highlighting the different recombination regimes discussed in the text. All measurements are normalised to their maximum.

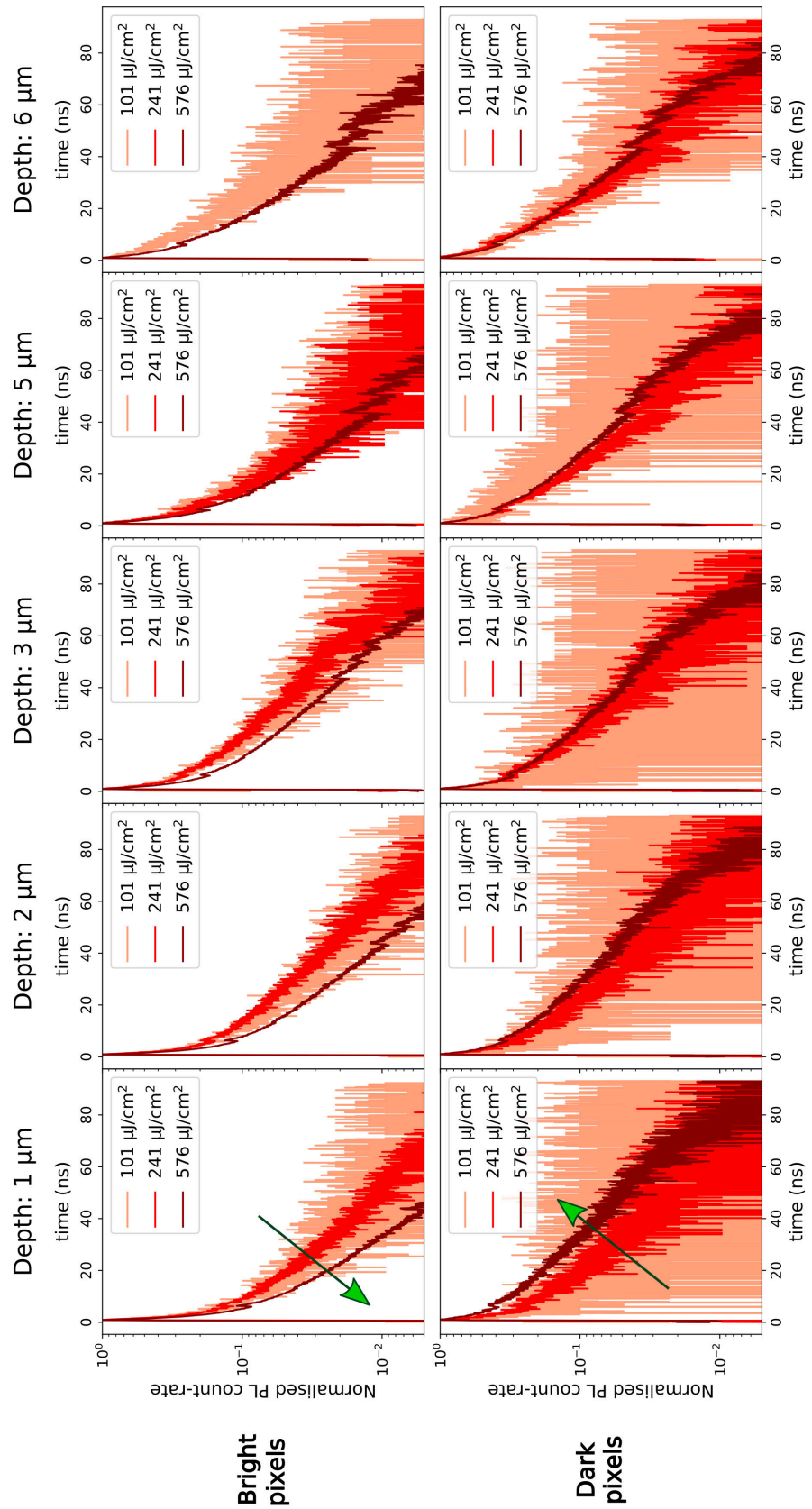

Fig. 4.19 **Statistics on fluence-dependent measurements on a micro-crystal film of $MAPbBr_3$ using 2P-TRPL** with a resolution of ∼1.5 µm in depth. Each column shows TRPL measurements taken at a given depth, from 1 µm to 6 µm, with pulse fluences as stated on the legends. The top and bottom rows highlight measurements performed on bright and dark pixels, respectively, averaged across all such pixels at each depth. Bright pixels are defined as pixels where the PL count rate is above 30% of the maximum PL count rate on the whole 2D map (shown in Figure 4.18 (a)), while dark grains have a PL count rate below 25% of this maximum. Green arrows in the left-most panel indicate the dependence of the lifetime upon an increase in excitation power, highlighting different recombination regimes. All measurements are normalised to their maximum.

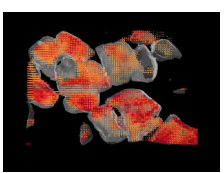

4.6 Conclusion

In summary, we have used time-resolved two-photon microscopy (2P-TRPL) as a four-dimensional (4D) imaging technique to explore buried recombination pathways in perovskite structures. We find stark differences between 1P (surface-dominant) and 2P (bulk-dominant) luminescence in $MAPbI_3$ thin films, with some grains showing bright luminescence from the surface but weak luminescence in the bulk, and some others showing the opposite behaviour. We increase the differences by considering light-induced passivated treatments, revealing that the surfaces are more selectively passivated than the bulk. We constructed for the first time time-resolved 3D PL images of $MAPbI_3$ and $MAPbBr_3$ micro-crystals, revealing substantial luminescence inhomogeneities even in structures which are nominally single crystals. In order to interrogate the cause of such inhomogeneities, a future experiment could look at the correlations between 3D tomography data and local crystallographic of structural data. Techniques such as nano-XRD or grazing-incidence wide-angle x-ray scattering (GIWAXS) could help to investigate the link between PL heterogeneity and strain.

In a nutshell, our work highlights the power of 2P-TRPL mapping as a sensitive 4D probe for defects both on the surface as well as buried beneath the surfaces and at interfaces. Understanding and eliminating these loss pathways will be crucial for further development of perovskite PV solar cells and LED devices. Another key parameter for the design and performance of thin-film planar-heterojunction solar cells is the ability of charge carriers to diffuse to the electron- and hole-extraction layers. In the next chapter, we shall adapt and apply 2P-TRPL microscopy to map carrier diffusion in 3D and 2D halide perovskite crystals.

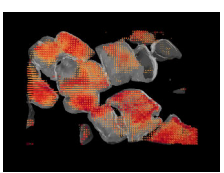

4.7 S'il vous plaît, raconte-moi l'Univers. (If you please, tell me about the Universe.) 4

Quelques minutes plus tard, le petit prince chuchota :

— Je l'entends ! On dirait qu'il ronronne... Est-ce un chat invisible ?

— Pas exactement. C'est Léon, je l'ai apprivoisé il y a longtemps déjà. C'est un petit électron. Un petit grain d'électricité. Je crois qu'il s'est endormi au creux de ta main. Peu de gens le savent et il faut tendre l'oreille, mais les électrons ronronnent...

— Je l'entends, mais je ne le vois toujours pas..., dit le petit prince, un peu déçu.

— Malheureusement, je n'ai pas ici de quoi te le montrer. Je peux te le décrire, mais il te faudra un brin d'imagination.

Le petit prince ferma les yeux.

— Vois-tu, contrairement au chat il me laisse dormir le matin. Et quand il est content il émet un photon, un petit grain de lumière plus petit que lui encore. Avec de bons yeux, on peut le voir la nuit. Il a sa petite Lune pour lui tout seul, et passe son temps à tourner autour. Il disparaît parfois, pour réapparaître ailleurs: comme nous, il doit aimer les voyages. Il est heureux, Léon. Un peu timide, mais pas simplet. Petit électron libre qu'il est...

Le petit prince, qui avait toujours les yeux fermés, esquissa un sourire serein.

— Tous les physiciens ont-ils un ami électron ?

— Pas tous. Certains ont d'autres tout petits amis un peu comme Léon, que l'on appelle généralement « particules ». Parfois, les physiciens se réunissent, invitant leurs particules à jouer aux quilles. Ils construisent des pistes de course géantes, que l'on appelle des « accélérateurs ». Quand les particules se rencontrent et se cognent, parfois de nouvelles apparaissent ! C'est tellement amusant que les parties de quilles peuvent durer des années.

— Est-ce de la magie ?, demanda le petit prince intrigué.

— En quelque sorte. Mais le prestidigitateur est si doué que même les physiciens les plus malins et les plus déterminés n'arrivent pas toujours à percer les secrets de ses tours... Néanmoins, on continue d'essayer. Ce jeu de piste géant s'appelle « la Science ».

A few minutes later, the little prince whispered:

— I hear him! It sounds as if he's purring... Is he a sort of invisible cat?

— Not really. His name is Léon. He is a very tiny electron, a grain of electricity. I think he fell asleep in your hand. Only a few people know that electrons purr...

— I hear him, but I still don't see him... said the little prince, somehow disappointed.

— Unfortunately, I haven't got anything here to help you see him. However, I can describe him for you, but you will need a wisp of imagination.

The little prince closed his eyes.

— You see, unlike a cat, Léon doesn't wake me up in the morning. When he is happy, he emits a photon, a tiny grain of light even smaller than him. With a very good eyesight, one can see him shine in the dark night. He has got his own Moon, for him alone, and loves to spin around it. Sometimes, he disappears and reappears somewhere else: I think he likes to travel. He is happy, Léon. A little bit shy, but truly free...

The little prince, whose eyes were still closed, raised a serene smile.

— Do all physicists have an electron as a friend?, asked he.

— Not all of them. Some have other little friends, similar to Léon, that we generally call "particles". From time to time, a few physicists gather and invite their particles to play skittles. They build giant race tracks for them, which we call "colliders". When particles meet and bump into each other, sometimes new ones appear! It is so entertaining that a single game can last for years.

— Is it magic?, asked the little prince, interested.

— In a way. But the magician is so skilful that even the most clever and resilient among the physicists struggle to solve the mysteries of his magic tricks... Nevertheless, we keep trying. This giant paper chase is called "Science".

Chapter 5

Visualising carrier diffusion in halide perovskite crystals

Efficient charge-carrier diffusion from their point of generation to the electron- and hole-collection layers in a device stack is essential for good performance of a solar cell. Here, we develop a time-resolved two-photon photoluminescence (2P-TRPL) tomography configuration which we use to explore the charge-carrier diffusion in $MAPbBr_3$ single crystals in different directions at different depths. Mapping the PL originating from charge-recombination as a function of distance from the location of excitation at different depths in the crystal, we seek to separate the electronic diffusion from photon effects. We obtain statistics of local charge-carrier diffusion coefficients, with values ranging from 1 to 2.5 cm^2/s, revealing anisotropic carrier transport that would be missed through macroscopic measurements. Owing to the resolution of our confocal microscope, we are able to observe local heterogeneity at the micro-scale in the diffusion properties. Fluence-dependent measurements allow us to relate this heterogeneity to the local concentration of defects.

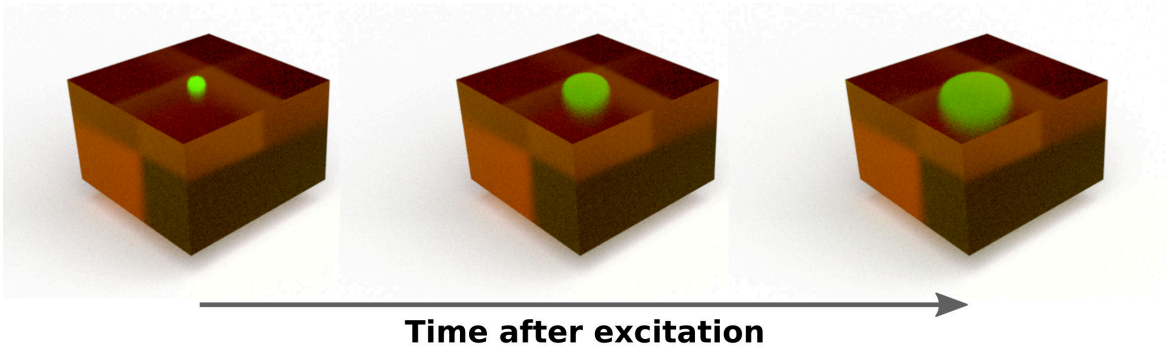

Fig. 5.1 **Schematic of the proposed carrier diffusion in a $MAPbBr_3$ single crystal.** The photoluminescence is shown in green.

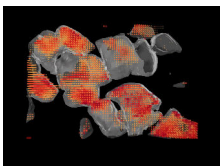

5.1 Introduction

In a working thin-film solar cell, free charge-carriers (electrons and holes) are collected separately on either side of the active layer (in this case a perovskite layer)[180]. Photovoltaic devices based on simple thin-film planar-heterojunction architectures are possible for materials with charge-carrier diffusion lengths that are sufficiently long to allow for charge migration through a whole absorber layer. As an illustration, Figure 5.2 shows a simple pervoskite-based thin-film solar cell design, where electrons (e^-) and holes (h) are collected in a layer of Spiro-OMeTAD and a layer of TiO_2, respectively. The working theory is that the devices work in a diffusion-limited regime rather than built-in fields driving carrier collection (i.e drift). Consequently, the design and performance of these devices is strongly impacted by the distance over which charge-carriers are able to diffuse. Identifying the factors limiting charge-carrier diffusion in perovskite structures is therefore crucial to the development of efficient solar cells[44]. We have discussed and shown in previous chapters that state-of-the-art perovskite thin films and single crystals contain traps that act as non-radiative loss pathways, but their impact on the proportion of energised carriers that can diffuse and contribute efficiently in an operating device needs to be further investigated.

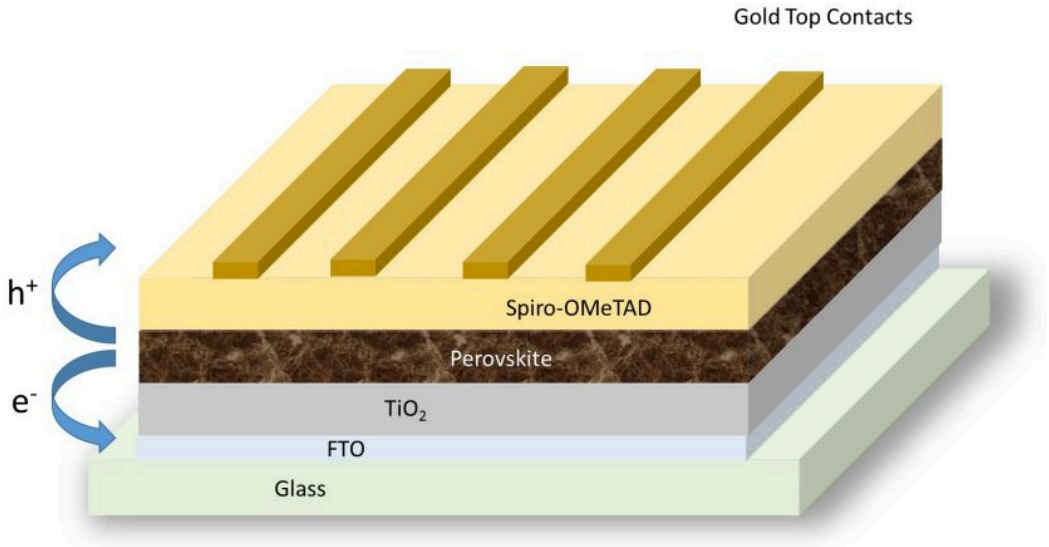

Fig. 5.2 **A simple thin-film based perovskite solar cell.** Electrons (e^-) and holes (h) are collected in a layer of Spiro-OMeTAD and a layer of TiO_2, respectively. Credit: Clean Energy Institute, University of Washington.

In this chapter, we explore the diffusion of charge-carriers in the bulk of a 3D $MAPbBr_3$ perovskite single crystal. Although these have well documented optical characteristics (optical indices[117], exciton binding energy[181, 182], reabsorption[183]), an uncertainty

remains over their diffusion properties. Studying single crystals, which typically contain a lower concentration of defects than thin films[149], is also fundamental to unveil the intrinsic properties of perovskites materials. This is particularly relevant as some of the carrier diffusion lengths reported in literature for perovskite materials extend much further ($\gg$ 10 µm) than the usual grains sizes in standard perovskite films ($\sim$0.1-1 µm)[184–186]).

To date, diffusion in these materials has been primarily explored using surface-sensitive measurements such as conventional one-photon (1P) microscopy. Some studies have reported very long diffusion lengths[43, 187], exceeding 170 µm from these measurements[185]. Building on our previous work unveiling buried heterogeneity in the PL emission within the bulk of $MAPbBr_3$ single crystals[145], here we map the carrier diffusion as a function of depth and fluence by means of two-photon PL time-resolved (2P-TRPL) microscopy. Monitoring the 2P-TRPL as a function of distance from the excitation spot, we herein provide unprecedented insight into buried charge-carrier diffusion in these perovskite structures at depths where surface-related optical distortions such as internal wave-guiding would have less impact on the measurements. Indeed, recent work reports that 15% of the emitted photons diffuse on a distance larger than 10 µm along the surface in $MAPbI_3$ thin films, enhancing the contribution from photon recycling to the measured PL as well as the out-coupling of long-range photons[188]. Photon recycling is the consecutive re-absorption of a photon generating charge carriers and their radiative recombination, with a probability depending on the PL quantum yield of the material. Such photonics effects thus introduce a large uncertainty in the estimation of diffusion coefficients[188], and so it is critical to disentangle their contribution from pure carrier diffusion.

It is well established that carrier dynamics and recombination mechanisms are different at the surface of perovskites (where most of the traps are located) than in the bulk[189, 190]. Near the surface, we expect the time-dependent broadening of the PL spatial profile to be a convolution of the photonic contribution (direct emission) and the emission from carrier recombination events. In thin films, the photonic contribution has been shown to dominate the overall diffusion at distances up to $\sim$9 µm from the excitation spot[188]. Whether this photonic contribution solely is a surface effect or persists in the bulk of single crystals is however an open question, and this is what we propose to address. Depth-dependent 2P-TRPL measurements in a millimetre-size crystal allow us to clearly resolve different regimes as we probe the PL near the surface or deeper into the depth of the crystal. Our results could help to quantitatively distinguish between the electronic and photonic contributions which are otherwise difficult to decouple in a thin-film. We propose a preliminary model to simulate the impact of photon reabsorption and recycling on the diffusion as a function of depth (z). From the 2P-TRPL data, we extract electronic diffusion

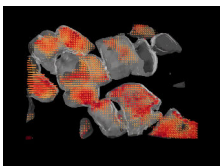

coefficients ranging from 1 to 2.5 cm^2/s. Our results reveal a spatial heterogeneity in diffusion that is not captured in macroscopic measurements, affecting both photon and charge-carrier diffusion. Fluence-dependent measurements reaveal further information on the heterogeneity, highlighting pockets where longer PL decay times are correlated with lower diffusion coefficients, underlying the detrimental impact of traps on the diffusion.

This work is the subject of a manuscript currently in preparation, and this chapter gives an account of the progress at the time of writing this thesis. I performed the 2P-TRPL experiments at the Molecular Foundry, Berkeley Lab, between January and March 2018 with the help of Edward Barnard. The samples were fabricated by Ayan Zhumekenov at KAUST, Saudi-Arabia. I carried out the data analysis, according to the methodology given in Chapter 2.4. The theoretical model and simulations presented herein are the result of collaborative work between Géraud Delport, Miguel Anaya, Rosemonde Chahbazian and myself. These simulations are still at an early stage of development, and their improvement constitute an on-going project. Preliminary diffusion data obtained on 2D (n-1)$MAPbI_3$*PEA_2PbI_4 perovskite single crystals, synthesised by Ayan Zhumekenov using long A-site cations (Phenethylamine or PEA) are also presented. Even though the diffusion along a backbone might be very good in these crystals, our measurements highlight the impact of randomly oriented inorganic separation layers which appear to be slowing the net diffusion down.

5.2 The optical setup

The optical setup used in this project is based on the 2P-TRPL microscope described in Chapter 2.1.3 and used in Chapter 4. It is equipped with a 100x objective lens of numerical aperture $NA = 0.95$ (Figure 5.3 **a**). The OPO used as light source is tuned to 1200 nm. To monitor the PL emission as a function of distance (x) from the 2P-excitation spot (x = 0), a raster scanning fibre (25 µm core) is implemented in the collection arm of the microscope (Figure 5.3 **b**), coupled to a single-photon avalanche photodiode (SPAD). A one-dimensional (1D) 2P-TRPL emission profile, centred around x = 0, is measured along x in steps of 500 nm on the sample. Individual 2P-TRPL traces are acquired with an integration time of 20 sec. This measurement is repeated at different depths (z) below the (x,y) plane by changing the depth-of-focus, with a step of 1 µm. The progressive spatial spreading of the PL emission with time (delay from the laser pulse) is extracted from the 2P-TRPL data (Figure 5.3 **c**), and a Gaussian fit is applied for $x < 0$ and $x > 0$ separately. This lateral separation is performed in order to account for any asymmetry of the PL profile, as explained in Chapter 2.4. The variance of the Gaussian statistics as a function of time, $\sigma_x(t)$ is then extracted from the fit and used as a measurement of the diffusion.

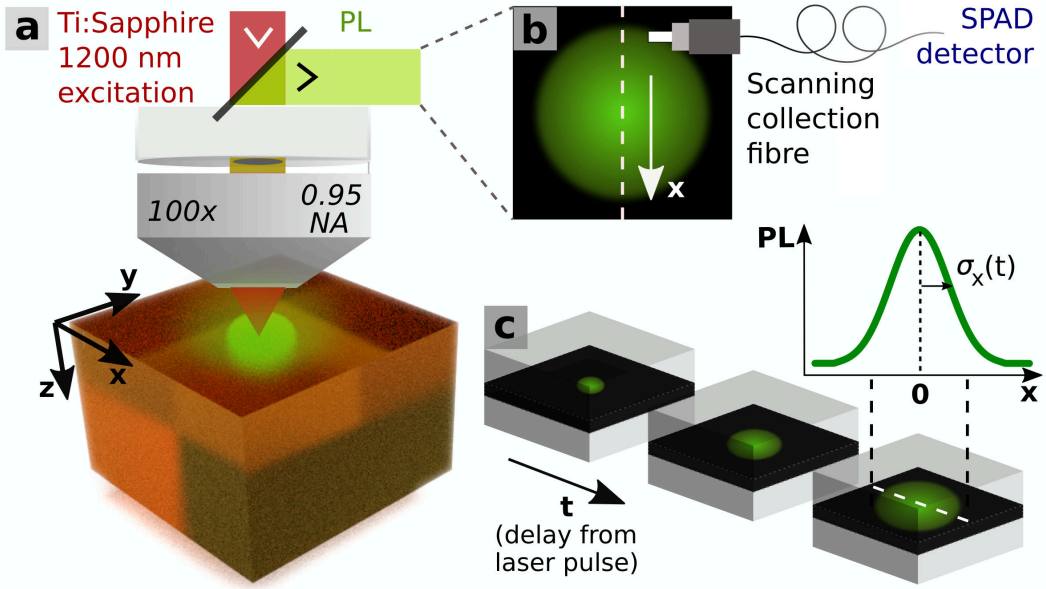

Fig. 5.3 **Specificities of the setup used for 2P-TRPL diffusion measurements.** (a) The 2P-TRPL microscope as described in Chapter 2.1.3. (b) At each depth (z), a collection fibre is raster scanned along the x direction across the PL image. (c) Schematic of the progressive spreading of the PL image with time (delay from laser pulse) due the diffusion of carriers and illustration of the Gaussian fit applied in the analysis to obtain $\sigma_x(t)$ (variance of the Gaussian statistics as a function of time).

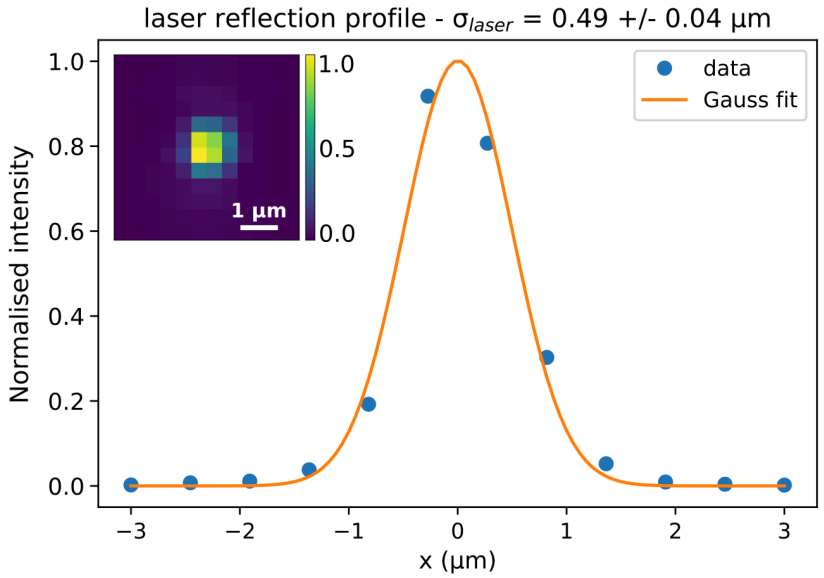

Fig. 5.4 **Resolution of the diffusion microscope.** The $\sigma_{laser} \sim 0.5$ µm of the laser reflection measured on the surface of a $MAPbBr_3$ single crystal gives a lower bound to the imaging resolution with the raster scanned collection fibre. The 2D (x,y) map of the laser reflection is shown as inset, the colour-scale representing the normalised light intensity.

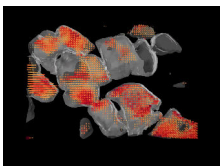

In principle, this setup offers the possibility to map the diffusion in the (x,y) plane at different depths (z) to generate 3D diffusion maps. Due to the current limitations in collection efficiency and detection sensitivity, the integration time per pixel has to be above 20 sec in order to obtain good enough signal-to-noise ratio, therefore limiting the size of the maps that can be acquired on the sample in a reasonable time. Therefore, the measurement conditions utilised here were a compromise between sufficiently long integration times for reasonable signal while minimising potential photo-bleaching for long illumination times. In order to characterise the detection resolution of our setup, we carry out a 2D (x,y) map of the laser reflection at the surface of a $MAPbBr_3$ crystal. This map is shown as inset in Figure 5.4. We perform a Gaussian fit on the laser profile (Figure 5.4) and measure a $\sigma_{laser} \sim 0.5$ µm. This corresponds to a FWHM $\sim$ 1.2 µm, which is consistent with a diffraction limited resolution.

Figure 5.5 shows data measured on a $MAPbBr_3$ single crystal with an 2P excitation density of $\sim$1.3 mJ/cm^2. A photograph of the sample (and the holder) is displayed in Figure 5.6, together with a schematic showing its dimensions (inset). The raster scanning starts at the surface of the sample, and stops at z = 10 µm in depth to cover a region of 10x10 µm.

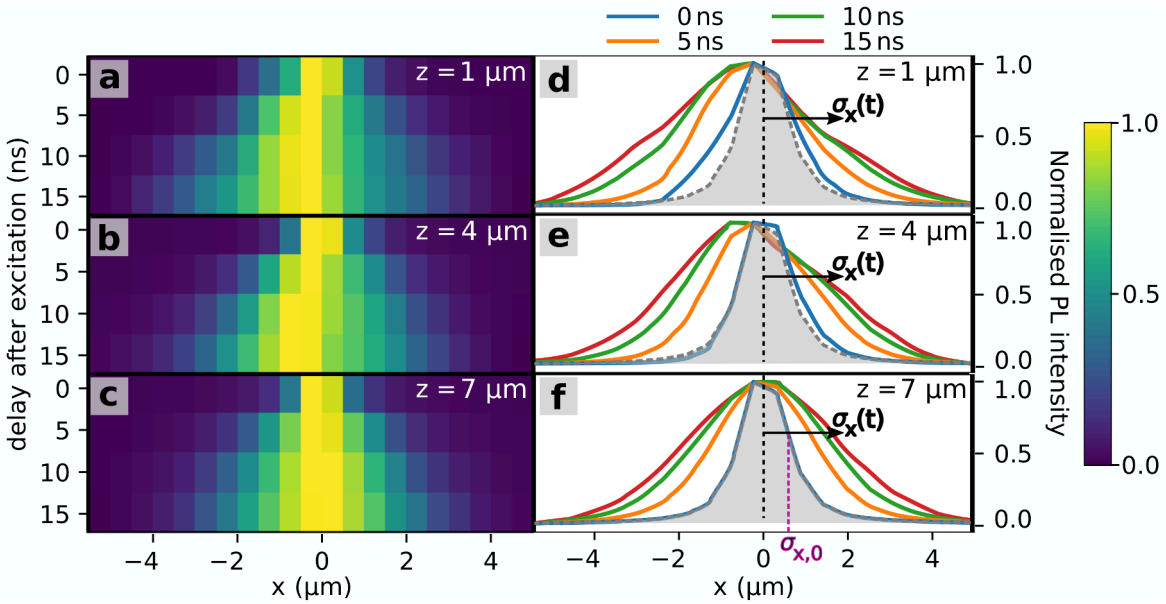

Fig. 5.5 **Time-dependent PL emission profile at different depths in the crystal.** The measurements were performed with an excitation fluence of $\sim$1.3 mJ/cm^2. The extent of the PL profile for different delays t are displayed for z = 1 (a and d), z = 4 (b and e) and z = 7 (c and f) µm. The PL profile at z = 7 µm and t = 0, corresponding to our maximum resolution (see Figure 5.4) is used as a reference throughout. $\sigma_x(t)$ is extracted from the fit as a measure of the diffusion for further analysis.

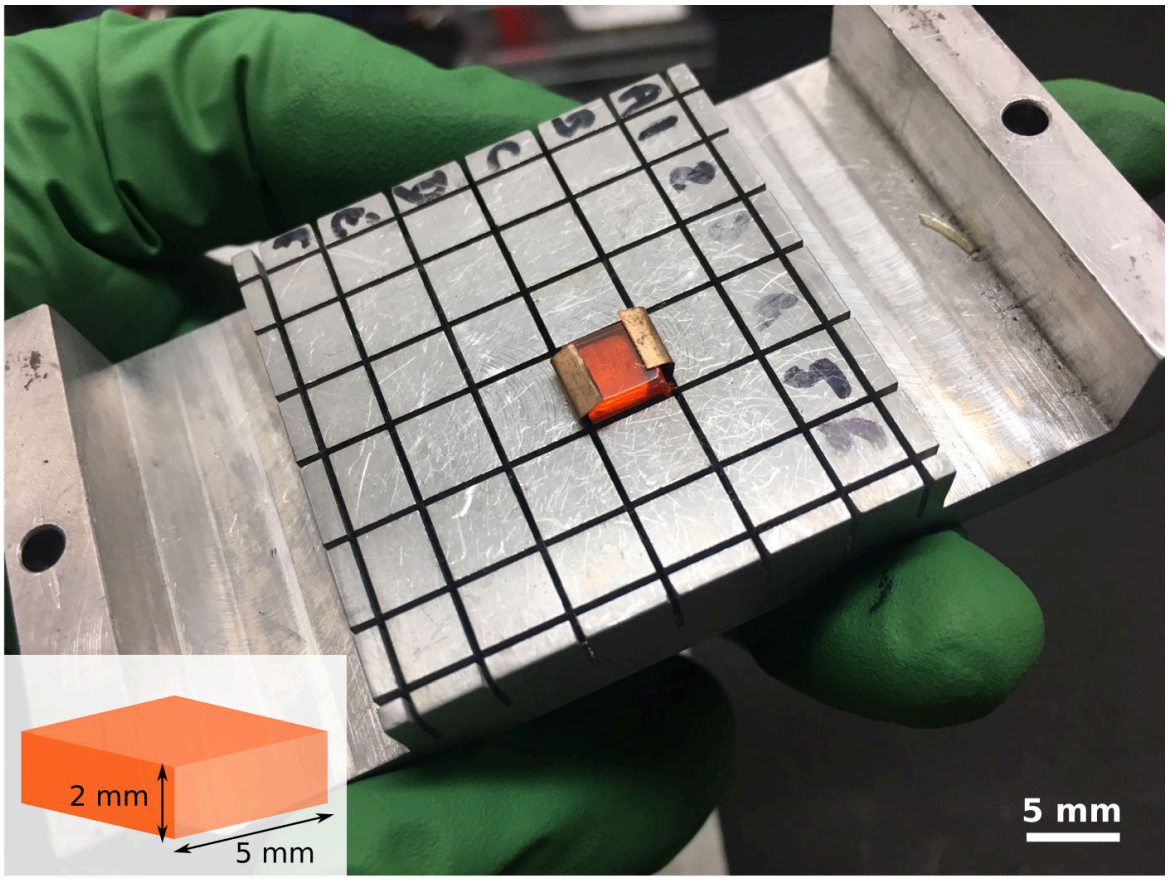

Fig. 5.6 **3D $MAPbBr_3$ single crystal used for diffusion experiments**, clamped down mechanically on a sample holder. The crystal's dimensions are shown as inset.

We map the 2P-TRPL emission on the (x,z) cross-section over an area of 10x10 µm. The 1D PL intensity strips at z = 1 µm, z = 4 µm and z = 7 µm are shown in Figure 5.5 **a-c** while panels **d-f** show the corresponding PL profiles. At z = 7 µm and for t = 0, $\sigma_{x,0} \sim 0.5$ µm, which corresponds to the maximum resolution of our setup. At each depth we observe a widening of the PL beam as a function of the delay with respect to the laser pulse (t = 0), which can be explained by a transport of charges away from the point of excitation. From this first figure, two key observations can be made. The first is a broadening of the PL profile measured immediately after excitation (at t = 0) at z = 1 µm, as compared to the profile measured deeper at z = 7 µm (blue-filled profile in Figure 5.5 **d-f**). The origin of this broadening could be fast carrier diffusion within our time resolution. It could also be other possibilities such as defect-induced scattering or other photonic effects taking place near the surface of the crystal. Secondly, at z = 1 µm and z = 4 µm, we observe an asymmetry of the PL emission profile which disappears further down in the bulk, which is a first indication of the presence of local spatial differences in the concentration of traps within the crystal.

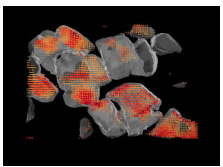

5.3 From carrier diffusion to PL spatial spread

As introduced in Chapter 1.4.1, the carrier density $n(t)$ depends on the recombination rate (Equation 1.5). As a first approximation here we extract the diffusion length directly from the variance of the PL profile. To be accurate, the data analysis should take into account weighted contributions from $n(t)$ and $n^2(t)$. Carriers will quickly dilute away from the excitation spot and most of the PL that we collect is coming from regions with low excitation density and therefore the recombination is primarily trap-limited. The linear (trap-assisted) term in the recombination rate equation, $A_{trap}n(t)$ will dominate at most positions except for where we excite, x = 0, where the carrier density is sufficiently high. We note for completeness that as an approximation for the data analysis, we assume that we are in the monomolecular regime (although a fluence-dependent 2P-TRPL lifetime map would be needed to confirm this hypothesis). As a consequence of this hypothesis, the carrier population will be affected by traps and we cannot consider that the PL emission that we observe is directly proportional to n^2. Measuring the variance of the PL spatial profile as a function of time is thus one of the methods that can be employed to investigate the diffusion of charge carriers in perovskites. It is important to note, however, that the PL image is convoluted with the resolution (point spread function) of the microscope. To obtain the diffusion coefficient D from this measurement, we first need to define the relationship between D and the variance $\sigma^2(t)$ of the underlying distribution of carriers $c(t)$. As a starting point, assuming a Gaussian initial concentration (generated by a Gaussian laser pulse), Fick's second law of diffusion (Equation 1.4) can be solved analytically in 1D on a finite region with D constant[191].

Solving the diffusion equation for an instantaneous point source in 1D

$$\frac{\partial c(x,t)}{\partial t} = D\frac{\partial^2 c(x,t)}{\partial x^2} - \frac{c(x,t)}{\tau}, \tag{5.1}$$

where $c(x,t)$ is the density of charge carriers, D is the diffusion coefficient and τ is the electron-hole recombination time (lifetime)[130]. The general solution is of the form:

$$c(x,t) = \phi(x)e^{-\lambda t}, \tag{5.2}$$

after separation of the temporal ($e^{-\lambda t}$) and spatial ($\phi(x)$) parts of the equation. Inserting $c(x,t)$ in Fick's law (Equation 1.4) then leads to the eigenvalue equation:

$$\left[\frac{\partial^2}{\partial x^2} + \omega^2\right]\phi(x) = 0, \tag{5.3}$$

with $\omega^2 = \lambda/D - 1/(D\tau)$. The eigenfunctions of 5.3 are then sine and cosine functions:

$$\begin{aligned} \phi_{o,n}(x) &= \sin(\omega_{o,n}x), \\ \phi_{e,n}(x) &= \cos(\omega_{e,n}x). \end{aligned} \tag{5.4}$$

Assuming reflecting boundaries on either end of the line $[-L/2; L/2]$ and hence setting the probability current at $\pm L/2$ to zero, the eigenvalues come as:

$$\begin{aligned} \omega_{o,n} &= \frac{2\pi(n+1/2)}{L}, \\ \omega_{e,n} &= \frac{2\pi n}{L}. \end{aligned} \tag{5.5}$$

Using $\lambda_n = D\omega_n^2 + 1/\tau$ for odd and even modes, the spatial part of the solution is:

$$\phi(x) = \sum_{n=0}^{\infty} \left[A_{e,n} \cos\frac{2\pi n x}{L} + A_{o,n} \sin\frac{2\pi(n+1/2)x}{L} \right]. \tag{5.6}$$

The normalisation condition $1 = \int_{-L/2}^{L/2} \phi(x)dx$ fixes $A_{e,n} = 1/L$. To obtain a general expression for $A_{e,n}$, we first look for a particular solution for a one-dimensional, instantaneous point source at t=0 and x=0, giving the symmetric initial condition $c(x,0) = \delta(x)$. Since $\delta(x)$ (Dirac delta function) is even, all $A_{o,n}$ must vanish. On the interval $[-L/2; L/2]$, the delta function can be represented as:

$$L\delta(x) = 1 + 2\sum_{n=1}^{\infty} \cos\frac{2\pi n x}{L}. \tag{5.7}$$

Comparing coefficients with Equation 5.6 shows that $A_{e,n} = 2/L$ for $n > 0$. The full time-dependent solution of the diffusion problem is thus:

$$c(x,t) = \frac{1}{L} + \frac{2}{L}\sum_{n=1}^{\infty} \cos\frac{2\pi n x}{L} \exp\left\{ -\frac{4\pi^2 n^2 D t}{L^2} - \frac{t}{\tau} \right\}. \tag{5.8}$$

The time-dependent variance of the distribution function $c(x,t)$ can be calculated using the integral $\int_{-\pi n}^{\pi n} dy\, y^2 \cos(y) = 4\pi n(-1)^n$:

$$\begin{aligned} \frac{\sigma^2(t)}{L^2} &= \frac{1}{L^2}\int_{-L/2}^{L/2} dx\, x^2 c(x,t) \\ &= \frac{1}{12} + \frac{1}{\pi^2}\sum_{n=1}^{\infty} \frac{(-1)^n}{n^2} \exp\left\{ -\frac{4\pi^2 n^2 D t}{L^2} - \frac{t}{\tau} \right\}. \end{aligned} \tag{5.9}$$

The lowest non-trivial order is:

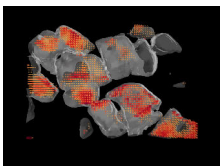

$$\frac{\sigma^2(t)}{L^2} = \frac{1}{12} + \frac{1}{\pi^2}\exp\left\{-\frac{4\pi^2 Dt}{L^2} - \frac{t}{\tau}\right\}. \tag{5.10}$$

To get the asymptotic behaviour at small t, the Euler-Maclaurin summation formula[192] can be used to rewrite the sum entering the expression of $c(x,t)$ as:

$$\begin{aligned}\sum_{n=1}^{\infty} \cos\frac{2\pi nx}{L}\exp\left\{-\frac{4\pi^2 n^2 Dt}{L^2} - \frac{t}{\tau}\right\} \\ = \int_0^{\infty} dn \cos\frac{2\pi nx}{L}\exp\left\{-\frac{4\pi^2 n^2 Dt}{L^2} - \frac{t}{\tau}\right\} - \frac{1}{2}, \\ = \frac{\exp\left\{-x^2/(4Dt) - (t/\tau)\right\}}{4\sqrt{\pi Dt/L^2}} - \frac{1}{2}.\end{aligned} \tag{5.11}$$

Inserting this expression in Equation 5.8 gives[130]:

$$\begin{aligned}c(x,t) &= \frac{1}{\sqrt{2\pi(2Dt)}}\exp\left\{-\frac{x^2}{2(2Dt)} - \frac{t}{\tau}\right\}. \\ &= \frac{e^{-t/\tau}}{\sqrt{2\pi(2Dt)}}\exp\left\{-\frac{x^2}{2(2Dt)}\right\}.\end{aligned} \tag{5.12}$$

This is valid for $Dt \leqslant L^2$, and it describes $c(x,t)$ as a Gaussian with variance:

$$\sigma^2(t) = 2Dt, \tag{5.13}$$

giving the often-quoted diffusion relationship. To convert the mathematical solution given in Equation 5.12 to real space, divide by the neglected dimensions, here the cross-sectional area of the system in the (y,z) plane, A_{yz}.

Instantaneous point source in 2D and 3D

Let us now consider the 2D case where $c(x,y,t=0) = \delta(x)\delta(y)$. For generality, we will assume anisotropic diffusion, $D_x \neq D_y$. The transport equation for this system is then:

$$\frac{\partial c(t)}{\partial t} = D_x\frac{\partial^2 c(t)}{\partial x^2} + D_y\frac{\partial^2 c(t)}{\partial y^2} - \frac{c(t)}{\tau}. \tag{5.14}$$

From Fick's Law (Equation 1.4) and by inspection of Equation 5.14, the diffusion in x depends only on the distribution in x and the diffusion in y depends only on the distribution in y. This leads us to propose that the solution to Equation 5.14 may be the product of two uncoupled solutions describing the distribution in x and y[193]:

$$c(x,y,t) = c_1(x,t)c_2(y,t). \tag{5.15}$$

Inserting this into Equation 5.14 and using solutions of the form of Equation 5.12 for $c_1(x,t)$ and $c_2(y,t)$, we find that

$$c(x,y,t) = \frac{e^{-t/\tau}}{4\pi t\sqrt{D_x D_y}} \exp\left\{-\frac{x^2}{4D_x t} - \frac{y^2}{4D_y t}\right\}. \tag{5.16}$$

To convert the mathematical solution to real space, divide by the neglected dimensions, here for example the thickness of the slab L_z. Similarly to the 1D case, we find the relationship between the variance of $c(x,y,t)$ and the diffusion coefficient D as:

$$\begin{aligned} \sigma_x^2 &= 2D_x t, \\ \sigma_y^2 &= 2D_y t. \end{aligned} \tag{5.17}$$

These results are easily generalised to the 3D case:

$$c(x,y,z,t) = \frac{e^{-t/\tau}}{(4\pi t)^{3/2}\sqrt{D_x D_y D_z}} \exp\left\{-\frac{x^2}{4D_x t} - \frac{y^2}{4D_y t} - \frac{z^2}{4D_z t}\right\}, \tag{5.18}$$

and

$$\sigma_i^2 = 2D_i t, \tag{5.19}$$

for i = (x,y,z). The dilution rate of an initial distribution may be described by the rate of change in the maximum concentration. For an instantaneous point source the maximum concentration, $c_{max}(t)$, occurs at the centroid and corresponds to the coefficient leading the exponential in Equations 5.12, 5.16 and 5.18. In 1D we have $c_{max}(t) \propto t^{-1/2}$, in 2D $c_{max}(t) \propto t^{-1}$ and in 3D $c_{max}(t) \propto t^{-3/2}$. Although the relationship between the variance $\sigma^2(t)$ and D as we project on x,y,z does not change with the dimensionality of the system, we see that the maximum concentration (which also depends on the recombination rate or lifetime) decays most rapidly in the least constrained system, i.e. the 3D system.

Starting with an initial distribution of carriers

So far we have described a system evolving from a δ function at t = 0. In 1D, the general solution to the diffusion equation with a constant diffusivity and the general initial condition $c(x,0)$ reads[194]:

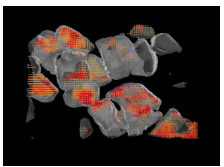

$$c(x,t) = \frac{1}{\sqrt{4\pi Dt}} \int_{-\infty}^{\infty} d\tilde{x}\, c(\tilde{x},0) \exp\left\{ -\frac{(x-\tilde{x})^2}{4Dt} - \frac{t}{\tau} \right\}, \tag{5.20}$$

where $\tilde{x}$ is the centre of the initial distribution. If the latter is a Gaussian: $c(\tilde{x},0) = c_0 \exp\{-x^2/(2\sigma_0^2)\}$, then it evolves with time as:

$$\begin{aligned} c(x,t) &= \frac{c_0}{\sqrt{4\pi Dt}} \int_{-\infty}^{\infty} d\tilde{x}\, \exp\left\{ -\frac{x^2}{2\sigma_0^2} \right\} \exp\left\{ -\frac{(x-\tilde{x})^2}{4Dt} \right\} \exp\left\{ -\frac{t}{\tau} \right\}, \\ &= \frac{c_0 e^{-t/\tau}}{\sqrt{4\pi Dt}} \int_{-\infty}^{\infty} d\tilde{x}\, \exp\left\{ -\frac{x^2}{2\sigma_0^2 + 4Dt} \right\}, \end{aligned} \tag{5.21}$$

using the property that a convolution of two Gaussian functions with variances σ_a and σ_b results in a Gaussian with variance $\sigma_a + \sigma_b$.

The variance of the distribution (or *mean square displacement*) $\sigma^2(t)$, evolves as:

$$\sigma^2(t) = \sigma_0^2 + 2Dt \tag{5.22}$$

The linear relationship between σ^2 and t in Equation 5.22 occurs in the special case of normal diffusion. In many physical systems where disorder is present, the distribution of particle hopping times has a heavy-tailed distribution[195]. Consequently, in 1D it is modified to $\sigma^2(t) = At^\alpha$, where α characterises the type of diffusion and A is an empirically observed scaling factor which has fractional time units. For $\alpha = 1$, we recover normal diffusion. For $\alpha > 1$, the transport is superdiffusive, in which the particles spread faster than in normal diffusion. This situation occurs in ballistic transport where the mean scattering time is long relative to the observation time. For $\alpha < 1$, the transport is said to subdiffusive. This situation occurs when some fraction of the diffusing particles experience longer waiting times between hops, thus slowing down diffusion. Subdiffusion occurs in disordered physical systems because as diffusion proceeds, particles become trapped at sites from which escape is less probable. In the following analysis, we use Equation 5.22 to fit our experimental data.

Solving the diffusion equation beyond the simple case

Although the equations derived so far are a good enough approximation for our case, in a real system it can happen that the initial distribution is not a Gaussian, that it is not symmetrical, or evolving in a medium with a complex geometry. The 2P-TRPL measurements reported herein reveal a local heterogeneity in a $MAPbBr_3$ perovskite single crystal, and it would make sense to explore diffusion numerically with a non-constant diffusion coefficient $D = D(x)$.

Several numerical resolution methods exist[196] for the diffusion equation. Here we shall just briefly outline how that could be implemented to further analyse our data. A way forward would be to discretise the partial differential equation (PDE) with finite difference approximations. In this framework, the spatial part of the diffusion equation $\Delta c(t)$ (Fick's second law, Equation 1.4) can be approximated using Taylor expansions. In the 1D case, $\partial^2 c/\partial x^2$ can be approximated in a few steps[197]:

$$\begin{aligned} c(x+\Delta x) &\approx u(x) + \Delta x \frac{\partial c}{\partial x} + \mathscr{O}\Delta x^2, \\ c(x-\Delta x) &\approx u(x) - \Delta x \frac{\partial c}{\partial x} + \mathscr{O}\Delta x^2, \end{aligned} \tag{5.23}$$

which can be solved individually to give the forward and backward difference operators. These are then added to give an approximation of the second order partial derivative:

$$\frac{\partial^2 c}{\partial x^2} \approx \frac{c(x+\Delta x) - 2c(x) + c(x-\Delta x)}{\Delta x^2} + \mathscr{O}\Delta x^2. \tag{5.24}$$

The diffusion equation $\partial c/\partial t = D(\partial^c/\partial x^2)$ thus become:

$$\frac{c(t+\Delta t) - c(t)}{\Delta t} \approx D\frac{c(x+\Delta x) - 2c(x) + c(x-\Delta x)}{\Delta x^2}. \tag{5.25}$$

This expression can be generalised to the 2D and 3D case. In the Forward-Time Central-Space (FTCS) explicit scheme, it can be solved numerically. If we use n to refer to indices in time and j to refer to indices in space, the above equation can be implemented in a programme as:

$$c[n+1, j] = c[n, j] + s(c[n, j+1] - 2c[n, j] + c[n, j-1]), \tag{5.26}$$

where $s = D\frac{\Delta t}{\Delta x^2}$. A simulation for an arbitrary Gaussian case in 1D, 2D and 3D confirms the relationship between the variance and D, $\sigma^2(t) = \sigma_0^2 + ADt$ with $A = 2$ (Equation 5.22). A simulation with a Gaussian squared, more relevant to our measurements considering that we use 2P excitation in our experiments, gives $A \sim 2.05$, very close to the Gaussian case. At the time of writing, more complex simulations, for example accounting for local heterogeneities in the diffusivity, haven't yet been performed but could be run in the future.

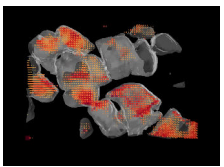

5.4 Fluence-dependent 2P diffusion in a $MAPbBr_3$ crystal

To investigate the heterogeneity arising in Figure 5.5 and explore the influence of trap filling on the diffusion, we perform fluence-dependent 2P-TRPL diffusion (x,z) maps with initial 2P excitation intensities of ∼584 μJ/cm^2 and ∼1.3 mJ/cm^2 on the same area of the sample. At each depth (z) and fluence we extract from the 2P-TRPL data a PL profile every 100 ps, which is reasonable in comparison to the temporal resolution of the setup discussed in Chapter 2.1.3, as explained in Chapter 2.4.

The sum of all TRPL traces measured on the sample is displayed in Figure 5.7 **I**, showing that the PL decays completely in less than 10 ns. We fit each PL profile over a time window of 7 ns, highlighted in red in Figure 5.7 **I**. Figure 5.7 **II** shows a selection of these PL profiles and their respective fit as a function of depth and fluence at t = 0 (Figure 5.7 **II a-b**) and t = 7 ns (Figure 5.7 **II c-d**). We note a good agreement of the data and the fit across the analysis window (0 ns to 7 ns). From the fit we extract the time-dependent outward diffusion $\sigma_x(t)$. Figure 5.7 **III a-b** gives the mean error (as a percentage) on $\sigma_x(t)$ across the measurement window at low and high fluence, respectively. Contour lines help to visualise the confidence intervals, and emphasize the large uncertainty (from 20% to >40%) arising at low fluence beyond z = 6 μm after 3 ns. Despite the low signal-to-noise ratio in this quadrant, we are able to fit $\sigma_x^2(t)$ according to Equation 5.22 and obtain D values consistent with the rest of the dataset. The result of the fit of $\sigma_x^2(t)$ on the entire dataset is shown in Figure 5.8.

In Figure 5.8, we observe an initial broadening of $\sigma_{x,0}$ close to the surface on either side of x = 0. For x < 0 this broadening is up to 4 times larger (400 %) than our detection resolution at z = 0 and t = 0, and 2 times (200 %) larger at z = 1 μm. It persists for ∼3 ns. For x > 0, the maximum broadening is of ∼150 % and this persists until z∼ 4 μm. Based on the assumption that the overall diffusion consists of the combined contributions from direct photons and charge-carriers[188], we propose that photonic effects initially dominate the overall diffusion near the surface. This "photonic" part of the diffusion below ∼3 ns at z = 0 and z = 1 μm is contained in the y-intercept as the initial broadening of $\sigma_{x,0}$. We only fit the behaviour of the curve after the intercept, as a way of separating the contribution of photons from that of charge carriers. A linear regression is applied to the data, and the diffusion coefficient (slope) is extracted at each depth separately for x < 0 (blue) and x > 0 (red). At z = 0 and z = 1 μm, the fit is applied on the measured $\sigma_x^2(t)$ for t > 3 ns, with the initial value of the parameter σ_0 set to $\sigma_{x,laser}$ (the resolution of the microscope). Dashed lines on the linear fit in Figure 5.8 indicate the extrapolation made in regions dominated by photonic effects. Blue and red-filled areas around the fit help to visualise the standard error on the diffusion coefficient (slope), which is denoted by a label at each depth.

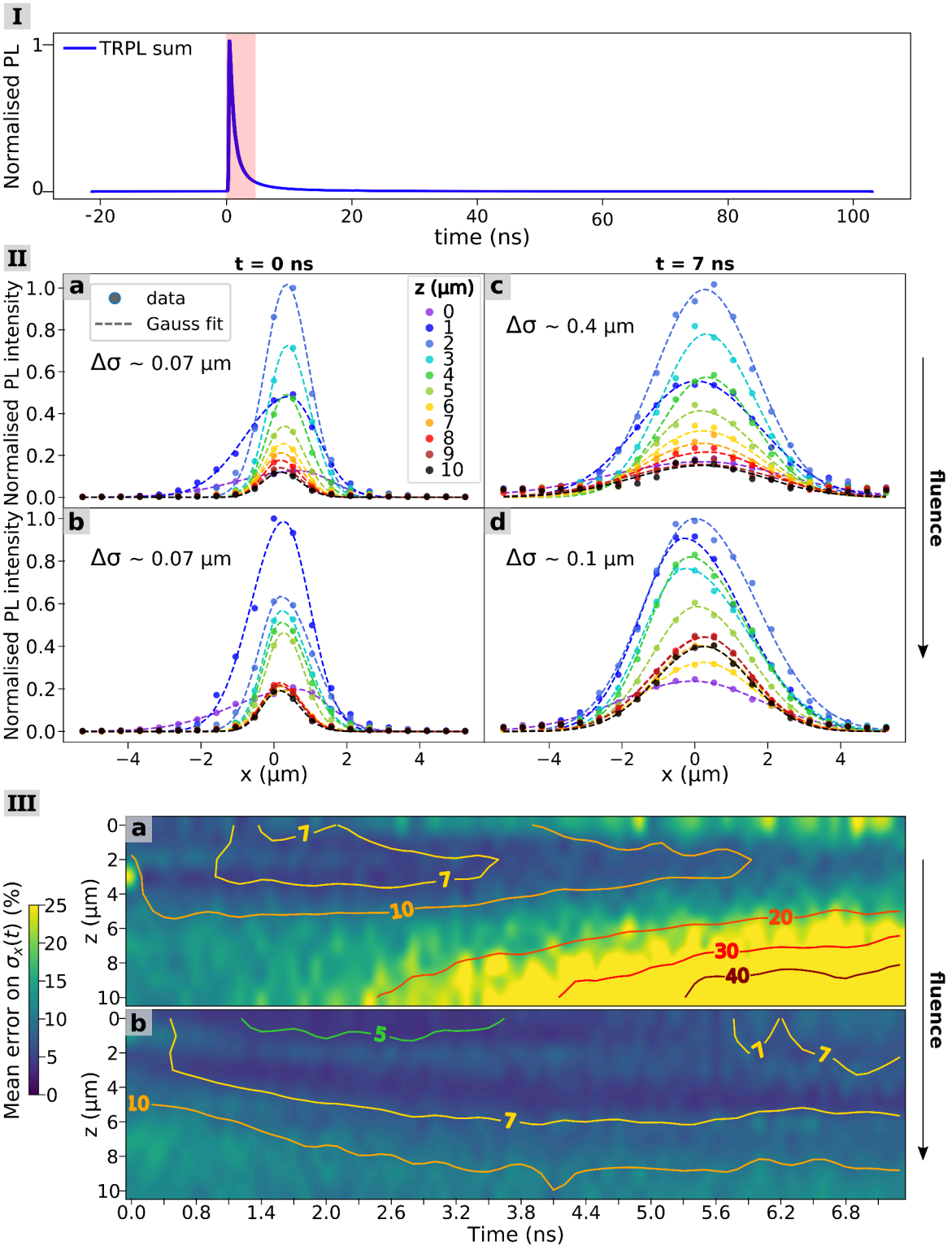

Fig. 5.7 **Quality of the signal and analysis across the measurement window**. **I** At each (x,z) coordinate, a 2P-TRPL measurement was performed with a pulse repetition rate of ~8 MHz. The red-shaded area highlights the time-interval used for further analysis. **II** PL profiles extracted from the 2P-TRPL measurement at different depths (z) and fluence for t = 0 (a-b) and t = 7 (c-d) ns after the excitation pulse. An asymmetrical Gaussian fit is applied on each profile. **III** Map of the error on $\sigma_x(t)$ extracted from the Gaussian fit, as a function of depth (z) and time, for low (a) and high (b) excitation fluence. Contour lines help to visuali the variations in uncertainty from <5% to >40% of $\sigma_x(t)$.

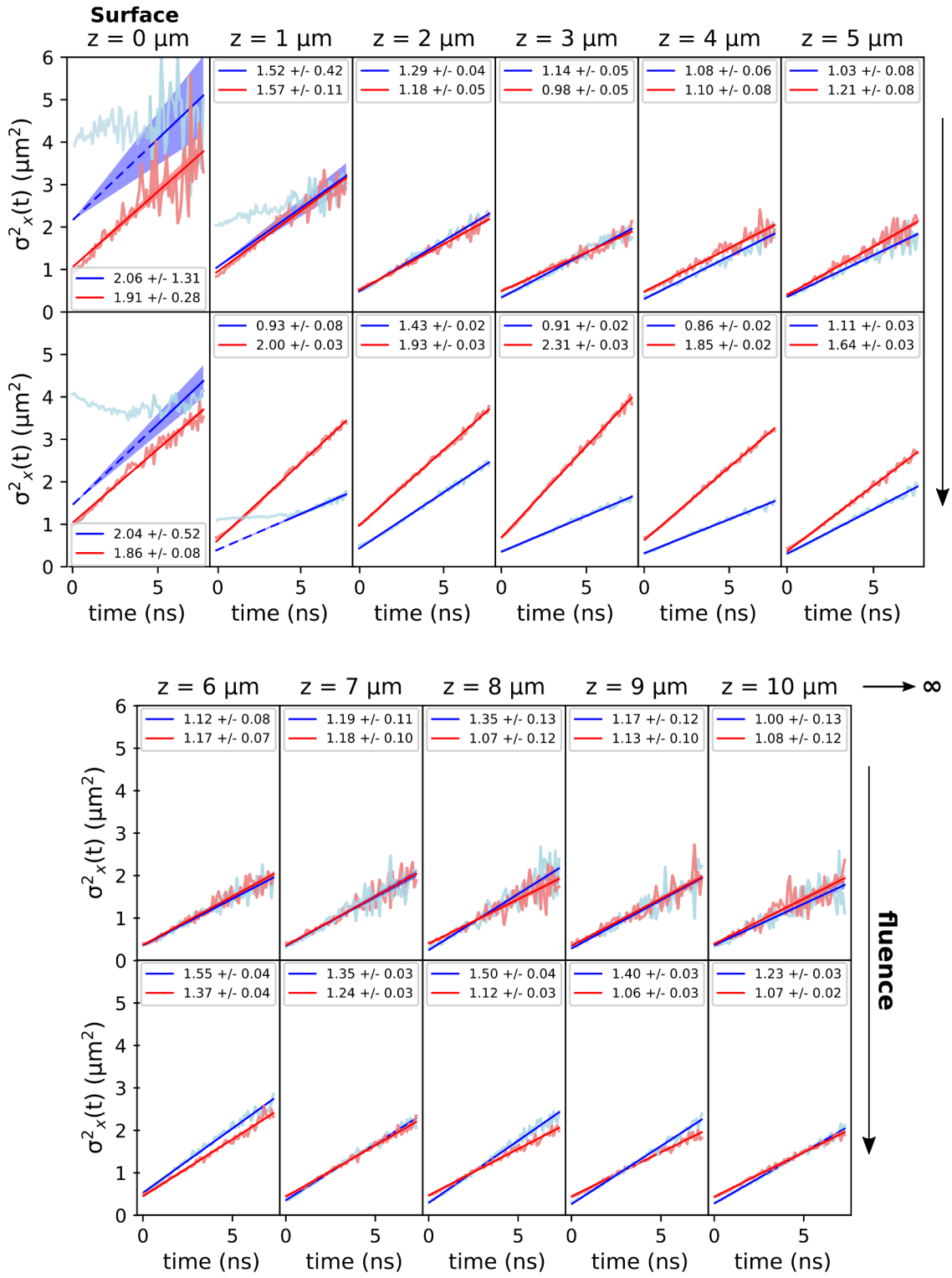

Fig. 5.8 **Fitting** $\sigma_x^2(t)$ measured at different depths in a $MAPbBr_3$ single crystal, with increasing fluence (from ~584 µJ/cm^2 (top row) to ~1.3 mJ/cm^2 (bottom row)), for x < 0 (blue) and x > 0 (red). The top and bottom figures show the data between z = 0-5 µm and z = 6-10 µm, respectively. The linear fit is overlaid on top of the data. Dashed lines indicate when an extrapolation was made. Filled areas around the fit help to visualise the standard error on the diffusion coefficient (slope), given in cm^2/s (inset in each panel).

The distribution of diffusion coefficients measured at low and high excitation fluence are displayed in Figure 5.9. A red marker identifies the mean of each distribution, which would be the value of D obtained from a macroscopic measurement. At low fluence, the distribution is narrow with a sharp peak around 1.2 cm^2/s and a macroscopic measurement would give a good representation of the diffusion. At high fluence, however, the distribution of D spreads across $\sim$0.8 to $\sim$2.4 cm^2/s with a maximum at $\sim$1 cm^2/s and a mean around $\sim$1.4 cm^2/s. In this case, we are able to observe a spatial heterogeneity in diffusion that is not captured in macroscopic diffusion measurements.

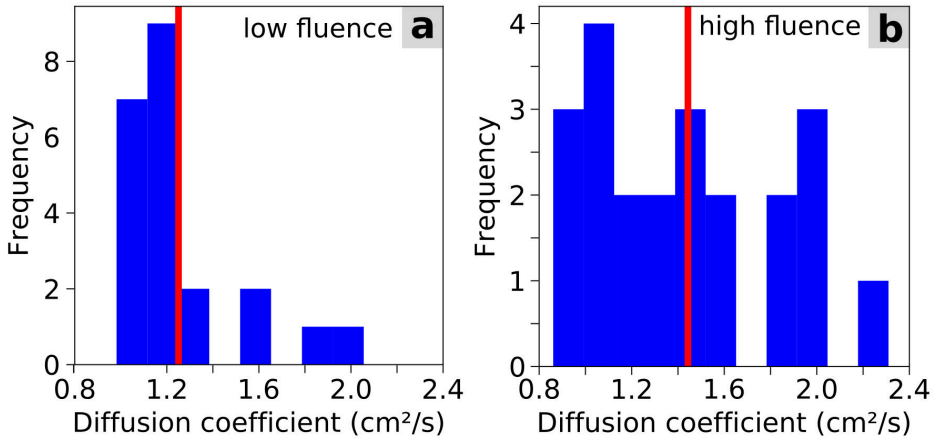

Fig. 5.9 **Distribution of diffusion coefficients as a function of fluence** The red marker indicates the mean of the distribution, corresponding to the result one might obtain from a macroscopic measurement.

In Figure 5.10 **a**, we show the outward diffusion $\sigma_x(t)$ and the fit from Equation 5.22 as a function of excitation fluence, at selected depths. In Figure 5.10 **b**, we plot the diffusion coefficient as a function of depth. These values are two orders of magnitude larger than the coefficients obtained for electronic diffusion in state-of-the-art triple cation polycrystalline thin films[188], which could in part be understood by the absence of the grain structure in the single crystals investigated here. Recently, grain boundaries have been shown to act as solid walls for charge carrier diffusion in perovskite thin films[184].

At low fluence, we observe the same diffusive behaviour for $x < 0$ and $x > 0$. We note a two-fold decrease of the diffusion coefficient D between $z = 0$ and $z = 2$ µm, from $\sim$2 cm^2/s to $\sim$1.2 cm^2/s, and a plateau from around $\sim$1.2 cm^2/s until the endpoint of our measurement ($z = 10$ µm). At higher excitation fluence, the diffusion for $x > 0$ is greatly enhanced between $z = 2$ and $z = 6$ µm, with D $\sim$2.5 cm^2/s instead of $\sim$1.2 cm^2/s at low fluence. This enhancement is consistent with the fact that the proportion of saturated traps increases with increasing fluence, enabling charge-carriers to diffuse further without being trapped. This effect is not

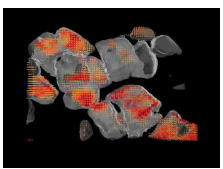

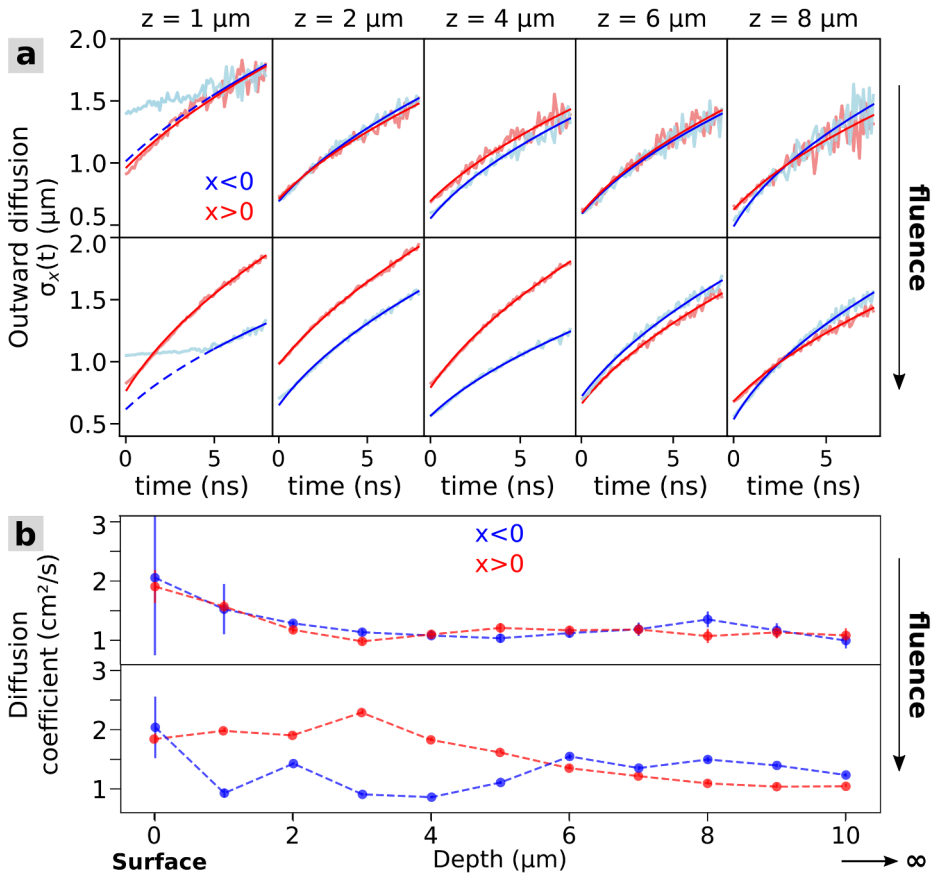

Fig. 5.10 **Outward diffusion $\sigma_x(t)$ as a function of depth and fluence** in $MAPbBr_3$ single crystal. (a) Experimental data and fit are shown for x < 0 (blue) and x > 0 (red) at selected depths. Dashed lines indicate when an extrapolation was made; (b) Diffusion coefficient D as a function of depth and fluence, for x < 0 (blue) and x > 0 (red).

observed for x < 0, where the evolution of D with depth at high fluence follows the behaviour seen at low fluence. This indicates that the density of traps is higher on this side of x = 0, and that a two-fold increase in the excitation fluence is still not sufficient to saturate the traps.

In order to evaluate this hypothesis, in Figure 5.11 we compare the PL intensity (Figure 5.11 **a-b**) and PL decay time (Figure 5.11 **c-d**) maps at low and high fluence. The PL lifetime is defined here as the time at which the PL intensity has decayed to $1/e^2$, ~87%, of its value at t = 0. Although no clear heterogeneity appears in the PL intensity map at high fluence, pockets of long decay times are visible, especially at x < 0 between z = 2 µm and z = 6 µm (highlighted by a dotted circle in Figure 5.11 **b** and **d**), precisely where the heterogeneity in diffusion is the largest. The PL decay time distributions at low and high fluence respectively in Figure 5.11 **e-f** show an overall faster decay time with fluence (the median is indicated by a red marker), which is consistent with higher diffusion coefficients.

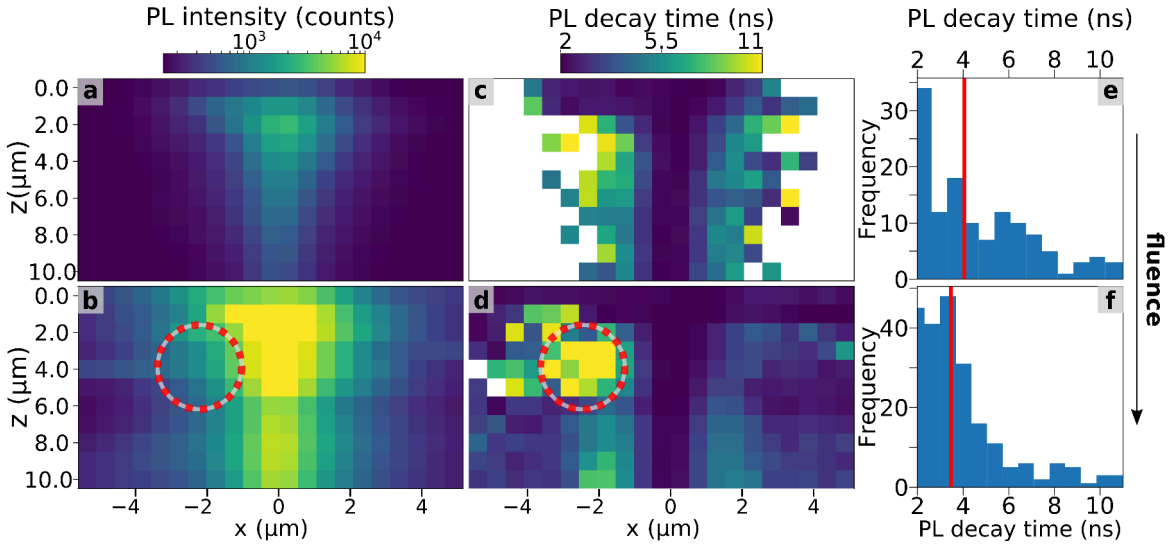

Fig. 5.11 **Direct comparison between PL intensity and decay time maps** in a $MAPbBr_3$ single crystal. (a-b) PL intensity and (c-d) PL decay time at low and high fluence. A pocket of long decay is highlighted by a dotted circle in (b) and (d). (e-f) Distribution of the PL decay time at low and high fluence.

Overall, the evolution of $\sigma_x(t)$ depends weakly on fluence. This can be understood as most of the carriers recombine rapidly at the excitation site x = 0, with the PL lifetime around this point being only ∼2 ns (Figure 5.11 **c-d**), leading to a low carrier concentration away from x = 0. We do not see any improvement of D with fluence deeper in the crystal (z > 6).

Figure 5.12 displays side-by-side the diffusion coefficient D (**a**), the average decay time (**b**), the average PL intensity (**c**) and $\sigma_{x,0}$, the PL spread at t = 0 (**d**), as a function of depth and fluence. The region between z = 2 and z = 6 µm where the anisotropy is seen is highlighted by a yellow box. The anti-correlation between diffusion coefficient and average decay time could mean that charge-carriers remain longer in areas were D is lower. This localisation could have different grounds such as a locally higher density of shallow traps, from which the carriers would be released and recombine at later times. The fact that this heterogeneity is not visible in the average PL intensity suggests that the same amount of carriers recombine on either side of x = 0 at the same absolute distance $|x|$. Assuming that charge carriers are localised at x < 0 and that they diffuse faster across the region where x > 0, we would expect more recombination events and therefore more PL emission at x < 0.

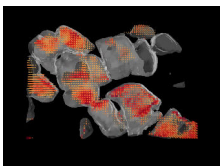

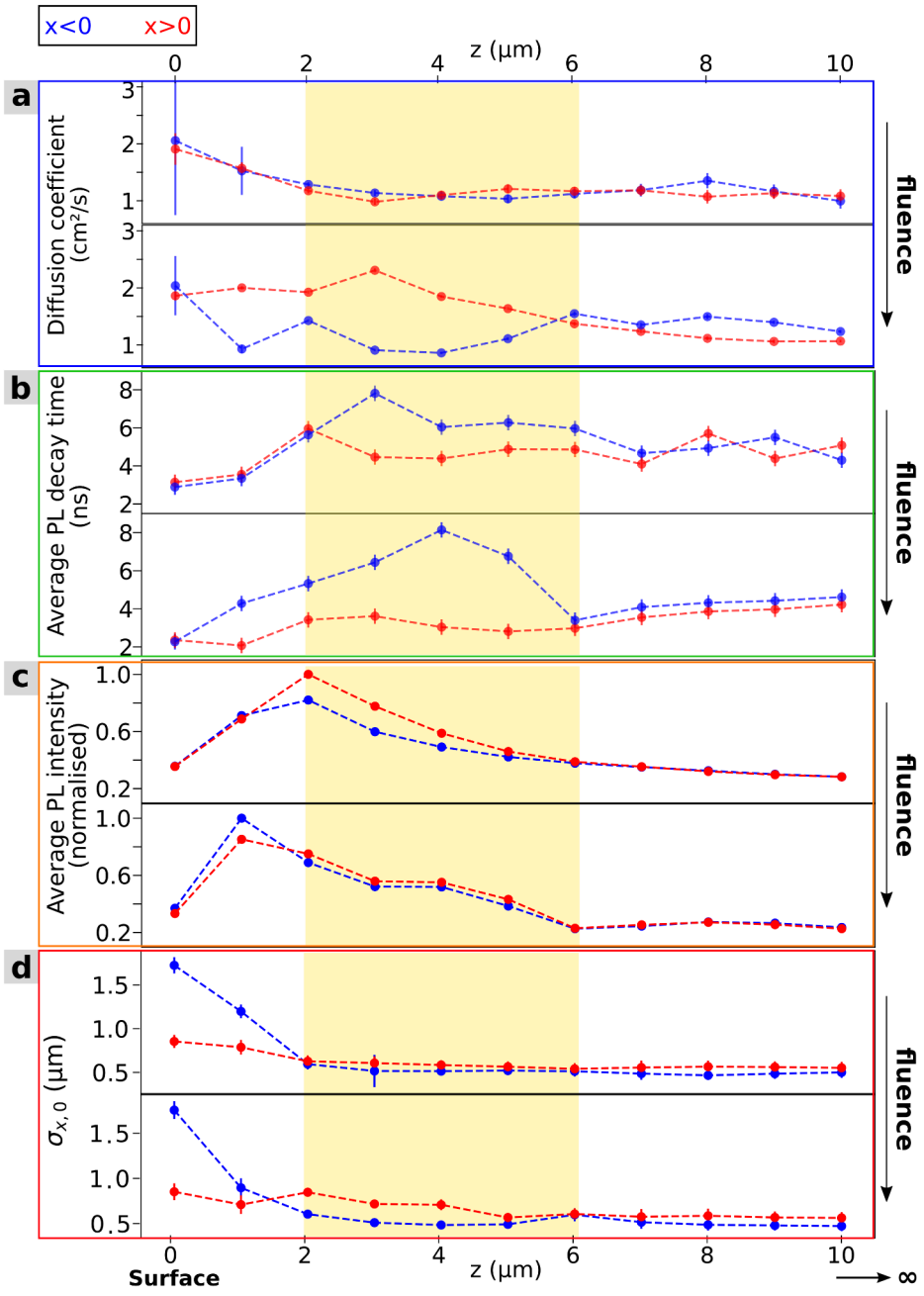

Fig. 5.12 **Direct comparison between our results** in a $MAPbBr_3$ single crystal. (a) the diffusion coefficient D, (b) the average PL decay time, (c) the average PL intensity and (d) $\sigma_{x,0}$ are displayed as a function of depth and fluence in a $MAPbBr_3$ single crystal. A yellow shaded window highlights the region where an anisotropy is observed, and where efficient diffusion and long decay times are anti-correlated.

The symmetry in the overall PL intensity on either side of x = 0 is an indication that the detected light does not solely arise from primary recombination events. Our hypothesis is that an extra contribution to the total PL intensity at x > 0 where D is larger could come from photon recycling. As discussed in introduction, this hypothesis is consistent with the broadening of $\sigma_{x,0}$ (anisotropic) observed at high fluence for x > 0 between z = 2 and z = 6 µm. Combined, these results would hence suggest that the PL quantum yield increases with D. It could be that the x < 0 region contains more traps than the x > 0 region. This conclusion sheds some light on the broadening of $\sigma_{x,0}$ at x < 0 close to the surface (z = 0-1 µm), that could originate from the fact that this region of the crystal is more prone to scattering, thus increasing the fraction of photons coupled out of the sample into the microscope. Another explanation could involve light-soaking at the surface in ambient atmosphere. We note however that at z = 0 the laser beam is only partially immersed in the material, and that optical artefacts could contribute to the very large broadening observed at this depth.

Finally, we note that below z = 6 µm the measured PL spread at t = 0 ($\sigma_{x,0}$) is of the order of our maximum detection resolution ($\sim$ 0.5 µm). According to Bercegol et al.[188] the overall PL spread contains the photonic and carrier contributions, we can infer that these photonic contributions appears to be prominent at the surface (in the first couple of microns) but less so in the bulk of this single crystal. Further into the depth of the crystal this photonic contributions, significant in regions of high diffusivity and potentially high PL quantum yield such as between z = 2 and z = 5 µm for x > 0, seems to reflect the relative contribution of photon recycling. Although careful optical modelling would be needed to disentangle photonic effects from carrier diffusion and obtain a quantitative assessment of photon recycling, our results demonstrate that two-photon depth-dependent diffusion mapping can be used as a powerful technique to assess their respective contributions.

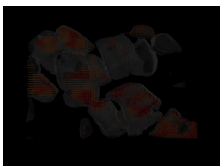

5.5 Preliminary results in 2D perovskites

The fluence-dependent 2P-TRPL diffusion measurement was reproduced in 2D iodide-based perovskites, stacks of perovskite sheets and organic layers with dimensionality (phases) n = 2 and n = 3 as illustrated in Figure 5.13. A photograph of the flakes is displayed in Figure 5.14, arranged according to their dimensionality (n=1, n=2, n=3 from top to bottom). A schematic shows their average dimensions (inset). The raster scanning starts at the surface of the sample, and stops at z=10 µm in depth to cover a region of 10x10 µm.

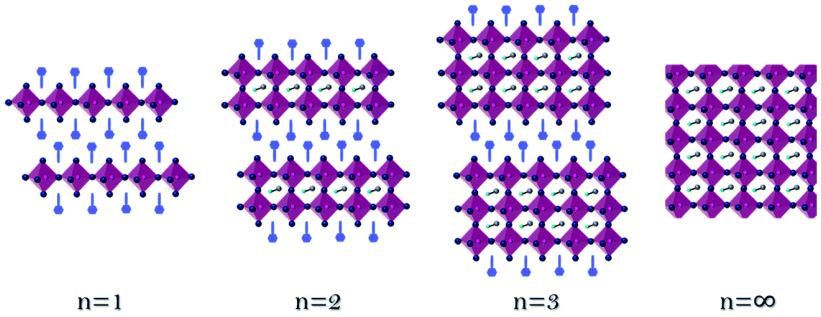

Fig. 5.13 **2D perovskite structure**, stacks of perovskite and organic layers in difference phases: n = 1, n = 2, n = 3 and n = ∞ the 3D single crystal phase. Figure taken from [198].

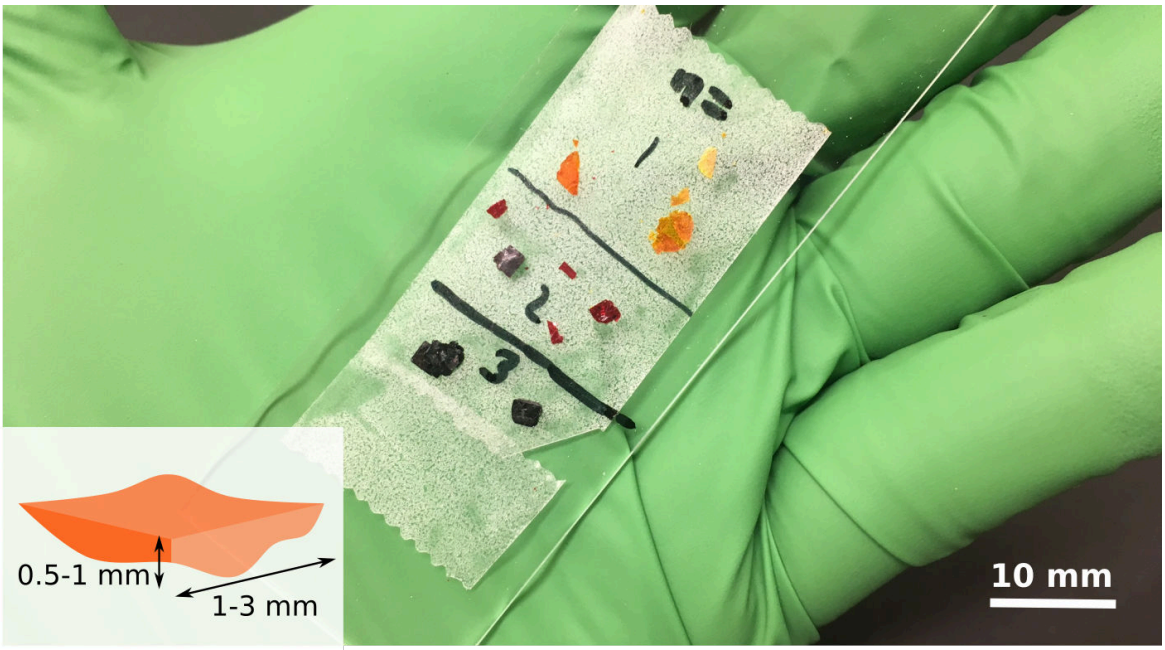

Fig. 5.14 **2D single crystal flakes used for diffusion experiments**, on tape. The flakes' average dimensions are shown as inset.

Figure 5.15 shows the outward diffusion $\sigma_x(t)$ as a function of depth with excitation fluence ~270 µJ/cm^2 (top row) and ~1.38 mJ/cm^2 (bottom row).

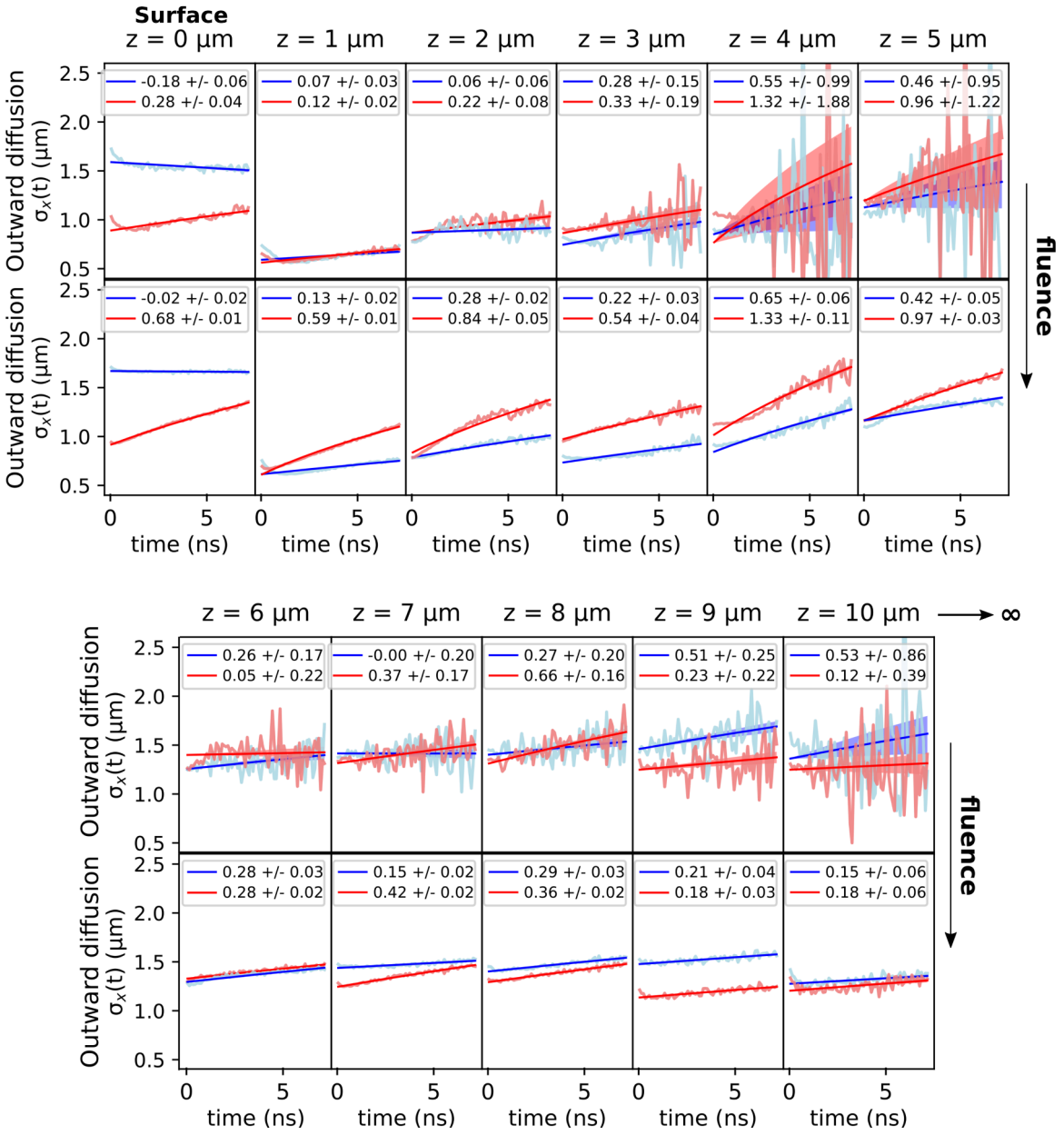

Fig. 5.15 **Outward diffusion $\sigma_x(t)$ as a function of depth and fluence** in $MAPbI_3$ 2D (n = 2) perovskite. Experimental data and fit are shown for x < 0 (blue) and x > 0 (red) at selected depths. The diffusion coefficients are printed in the labels in cm^2/s. The excitation fluence goes from ~270 µJ/cm^2 (top row) to ~1.38 mJ/cm^2 (bottom row).

This dataset gives encouraging preliminary results, but the experiment needs to be repeated. PL and spectral maps as well as diffusion maps need to be performed on fresh exfoliated samples, with a long-pass filter in the collection arm (which is missing for the measurements reported here).

We report diffusion coefficients ranging from ∼0.1 cm^2/s to ∼1 cm^2/s, on average two times smaller than in the $MAPbBr_3$ single crystal, suggesting that the carriers are effectively slowed down by the organic sheets. Similarly to the measurements reported earlier in $MAPbBr_3$, we see an asymmetry of the diffusive properties at high fluence on either side of x = 0, this time between z = 0 and z∼5 µm. We also note lower diffusion coefficients for x > 0 below z = 5 µm (Figure 5.16 **a**), which is correlated at both low and high fluence with a rise of the PL decay time and the PL average intensity (Figures 5.16 **b** and **c** and 5.17 **a** and **b**, respectively). In this deeper region, highlighted in Figure 5.16, the carriers appear to be slowed down and more localised. This localisation is consistent with the increase in $\sigma_{x,0}$ observed in the same region (Figure 5.16 **d**). We also note a decrease in PL intensity just above this region (Figure 5.17) between z = 4 µm and z = 5 µm that correlates with an increase in diffusivity (Figure 5.16 **a**).

Figure 5.18 **a** displays a close-up on the first 3 ns of the outward diffusion $\sigma_{x,t}$ as a function of depth (z), at high excitation fluence. The abrupt change in carrier recombination and diffusion properties observed at z ∼5 µm suggests the presence of different phases above and below this depth. From z = 1 to z = 3 µm (blue frame in Figure 5.18 **a**), the diffusion appears similar to the behaviour observed in the single crystal. It could be a 3D phase, as the sample was not exfoliated before measurement. From z = 6 µm down to the endpoint of our measurement (10 µm), the localisation of carriers is supplemented by an initial decline of $\sigma_{x,t}$ in the first nanosecond. This decline is highlighted in Figure 5.18 **b** at depths were it is prominent by yellow rectangles, and is probably due to the fast propagation of photons in the crystal preceding the normal diffusion of charge carriers. This suggests that the photon-generated population has decayed somewhat before the standard diffusion starts repopulating those regions, and it indicates the presence of a 2D phase (red frame in Figure 5.18 **a**) where the carriers are slowed down by the presence of organic layers separating the randomly oriented perovskite sheets (n layers). Between z = 3 and z = 5 µm, we observe a joint rise in D and in $\sigma_{x,0}$, indicating a local improvement in diffusion at the interface between both phases (green frame in Figure 5.18 **a**).

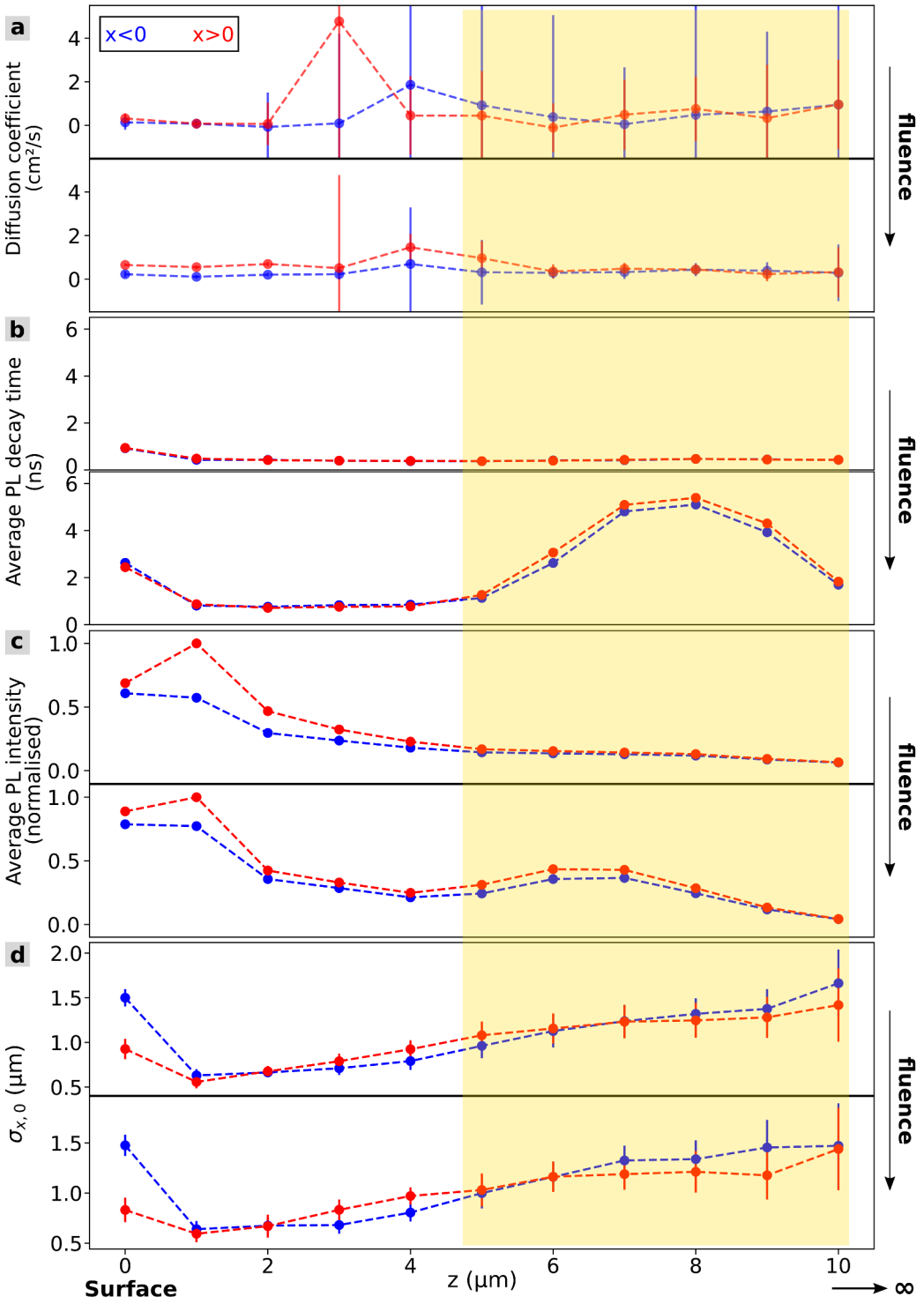

Fig. 5.16 **Direct comparison between our results** in $MAPbI_3$ 2D (n = 2) perovskite. (a) the diffusion coefficient D, (b) the average PL decay time, (c) the average PL intensity and (d) $\sigma_{x,0}$ are displayed as a function of depth and fluence in $MAPbI_3$ 2D (n = 2) perovskite. A yellow shaded window highlights a region between z∼5 and z∼10 μm where an enhancement of both the PL intensity and decay time is observed with increasing fluence.

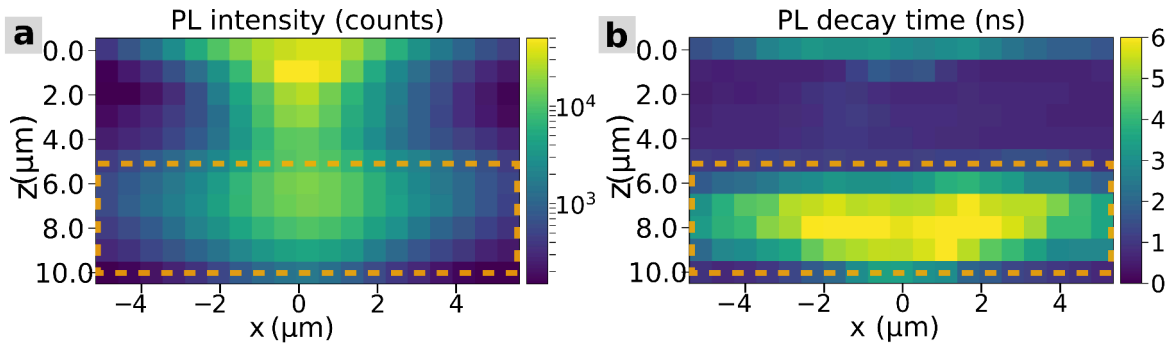

Fig. 5.17 **Direct comparison between (a) PL intensity and (b) decay time** in $MAPbI_3$ 2D (n = 2) perovskite at high fluence (∼1.38 mJ/cm^2). A region of high PL and long decay time is highlighted by a dashed orange rectangle.

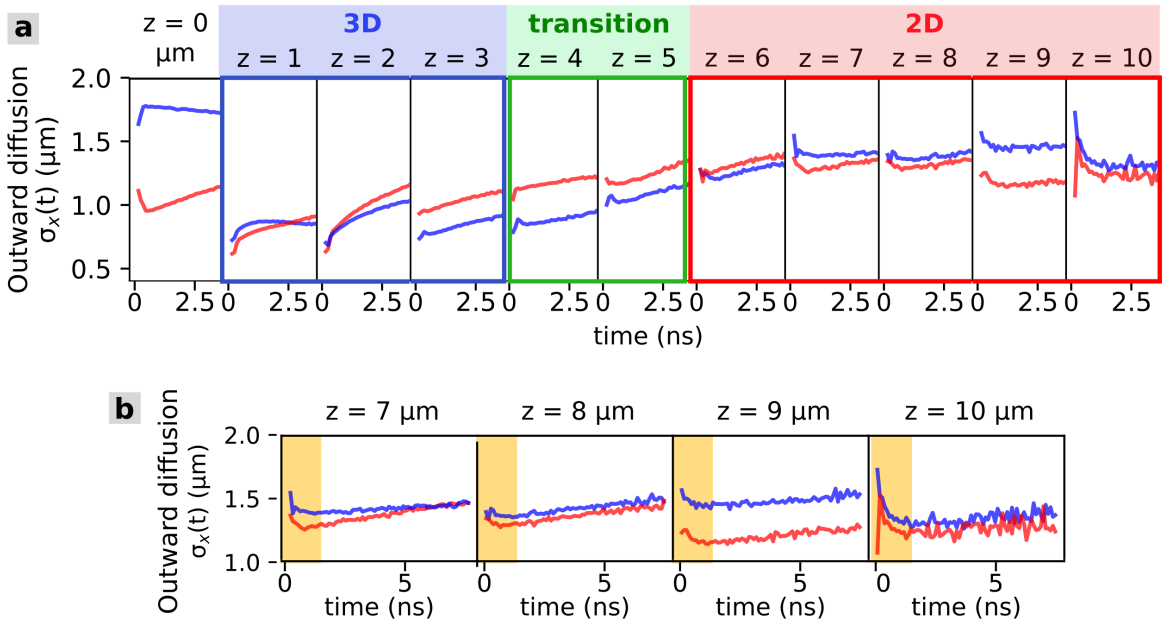

Fig. 5.18 **Close-up on the early diffusion** in $MAPbI_3$ 2D (n = 2) perovskite fo different depths (z), at high excitation fluence. (a) Different potential phases are proposed and in indicated by different framing colours: 3D in blue, 2D in red and the interface in green. (b) Yellow rectangles highlight an initial decline in $\sigma x,t$ in the first nanosecond at selected depths (where it is prominent and best observed).

At z = 0 µm, we observe again a broadening of $\sigma_{x,0}$ as in the single crystal. However, in contrast to the single crystal where it persists until z = 2 µm for x < 0, in this sample it disappears entirely at z = 1 µm. In these 2D materials, a distribution of phases with different n numbers is usually observed. Due to a difference in confinement between the different phases, we expect a mismatch between their optical absorption and emission (Stokes shift) and in

this picture photonic effects such as photon recycling should be less significant. In this case, the phase close to the surface appears to be a 3D phase, which could partly explain why we observe a significant broadening of $\sigma_{x,0}$ at z = 0. The other explanation, as mentioned earlier, is that this broadening could be an artefact of the optical measurement as the excitation beam is not fully immerse in the crystal at z = 0. Future experiments on exfoliated samples and rigorous optical modelling would further clarify these observations.

Finally, we show in Figure 5.19 preliminary measurements performed in 2D (n = 3) perovskite at high fluence (∼1.38 mJ/cm^2). No asymmetry or heterogeneity is visible, and the diffusion coefficients are higher on average (∼0.34 cm^2/s) than in the 2D (n = 2) sample but lower than in the 3D crystal. The charge carriers diffuse more efficiently in the thicker perovskite sheets.

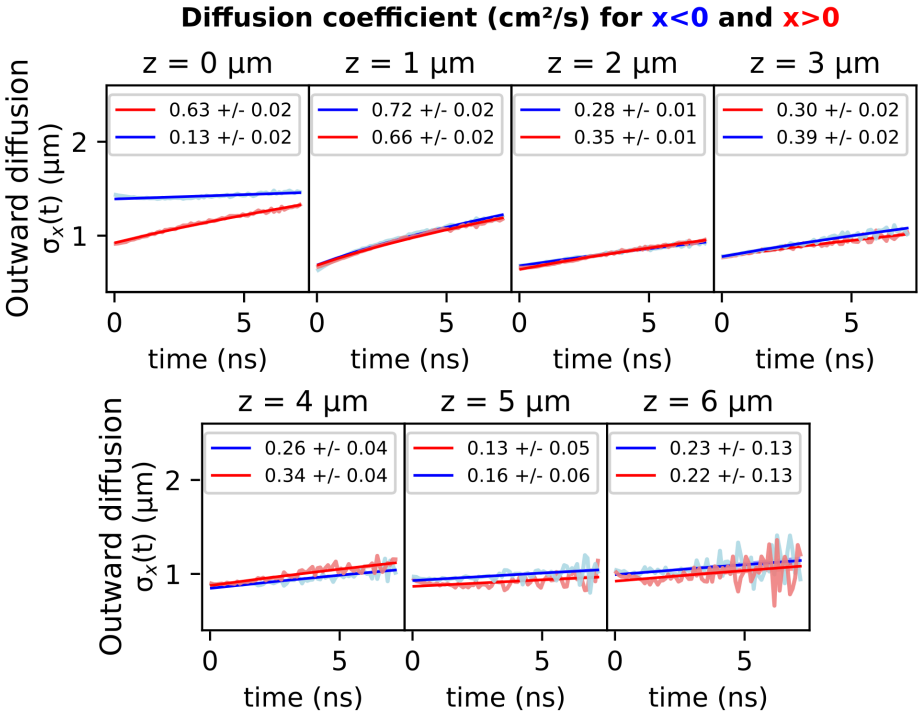

Fig. 5.19 **Outward diffusion $\sigma_x(t)$ as a function of depth and fluence in $MAPbI_3$ 2D (n = 3) perovskite.** Experimental data and fit are shown for x < 0 (blue) and x > 0 (red) at selected depths. The diffusion coefficients are printed in the labels. The excitation fluence is ∼1.38 mJ/cm^2.

5.6 Modelling $\sigma_{x,0}$ near the surface of a crystal

The coefficient $\sigma_{x,0}$, the spatial extent of the PL profile at t = 0, depends on experimental parameters (optical resolution, 2P absorption coefficient) but also on physical effects acting within the temporal resolution of the experiments (∼100 ps). One of these effects could be the photonic transport of early PL inside the crystal before it is reabsorbed to generate carriers further away from the centre. The contribution of radiative transport at time zero is, in fact, a well-known effect in thin-film solar cells[199, 200]. This effect would happen at each depth but may be amplified closer to the surface due to the high refractive index of perovskite and the total internal reflection of the PL with its surface interface. The asymmetry of this effect could be due to local differences in surface properties impacting photon wave-guiding. This might be caused by the presence of local defects or crystal boundaries inducing a local change in the optical properties of the crystal (refractive index, scattering) impeding the out-coupling efficiency and leading to a local rise in photon recycling events. The total internal reflection angle could also change locally due to surface roughness or facets, or tilt.

To investigate the cause of the broadening of $\sigma_{x,0}$ close to the surface and disentangle the contributions from photon recycling and carrier diffusion, the isotropic emission and propagation of PL inside the crystal needs to be rigorously modelled. We did attempt to make sense of the broadening near the surface observed in the $MAPbBr_3$ single crystal using a very simple ray optics model. We report the details of this model here. Although it does not fit our data, it indicates that photon recycling plays a significant role near the surface and it is a starting point towards a more complex simulation. For our preliminary optical modelling, we adopt a ray optics approach, taking into account the internal reflection of light at the interface between perovskite and air at the surface of the crystal. We model the PL as being emitted from a point source and propagating isotropically away from it in 3D, where its intensity scales as $1/r^2$. We also consider the exponential extinction of the PL according to Beer-Lambert's law due to the high absorption coefficient of perovskite at the PL wavelength (∼560 nm). Recently, Richard Ciesielski et al. reported a 2D model of PL reabsorption horizontally in large crystal perovskite films[184]. They express I_{guided}, the intensity of the waveguided PL, as a convolution of the initial PL profile I_{direct} and Beer-Lambert's law:

$$I_{guided} = A.I_{direct} \star \frac{\exp(-\alpha d)}{d}, \tag{5.27}$$

where α describes the extinction of the PL propagating within the crystal due to scattering and absorption, d is the distance from the excitation point and A is an amplitude factor accounting for the scattering efficiency and detection sensitivity. In order to adapt it to our 3D single-crystal case, we add a second term to the exponential decay function accounting for

total internal reflection of photons at the surface. This happens when their angle of refraction is larger than the critical angle $\theta(x,z) > \theta_c$. The critical angle depends on the refractive indices of air n_{air} and perovskite n_p, according to Snell's law. Figure 5.20 **a** shows two light rays r_1 and r_2 going from the excitation point **A** at x = 0 to the collection point **B** at x = d, at the same depth z = z_1. The light rays r_1 and r_2 travel a distance d_1 = d and $d_2 = \sqrt{4z_1^2 + d^2}$, respectively. When the PL is emitted deeper in the bulk at z = z_2 (point **C**), due to a wider escape cone (and reabsorption) light rays can only travel from **C** to **D** along x, as r. Figure 5.20 **b** shows the evolution of the escape cone with excitation depth. Two light rays emitted from **A** at an angle $< \theta_c$ (1) and $> \theta_c$ (2) are emitted outside and reflected inside of the crystal, respectively.

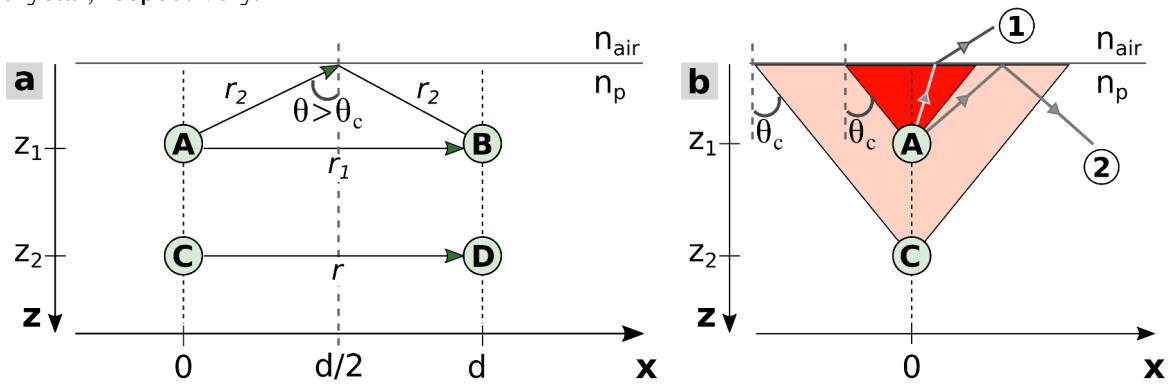

Fig. 5.20 **Light rays propagating from the excitation point to a collection point.** (a) The ray r_1 propagates directly from **A** to **B** at z = z_1, while r_2 undergoes total internal reflection at the surface, θ_c being the critical angle; at z = z_2 deeper in the bulk, there is only one light ray r going from **C** to **D**. (b) Escape cone as a function of excitation depth, with a light ray emitted outside of the crystal (1) and another one reflected inside (2). n_{air} and n_p are the refractive indices of air and perovskite, respectively.

We name $I_{PL}(x,z)$ the convolution of the PL profile I_0 with the exponential decay function:

$$I_{PL}(x,z) = I_0 \star \left[\frac{\exp(-\alpha x)}{x^2} + A(x,z) \frac{\exp(-\alpha\sqrt{4z^2+x^2})}{4z^2+x^2} \right], \tag{5.28}$$

where $A(x,z) = 0$ or 1 depending on whether the light is emitted within the escape cone or if it is reflected at the surface. Using Snell's law, we define:

$$\begin{aligned} \theta(x,z) &= \arctan\left(\frac{x}{z}\right), \\ \theta_c &= \arcsin\left(\frac{n_{air}}{n_p}\right), \end{aligned} \tag{5.29}$$

and $A(x,z)$ as:

$$A(x,z) = \begin{cases} 0, & \text{if } \theta(\frac{x}{2},z) < \theta_c, \\ 1, & \text{if } \theta(\frac{x}{2},z) > \theta_c. \end{cases} \tag{5.30}$$

The absorption coefficient α in Equation 5.28 for I_{PL} depends on the wavelength λ of the light (*Napierian spectral absorption coefficient*): $\alpha_\lambda = \frac{4\pi k}{\lambda}$, where k is the imaginary part of the complex refractive index $N = n + ik$. Since we collect only the red-most tail of the PL emission (using a tunable long-pass filter) in our 2P-TRPL measurements, as an approximation we input in our simple model the absorption coefficient $\alpha \sim 0.08$ µm^{-1} reported for $\lambda = 560nm$[117]. Our main interest being to investigate the broadening of $\sigma_{x,0}$, we generate an initial Gaussian profile of amplitude 1 and σ_0 = 0.5 µm (dashed curve in Figure 5.21), consistent with the resolution of our microscope. We then apply the convolution for x ∈ [-1,1] µm and z ∈ [0.25,2.25] µm. Figure 5.21 shows the resulting profiles as a function of depth which we fit with a Gaussian function to monitor σ_0, as shown in inset. We observe an enhancement of σ_0 up to 7% near the surface compared to its value at z = 2 µm. Although this decrease in the first 2 µm is consistent with our measurements in the $MAPbBr_3$ single crystal, the amplitude of the enhancement close to the surface is a lot smaller than what we observe experimentally, especially when considering that only photon recycling events resulting from this boost would contribute to the measured PL. In the $MAPbBr_3$ single crystal, we observed a broadening of $\sigma_{x,0}$ of up to ∼400% near the surface.

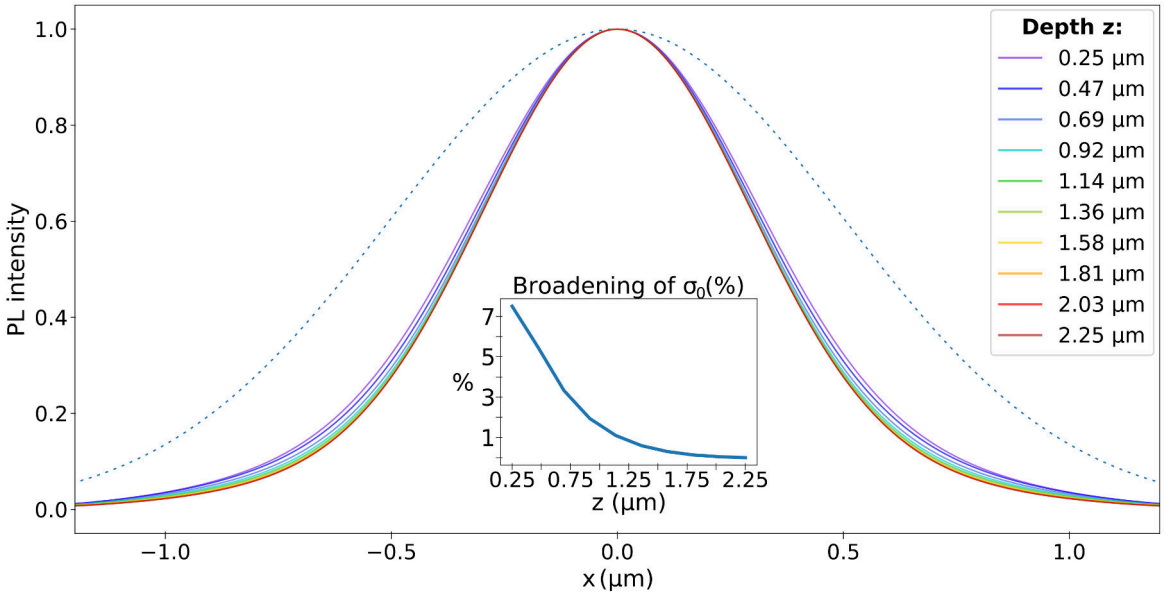

Fig. 5.21 **Broadening of σ_0 near the surface.** The dashed curve represents the initial PL profile for our simulation. The evolution of σ_0 with depth is shown as inset.

The results of this simple simulation are not sufficient to fully explain what was observed experimentally, but they constitute a solid platform for ongoing future work. A more realistic model accounting for the heterogeneous diffusive properties observed experimentally would need to draw on more complex simulations. We suggest two routes:

1. Finite-difference numerical resolution of the diffusion equation accounting for non-constant diffusivity ($D = D(x)$) and a Gaussian squared initial distribution (from 2P non-linear absorption). The evolution of the distribution with time could be simulated, and convoluted to an exponential decay function (re-absorption and wave-guiding).

2. Finite-difference time-domain (FDTD) calculations could help to solve Maxwell's equations for a point source emitting light at different depths inside the crystal, mapping the PL spectrum of $MAPbBr_3$ with a wavelength-dependent refractive index. Such a simulation could include surface roughness or defects which could influence photonic effects near the surface. Such measurements would be complemented with PL spectra and morphology measurements to couple back to the model the precise thickness or surface variation at any different phase.

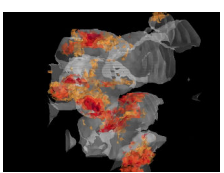

5.7 Conclusion

In this chapter we reported two-photon diffusion measurements performed on a $MAPbBr_3$ single crystal as well as preliminary data for $MAPbI_3$ 2D (n = 2 and n = 3) perovskites. Using a time-resolved microscope with a scanning fibre in the collection arm, we mapped the outward diffusion as a function of depth and fluence. We extracted from the measurements diffusion coefficients from 1 to 2.5 cm^2/s in the single crystal, and from $\sim$0.1 cm^2/s to $\sim$1 cm^2/s in 2D (n = 2) perovskite. We attribute the lower diffusivity in 2D materials to the fact that the n layers (perovskite sheets) are in general randomly oriented with respect to each other. Charge carriers thus have a more tortuous diffusion path in 2D crystals than in 3D analogues, and are effectively slowed down despite good transport through the PbI_2 backbone.

In contrast to other studies using conventional one-photon microscopy and other surface-sensitive techniques, 2P-TRPL was used to visualise buried charge-carrier diffusion in these perovskite structures. Scanning the detection revealed an anisotropic and heterogeneous diffusion at high fluence in both the single crystal and the 2D (n = 2) sample. Depth-dependent measurements allowed us to observe the diffusion of charge carriers deeper in the bulk where the photonic contribution is less prominent. The initial spread of the PL profile ($\sigma x, 0$) measured as a function of depth reduces to the detection resolution of our microscope within 3 µm from the surface (z = 3 µm) and until the endpoint of our measurement (z = 10 µm), indicating that the weight of the photonic contribution in the overall diffusion in the bulk is small. Moreover, a local enhancement of $\sigma_{x,0}$ observed in a region of high diffusivity was identified as a signature of enhanced photon recycling. Although a quantitative assessment of this effect would require careful modelling, our results indicate that 2P-TRPL diffusion mapping could in the future enable us to disentangle the photonic and carrier contributions to the overall diffusion. A significant broadening of the PL emission just after the laser pulse near the surface was observed in all samples. The broadening of up to $\sim$400 % in the single crystal compared with the PL measured deeper suggests that photonic effects can play a large role at the surface and less so in the bulk. We note however that this surface-broadening could also be a consequence of light-soaking in ambient atmosphere.

Comparing diffusivity, PL intensity and PL decay time highlighted the negative impact of traps on the diffusion efficiency. Low diffusion coefficients at low fluence were seen to increase with increasing fluence, as more traps are saturated. Our results, especially for the $MAPbBr_3$ single crystal, indicate that carriers move faster across pristine regions in the material where they potentially generate more photon recycling as well (observed as a local

increase in $\sigma_{x,0}$). A localisation of these carriers was observed in regions were the diffusion coefficient is lower.

Finally, we attempted to model the photonic contribution to the PL via photon-recycling at different depths in a single crystal. Although our simple model based on ray-optics does not entirely quantitatively explain our data, the results of the simulations seem to confirm the role of photon-recycling. It is a first step towards more complex numerical simulations, such as FDTD simulations.

In the future, further experiments would need to be performed in order to build statistics and complement our existing dataset, especially on 2D crystals. Due to the presence of different phases in these materials, one could probe a very different diffusion behaviour on a different region of a sample. In particular, PL maps, spectral maps and lifetime maps would need to be measured as well as 2P-TRPL diffusion maps and morphology information. The data analysis should be made more thorough and include a correction for the distortion caused by the refraction at the surface of the sample.

So far in this thesis, we have investigated the photo-physics of novel photovoltaic materials. We have seen how exploring the absorption and emission of light in a semiconductor could allow one to study the mechanisms underlying the generation and recombination of charge-carriers. In bulk materials, billions of atoms and electrons contribute to create macroscopically observable phenomena. Due to the complexity of their interactions with one another, it is very difficult to understand their intricate behaviour at a fundamental level. If the charge and mass (influencing their mobility) of carriers are of utmost interest and importance in solar cells, electrons possess a third attribute that hasn't been introduced yet: a spin. There exist simpler systems in which this quantum property of matter can be addressed at the fundamental level, such as single atoms and quantum dots. In the next and last chapter, we study single impurities in diamond: the Silicon-Vacancy (SiV) colour-centre, and examine how light can be used to probe and manipulate their spin states.

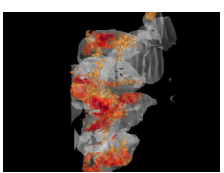

5.8 S'il vous plaît, raconte-moi l'Univers. (If you please, tell me about the Universe.) 5

Après avoir remis Léon dans son nid de coton, le petit prince regarda à nouveau le carnet gribouillé qui flottait près de lui.

— Je ne savais pas que les magiciens parlaient une langue si étrange...

— En réalité, répondit le physicien, ce magicien-là ne parle pas.

— Est-il muet ?, s'inquiéta le garçon.

— Non il va bien, rassure-toi. Il n'est simplement pas bavard. Il veut veiller sur ses secrets, comprends-tu... Et comme il ne parle pas, nous devons lui prêter une voix, un support pour traduire les messages qu'il nous transmet autrement. C'est une sorte de code que l'on appelle « Mathématiques ».

Le petit prince choisit une page et l'inspecta de plus près.

— Pour moi, tout cela ne veut rien dire.

— Disons que cela demande un peu d'entrainement. Mais en dehors du message, que vois-tu ?

— Je vois des symboles. Des petits, des grands. Des élancés et des étriqués, tous enlacés avec de petites lettres et parfois quelques chiffres... Maintenant qu'ils me font moins peur, je les trouve plutôt jolis.

— Eureka !, s'exclama le physicien. Vois-tu, l'Univers est comme ça. Il est graphique, symbolique et joli. Alors nous essayons d'écrire son histoire à son image, pour que cela le représente au mieux. C'est une forme d'art, nous sommes en quelque sorte des peintres réalisant son portrait. Il est très susceptible et nous ne voulons pas le vexer, ...

A peine le physicien eut-t-il fini sa phrase que Quantique, son astéroïde, les emporta sur la rampe d'un toboggan géant.

— Que se passe-t-il ?! Où sommes-nous ?!, s'écria le petit prince affolé.

The little prince put Léon back in his cotton nest, and took a closer look at the doodle notebook floating next to him.

— I didn't know that magicians spoke such a strange language...

— To tell the truth, this magician doesn't speak.

— Is he dumb?, the boy got worried.

— No, he is fine, don't worry. He is just not very talkative. He wants to protect his secrets, you see... Because of his silence, we have to give him a voice, a backing to record and translate the messages he gives us anyway. It is a sort of code we call "Mathematics".

The little prince picked up a page, and examined it more carefully.

— For me, all of this has no meaning.

— Well, I have to say that reading it requires some training... But besides the meaning, what do you see?

— I see symbols. Tiny ones, bigger ones. Some slender and some skimpy, all of them interlacing with some small letters and sometimes numbers... Now that they no longer scare me, and I find them elegant.

— Eureka!, the physicist exclaimed. You see, the Universe is like this. He is graphic, symbolic and elegant. Therefore, we try to write his story in a way that reflects his own character. It is a sort of art, we are somewhat like painters drawing his portrait. He is very susceptible, and we don't want to upset him, ...

In a matter of seconds, Quantum, the physicist's asteroid had taken them on the ramp of a giant slide.

— What's going on?! Where are we now?!, cried out the little prince, terrified.

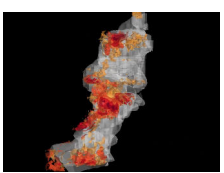

Chapter 6

Towards the optical control of single spins in diamond

6.1 Interests and novelty, introduction to the SiV^- centre

One well-established way of addressing quantum states of matter is to use light [201–203]. More precisely, coherent light: laser emission. Using photons of the right energies enables for instance to drive an atomic or atom-like system into a particular state to form a quantum bit, or "qubit" [204, 205]. Such coherent superposition state can be obtained for various isolated quantum systems [206] such as the electron spin (up and down, equivalent of the classical bits 0 and 1) in an atom. Multiple qubits in a superposition state can be combined to form quantum registers which then represent large numbers. In classical computers, parallel computing is performed by having several processors linked together, each doing one operation at a time. In contrast, a single quantum processor can perform parallel operations. Two or more qubits can be connected when their quantum states are entangled [69, 207].

Optical control of electron spins has proven versatile, being achieved on various materials and confined systems such as trapped ions [208] or semiconductor quantum dots [209, 210] (whose large size in comparison to single atoms increases their coupling to photons), and diamond samples containing particular kinds of defects [71, 211]. While pure diamond transmits visible light and appears as a clear colourless crystal, the implantation of defects such as impurities or vacancies in the diamond lattice during the gemstone's formation can lead to changes in the electronic band structure and therefore a change in colour - this is how boron defects made the famous Hope Diamond so remarkably blue. The local electronic perturbation caused by such defects, called "colour-centres", creates discrete electronic states within the insulator's bandgap similar to those of an atom, whose spin states can be addressed

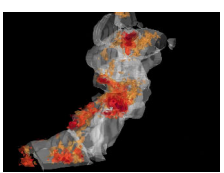

individually and manipulated with light. These systems offer a high potential for solid-state quantum information processing.

The most extensively studied diamond colour-centre so far is the negatively charged nitrogen-vacancy (NV) centre [212], formed by the replacement of a carbon atom by a nitrogen atom and an adjacent vacancy. At room temperature, very high spin coherence times were achieved for NVs in ultra-pure bulk [213] (up to 2 milliseconds) and nano [214] (up to 60 microseconds) diamond, as well as proximity entanglement between NV centres [215]. At cryogenic temperatures, the entanglement between an optical photon and a NV spin qubit [216] was achieved, paving the way towards entanglement at a distance [217]. Furthermore, NVs can couple to their microscopic environment with parameters such as temperature and electromagnetic fields, offering promising sensing applications [218, 219] such as magnetometry [220–222], and thermometry [223], even in a living cell [224]. A practical method for atomic-scale nuclear spin imaging in biomolecules using such centres in diamond was recently proposed [225].

The weakness of the NV centre resides in its optical emission spectrum: due to a strong vibronic coupling, most of its emission spectrum lies in the phonon sidebands (with a spectral width of about 100 nm), leaving only 3 to 5 percent to the zero-phonon-line (ZPL) at cryogenic temperatures (4 K), limiting strongly the rate of entanglement events [74]. Indeed, the use of indistinguishable photons is required to mediate entanglement at a distance, and this can be achieved only without any phonon coupling. While much effort is now put in the quantum optics community to couple NV centres to resonant microcavities in order to enhance their ZPL emission [226–228, 187], we orientate our study towards an alternative centre composed by a substitutional silicon impurity and a vacancy: the negatively charged silicon-vacancy (SiV^-) centre. Although SiVs are less abundant in nature than NVs and constitute a much recent field of study, they show more promising optical properties with 80 percent of their emission [72] in a narrow ZPL at 737 nm [229] (Figure 6.1 **b**)) and a minimal phononic sideband at 766 nm [230] (at 4 K). Moreover, they have been reported as the brightest diamond-based single-photon emitters [231]. The pioneering experimental and theoretical work completed previously in my group and with our collaborators in Saarbrucken (Becher group), particularly over the last four years, has unravelled the electronic structure of ^{28}Si SiV^- centres grown using High-Pressure, High-Temperature (HPHT) synthesis from graphite [77, 66]. This contributed to a profound understanding of its internal level structure which made optically accessible the electron spin of these defects.

Although the emission line at 737nm was first observed in 1980 [232], the description and modelling of the molecular structure of the SiV^- only started in 1991 when Clark and Dickerson investigated an annealed chemical vapour deposition (CVD) grown diamond in

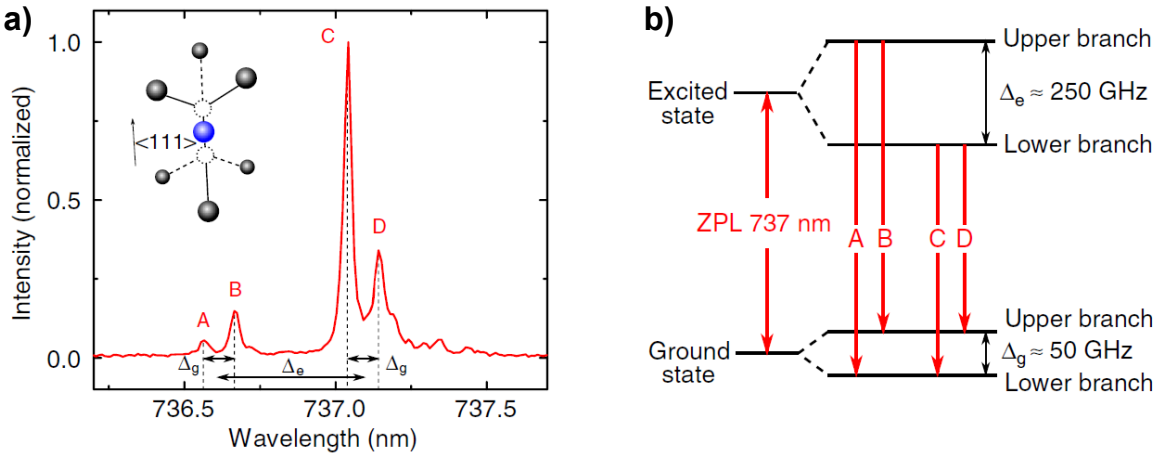

Fig. 6.1 **Electronic levels of an SiV$^-$ centre at zero magnetic field (figure taken from [66]).** Molecular structure and fluorescence of a centre off resonance (**a**)) revealing four transitions (**b**)).

which ^{28}Si atoms had been implanted. They were the first to report an evidence that the centre is composed of a silicon atom and a vacancy [233]. Within the crystal lattice, an implanted silicon atom does not exactly sit in place of the carbon atom that it replaced. Instead, as predicted by the first *ab initio* calculation in 1996 [234] and illustrated in the inset in Figure 6.1 **a)**, it is believed that the silicon atom relaxes to an interstitial lattice position with a split-vacancy between the unoccupied lattice sites (dashed circles) and the nearest neighbour carbon atoms (grey), with a D_{3d} symmetry [77, 65, 235]. First believed to lie along the <110> direction [236], the SiV$^-$ is now widely accepted as being oriented along the <111> bond axis [77]. Due to this split vacancy, the extra electron of the SiV$^-$ centre sees a double-well potential, giving it two possible orbital configurations with the same energy. Besides, the electron possesses intrinsically another degree of freedom: its spin state which can be up or down. Since there are four possible arrangements (combinations) of orbital and spin degrees of freedom (spin up and spin down for each of the two orbitals), both the ground and excited states are four-fold degenerate. Because of spin-orbit coupling - an interplay between the orbital motion and spin of the electron, the orbital degeneracy is lifted and therefore the total degeneracy becomes a two-fold (spin only) at zero magnetic field leading to a four line fine-structure [234, 66] (Figure 6.1). By exposing single SiVs to a magnetic field where the Zeeman effect lifts the remaining spin degeneracy (Figure 6.2 **b)**) it was shown that SiVs possess a spin $1/2$ [77, 66]. Simulations are now available and routinely used to fit the experimental data (C. Hepp's PhD thesis [65] p.151) and thereby extract the different parameters, or "interaction terms" of the total Hamiltonian describing the system:

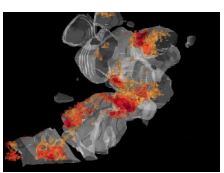

$$\mathbb{H} = \mathbb{H}^0 + \mathbb{H}^{SO} + \mathbb{H}^{JT} + \mathbb{H}^{Z,L} + \mathbb{H}^{Z,S} + \mathbb{H}^{strain}(+\mathbb{H}^{hyperfine}), \tag{6.1}$$

where $\mathbb{H}^0$ is the non-perturbed Hamiltonian, $\mathbb{H}^{SO}$ is the spin-orbit Hamiltonian (responsible for the splitting at 0 Tesla), $\mathbb{H}^{JT}$ is the Jahn-Teller matrix while $\mathbb{H}^{Z,L}$ and $\mathbb{H}^{Z,S}$ are the Zeeman terms (responsible for the magnetic field splitting) [65]. $\mathbb{H}^{strain}$ refers to the perturbation cause by the crystal strain at the vicinity of the emitter, and $\mathbb{H}^{hyperfine}$ accounts for the hyperfine interaction between the electron spin and the nuclear spin in some isotopes of Silicon (here ^{29}Si, as ^{28}Si does not have a nuclear spin). Calculating the eigenvalues of this matrix yields the energies of all SiV$^-$ levels in the given perturbation. All the perturbation terms present interactions which act exclusively among states of ground or excited state manifold. For the calculation of optical transitions connecting the ground and excited states, we use the selection rules on optical transitions described by the model [65].

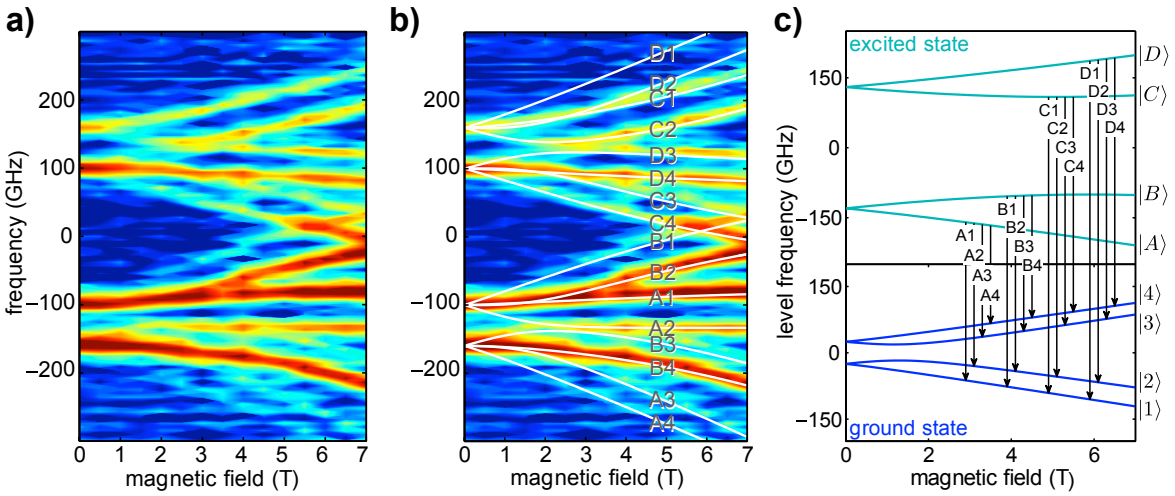

Fig. 6.2 **Splitting of the electronic energy levels of an SiV$^-$ centre with magnetic field.** The measured fluorescence spectrum (**a**)) is successfully fitted by our model (white lines in **b**)) predicting allowed transitions and level frequencies (**c**)).

We were able to create and measure coherent superposition states[237] of the electron spin that could be used as qubits[67, 75]. This was done using resonant laser excitation at cryogenic temperatures. These experiments also unravelled one of the main known limitations of the SiV$^-$ colour centre: to date, the longest measured ground state spin coherence time T_2^* is of the order of 115 ns[238]. This fast decoherence (in comparison to the NV centre) was recently attributed to interactions between the electron and lattice phonons [76]. Within a collaboration with the Nanophotonics group (Marko Lončar) at Harvard, we were then involved in a project focusing on actively reducing the electron-phonon interactions using

strain. The core of my project was then directed towards the optical coherent control of the electron spin in ^{28}Si SiV$^-$ and the nuclear spin of ^{29}Si which could be used as a quantum register (the projection of nearby nuclear spin qubits onto a well-defined state from the read-out of the electronic spin [239] has been realised with ensembles of NV centres [240]), along with the improvement of T_2^*. To this end, both optical and microwave pulses can be used to manipulate single spins. Recent work on NV centres had shown that decoupling dynamically a single centre's spin from the surrounding spin bath using nanosecond microwave pulses can improve the coherence time by more than 25 times [241]. These constituted necessary enabling steps towards the entanglement of spatially separated emitters (achieved with NV centres [242]), the implementation of quantum logic gates and the integration of these systems as nodes on chip for quantum networks [207] (Figure 6.3) can be considered possible. Besides quantum information processing, solid-state single emitters such as NV and SiV$^-$ centres are a good platform for investigating quantum phenomena, they are good systems on which to perform Bell's inequality experiments, for example.

6.2 The context for my work

When I arrived on the project, we started off by characterising a new HPHT (High-Pressure, High-Temperature grown) diamond, cut along the <111> direction before implantation. On the surface of the diamond, a solid immersion lens (SIL) array had been carved (with a SIL diameter of 1 µm) by our collaborators in Saarbrucken and in particular J. Becker, in C. Becher's group. My work in the field of quantum optics with SiV$^-$ centres then started with coherent population trapping (CPT) measurements on this sample. Our main results are presented in Section 6.3.2.

With the departure of C. Hepp from the group, we went on to explore another setup and another sample recently processed by J. Zheng (Englund group, at MIT) as part of the efforts directed towards an improvement of the light collection efficiency, one of the main limitations identified previously. On one side of that chemical vapour deposition (CVD) grown single crystal bulk diamond ($2\times2\times0.5$ mm^3) were patterned thirty 5×6 matrices of bullseye gratings (Figure **??**). The predicted collection efficiency with a numerical aperture (NA) of 0.4 was 41.1% from the bottom side and 1.4% from the top side, resulting in a directionality of 30 [243]. Our measurements showed an enhancement of about 5 from the back side with respect to the front side (Figure 6.5), although 99% of the bullseye structures appeared empty on the photo-luminescence maps. The same 660nm laser as the one used to excite the SiVs non-resonantly on the ^{29}Si sample was used, and the yield remained the same even after careful alignment of the optical microscope and the spectrometer's CCD.

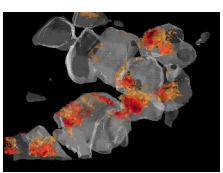

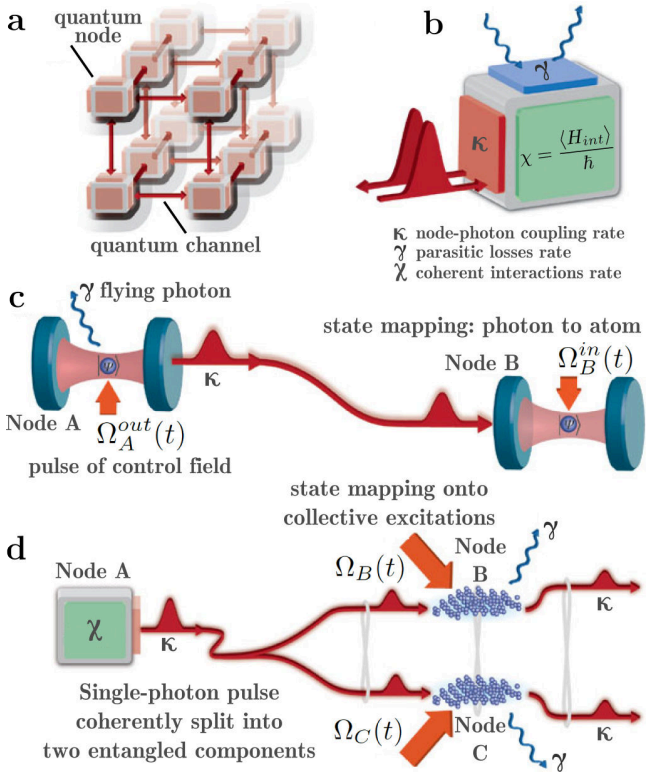

Fig. 6.3 **Quantum networks (adapted from The quantum internet, Kimble [207]).** In **a** is a notional quantum network composed of quantum nodes for processing and storing quantum states and quantum channels for distributing quantum information. The quantum interface between matter (coloured cube) and light (red curves) is depicted in **b**. In **c** quantum state transfer and entanglement distribution from node A to node B is shown in the setting of cavity quantum electrodynamics (QED). **d** shows the distribution of entanglement by using ensembles of a large number of atoms.

The discrepancy of a factor of 6 is suspected to be caused by the thickness of the sample introducing aberrations, imperfectly etched sidewall profiles and a deviation in the position of the SiV^-s from the one predicted by the simulation. A new generation of bullseye gratings patterned on diamond membranes is now being fabricated at MIT, to try and correct for the problems reported after our measurements.

We then moved from this characterisation to the setting up of an ultrafast optical setup for the coherent control of the SiV^- spin. Two pulsed beams, each of tunable repetition rate with a pulse width of about 3ps, travel along two different optical paths. On one of them, a translation stage holding a retro-reflector allows to tune the time delay between two pulses across an interval of 2 ns. Finally, the two beams which can be used for time-resolved manipulations and measurements are recombined and coupled to an optical fibre. The fibre then carries the light to the sample in the cryostat via a confocal microscope. This setup, its

specifications and its characterisation is the object of Section 6.4. When I left the group, this experiment was ready to be tested on the previously characterised ^{29}Si sample.

On the side of these experiments, which constituted then the core of my work, I contributed to another project led by S. Meesala and Y.-I. Sohn, our collaborators within the Lončar group at Harvard: observing the effects of strain-tuning on the rate of first-order electron-phonon transitions [76], and hence the ground state spin coherence time of the SiV$^-$. The main results of this collaboration, published in Physical Review B[78] and Nature Communications[79] in 2018 are presented in Section 6.3.3. They had already developed state-of-the-art expertise in the fabrication of diamond micro and nano structures. Building on their extensive work towards the development of Faraday cage angled-etching [244], high quality-factor optical nanocavities [245] and diamond optomechanical crystals [246], S. Meesala and Y.-I. Sohn had recently demonstrated enhanced strain coupling of Nitrogen-Vacancy spins to nanoscale diamond cantilevers [247]. From our knowledge of the electronic structure of the SiV$^-$ [77], they had just designed electrically actuated cantilevers which have enabled us to explore the effects of strain on the energy splitting and coherence time of this colour-centre. Together, we were able to test a recently proposed model of the electron-phonon processes occurring in this system [76]. Since we were looking at single-photon emitters, strategies had to be found to collect as many photons as possible. In order to improve the light collection efficiency, several methods have been developed [248]. Some are based on cavity quantum electrodynamics (QED): waveguides, microcavities, micropillars (offering a confinement in the plane of the microcavity) and surface plasmons (in photonic crystals and metal mirror-based microcavities).

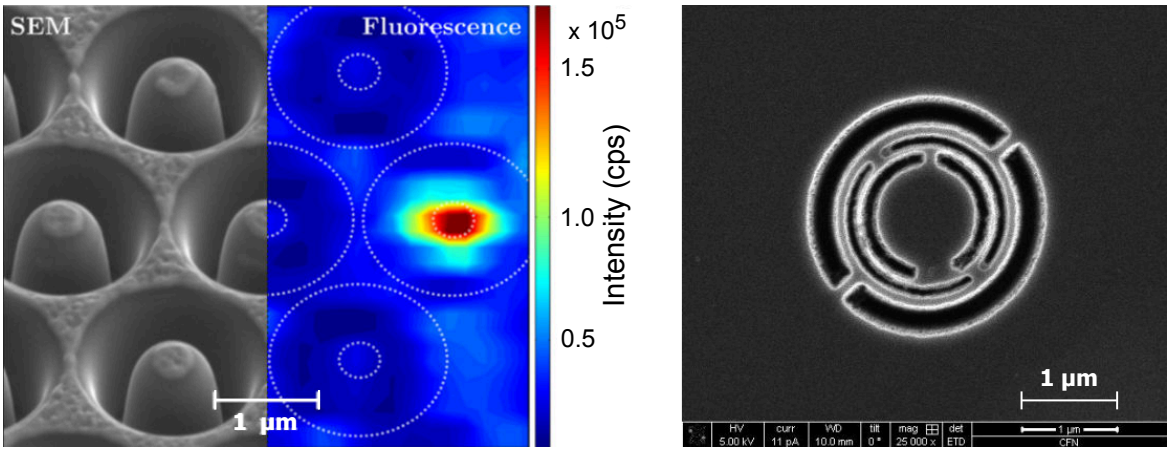

Fig. 6.4 **Light collection strategies**. SEM images of SILs (courtesy of B. Pingault [67], **left**) and a bullseye grating (courtesy of J. Zheng [249], **right**) used in our samples in order to improve the collection of photons emitted by single SiV$^-$ centres.

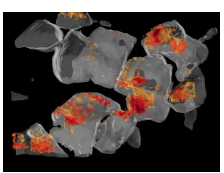

With our collaborators in Saarbrucken (Becher group) and at MIT (Englund group), we used geometrical approaches such as solid immersion lenses (SIL) [250] (Figure 6.4 **a**)) and bullseye gratings [187, 249] (Figure 6.4 **b**)) (which scatter photons out so they can be easily collected). The first bullseye sample fabricated at MIT and sent to us for measurement by J. Zheng and T. Schroder gave encouraging results with a five times improvement on the collection efficiency [243] (Figure 6.5).

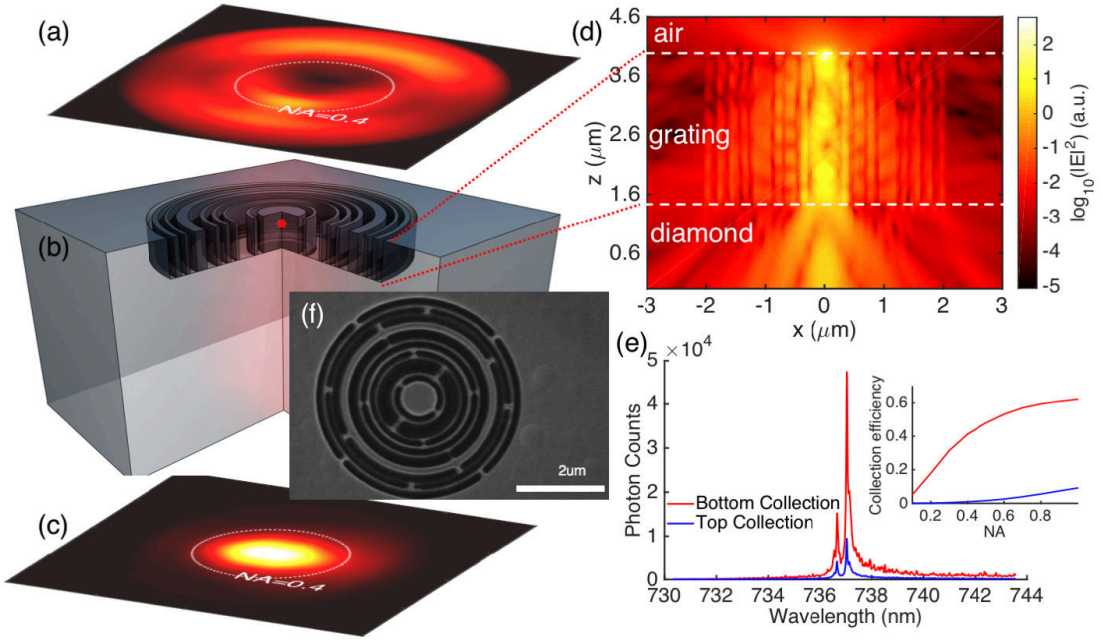

Fig. 6.5 **First generation of bullseye sample (figure taken from [243]).** (**a**) Simulated farfield collection profile for fluorescence from the top side of the circular grating. The white dotted circle indicates a solid-angle corresponding to an NA=0.4. (**b**) Perspective view of the circular grating structure. (**c**) Simulated farfield collection profile for fluorescence from the bottom side of the circular grating (same colour scale as in (**a**). (**d**) Simulated $|E|^2$ distribution in the cross-section view (log_{10} scale). (**e**) Measured spectrally-resolved fluorescence intensity from a fabricated device. The inset shows the estimated collection efficiency from top and bottom collection from simulation data. (**f**) SEM image of the fabricated circular grating in diamond.

6.3 Coherent Population Trapping: preparing a quantum bit.

Thanks to their very good optical properties and because most of the photons emitted are in the zero-phonon line, SiVs could potentially succeed where NVs show some weaknesses and become good systems for quantum information processing. Like every classical computer, a quantum computer needs to be able to create and store bits (memory), combine them and perform operations on them (processor, CPU). Coherent superposition states, which can be used as qubits, have been achieved when driving simultaneously two electronic transitions from two sublevels of the degenerate ground state to the same excited state (for instance the transitions C1 and C2 in Figure 6.2 **c)**), creating a new state no longer in resonance with the excitation frequency, thus causing a dip in the emitter's fluorescence spectrum: a dark state [67, 75]. This is called coherent population trapping (CPT), and was first observed by Alzetta and Gozzini in 1976 during what is known as "the Pisa experiment" [251]. In order to understand CPT, we first need to look at the physics of two and three-level systems.

6.3.1 Brief overview of resonant light-atom interactions

Let us first consider an atom with only two levels, forming a single transition. The waves function amplitude coefficients for the lower and upper states are respectively c_1 and c_2. The probabilities of measuring the system in each state are then $|c_1|^2$ and $|c_2|^2$. In order to understand how this system will interact with resonant light, the time-dependent Schrodinger equation can be solved for the Hamiltonian:

$$\hat{H} = \hat{H}_0(\mathbf{r}) + \hat{V}(t), \tag{6.2}$$

where $\hat{H}_0(\mathbf{r})$ describes the atom in the dark, and $\hat{V}$(t) accounts for perturbation linked to the light-atom interaction, and the general solution

$$\Psi(\mathbf{r},t) = \sum_i c_i(t)\,\psi(\mathbf{r})\exp^{-iE_it/\hbar}, \tag{6.3}$$

where the subscript i runs over all the eigenstates of the system (here, 1 and 2). Assuming that, in a semi-classical approach, the light-atom interaction is given by the energy shift of the atomic dipole in the electric field of the light of angular frequency ω polarised along the x-axis (arbitrarily) [252]:

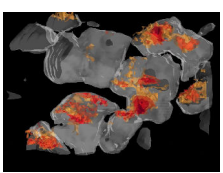

$$\begin{aligned}\hat{V}(t) &= e\mathbf{r}.\mathscr{E}(t)\\ &= ex\mathscr{E}_0\cos\omega t\\ &= \frac{ex\mathscr{E}_0}{2}(e^{i\omega t}+e^{-i\omega t}),\end{aligned} \tag{6.4}$$

the perturbation matrix elements are given by:

$$V_{ij}(t) = -\frac{\mathscr{E}_0}{2}(e^{i\omega t}+e^{-i\omega t})\mu_{ij}, \tag{6.5}$$

where $\mathscr{E}_0$ is the amplitude of the electric field and μ_{ij} is the dipole matrix element:

$$\mu_{ij} \equiv -e\langle i|x|j\rangle\,. \tag{6.6}$$

It can be shown that strong interactions with a resonant laser will cause the electron to oscillate back and forth between the two levels at a rate called Rabi frequency, Ω_R [252]:

$$\Omega_R = |\mu_{12}\mathscr{E}_0/\hbar|, \tag{6.7}$$

giving rise to the probabilities:

$$\begin{aligned}|c_1(t)|^2 &= \cos^2(\Omega_R t/2),\\ |c_2(t)|^2 &= \sin^2(\Omega_R t/2).\end{aligned} \tag{6.8}$$

If the system under consideration now possesses three levels, arranged in a Λ scheme (Figure 6.6), and is initially in the following state:

$$|\psi(t=0)\rangle = c_1|g_1\rangle + c_2|g_2\rangle, \tag{6.9}$$

where c_i is the amplitude for the atom to be in g_i. Transitions from the ground states to the excited state can be driven by two laser fields with frequencies ω_1 and ω_2, each with a Rabi frequency as in equation (6.7).

Since the probability amplitude to absorb a photon from g_i is proportional to the Rabi frequency corresponding to that transition, the probability amplitude to have an absorption process from g_i to e is proportional to $c_i\Omega_i$. If c_1 and c_2 in (6.9) are such that:

$$c_1\Omega_1 + c_2\Omega_2 = 0, \tag{6.10}$$

the two absorption amplitudes interfere destructively and the atom cannot be excited [253].

Another way of describing this phenomenon, is to look again at the interaction Hamiltonian $\hat{V}$ in equation (6.2) in the dressed-state picture, considering the atom and the laser photons as a single system (atom+photons) [254]. The three states can now be written as:

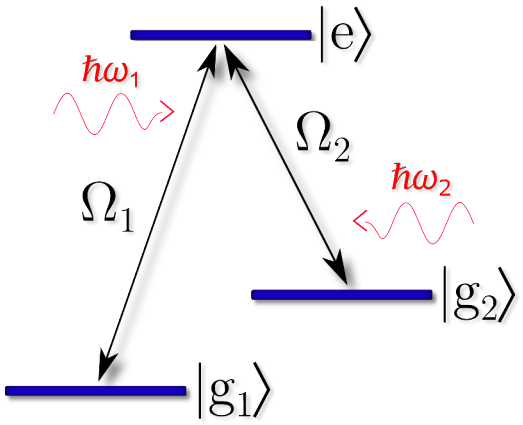

Fig. 6.6 **Three-level Λ system** with Rabi frequencies Ω_1 (pump) and Ω_2 (Stokes).

$$|e,N_1,N_2\rangle \ , \ |g_1,N_1+1,N_2\rangle \ , \ |g_2,N_1,N_2+1\rangle \ , \tag{6.11}$$

N_1 and N_2 being the number of photons with frequency ω_1 and ω_2 respectively. The matrix elements of the perturbation $\hat{V}$ are then:

$$\begin{aligned} \langle e,N_1,N_2|V|g_1,N_1+1,N_2\rangle &= \frac{\Omega_1}{2}; \\ \langle e,N_1,N_2|V|g_2,N_1,N_2+1\rangle &= \frac{\Omega_2}{2}. \end{aligned} \tag{6.12}$$

If the Raman condition is satisfied, i.e if:

$$\hbar(\omega_1-\omega_2) = E(g_2) - E(g_1), \tag{6.13}$$

the two levels $|g_1,N_1+1,N_2\rangle$ and $|g_2,N_1,N_2+1\rangle$ have the same energy, their separation being $E(g_2)$ - $E(g_1)$ + $\hbar(\omega_2-\omega_1)$.

The two orthogonal linear combinations of these two states are:

$$\begin{aligned} |G\rangle &= \frac{\Omega_1}{\Omega}|g_1,N_1+1,N_2\rangle + \frac{\Omega_2}{\Omega}|g_2,N_1,N_2+1\rangle; \\ |G'\rangle &= \frac{\Omega_2}{\Omega}|g_1,N_1+1,N_2\rangle - \frac{\Omega_1}{\Omega}|g_2,N_1,N_2+1\rangle, \end{aligned} \tag{6.14}$$

where

$$\Omega = \sqrt{\Omega_1^2+\Omega_2^2}. \tag{6.15}$$

From equation (6.12) and equation (6.14), it comes that:

$$\langle e,N_1,N_2|V|G\rangle = \frac{\Omega}{2}; \qquad \langle e,N_1,N_2|V|G'\rangle = 0. \tag{6.16}$$

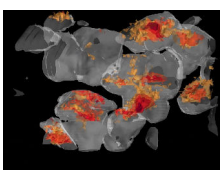

The state $|G'\rangle$ is then decoupled from the excited state $|e,N_1,N_2\rangle$. When the atom is in this state, there is no fluorescence any more: it is in a dark state. The state $|G\rangle$ is called a 'dressed state', and we shall further explore this when introducing Stimulated Raman adiabatic passage (STIRAP) in Section 6.4.1.

6.3.2 Coherent Population Trapping in ^{29}Si

In order to explore the spin states, we place the sample in a magnetic field to lift the spin degeneracy (Zeeman effect). We use a dry closed-cycle cryostat cooled down to 4K (attocube AttoDRY) equipped with a superconducting magnet allowing us to apply a field up to 9T. The light coming from a non-resonant continuous-wave (CW) 660nm laser and two resonant tunable laser diodes (Toptica DL, CW 737nm, 1kHz bandwidth) is coupled to a fibre and carried to the sample through a confocal microscope. Piezoelectric stages in the three directions of space are used to align the microscope on a single centre, with the help of a spectrometer and a CCD camera. The photons emitted by the SiV^- are collected through a 0.65NA lens and detected by an avalanche photodiode (APD).

The strategy for a better light collection efficiency was to use solid immersion lenses (SIL) [250] (Figure 6.4 **a**)). We identified individual SiV^- centers in the vicinity of the SIL arrays on an <111>-HPHT (High-Pressure, High-Temperature grown) diamond. For these colour centres we first measured the splitting between the transitions while increasing the magnetic field to characterise their coupling to strain and the parameters of the Hamiltonian 6.1. Figures 6.8, 6.9 and 6.10 show the magnetic field dependency for the ground and excited states of three different centres (measurement and simulations). The first one (Figure 6.8) is perfectly fitted using parameters for an unstrained SiV^- center, hence it is a good case study for unstrained nuclear spin coupling. The avoided crossing is happening at 1.5T. The second one (Figure 6.9) appears to be strained. The uni-axial strain model yields a ground state splitting of 61 GHz, i.e. roughly 17 GHz additional splitting from the strain interaction. Finally, the third one exhibits an unusual splitting revealing that it may have a not uni-axial strained environment (Figure 6.10). The resulting level splitting shows that the ground states are split by approximately 48 GHz, about 4 GHz more than usual.

The spin orientation for the different energy levels of the SiV^- depends on the angle between the centre's axis and the magnetic field. The transverse field components lead to a finite spin overlap for all ground and excited states, resulting in additional optical transitions. Because of this mixing, we are able to drive resonantly the transitions from both Zeeman sublevels of an orbital level to the same excited state (for example, the transitions C_1 and C_2 in Figure 6.8). On the spectra in Figure 6.2 **a)** and **b)**, measured on the unstrained SiV^-

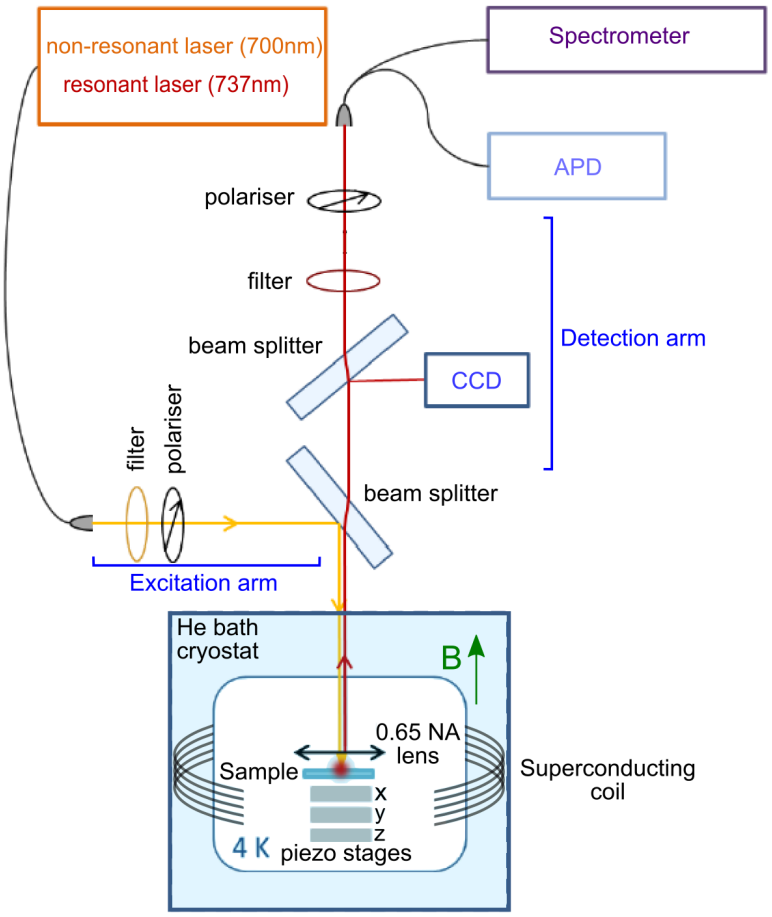

Fig. 6.7 **Optical setup for the CPT experiment** (courtesy of C. Hepp and B. Pingault).

of Figure 6.8, a hyperfine structure due to the coupling between the electron and nuclear spin (both one-half) is clearly visible: each of the eight sublevels splits into two with the presence of a magnetic field, one associated with a nuclear spin up and the other one with a nuclear spin down. This extra-splitting is thought to be responsible for the presence of the two CPT dips, corresponding to nuclear spin projection measured via electron-nuclear hyperfine coupling mechanism (Figure 6.11).

We then explored the magnetic field dependency of the hyperfine splitting, on a single emitter, at 3.5K. We measured CPT spectra for different magnetic fields with a step of 0.5T near the avoided crossing. We did so for two transitions: D1-D2 before the avoided crossing and D1-D3 after it (Figure 6.8). By sweeping the magnetic field over the region of the avoided crossing, we relax the spin-state orthogonality in order to decouple the spin-spin interaction from the spin-orbit coupling (responsible for the state-mixing) and study the effect of the spin-spin interaction on the CPT. As the magnetic field is varied over the avoided

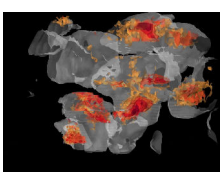

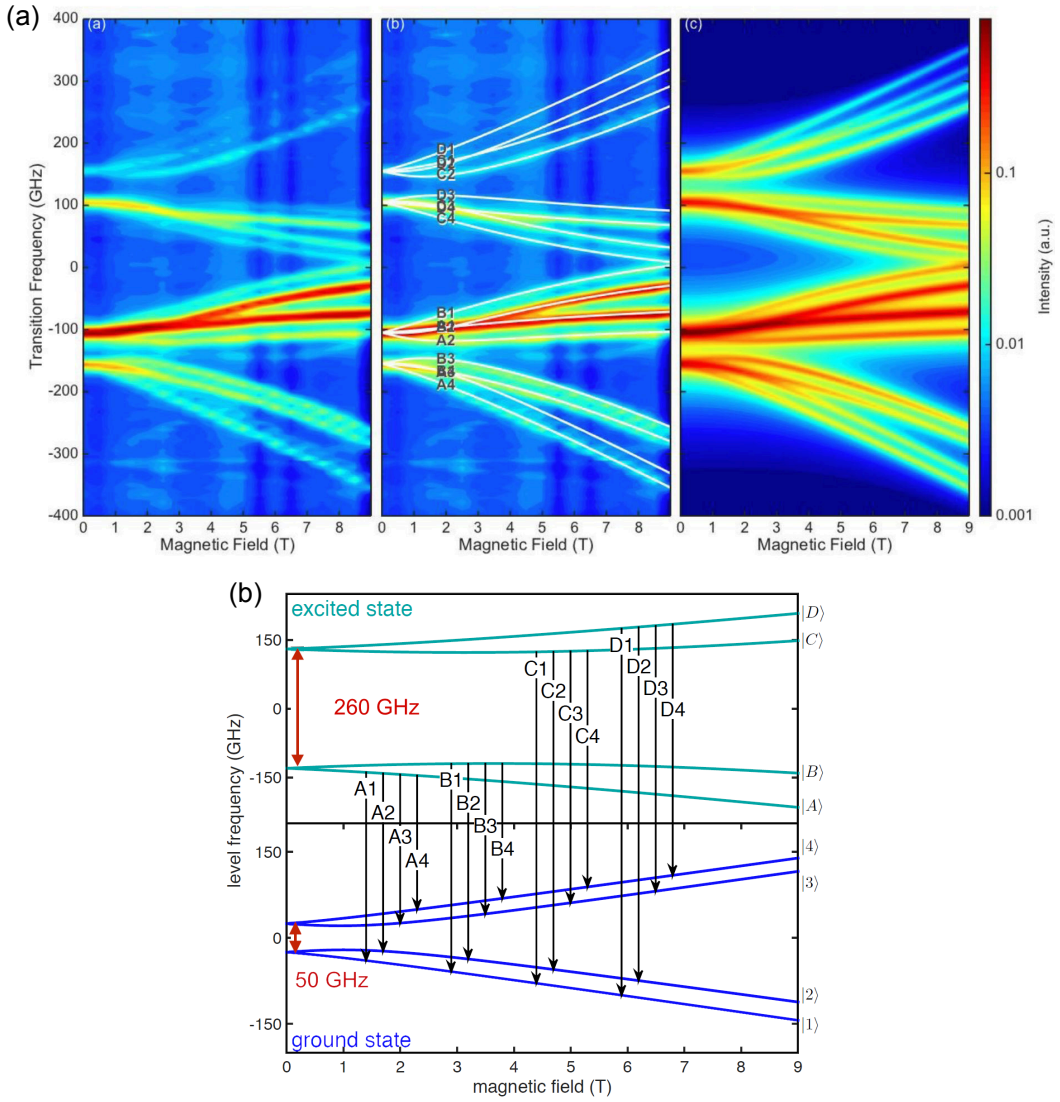

Fig. 6.8 **Unstrained emitter, B-Field map.** **(a)** Experimental data and comparison with simulations. **(b)** Simulated allowed transitions.

crossing. From 0 to 1.5T, the dark state is generated between states D1 and D2, while above 1.5T, the dark state is generated between D1 and D3. The results show a very clear narrowing of the hyperfine splitting around the avoided crossing (Figure 6.12). At the time, our model was not able to simulate this result, and our efforts were directed towards the understanding of this figure.

The width of each CPT dip is proportional to the decoherence rate between the two driven states, on top of a constant power broadening due to the lasers [255]: The longest spin coherence time so far reported, identified as the free induction decay time T_2^*, is 115ns at a temperature of 3.6K[238]. Going back to quantum computing, the memory of the computer

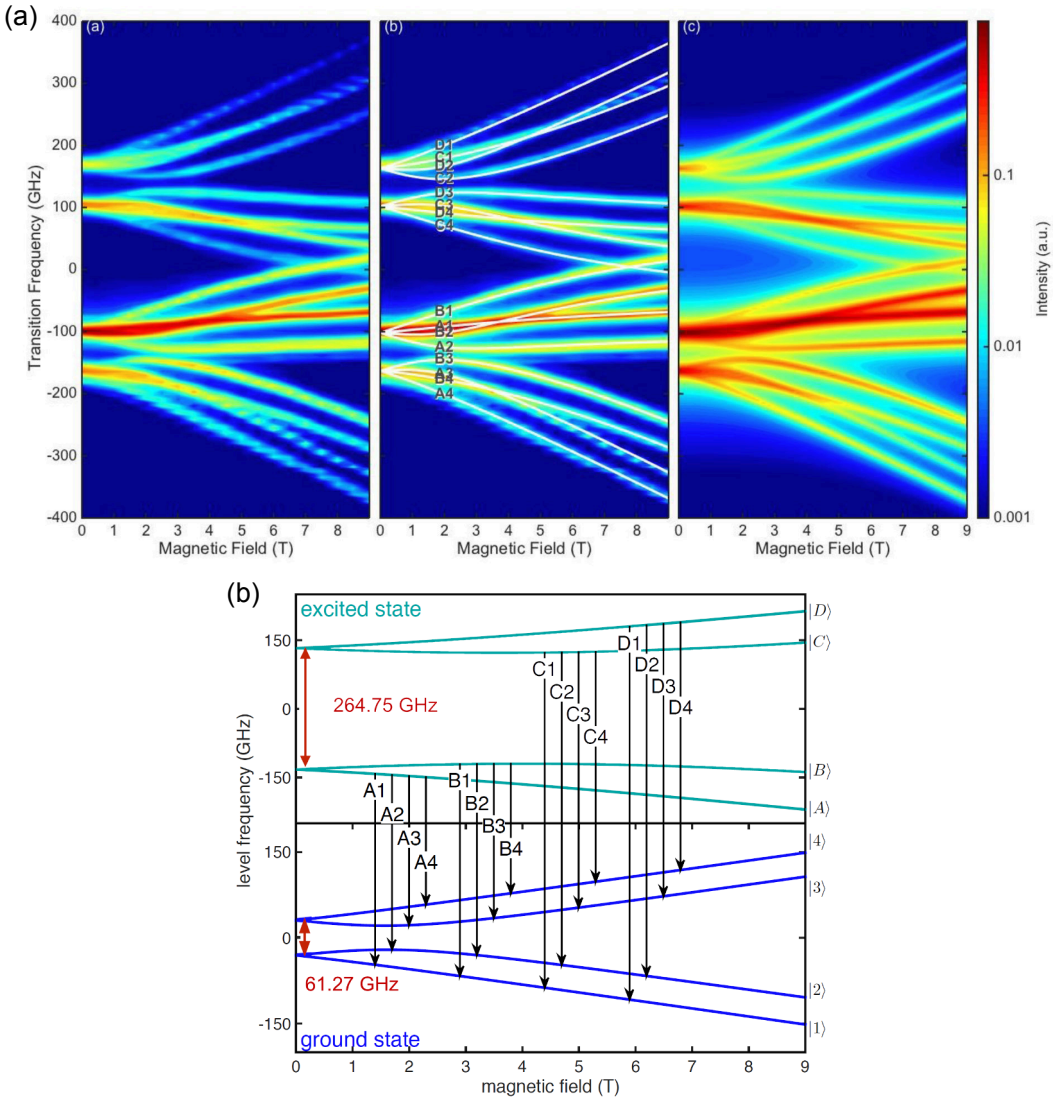

Fig. 6.9 **Uni-axially strained emitter, B-Field map. (a)** Experimental data and comparison with simulations. **(b)** Simulated allowed transitions.

is then limited by the qubit lifetime. The processes behind this decoherence have been associated with a first-order electron-phonon process [76]. Experimental results studying the temperature dependency of the CPT dip corroborated this hypothesis [67].

Besides lowering the temperature to a few millikelvin, which would prevent any phonon-coupling, other options are available to improve this quantum memory (or register). One is to transfer the qubit coded by the electron-spin to another system with a longer coherence time. The most suitable medium for that purpose is the nuclear spins because of their longer coherence time [206, 256, 203]. Both the $^{29}SiV^{-}$'s nuclear spin and the ambient ^{13}C spins were to be investigated for the long-term goal of inherent quantum memory systems. In

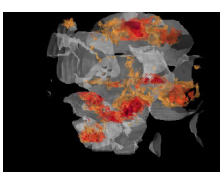

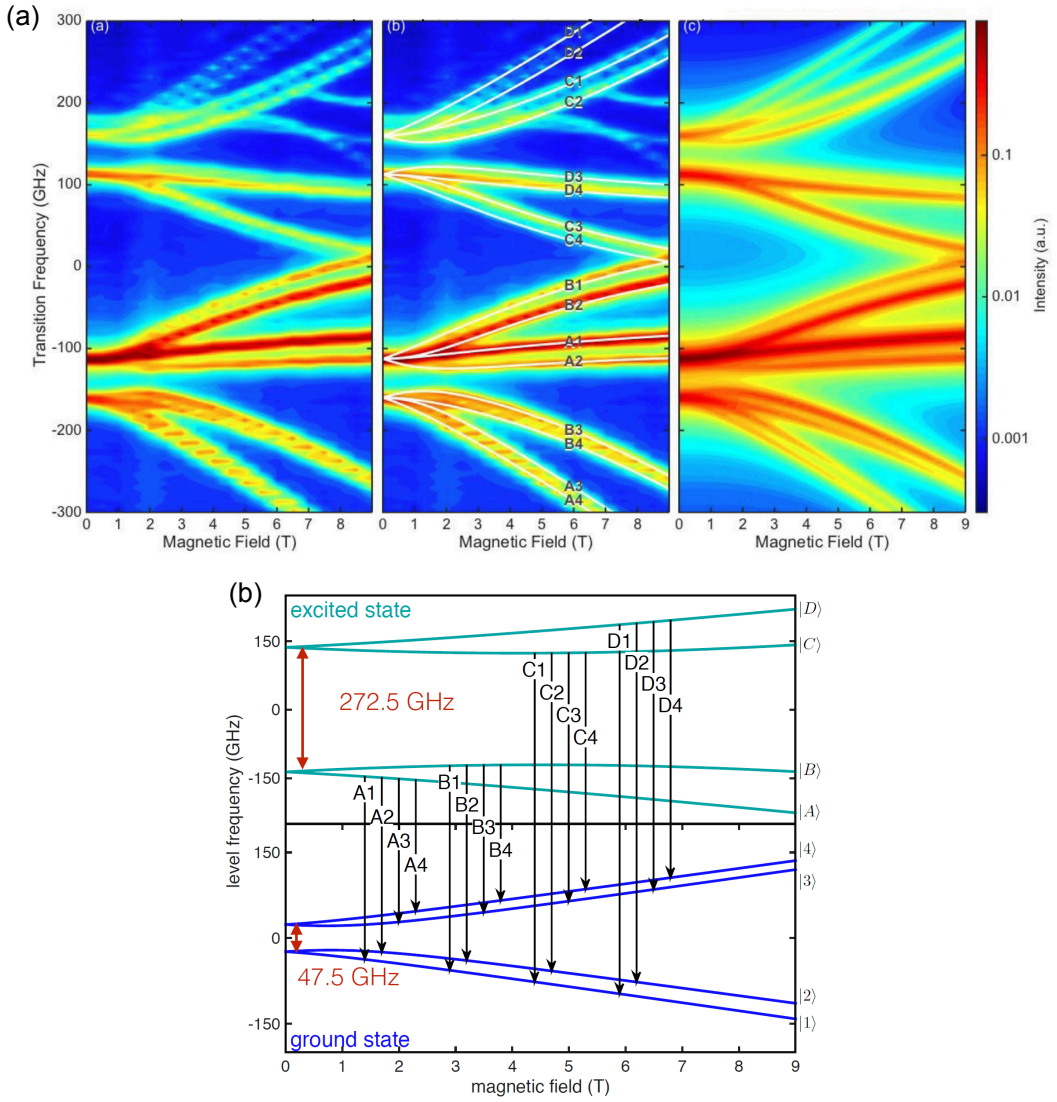

Fig. 6.10 **Not Uni-axially strained emitter, B-Field map. (a)** Experimental data and comparison with simulations. **(b)** Simulated allowed transitions.

$^{29}SiV^-$s, the degeneracies associated with nuclear spins are lifted by the hyperfine interaction [77, 66], enabling a selective addressing of nuclear spin states by external microwave or radio-frequency fields as for NV centres [257]. The successful demonstration of quantum-state transfer via electron-nuclear hyperfine coupling in $^{29}SiV^-$s would allow SiV^- centres to have their own long-term information storage.

We tried to observe nuclear spin jumps on emitters which were initially very stable. To do so, we tuned both lasers to match the CPT conditions and measured a time trace of the photon counts using short measurement intervals (5-50 ms). When the nuclear spin flips from one projection to the other, then we should periodically lose the CPT conditions and

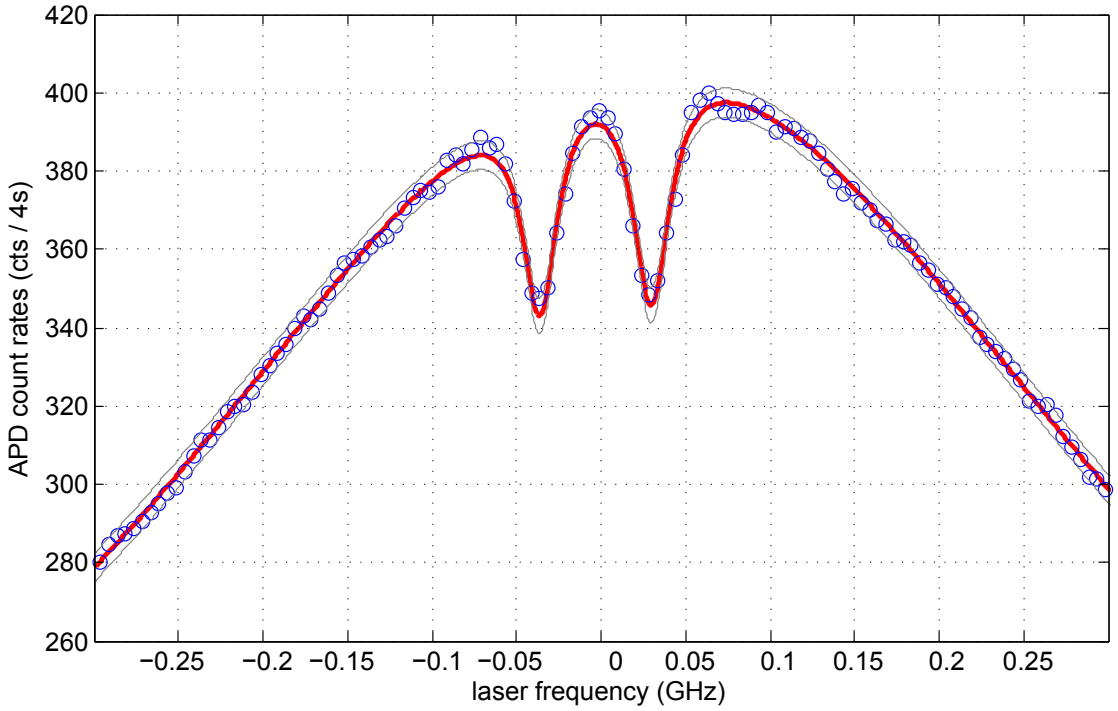

Fig. 6.11 **Coherent population trapping on a single unstrained ^{29}Si SiV$^-$ centre at 8 Tesla using transitions D_1 and D_3.** The two dips in the fluorescence are the signature of the electron-nuclear hyperfine coupling, and constitute a coherent superposition state that could be used as a qubit.

see the count rate drop and increase. We expected a telegraph noise signal, similar to the one observed in the NV single shot readout [258]. However, a few problems arose during the measurement. The measured photon count rate requires to be sufficiently large to avoid being limited by the shot noise. If we have 3000 counts per second, then we have 150 counts per 50 ms, and the signal-to-shot-noise ratio will be $\sqrt{150} \approx 12$ counts during this measurement interval. The CPT contrast is usually less than 30% (measured as depth of the dip over height of the underlying peak). In our example, we would hence be comparing a drop/increase of about 45 counts to the noise. Spectral diffusion adds to the shot noise, thus we would need to stabilise the emitter strongly against spectral diffusion. We tried to observe these nuclear jumps. The count rates which we observed for some emitters would be sufficient, but could so far not suppress the spectral diffusion sufficiently even with the use of a non-resonant 830nm laser during the measurement.

Another pathway towards a longer coherence time is to explore the effects of strain on the ground state splitting, and see if that can be used as a means to decouple the transitions from the main phonon modes in the crystal. On the same sample as the one described so far, we looked for emitters showing evidence of strain. However, all these exhibited again

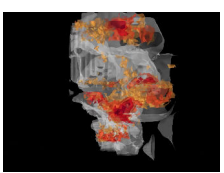

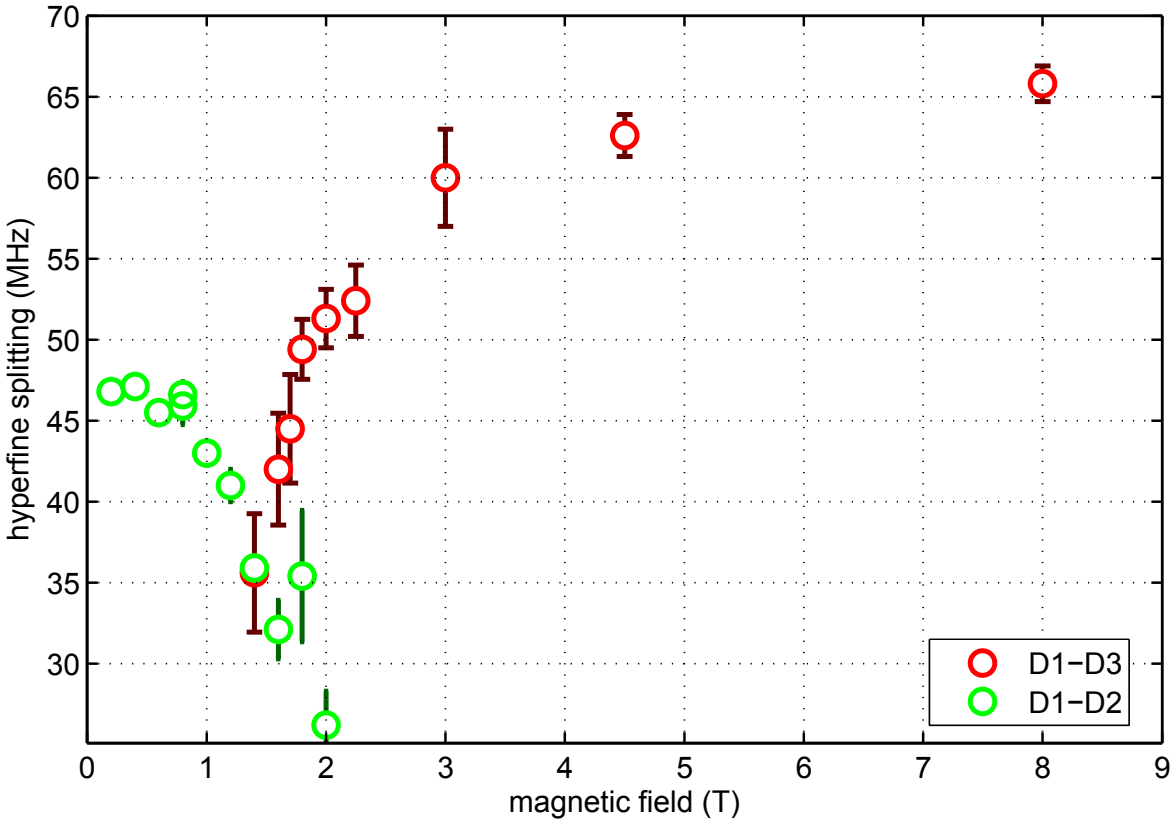

Fig. 6.12 **Hyperfine splitting for an unstrained emitter with increasing magnetic field.** Using the transitions D_1 and $D_2(D_3)$ before(after) the avoided crossing. Clear minimum around the avoided crossing (1.5T).

very strong spectral diffusion making CPT hard if not impossible to obtain, and lowering considerably the precision on the estimation of the dip's width. As an example, the graph on Figure 6.13 shows the spectra recorded on the strained emitter characterised earlier in Figure 6.9. These are CPT scans at a magnetic field of 0.8T between the transitions C_1 and C_2, with an integration time of one second per frequency step and powers below saturation (45nW on C_1 and 500nW on C_2). The non-resonant 830nm laser was on for the whole measurement. Another non-resonant laser at 660nm was added after about 20 scans, which made the spectral diffusion even worse.

We had the pleasure to collaborate with Marko Lončar's Nanophotonics group at Harvard, and more specifically with two PhD students: Srujan Meesala and Young-Ik Sohn whose expertise lies in the design and fabrication of diamond micro and nano photonic structures. They designed and fabricated electrically actuated diamond micro-cantilevers on chip, on which they implanted ^{28}Si atoms with a great spatial precision. Applying voltage to these devices creates an electric field strong enough to bend them, and therefore tune the strain

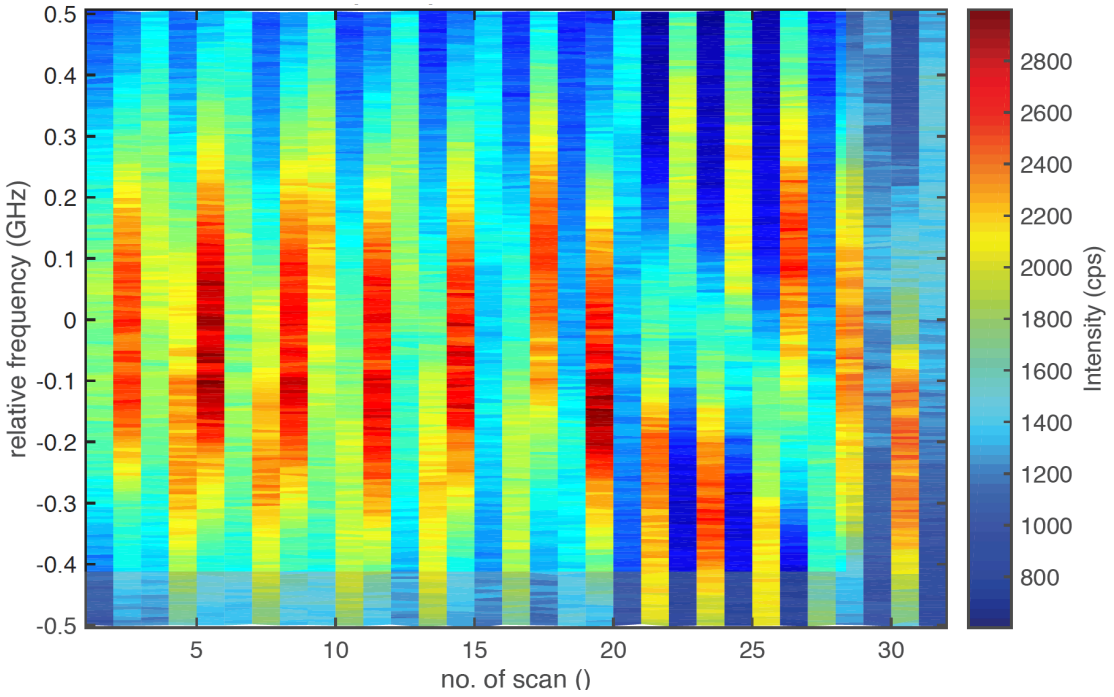

Fig. 6.13 **Example of spectral diffusion** observed on a strained emitter. Each column is a CPT scan. The transition moves clearly from one scan to the next, making CPT almost impossible to achieve.

applied to the SiV^-s. With their presence and their help, here in Cambridge, we measured CPT with strain-tuning, on single emitters.

6.3.3 Electrically controlled strain tuning: electron spin-phonon decoupling and effects on the ground state coherence.

The fast decoherence of the SiV^- ground state has been attributed to a first order electron-phonon process [76]. The detuning of the SiV^- transitions from the main phonon modes of the surrounding crystal should then, according to this model, reduce the rate of electron-phonon interactions and thereby increase the coherence time. The upwards transition rate, which is the product of the phonon density of state (with an energy corresponding to the ground state splitting) and the Bose-Einstein probability distribution function [259], should have the same dependency on the strain than the ground state coherence time of the SiV^-. For transitions B and D, the upwards transition rate calculated in this way as a function of the ground state splitting is shown in Figure 6.16 **a**).

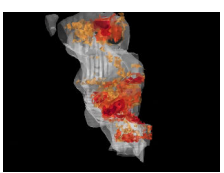

Strain induces local deformations of the lattice that break the symmetry at the vicinity of an emitter. The effect of uni-axial strain on the degeneracy of orbital states on single centres can be discussed using group theory [260]. The full treatment specific to SiV^- can be found in C. Hepp's PhD thesis [65], and predicts that the ground state splitting as well as the excited state and the centre-of-mass splitting depend on the applied axial strain. Measurement done on the cantilevers described earlier and shown in Figure 6.14 have proven that dependency. The shift in wavelength of the fluorescence from the four transitions (A, B, C, D at zero magnetic field) as a function of applied voltage (and therefore strain) and centre-of-mass (COM) splitting is shown in Figure 6.15.

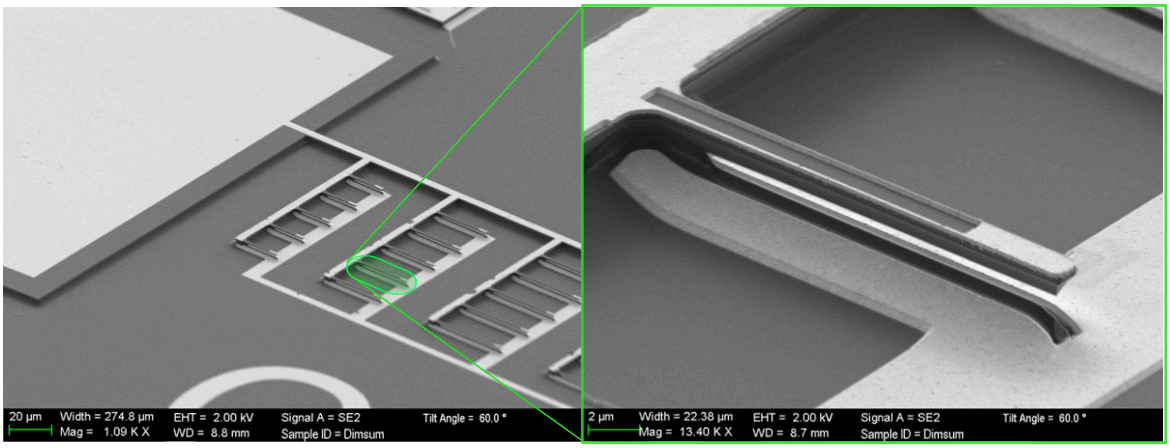

Fig. 6.14 **Scanning electron microscope (SEM) image of an electrically actuated strain tuning device using diamond micro-cantilevers.** (courtesy of Srujan Meesala and Young-Ik Sohn). Light colour: gold electrodes. Dark colour: diamond.

CPT measurements were then carried on a single emitter. In the setup, only one of the two 737nm resonant lasers was used, in conjunction with a Mach-Zehnder electro-optic modulator (amplitude modulation EOM). This choice was made in order to eliminate the relative phase noise between the two sources from the measurement [261], and increase the precision in the determination of the CPT dip width. The carrier was tuned in resonance with C_1 while the side-band was scanned across the C_2 transition. The radio-frequency (RF) power sent to the EOM sets the amplitude of the side-band. Preliminary results are shown in Figure 6.16 **b**). The visible decrease of the CPT linewidth with the increase of strain is encouraging and promising as it seems to follow the same trend as the theory curve. It is believed that the SiV^- studied was naturally pre-strained, hence we are measuring only on the right side of the peak shown in **a**).

These preliminary results that I contributed to are the proof of principle that a device-oriented approach can successfully lead to an improvement of the coherence time. These

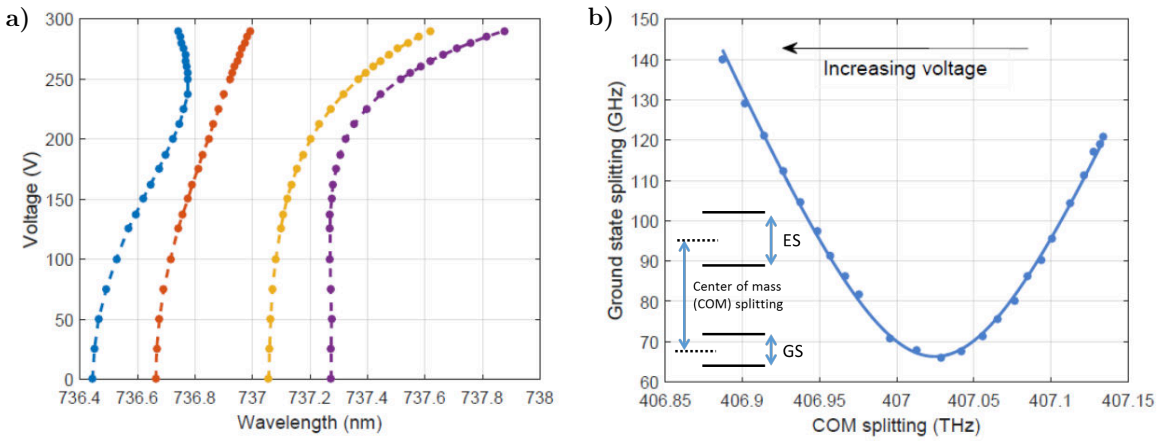

Fig. 6.15 **Strain dependency of the ground state, excited state and centre-of-mass splitting.** (courtesy of S. Meesala and Y.-I. Sohn). **a**) The position of the transitions A (blue), B (red), C (orange) and D (purple) were monitored as the voltage was increased. **b**) Ground state splitting as a function of the COM splitting, extracted from the measurement in **a**).

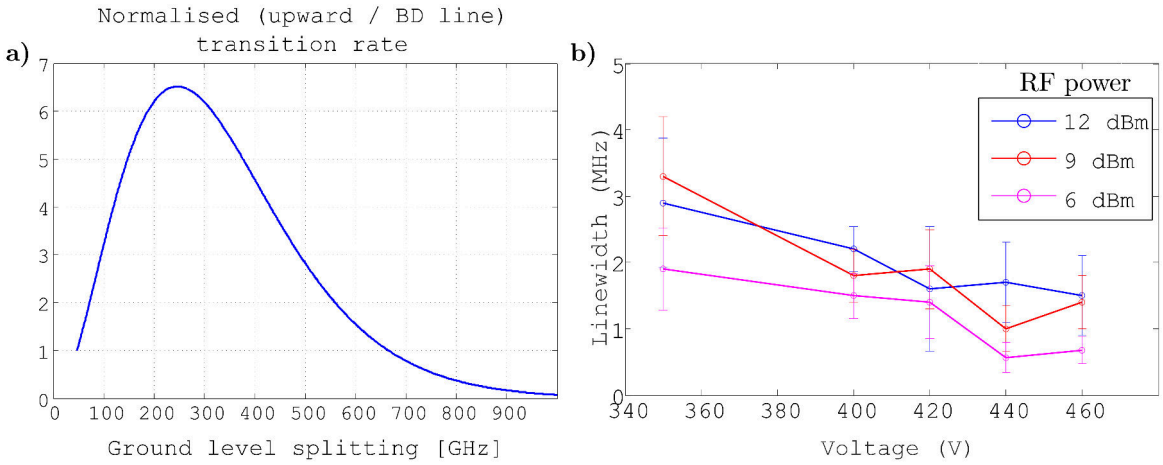

Fig. 6.16 **Effects of strain on the CPT linewidth** (data from Srujan Meesala and Young-Ik Sohn). **a**) Phonon-induced upwards transition rate as a function of the ground state splitting (simulation on the B and D lines). **b**) Preliminary results using C_1 and C_2 transitions for different C_2 driving powers showing a decrease in the CPT linewidth.

experiments were repeated and complemented over a longer period of time The full results which were later published [78, 79] show strong coupling between the silicon-vacancy spin and single phonons, which can lead to the realisation of phonon-mediated quantum gates and nonlinear quantum phononics. However, it requires the use of advanced fabrication techniques (clean room) and a lot of research and development will be needed until good reproducibility can be achieved. Another route would be to develop the ability to perform operations on the spin faster than the decoherence timescale: dynamical decoupling and

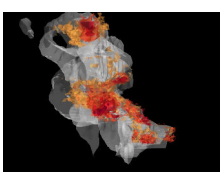

ultrafast optical control. This became my main focus for a few months, and will be detailed throughout the following section.

6.4 A route to the ultrafast optical control of the SiV$^-$ spin

6.4.1 Motivation and proposed experiments

SiV$^-$ centres show encouraging optical properties and are therefore good candidates for quantum computing and simulations. In 2000, DiVincenzo defined a set of requirements for the physical implementation of quantum computation [80], referred to as the "DiVincenzo criteria", and are: 1) a scalable physical system with well-characterized quantum bits (qubits), 2) the ability to initialise qubits, 3) long coherence times compared to gate times, 4) a universal set of quantum gates, and 5) the ability to measure the final state. More recently, some of the requirements have been revised for a more general system [69, 262]. A gate, in the DiVincenzo criteria, is a unitary operation that moves the qubit from one superposition state to another. The achievement of coherent population trapping constituted the proof that quantum superposition states, and therefore quantum bits, can be created and measured using the electron spin of the colour-centre. Because quantum computing requires the ability to perform operations on such bits, which can be described as quantum logic gates, the next natural step for us is to realise the coherent control of the spin. This two-level system can be represented as a vector in the Bloch Sphere: a unit sphere where a vector starting at the origin and pointing to the north or south poles represent a basis state of the qubit. A vector pointing to any other position on the surface is a superposition state ψ (Figure 6.18) defined in that basis as:

$$\psi = \cos\left(\frac{\theta}{2}\right)|1\rangle + e^{i\phi}\sin\left(\frac{\theta}{2}\right)|2\rangle \tag{6.17}$$

In this picture, a gate is represented as a rotation or series of rotations of the vector about one or several arbitrary axes. Such gates have been implemented in various two-level systems [263, 69]. Since the first demonstration of a fundamental quantum logic gate in the internal and external degrees of freedom of a single trapped atom [264], implementations have been realised using optical modes of photons[265, 266], hyperfine atomic states in neutral atoms[267, 268] or ions[269–272], ultracold molecules[273] spin states in semiconductors[274–277], quantisation of charge[278], flux, or phase in superconducting Josephson junctions[279]. Milestones towards a large-scale ion-trap quantum computer have also been achieved[280].

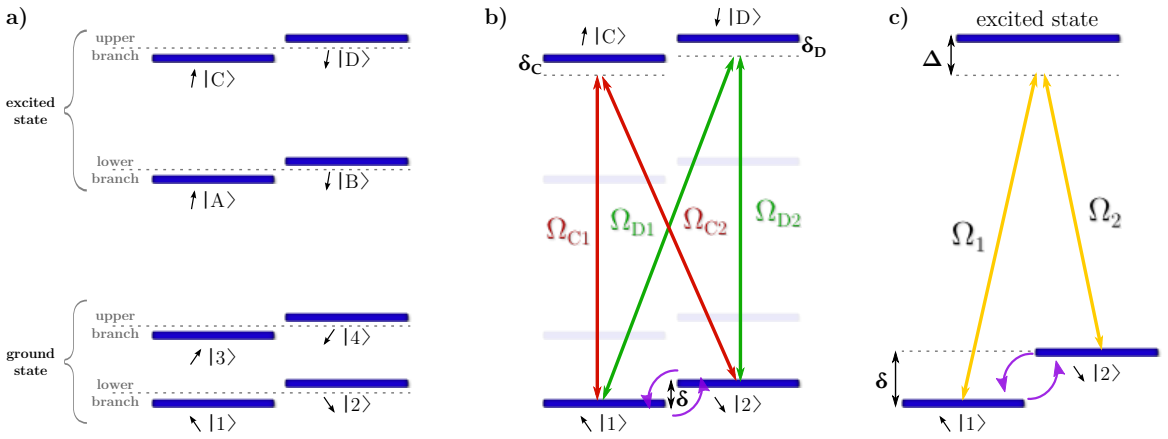

Fig. 6.17 **Lambda systems within the SiV$^-$ electronic structure. a**) Splitting of the ground and excited states in a magnetic field. **b**) Two Λ systems between the lowest ground state and highest excited states that can be used for ODROs and STIRAP. These transitions have been reported as the brightest for the SiV$^-$ [66]. **c**) Detuned Raman scheme for ultrafast transfer of spin population.

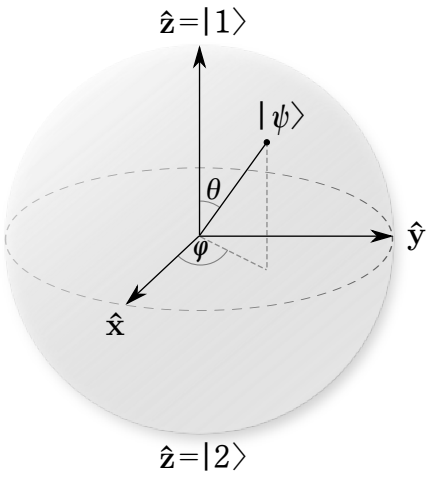

Fig. 6.18 **Bloch sphere.** Representation of the pure state $|\psi\rangle$ space of a two-level system (qubit). Here $|1\rangle$ and $|2\rangle$ represent the two spin states of the SiV$^-$ as in Figure 6.17.

The first goal for SiV$^-$ would be to achieve optical control of the spin and the ability to transfer the population from one spin state to the other. The presence of a magnetic field, and more precisely transverse magnetic field components, leads to a finite spin overlap for all ground and excited states, resulting in additional optical transitions (Figure 6.17 **a**). Because of this mixing, it is possible to form three-level lambda systems within the SiV$^-$ electronic structure, as depicted in Figure 6.17 **b**). A modest dipole detuning, indicated in the figure by δ_1 and δ_2, protects the optical spin control from radiative decay of the excited states.

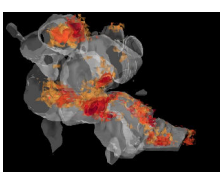

Transfer of population can hence be done via the excited state. This intuitive solution has however two main disadvantages: one has to wait for the electron to relax from the excited state to the ground state, and in some cases this relaxation occurs along a non-radiative path, for example via vibronic states [67, 77, 65]. Starting from CPT, it is possible to use the dark state as a platform to realise the inversion of population adiabatically, avoiding the excited state. This method is called "stimulated Raman adiabatic passage" (STIRAP) and will be described in Section 6.4.1. Optical spin control can also take place via optically driven Rabi oscillations (ODROs).

Optically driven Rabi oscillations (ODROs)

As explained earlier in Section 6.3.1, in a two-level system the population in each state depends on the Rabi frequency associated with the transition (equations 6.8), which itself is proportional to the amplitude of the electric field and therefore the intensity of the light used to drive the transition. It can be shown that in the limit that two simultaneous, Raman-resonant optical fields coupling to the two dipole transitions in the Λ system are sufficiently detuned from the respective dipole transitions, the excited state dynamics can adiabatically follow the incident optical fields as well as the dynamics of the two spin states. In this limit, the Λ systems in Figure 6.17 **b**) can be reduced to a two-level spin system, with the effective Rabi frequency for the optically driven spin transition given by [281]:

$$\Omega_R = \frac{\Omega_{X1}\Omega_{X2}}{2|\delta_X|}, \tag{6.18}$$

where Ω_{X1} and Ω_{X2} are the Rabi frequencies for the respective dipole optical transitions (the subscript X corresponds to the chosen excited state) and δ_X is the average detuning of the optical fields from the respective dipole transitions. A slightly-detuned (red-shifted) optical pulse can then be used to manipulate the population of the two ground states (the measurement sequence is depicted in Figure 6.19), which should oscillate as the excitation power is swept. Depending on the polarisation selection rules of the spin states, it may be that two pulses of two different polarisations are needed, each addressing one transition. In our case, the polarisation selection rules applicable to the orbital states were predicted, calculated and measured [77], but not the ones affecting the spin. This is therefore something that we can now explore.

Flipping the spin corresponds to a rotation with an angle $\theta = \pi$ on the Bloch sphere, from one pole to the opposite one. Therefore, an ODRO pulse of just the right power to flip the spin is called a π pulse. The spin-lattice relaxation time, T_1, can also be measured by applying a π pulse and measuring the population of the upper state with different waiting

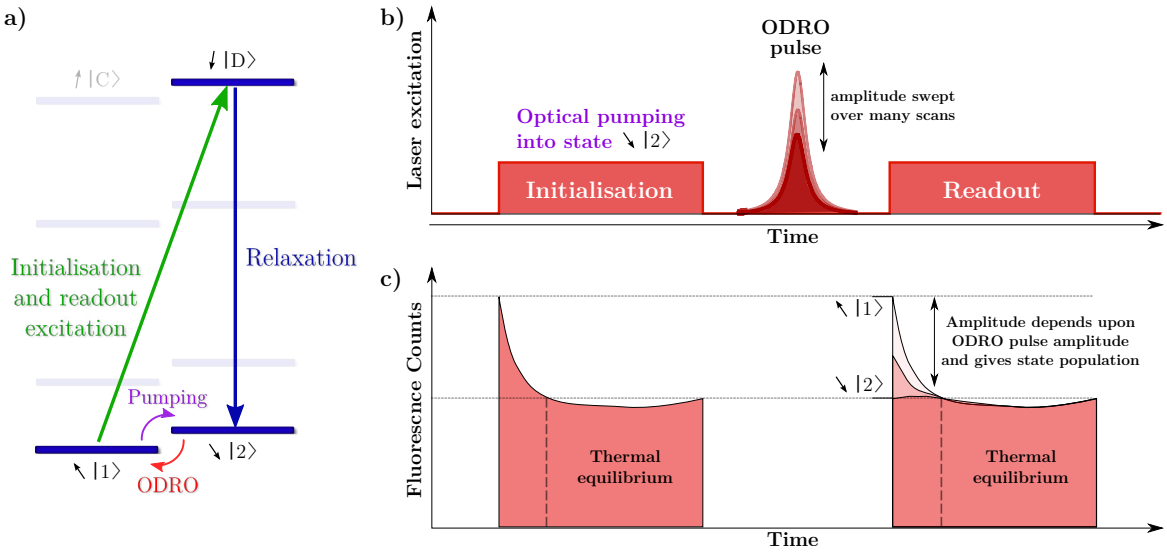

Fig. 6.19 **Optically driven Rabi oscillations measurement sequence.** **a**) Initialisation: optical pumping into state $|2\rangle$. When the amplitude of the ODRO pulse is right, the population is flipped back into $|1\rangle$. Readout: same pulse as for initialisation. **b**) Pulse sequence for ODRO. The amplitude of the ODRO pulse is swept during the measurement. **c**) After long integration, the height of the fluorescence leading-edge depends upon the population.

times, until it decays. Another type of experiment uses projections to and from the equatorial plane of the Bloch sphere, or $\pi/2$ pulses, to study the spin free precession and coherence time: Ramsey interferometry.

Ramsey interferometry and spin precession measurement

Developed in 1949 by Norman Ramsey [282], this technique was used by Serge Haroche and David J. Wineland for their experiments in cavity quantum electrodynamics (QED) in which they used microwave-frequency photons to verify the quantum description of electromagnetic fields and for which they got the Nobel Prize in 2012 [283]. The measurement procedure consists in applying two phase coherent $\pi/2$ pulses separated by a delay Δt, during which the spin precesses freely in the equatorial plane of the Bloch sphere. If the delay between the pulses is an integer multiple of the spin precession time, the probability of measuring the system in the same state as the initial state is maximum. It is minimum for half a period. As the delay gradually increases, oscillations (or fringes) will build up. After a number of revolutions around the Bloch sphere, the spin will start to be affected by dephasing processes, and the oscillations will be increasingly damped after each period. The envelope of the oscillations gives the spin-spin relaxation time T_2. Ramsey interferometry was realised on SiV$^-$ centres using microwaves[238].

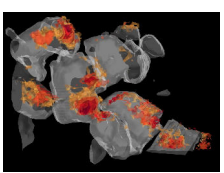

Stimulated Raman adiabatic passage (STIRAP)

Described and observed for the first time in 1990 [284], the STIRAP concept has been successfully applied in many different fields of physics, chemistry, and beyond [285]. It was successfully applied to NV centres [286] and at a similar occasion compared with ODROs [287]. Considering the system depicted in Figure 6.17 **b**), two resonant CW beams satisfying the CPT conditions with either excited state will drive the electron into a coherent superposition of the two spin states. Let us now consider the case where the two beams are not continuous, but pulsed. The STIRAP process involves coherent excitation in a three-state chain, $|1\rangle$-$|e\rangle$-$|2\rangle$ induced by two pulsed fields, **P** with carrier frequency ω_P linking states $|1\rangle$ (ground) and $|e\rangle$ (excited), and **S** with carrier frequency ω_S linking states $|2\rangle$ (ground) and $|e\rangle$ (Figure 6.20 **a**). If the population is initially prepared in $|1\rangle$, then a pulse **S** will not trigger any excitation. But if during that pulse some light resonant with the second transition ($|1\rangle$-$|e\rangle$) is sent to the system, the latter will be brought to a coherent superposition state (CPT conditions). If that light remains on as the pulse **S** ends, the final situation is the opposite of the one we started with and the population has been transferred to $|2\rangle$. In other words, if two pulses **S** and **P** are sent consecutively to the system with a small enough delay (delay and amplitude conditions can be calculated [288]) such that they overlap (Figure 6.20 **b**), they realise an adiabatic passage of the population from $|1\rangle$ to $|2\rangle$ via the dark state. If STIRAP is properly implemented the population in $|e\rangle$ remains negligible and thus no loss occurs by spontaneous emission (Figure 6.20 textbfc).

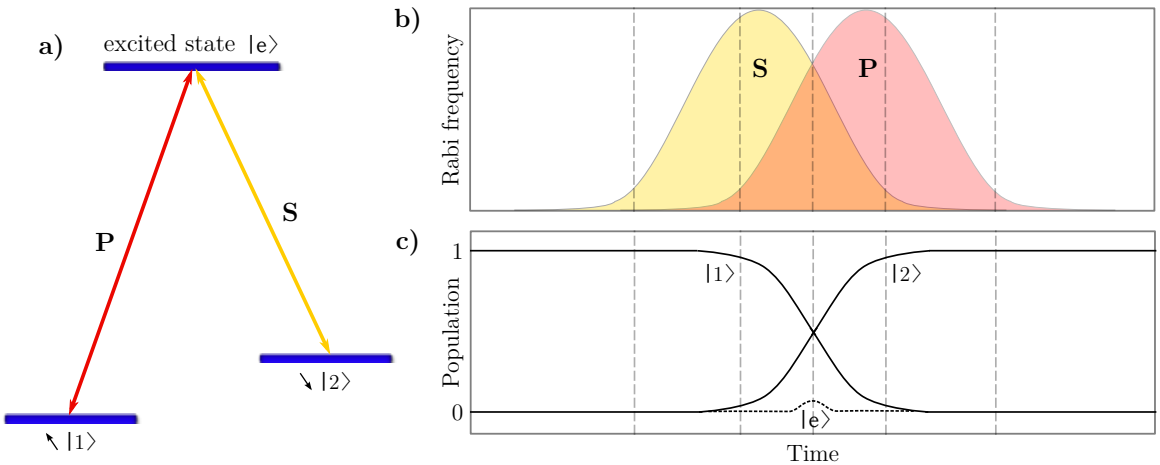

Fig. 6.20 **Stimulated Raman adiabatic passage (STIRAP) in a Λ system (adapted from [285]).** **a**) Three-level system with Rabi frequencies **S** and **P**. **b**) Pulse sequence used for STIRAP. **c**) Adiabatic transfer of population between the two ground states via the dark state.

The main advantage of STIRAP over ODROs is that the former is immune to the spectral diffusion as long as the adiabatic condition is satisfied. So far, all optical manipulations state

acted on the angle θ (Figure 6.18). In order to achieve full optical control (in group theory also referred as SU(2) control) of the spin and cover the entire Bloch sphere, rotations around the $\hat{z}$ axis need to be made accessible. This can be done using very short and intense pulses of subresonant photons: ultrafast manipulations [289, 290, 277].

Ultrafast manipulation of electron spins

An explanation of rotations by ultrafast optical pulses is based on optical Stark shifts [291, 262, 292]. The Stark effect is the electric analogue of the Zeeman effect. As described earlier, the presence of an external magnetic field lifts the spin degeneracy of the SiV^-, and any transverse component to the magnetic field precesses with the Larmor frequency. If the pulse duration is short compared to the Larmor period, the mixing of states by the magnetic field can be ignored and the energy levels and optical selection rules can be approximated as the zero field case [262] (Figure 6.21 **a**)). Assuming that it is possible to tune the polarisation of the pulse so that it affects only one of the transitions (for SiV^- the polarisation selection rules on the transitions originating from the spin sublevels have not been characterised yet). If this pulse is red-detuned (Figure 6.17 **c**)), it will cause a blue shift of the transition, known as the optical Stark effect [293] (Figure 6.21 **b**)). The light creates an effective magnetic field pointing along its propagation direction [294], exerting a torque on the spin causing it to precess with a frequency dependent on the induced splitting. After the duration of the pulse, this effective splitting disappears and the phase accumulated in this basis is recognised as a spin rotation in the magnetic field basis [295, 296]. This effect was observed and used for ultrafast optical manipulation of single spins in quantum wells [297, 298] and quantum dots [277, 299, 300], ultrafast Ramsey interferometry was used recently to implement qubit gates with cold rubidium atoms [301]. Importantly, ultrafast Rabi and Ramsey experiments have been recently conducted on a single SiV^- centre [302], although on orbital levels only (not on spin states).

In order to perform a transfer of population, the ultrafast pulse has to be wide enough to excite the two transitions: it must be wider than the spacing δ corresponding to the splitting between the states $|1\rangle$ and $|2\rangle$ (Figure 6.22 **a**)). Assuming that the pulse is Fourier transform limited, and hence that its duration Δt is the shortest possible for its optical spectrum $\Delta\nu$, the time-bandwidth should be $\Delta t\Delta\nu \approx 0.315$ [303]. The value of this product depends on the pulse profile, and autocorrelation traces for Mira HP pulses suggest by their functional form that they are best described by a sech^2 (more than a Gaussian) [304]. The pulse bandwidth is therefore $\Delta\nu \approx 100$GHz. The splitting δ between the two spin manifolds of the SiV^- under consideration varies from a few GHz to about 50GHz depending on the strength of the applied magnetic field, which is always less than $\Delta\nu$. A single pulse will thus induce the desired

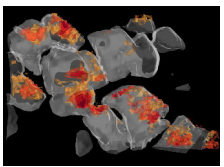

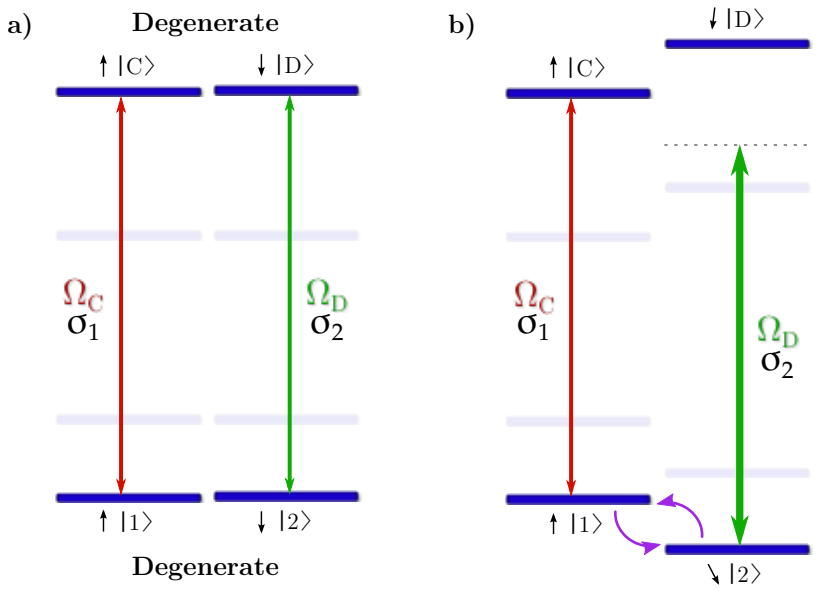

Fig. 6.21 **Optical Stark shift (adapted from [262]). a**) Electronic structure of the SiV$^-$ in the absence of magnetic field and before optical excitation, showing spin and polarisation selection rules. **b**) Blue-shifting of the transition during an ultrafast optical pulse which would couple to the D transition only (due to polarisation selection rules).

transitions. In fact, the direct measurement of the pulse spectral width on a spectrometer gives $\Delta\nu \approx 160$GHz (Figure 6.22 **b**)), which may indicate a small chirp probably due to self-phase modulation arising from the Kerr effect in the crystal. Also, the pulse arrival time determines the relative angle between the spin and rotation axis as the spin precesses about the magnetic field at the Larmor frequency and thus sets the total torque felt by the spin [262]. It is hence important to be able to finely delay the pulse in time.

6.4.2 The optical setup

In order to explore the physics just described and walk down that path towards full optical control of the SiV$^-$ spin, we prepared an ultrafast setup which will be described in details in this section. A picosecond Ti:Sapphire laser (76MHz) is used to generate the light that will serve for all experiments. Its output is split into two beams (one of which can be delayed), which can be used for example as pump and probe, respectively. In order to decrease and tune its repetition rate to accommodate different measurement sequences, acousto-optic modulators (AOM) were installed in the 'pump' and 'probe' optical paths which are controlled by a delay generator synchronised with the laser's output signal. An introduction to pulsed light sources and optical switches is given in Chapter 2.1.2).

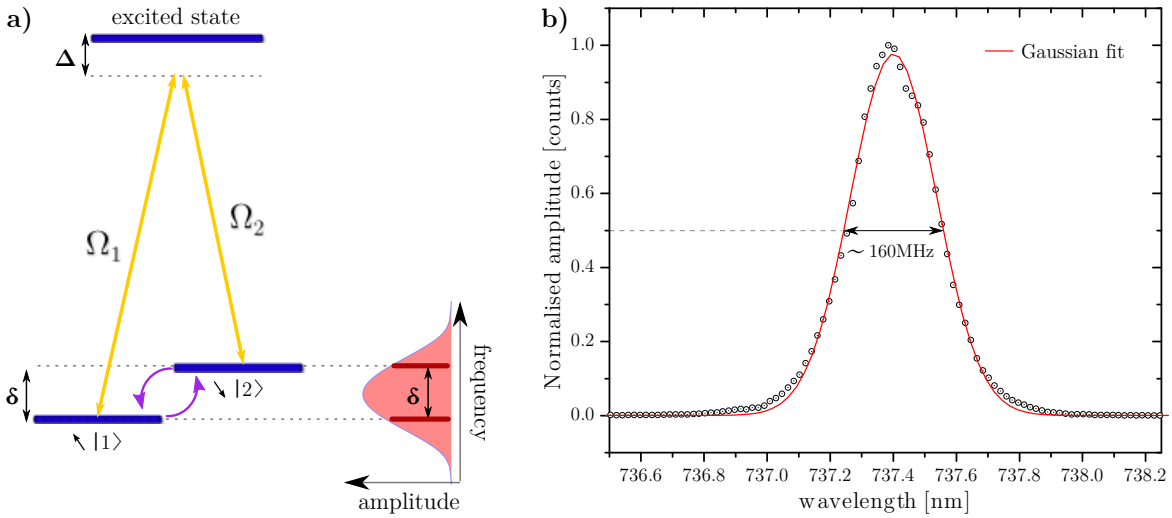

Fig. 6.22 **Ultrafast manipulation of electron spin with a single pulse in a Λ system. a)** The ultrafast pulse has to contain at least a pair of frequencies with the right spacing δ corresponding to the splitting between the states $|1\rangle$ and $|2\rangle$. **b)** Spectral width measurement on our laser.

Generation of pulse sequences

Some experiments, such as Ramsey interferometry and spin-echo, necessitate the use of two or more pulses and a finely adjustable time-delay between them. In the case of Ramsey, that time-delay should be tunable from zero to the ground-state spin coherence time (to date, around 115 ns [238]), where the damping due to the dephasing becomes maximum and the oscillations cannot be observed anymore. Since the delay stage is about 20 cm long and since the light beam travels back and forth, the maximum optical path difference between the two beams that can be finely tuned with this stage is about 40 cm, corresponding to a delay Δt of about 1.3 nanoseconds. Besides this fine analog delay, the repetition of the laser can be used as digital sampling rate over a longer time window, hence with a step of 13 nanoseconds. In order to do so, the pulse sequence sent to the AOMs by the delay generator (Figure 6.23) can be set such that the two AOMs do not pick the same pulses. One of them can pick the n^{th} pulse with a delay of $13n$ nanoseconds with respect to the other one (13 ns is then the incremental delay step). This is illustrated in Figure 6.24.

For more precision, the duration of the pulses could be measured via auto-correlation using a non-linear crystal. On the same principle, cross-correlation could be used to optimise the overlap of the pulses coming from each AOM when the total delay $n + \Delta t$ is set to zero. When two pulses overlap in space and time in a non-linear crystal, such as barium borate (BBO), a wave with twice the optical frequency is generated (second harmonic (SH) generation, Figure 6.25. This will be implemented in our setup in the future.

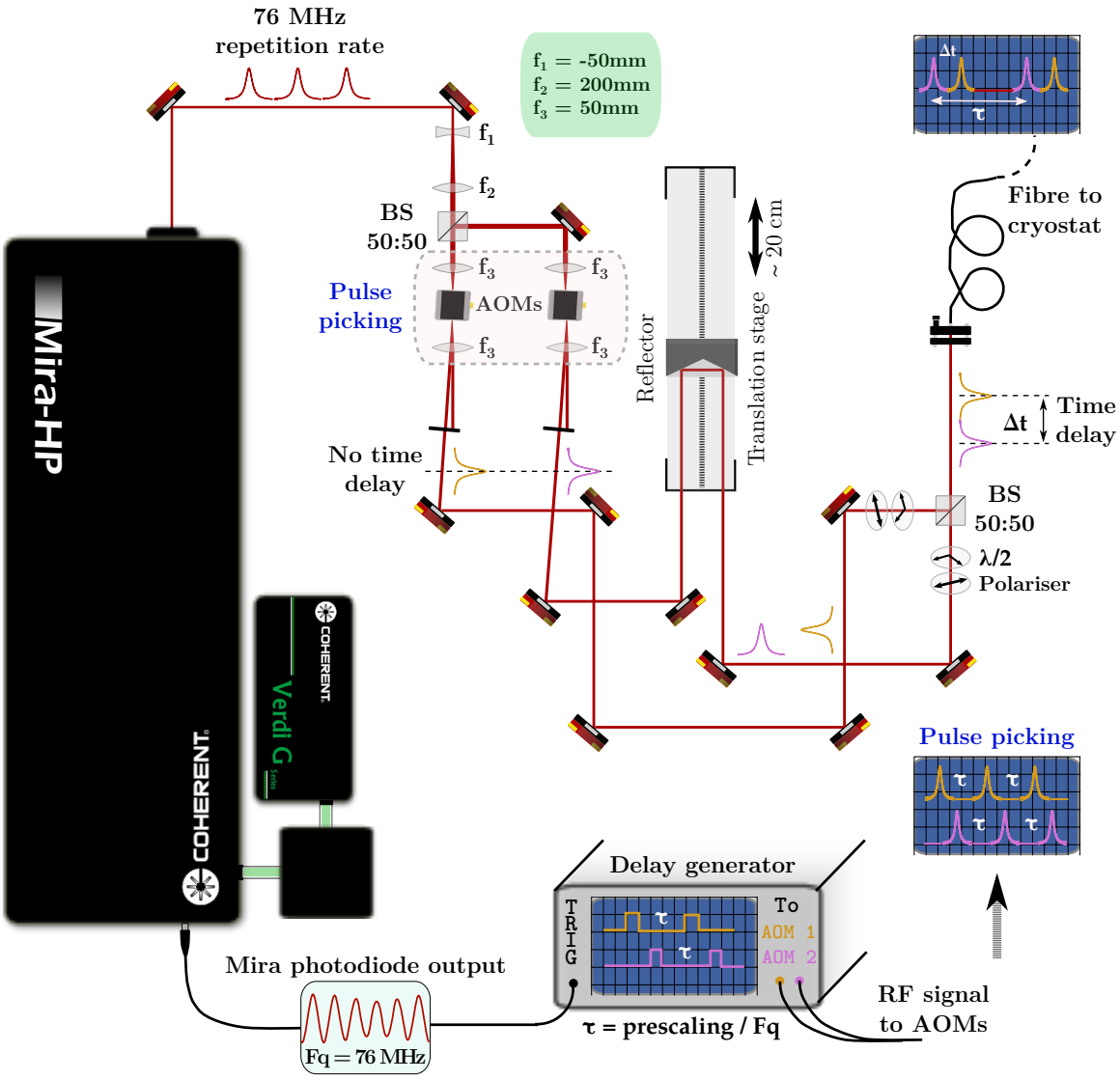

Fig. 6.23 **Ultrafast optical system for coherent spin control experiments.**

The delayed beam would be used as a probe to scan the other beam's profile as they cross in a non-linear crystal **a**), as it would be moved across the latter in time (Figure 6.26 **b**)). The amplitude of the auto-correlation signal depends on the overlapping in time and is maximum when the time delay between the two pulses is zero (Figure 6.26 **c**)). The pulse duration can be obtained from the full-width-half-maximum (FWHM) of the SH trace.

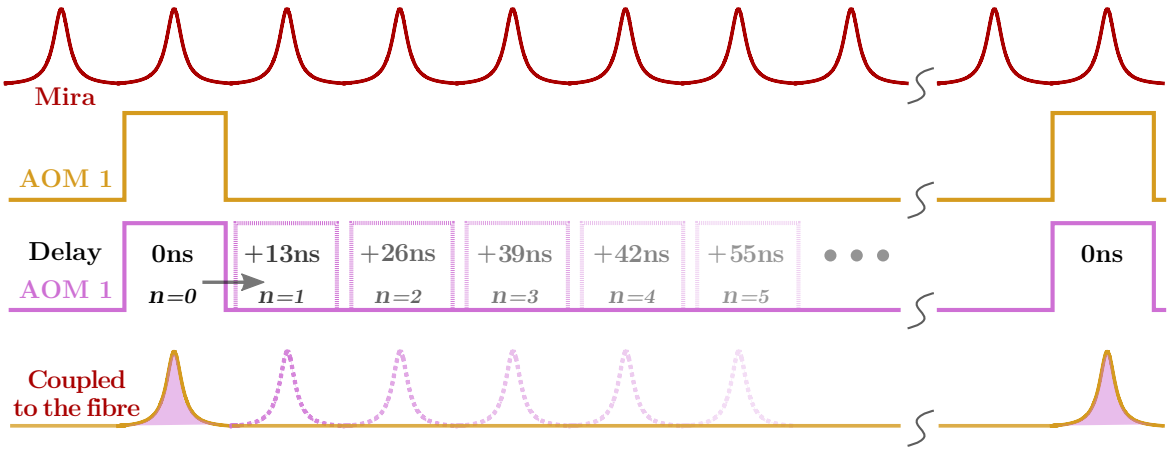

Fig. 6.24 **Digital sampling based on the relative delay between the RF pulses sent to each AOM.** Pulses of light used in the experiment can be incrementally delayed by steps of 13 ns.

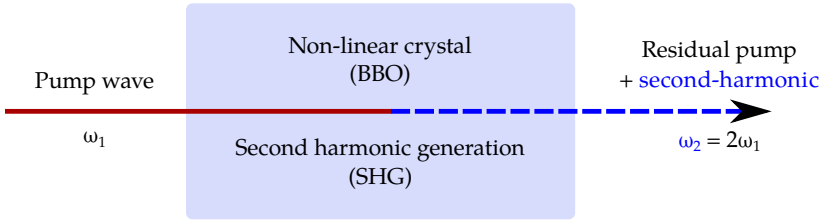

Fig. 6.25 **Second harmonic generation in a non-linear crystal.**

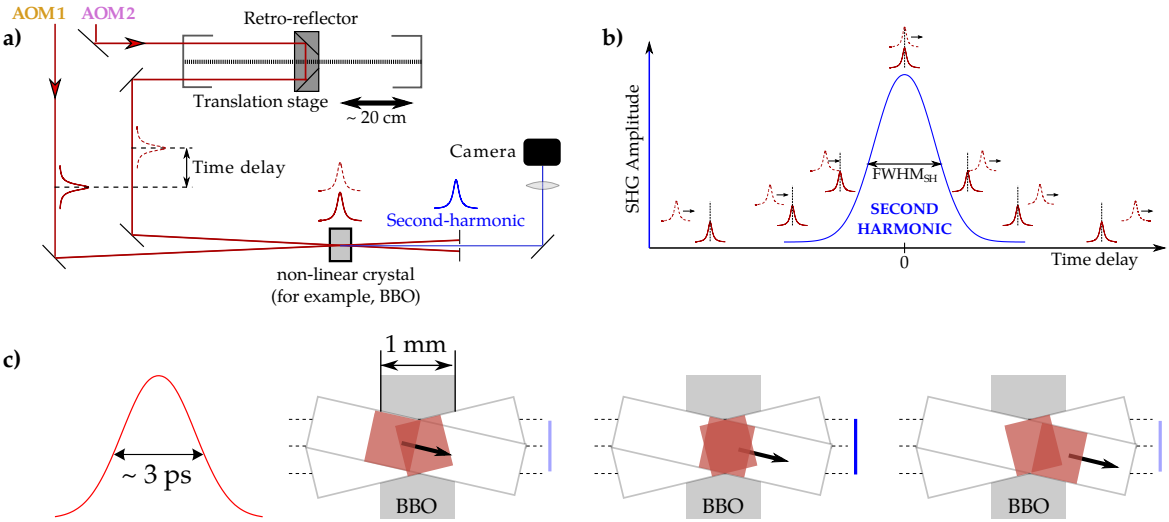

Fig. 6.26 **Cross-correlation of two pulses. a**) Both beams cross in a BBO crystal, generating a second-harmonic (SH) wave when the pulses overlap in space and time. **b**) The delayed beam (dashed) is used as a probe to scan the other beam's pulse profile. **c**) The SH signal amplitude depends on the overlapping in time and is maximum when the time delay is zero.

6.5 Conclusion and outlook

Building on previous work done in my group on ^{28}Si [67], we first measured the coherent population trapping (CPT) in single ^{29}Si-vacancy centres which, unlike ^{28}Si, possess a nuclear spin. The magnetic field dependence of the hyperfine splitting due to the latter was characterised, and a clear minimum was observed near the anti-crossing (at 1.5T) where the electron spin orthogonality is relaxed. To date, the model for the SiV^- electronic structure [77] does not take into account the nuclear spin, which now needs to be implemented and tested in the light of these results. We were able to observe an increase of the energy level splitting with strain on a few emitters, a first step towards the reduction of the electron-phonon interaction rate believed to be the main cause of fast decoherence [76]. However, strong spectral diffusion prevented us from characterising the CPT linewidth[67, 75] and hence the spin coherence time as a function of strain. In order to increase the reported spin coherence time of 115 ns[238], three pathways have been considered. Cooling down to a few millikelvin would eliminate most of the phonons, but necessitates the use of complex and expensive equipment (dilution fridge) and hence would not facilitate the implementation of SiV^- on chip. With the help of S. Meesala and Y.I. Sohn from the Lončar group in Harvard, we have started to explore a device-oriented approach: the use of electrically-actuated diamond micro-cantilevers which allow to tune the strain applied to single SiV^- centres. Our preliminary CPT results show a narrowing of the linewidth with increasing strain, which is consistent with the theoretical predictions.

The third and last pathway, which was the main focus of my PhD, is to perform operations on the spin that are faster than the decoherence: ultrafast optical control. For that purpose, we designed and characterised a setup that could allow one to cover the range of experiments needed from optically driven Rabi oscillations and stimulated Raman adiabatic passage to full ultrafast optical control over the entire Bloch sphere. Building on the work done recently on quantum dots [277, 300], the response of SiV^- centres to ultrafast and intense light pulses would need to be first modeled and tested experimentally.

6.6 S'il vous plaît, raconte-moi l'Univers. (If you please, tell me about the Universe.) 6

— Ne t'inquiète pas, dit le physicien d'une voix posée et rassurante. Quantique sait ce qu'il fait et nous serons bientôt en lieu sûr. Ce que tu vois-là, en bas du toboggan en forme d'escargot, c'est un « trou noir ». Un trou noir, c'est un peu comme un puits. Mais il est tellement profond que même la lumière qui s'y engouffre n'arrive pas à en sortir ! C'est pourquoi il nous parait si noir.

— Pourquoi l'Univers installe-t-il des toboggans à côté des puits ? J'ai trouvé un jour un puits dans un désert, sur la Terre... Mais il n'y avait pas de toboggan.

— Je vais essayer de te répondre, mais j'ai un ami qui ferait cela bien mieux que moi. Il s'appelle Albert. Albert Einstein. C'est lui qui a écrit ce bout de l'histoire. Mon astéroïde est un farceur, mais il n'est pas le seul ! L'Espace et le Temps en sont aussi. Dis-moi, as-tu déjà joué aux billes ?

— J'y ai joué une fois, dans le désert. Pourquoi donc me demandes-tu cela ?

— Parce que posées dans le sable, elles y forment un petit creux à l'image de leur silhouette, pour s'y sentir plus à l'aise. Et vois-tu les étoiles, les planètes et les trous noirs sont un peu comme les billes. Le trou noir que tu vois là a creusé le sable de l'Univers, et cela a formé un toboggan. Nous autres physiciens appelons ce bac à sable « l'Espace-Temps ».

Pendant qu'il achevait son explication, Quantique les avait transportés vers un lieu plus paisible, peuplé d'étoiles millénaires.

— Puis-je te poser une dernière question ?, se risqua le petit prince.

— Autant que tu voudras, lui assura le physicien.

— Pourquoi l'Univers parle-t-il si doucement ?

— En vérité ce que tu entends là, ce sont les échos d'un cri qu'il a poussé à sa naissance, quand il était encore plus petit que Léon, il y a 13.7 milliards d'années... Il n'a plus vraiment parlé depuis ce jour-là. Peut-être s'était-il trop écorché la voix. Il a hurlé tellement fort que son souffle continue d'éloigner les étoiles. Nous avons appelé son jour de naissance « Big Bang ».

— Don't worry, said the physicist with a calm and reassuring voice. Quantum knows what he is doing, and he will soon take us to a safe place. What you see here, at the bottom of the slide, is a "black hole". A black hole is like a well. But it is so deep that even light cannot escape from it! That is why we see it "black".

— Why does the Universe set up slides next to wells? One day, I found a well in a desert on Earth... But there was no slide.

— I will try to answer your question, but I have a friend who would do so a lot better than I could. His name is Albert. Albert Einstein. He is the one who wrote this part of the story. My asteroid is a prankster, but it is not the only one! So are Space and Time. Tell me something: have you ever played with marbles?

— I did once, in a desert. Why did you ask me this question?

— Because once on the sand, they dig a small dip of their shape, to feel more comfortable. And you see, stars, planets and black holes are somewhat like marbles. The black hole that you see here dug a hole in the Universe's sand, and this gave form to a slide. We-all physicists call this sandpit "the Space-Time".

While he was finishing his explanation, Quantum took them to a quieter place, among the oldest stars.

— Can I ask you a last question?, dared to say the little prince.

— As many as you wish, assured the physicist.

— Why does the Universe speak so softly?

— Actually, what you can hear now is just the echo of a cry he let out at birth, when he was even smaller than Léon, 13.7 billion years ago... Since that day, he has not said a word. Maybe his voice was damaged. He screamed so loudly that the blast of air is still separating the stars. We called his birthday "the Big Bang".

Chapter 7

General conclusion and Outlook

From linear to quantum optics, this thesis followed the path of light to explore the photophysics of metal halide perovskites - novel photovoltaic materials, and the Silicon-vacancy (SiV) colour-centre in diamond - a novel system for quantum information and sensing. This chapter highlights the main contributions of the present work to the state-of-the-art. It summarises the key findings and the open questions raised by previous chapters, opening up a discussion on future work. Finally, it gives a brief account of interesting emerging research and speculates on how the optical techniques and strategies developed herein could be combined to take the field forward.

7.1 On the richness of difference

Interesting science arises from originality. In solid-state physics, materials are often just a host for what really arouses curiosity: impurities, defects, local properties, new particles or quasi-particles, ... whenever and wherever the unexpected comes to meet the predictions. The real complexity generally emerges from their interactions with the host: the encounter between the peculiar and the usual. In this thesis, the focus evolved from macro (bulk) to micro measurements, downscaling from the many-body to single atoms. Defects in perovskite structures and silicon impurities in diamond were successively in the spotlight. The impact of local environment on charge-carrier recombination dynamics, in the first case, and on single electron-spin coherence time, in the second case, were explored by means of optical microscopy.

7.2 Main thesis outcomes

A range of optical techniques were optimised and used for the first time to study perovskites and SiVs. Building on conventional confocal microscopy, two-photon 3D time-resolved photoluminescence mapping was used to explore buried recombination dynamics and diffusivity below the surface of perovskite structures. An ultrafast optical system was designed and characterised for coherent spin control experiments on SiV centres.

7.2.1 Progress on perovskites

State-of-the-art

Despite high defect levels of the order of 10^{15} cm^{-3} in polycrystalline films, a million times higher than in gallium arsenide (GaAs) or silicon (Si), polycrystalline perovskite devices still operate remarkably well[9]. At the time where our project started, in May 2017, the impact of local environment such as lattice defects and strain on the mechanical and optoelectronic properties in these materials was not fully known . To date, further research is needed to achieve the full picture but some of the work reported in this thesis sheds some light on these questions. Published studies reported a low-temperature phase transition in thin films[139–141] that is suppressed in randomly-oriented powdered samples[139], indicating the potential impact of grain size on the phase transition. This work motivated the experiments presented in Chapter 3. To the best of our knowledge, no systematic study on the influence of grain size on the phase transition in perovskite thin films has yet been reported.

Photoluminescence maps in thin films have revealed a grain-to-grain[157] heterogeneity in the emission from surfaces leading to substantial losses in PV and LED devices[158, 48, 159]. Conventional one-photon PL microscopy being a surface sensitive technique (due to the high absorption coefficient of perovskites), very little is known about the presence of traps below the surface of films and single crystals, and their impact on charge-carrier generation and recombination pathways. Strong two-photon absorption in perovskites has been reported[163–165] and macroscopic two-photon measurements has revealed the existence of different recombination pathways in the bulk and at the surface of films[166, 167], single crystals[168, 169], quantum dots[170] and microplates[171]. However, before our contribution reported in Chapter 4, no mapping of the photoluminescence at the micro-scale using two-photon excitation had been made to investigate the penetration of passivation treatments in thin films or local heterogeneities in single crystals.

The distance over which charge-carriers are able to diffuse is known as a limiting factor in the design and performance of perovskite-based thin film solar cells[44], working in

a diffusion-limited regime rather than drift. However, an uncertainty remains over their diffusion properties. Some studies have reported very long diffusion lengths[43, 187], greater than 170 µm from surface-sensitive measurements[185]. At the surface of perovskite materials, photonics effects such as waveguiding and photon recycling are suspected to introduce a large uncertainty in the estimation of diffusion coefficients[188]. At the time of writing, no direct optical mapping of charge-carrier diffusion in the bulk of perovskite structures using two-photon microscopy has been reported, which could disentangle surface effects from intrinsic carrier diffusion and elucidate the contribution of photon recycling. To the best of our knowledge, two-photon diffusion mapping has never been reported in high quality perovskite single crystals.

Influence of grain size on the low temperature phase transition in $MAPbI_3$ thin films

Grain size in polycrystalline halide perovskite films is known to have an impact on the optoelectronic properties of the films, but its influence on their soft structural properties and phase transitions is unclear. Our optical (PL and absorption) and structural (XRD) study of the influence of the grain size on the low-temperature phase transition in $MAPbI_3$ perovskite polycrystalline thin films suggests that local strain plays a role in inhibiting the low-temperature tetragonal-to-orthorhombic phase transition. We show that the phase transition is increasingly suppressed with decreasing grain size, and that in the extreme case of very small grains this transition is almost entirely suppressed.

Strain appears therefore as an important parameter in the design of perovskite-based solar-cells, as a lever for controlling phase behaviour. The nature and strength of this strain needs to be further investigated, and future experiments could include correlated micro-PL and structural mapping at the micro scale or beyond. Advanced structural characterisation techniques such as Transmission Electron Microscopy (TEM), nano-XRD measurements, X-ray Photoemission Spectroscopy (XPS) or Grazing-Incidence Wide-Angle X-ray Scattering (GIWAXS) could be used. In order to further explore the link between mechanical and optoelectronic properties, the influence of grain size in thin films could be explored at different pressures and in different environments (atmospheres).

Probing buried recombination in perovskite structures: 3D time-resolved tomography

We use a technique recently developed to probe carrier lifetimes in semiconductors[115, 113], time-resolved two-photon confocal photoluminescence (2P-TRPL), to compare local surface and bulk recombination properties in $MAPbI_3$ and $MAPbBr_3$ polycrystalline and micro-crystal films. The penetration depth of surface passivation, one of the most commonly

used and efficient strategies to improve the photovoltaic performance of perovskite solar cells[50], and in particular light and atmospheric treatments[51–54], is yet to be assessed. Our 2P-TRPL measurements on passivated thin-films indicates that light-induced passivation approaches are primarily surface-sensitive. 3D tomography on $MAPbBr_3$ micro-crystals reveal that even nominal single crystals still contain heterogeneous defects that impact charge-carrier recombination[145]. Fluence-dependent 2P-TRPL measurements confirm that the heterogeneity in brightness is correlated with an heterogeneity in recombination dynamics (trap-assisted for dark grains and bimolecular for bright grains).

Here again, lattice defects and strain could be the cause of local differences in recombination dynamics, and would be best explored by correlating 3D tomography images with structural characterisation techniques with a micro-scale resolution. Local chemical composition would need to be investigated as well (such as Energy-dispersive X-ray spectroscopy, STEM-EDX), as composition separation could lead to local lattice mismatches and emergent residual strains consequently. Our work demonstrates the relevance of 3D tomography for the exploration of buried recombination, and future experiments could include measurements in working devices: single junction and tandem solar cells (perovskite-silicon) in-operando to identify the influence of interfaces in the recombination dynamics. This powerful technique could be used to study the nature of defects in perovskites and how they affect surfaces and interfaces between different crystal regions, which is still an open question. They could include crystal defects due to broken bonds and extrinsic impurities[33].

Future work could involve complex optical modelling in order to extract quantitative trap density from the measurements. Such a model would include a correction for the aberrations due to the refraction at the surface of the structures, impacting the depth of focus which is currently under-estimated (see Chapter 2.1.3). It would also account for the topography of the surface, it's angle with respect to the objective lens and more generally the out-coupling efficiency. Surface roughness and local scattering off defects could be estimated through *Finite-difference time-domain simulations* or multi-physics simulations, based on SEM images or topographic measurements, and deconvolved from the measured signal. Finally, a model of the reabsorption and photon recycling could be used to correct for any attenuation or amplification of the PL emitted at each point within the micro-crystals.

Visualising carrier diffusion in halide perovskite crystals

Building on our previous work on two-photon 3D tomography[145], we developed a technique to map the outward carrier diffusion at different depths in a semiconductor by monitoring the photoluminescence as a function of distance from the two-photon-excitation spot.

The technique is primarily applied to $MAPbBr_3$ crystals, but we also perform preliminary measurements for $MAPbI_3$ 2D (n=2 and n=3) perovskites. We report diffusion coefficients from 1 to 2.5 cm^2/s in the 3D single crystal, and from $\sim$0.1 cm^2/s to $\sim$1 cm^2/s in 2D (n=2) perovskite, attributing the lower diffusivity in 2D materials to the fact that charge carrier diffusion is effectively slowed down by the organic layers in the 2D structure. Our results revealed a spatial heterogeneity in diffusion that would not be captured by macroscopic diffusion measurements.

Depth-dependent mapping allows us to visualise buried charge-carrier diffusion in these perovskite structures. Scanning the detection revealed an anisotropic and heterogeneous diffusion at high fluence in both the single crystal and the 2D (n = 2) sample. The initial spread of the PL profile ($\sigma_{x,0}$) measured as a function of depth reduces to the detection resolution of our microscope within 3 µm from the surface and until the endpoint of our measurement at 10 µm. Building on a recently published study of diffusion in perovskite thin films[188], these results indicate that the weight of the photonic contribution in the overall diffusion in the bulk is small. Moreover, a local enhancement of $\sigma_{x,0}$ observed in a region of high diffusivity was identified as a signature of enhanced photon recycling. Although a quantitative assessment of this effect would require careful modelling, our results indicate that 2P-TRPL diffusion mapping could in the future enable us to disentangle the photonic and carrier contributions to the overall diffusion. We observe a significant broadening of $\sigma_{x,0}$ near the surface in all samples compared with the PL measured deeper. This broadening is consistent with the current working hypothesis that photonic effects are prominent on the diffusion measured close to the surface of perovskite structures.

In the future, a model of the re-absorption and recycling within single crystals involving FDTD simulations should be developed and further experiments performed in order to fully elucidate the role of photon recycling in the diffusion and disentangle it from measured charge-carrier mobility. Correlating the strength of the contribution from photon recycling to the local environment could provide us with another lever to fabricate materials with a high PL quantum yield and excellent charge transport. The capacity to decouple photon recycling and transport could lead in principle to the ability to manipulate the fraction of each effect by design, thus designing new devices exploiting different components of each.

7.2.2 Progress on the SiV centre

State-of-the-art

At the time where our project started, in April 2015, the ^{28}Si-based SiV colour-centre in diamond was still a very young system. Its molecular[77] and spectroscopic properties had

just been unveiled by spin-tagged resonance fluorescence, with a spin -1/2 and a spin-state purity approaching unity in the excited state, highlighting the potential of the centre as an efficient spin-photon quantum interface[66]. The SiV had the advantage of being the brightest reported colour centre in diamond[305], with an emission concentrated to about 80% into its zero-phonon-line (ZPL) even at room temperature[231], thus making it a promising single-photon source for entanglement at a distance. The all-optical coherent population trapping (CPT) of the electron spin, or in other words the preparation and readout of a quantum superposition state (or quantum bit) had just been realised[67]. These CPT measurements indicated a very short coherence time of the order of 45 ns. This short coherence time was thought to be due to strong electron-photon coupling. To overcome this limitation, different pathways leading to longer coherence times could be explored: using ^{29}Si-based colour centres instead of ^{28}Si, decoupling the phonon modes from the electronic transitions, or lowering the temperature to the mK range. Despite the short coherence time, two first step towards the coherent control of the SiV had just been achieved: Rabi and Ramsey experiments with ultrafast optical pulses[302] (on orbital levels only) and with microwaves[238] (on spin states). The next logical direction to take was the all optical ultrafast optical control of the SiV spin[306]. Spin physics and quantum control at interfaces, such as the effect of strain and temperature on the electron-nuclear hyperfine coupling could also be examined.

Coherent Population Trapping in SiVs with Si^{29}

New samples had just been fabricated by our collaborators in the Becher group (in Saarbrücken) with ^{29}Si-based colour centres instead of the ^{28}Si use previously. ^{29}Si possesses a nuclear spin that could potentially have a much longer coherence time. At the time, the hope was that this nuclear spin could be used as a quantum register. The projection of nearby nuclear spin qubits onto a well-defined state from the read-out of the electronic spin [239] had been already realised with ensembles of Nitrogen-vacancy (NV) centres [240].

As a first step towards harnessing the nuclear spin of the ^{29}Si-based SiV, we explored the magnetic-field dependency of the hyperfine splitting on single emitters at 3.5 K. We measured CPT spectra for different magnetic fields near the avoided crossing. We did so for two transitions before and after the avoided crossing. By sweeping the magnetic field over the region of the avoided crossing, we relaxed the spin-state orthogonality in order to decouple the spin-spin interaction from the spin-orbit coupling (responsible for the state-mixing) and studied the effect of the spin-spin interaction on the CPT. The results showed a very clear narrowing of the hyperfine splitting around the avoided crossing (Figure 6.12). At the time, our model was not able to simulate this result, but this experimental evidence constitutes a strong basis for the thorough modelling of the nuclear spin and its coupling to the electron

spin in these systems that could be the object of future work. We did not attempt to address the nuclear spin directly, and that could also be the object of future work.

Influence of strain on the electron-phonon coupling

Mechanical strain was thought to induce local deformations of the lattice that could break the symmetry at the vicinity of an emitter therefore changing its ground state splitting as well as the excited state and the centre-of-mass splitting. We performed optical spectroscopy measurements on SiV centres implanted on electrically actuated micro-cantilevers in diamond. These measurements revealed a strain-dependent ground state splitting, confirming the theoretical predictions. We then performed CPT experiments and monitored the CPT linewidth as a function of strain. Our results successfully demonstrated that strain-tuning via a device-oriented approach could be used to decouple the ground state splitting from the main phonon modes in the diamond lattice and increase the coherence time.

A route to the ultrafast optical control of the SiV

The third and last pathway to overcome the short coherence time of the SiV spin was to perform operations on the spin that are faster than the decoherence: ultrafast optical control. For that purpose, we designed and characterised a setup that could allow one to cover the range of experiments needed from optically driven Rabi oscillations and stimulated Raman adiabatic passage to full ultrafast optical control over the entire Bloch sphere. The response of SiV^- centres to ultrafast and intense light pulses would need to be first modelled and tested experimentally. Although the focus should first be made on the electronic spin, addressing the nuclear spin and exploring how it could be used as a quantum register remains a milestone that we shall work to achieve. Ultimately, future work could lead to the entanglement of two SiV^- centres, providing an assessment of the suitability and pertinence of these systems as spin-photon entangled nodes and universal quantum gates for on-chip quantum networks.

7.3 Strain as a common thread

We have shown how strain could be used to increase the short coherence time of SiVs, by decoupling the electronic ground-state splitting to the main phonon modes in the diamond lattice. In perovskites, we observe heterogeneities in the photoluminescence due to local strain, but the impact of the latter on diffusion and charge recombination dynamics at the micro-scale has not been clearly investigated yet. In particular, its impact on the electron-phonon coupling in perovskites is still an open question.

In light of the mechanical softness of hybrid perovskites, it has been proposed that the main source of scattering limiting charge-carrier mobilities and governing emission line broadening could be the interaction with phonons[307, 308]. It has been later demonstrated unambiguously that Fröhlich coupling to optical phonons is the predominant cause of linewidth broadening in these materials at room temperature, with scattering from acoustic phonons and impurities being a minor component[309, 310]. Recent ab-initio theoretical work points to the polaronic nature of the charge transport in these materials[311, 312]. Most recently, vibrational modes in lead halide pervoskites have been shown to exhibit a mixed nature in between those of phonons found in crystalline materials and propagons, diffusons, and locons found in glasses[313]. While strain has been shown to govern electron-phonon coupling in SiV centres, this link has not been established in perovskites. Further experiments such as neutron scattering could be coupled in with optoelectronic measurements to investigate phonon modes in perovskite structures. Temperature-dependent 3D tomography and diffusion mapping could also help to elucidate the effect of local environment on the electron-phonon coupling.

7.3.1 Strong-coupling as a way to decouple polarons

Besides impeding carrier mobility, polarons could play a role in the photobleaching of perovskites. Recently, it was demonstrated that strong coupling between organic molecules and plasmonic nanocavities can significantly alter the photobleaching reaction in organic materials such as those used for organic solar cells by means of nanoantennas[314] and cavity QED[315]. Such experiments could be attempted on perovskite materials as well, deposited or evaporated on micro-and nano-structured substrates. The fabrication of perovskite films on top of - or embedded in - phononic crystals and acoustic metamaterials[316] could also be explored as a route to electron-phonon decoupling, via the engineering of a phononic bandgap corresponding to the main phonon modes (energies) involved in this effect.

7.3.2 Taking advantage of strain and symmetry breaking in perovskites

The nature and role of strain in hybrid perovskite materials has recently become a very active research question. Earlier this year, the residual strain distribution profiles in mixed perovskite thin films was investigated by means of grazing incident X-ray diffraction (GIXRD) measurement[317]. The tensile strain in the films was modulated by tuning the temperature gradient during film processing and annealing. The authors report better device performance with lower tensile strain. Deformation potential scattering mechanisms playing an important role in the electron–phonon coupling in inorganic semiconductors[309], it would be interest-

ing to monitor strain-dependent charge carrier diffusion and recombination dynamics using a similar methods. Practical implementation of strain-tuning could include deposition (evaporation) on patterned substrates, the use of lattice mismatch with different electron or hole extraction layers, epitaxial growth[318] and stoichiometry[319]. Strain engineering could also induce ferroelectricity in material systems that would be otherwise non-ferroelectric in bulk.

Another potential effect of strain would be local deformations of the lattice, locally breaking its symmetry. An intense debate surrounds the centro-symmetry of hybrid perovskites and the existence of a conduction-band splitting due to the Rashba effect[320], lifting the spin-degeneracy in *k*-space via spin-orbit coupling. Reported in 2D perovskites[321] similar to the structures studied in Chapter 5 and nano-crystals[322, 323], it was first claimed as present in bulk single crystals ($MAPbI_3$)[324] and later shown to be an artefact of Density functional theory (DFT) calculations in these centro-symmetric materials[325], although possibly present at the surface[325, 326]. When present, the Rashba effect would impede the recombination rate due to a spin-forbidden transition, but it would also enable spin-selective optical manipulations. The Rashba parameter has been reported as being comparable with the highest values reported for bulk crystals, thus rendering perovskite structures promising for spintronics[327]. It has also been proposed[328] that the strength of Rashba splitting can be controlled via an external electric field in the direction perpendicular to the plane. Such an approach may find application in spin field-effect transistors to generate, control and detect spin current and prepare spin states[329]. Symmetry breaking via strain or grain boundaries[330] could be engineered on purpose.

Finally, a noncentrosymmetric crystal structure in a ferroelectric material can lead to a peculiar kind of charge separation under illumination called the bulk photovoltaic (BPV) effect. It is a second-order nonlinear optical effect that intrinsically converts light into electrical current and which is free from the thermodynamic Shockley-Queisser limit[331, 332]. It was recently shown that ordinarily centrosymmetric materials can lose their inversion symmetry under local strain, leading to strain gradient-induced bulk photovoltaic effect, called the *flexo-photovoltaic effect* or *force-induced PV*, which functions in the absence of a p-n junction[333, 334]. Although the ferroelectric properties of hybrid perovskites such as $MAPbX_3$ (X=I or Br) studied in this thesis are not clear[335, 336], a few organic-inorganic perovskite ferroelectrics containing halides, cyanides, and formates were developed as competitive candidates for microelectromechanical systems (MEMS)[13, 337–341]. Tailored Engineering of an unusual two-dimensional multilayered perovskite ferroelectric for a high-performance photodetector[342] and metal-free three-dimensional perovskite ferroelectrics[343] were also reported. BPV studies have focused on ferroelectrics because

the original observation of the effect was in ferroelectrics and also because of its attribution to built-in fields. However, today, BPVs are understood through the lens of nonlinear optics and topology, namely the evolution of the wavefunction in momentum space[344].

7.3.3 Towards quantum optomechanics on chip with SiVs

To realise quantum networks on chip, individual quantum nodes (or spins) have to be interfaced. This interfacing could be done optically, but it could also be achieved via spin-coupled quantum optomechanics [345–347] involving hybrid mechanical systems. Working at those interfaces could enable one to measure spin-dependant forces, interface quantum mechanics with mechanical resonators, generate and observe non-classical states of motion [348–355]. In the footsteps of SiV-cavity coupling and optical switching[356], the strain-tuning devices used for our CPT measurements constitute for instance a good platform for the experimentation of strong coupling between the silicon-vacancy spin and single phonons, which could lead to the realisation of phonon-mediated quantum gates and nonlinear quantum phononics. Eventually, in the future, arrays of optomechanical resonators could be nano-fabricated on chip with deterministically-implanted ^{29}Si-based SiV centres, interlinked via the exchange of phonons to fabricate quantum processors possessing their own quantum register within their nuclear spin degree of freedom. Owing to the advantageous optical properties of the SiV centre and the indistinguishability of emitted photons (80% emitted in the ZPL), optical entanglement at a distance could then be implemented between individual quantum networks, that could add to the computing power the reliability of secure quantum communications. Diamond being a very robust and inert material, it could be an interesting single-photon source for free space optical communications on cutting-edge platforms such as quantum satellites[357]. Finally, the remarkable sensitivity of the SiV centre to strain makes it a promising candidate for the design of very precise free standing (nanodiamonds) or integrated optically-readable, bio-compatible strain sensors in the solid state, that could provide non-invasive and extremely precise contact-less strain measurements.

7.4 S'il vous plaît, raconte-moi l'Univers. (If you please, tell me about the Universe.) 7

Le physicien retroussa une de ses manches pour regarder sa montre.

— Il faudrait que tu rentres à présent, chuchota-t-il. Ta fleur doit avoir soif. Tiens, prends donc mon télescope et dis-moi si tu vois ta planète.

Le petit prince posa son regard dans l'étroit oculaire, puis fit pivoter la monture jusqu'à apercevoir une petite perle blanche peuplée de trois volcans, une fleur avec quatre épines et un mouton mangeant un baobab.

— La voilà !, s'écria-t-il.

Le physicien s'empara alors d'un petit aimant, qu'il lança en direction de la planète. Tel l'eau d'un lac heurtée par une pierre, l'océan galactique qui bordait son astéroïde se mit à osciller. Cette onde se propagea jusqu'à rider l'immensité à perte de vue.

— Alors saute maintenant, mon ami, avant que Quantique ne choisisse une nouvelle destination. Assieds-toi sur cette onde et laisse-toi porter par elle jusqu'à ta planète. Et surtout n'oublie pas une chose: n'écoute jamais les grandes personnes quand elles disent que la Science est trop sérieuse pour être amusante ou que la curiosité est un vilain défaut !

Après avoir salué et remercié le physicien, le petit prince sauta, et aussitôt l'astéroïde Quantique disparut.

« Celui-là, se dit-il, tandis qu'il glissait sur le sable ondé de l'Univers, celui-là serait méprisé par le businessman et incompris de la plupart des autres qui se moqueraient de sa fantaisie. Pourtant, je crois qu'il a su garder son âme d'enfant. »

Il eut un soudain sourire aux lèvres, et se dit encore :

« Oui, celui-là est vraiment fantasque, avec ses particules trop petites pour être vues et son Univers dont le souffle est trop léger pour être entendu... »

Puis, se souvenant de son renard apprivoisé, il conclut en un soupir de sagesse :

« Je crois qu'il essaie d'imaginer et de décrire ce qui ne peut être perçu. Mais après-tout, l'essentiel est invisible pour les yeux... »

The physicist rolled up one of his sleeves, and looked at his watch.

— You should head back now, he whispered. Your flower must be thirsty. Have a look through my telescope and tell me when you see your planet.

The little prince approached one of his eyes to the eyepiece, and rotated the telescope until he saw a little white pearl populated by three volcanoes, a flower with four spines, and a sheep crunching a baobab.

— There it is!, shouted he.

The physicist grabbed a small magnet, and threw it towards the planet. Like the surface of a lake hit by a stone, the galactic ocean surrounding his asteroid started to oscillate. This wave propagated as far as the eye could see.

— Jump now, my little friend, before Quantum chooses a new destination. Sit on this wave and it will carry you to your planet. Above all, remember this: never listen to grown-ups when they say that Science is too serious to be diverting, and that curiosity killed the cat!

After having thanked and greeted the physicist, the little prince jumped on the wave, and the Quantum asteroid disappeared.

"This man, he thought while gliding on the Universe's sand, this man would be despised by the businessman and misunderstood by most people who would make fun of his innocent ingenuity. But I think he never lost his inner child."

He suddenly raised a smile, and said to himself again:

"Yes, this man is really fanciful, with his particles too small to be seen and his Universe whose voice is too soft to be heard..."

Then, remembering his friend, the little fox, he concluded in a sigh full of wisdom:

"I think that he is trying to imagine and describe things that cannot be perceived. But after all, what is essential is invisible to the eye..."

References

[1] Nira Liberman and Yaacov Trope. The psychology of transcending the here and now, 2008.

[2] Antoine de Saint-Exupéry. *Le Petit Prince*. Reynal and Hitchcock, 1943.

[3] Colin A. Ronan. *Science: Its History and Development Among the World's Cultures.* Facts on File, 1983.

[4] Walter Farber. *Witchcraft, Magic, and Divination in Ancient Mesopotamia. Civilizations of the Ancient Near East.* Charles Schribner's Sons, MacMillan Library Reference USA, 1995.

[5] Tzvi Abusch. *Mesopotamian Witchcraft: Towards a History and Understanding of Babylonian Witchcraft Beliefs and Literature.* Brill, 2002.

[6] Gustav Freytag. *Freytag's Technique of the Drama: An Exposition of Dramatic Composition and Art - Third Edition - An authorized translation from the sixth German edition by Elias J. MacEwan*. Scott, Foresman and Company, 1900.

[7] I. Newton. *Philosophiae naturalis principia mathematica*. J. Societatis Regiae ac Typis J. Streater, 1687.

[8] C.R. Kalaiselvi, N. Muthukumarasamy, Dhayalan Velauthapillai, Misook Kang, and T.S. Senthil. Importance of halide perovskites for next generation solar cells – a review. *Materials Letters*, 219:198 – 200, 2018.

[9] Samuel D. Stranks and Henry J. Snaith. Metal-halide perovskites for photovoltaic and light-emitting devices, 2015.

[10] D Weber. Ch3nh3pbx3, a pb(ii)-system with cubic perovskite structure. *Zeitschrift für Naturforschung B*, 33:1443–1445, 1978.

[11] Akihiro Kojima, Kenjiro Teshima, Yasuo Shirai, and Tsutomu Miyasaka. Organometal halide perovskites as visible-light sensitizers for photovoltaic cells. *Journal of the American Chemical Society*, 131(17):6050–6051, 2009. PMID: 19366264.

[12] Kim Chiho, Doan Huan Tran, Krishnan Sridevi, and Ramprasad Rampi. A hybrid organic-inorganic perovskite dataset. *Scientific Data*, 4, 2017.

[13] Wei Li, Zheming Wang, Felix Deschler, Song Gao, and Richard H. Friend. Chemically diverse and multifunctional hybrid organic–inorganic perovskites. *Nature Reviews Materials*, 2, 2017.

[14] Christopher Eames Eames, Jarvist M. Frost, Piers R. F. Barnes, Brian C. O'Regan, Aron Walsh, , and Saiful Islam. Ionic transport in hybrid lead iodide perovskite solar cells. *Nature Communications*, 6, 2015.

[15] M. M. Lee, J. Teuscher, T. Miyasaka, T. N. Murakami, and H. J. Snaith. Efficient Hybrid Solar Cells Based on Meso-Superstructured Organometal Halide Perovskites. *Science*, 338(6107):643–647, 2012.

[16] Hui Seon Kim, Chang Ryul Lee, Jeong Hyeok Im, Ki Beom Lee, Thomas Moehl, Arianna Marchioro, Soo Jin Moon, Robin Humphry-Baker, Jun Ho Yum, Jacques E. Moser, Michael Grätzel, and Nam Gyu Park. Lead iodide perovskite sensitized all-solid-state submicron thin film mesoscopic solar cell with efficiency exceeding 9%. *Scientific Reports*, 2, 2012.

[17] NREL. Nrel best research-cell efficiency chart.

[18] Zhengguo Xiao, Ross A. Kerner, Lianfeng Zhao, Nhu L. Tran, Kyung Min Lee, Tae Wook Koh, Gregory D. Scholes, and Barry P. Rand. Efficient perovskite light-emitting diodes featuring nanometre-sized crystallites. *Nature Photonics*, 11(2):108–115, 2017.

[19] Liuqi Zhang, Xiaolei Yang, Qi Jiang, Pengyang Wang, Zhigang Yin, Xingwang Zhang, Hairen Tan, Yang Michael Yang, Mingyang Wei, Brandon R. Sutherland, Edward H. Sargent, and Jingbi You. Ultra-bright and highly efficient inorganic based perovskite light-emitting diodes. *Nature Communications*, 8, 2017.

[20] Nana Wang, Lu Cheng, Rui Ge, Shuting Zhang, Yanfeng Miao, Wei Zou, Chang Yi, Yan Sun, Yu Cao, Rong Yang, Yingqiang Wei, Qiang Guo, You Ke, Maotao Yu, Yizheng Jin, Yang Liu, Qingqing Ding, Dawei Di, Le Yang, Guichuan Xing, He Tian, Chuanhong Jin, Feng Gao, Richard H. Friend, Jianpu Wang, and Wei Huang. Perovskite light-emitting diodes based on solution-processed self-organized multiple quantum wells. *Nature Photonics*, 10(11):699–704, 2016.

[21] Taesoo D. Lee and Abasifreke U. Ebong. A review of thin film solar cell technologies and challenges, 2017.

[22] Wiley A. Dunlap-Shohl, Yuanyuan Zhou, Nitin P. Padture, and David B. Mitzi. Synthetic approaches for halide perovskite thin films. *Chemical Reviews*, 119, 2019.

[23] Zhen Li, Talysa R. Klein, Dong Hoe Kim, Mengjin Yang, Joseph J. Berry, Maikel F. A. M. van Hest, and Kai Zhu. Scalable fabrication of perovskite solar cells. *Nature Reviews Materials*, 3, 2018.

[24] E. L. Unger, L. Kegelmann, K. Suchan, D. Sörell, L. Korte, and S. Albrecht. Roadmap and roadblocks for the band gap tunability of metal halide perovskites. *J. Mater. Chem. A*, 5(23):11401–11409, 2017.

[25] Giles E. Eperon, Maximilian T. Hörantner, and Henry J. Snaith. Metal halide perovskite tandem and multiple-junction photovoltaics. *Nature Reviews Chemistry*, 1, 2017.

[26] Tomas Leijtens, Kevin A. Bush, Rohit Prasanna, and Michael D. McGehee. Opportunities and challenges for tandem solar cells using metal halide perovskite semiconductors. *Nature Energy*, 3, 2018.

[27] Luis K. Ono, Nam-Gyu Park, Kai Zhu, Wei Huang, and Yabing Qi. Perovskite Solar Cells—Towards Commercialization. *ACS Energy Letters*, 2017.

[28] Nam Gyu Park, Michael Grätzel, Tsutomu Miyasaka, Kai Zhu, and Keith Emery. Towards stable and commercially available perovskite solar cells, 2016.

[29] Yicheng Zhao, Jing Wei, Heng Li, Yin Yan, Wenke Zhou, Dapeng Yu, and Qing Zhao. A polymer scaffold for self-healing perovskite solar cells. *Nature Communications*, 2016.

[30] Henry J. Snaith and Peter Hacke. Enabling reliability assessments of pre-commercial perovskite photovoltaics with lessons learned from industrial standards. *Nature Energy*, 3, 2018.

[31] Qianqian Lin, Ardalan Armin, Ravi Chandra Raju Nagiri, Paul L. Burn, and Paul Meredith. Electro-optics of perovskite solar cells. *Nature Photonics*, 9:106–112, 2015.

[32] Atsuhiko Miyata, Anatolie Mitioglu, Paulina Plochocka, Oliver Portugall, Jacob Tse-Wei Wang, Samuel D. Stranks, Henry J. Snaith, and Robin J. Nicholas. Direct measurement of the exciton binding energy and effective masses for charge carriers in organic–inorganic tri-halide perovskites. *Nature Physics*, 11:582–587, 2015.

[33] Jenny Nelson. *The Physics of Solar Cells*. Imperial College Press, 2003.

[34] Joseph S. Manser and Prashant V. Kamat. Band filling with free charge carriers in organometal halide perovskites. *Nature Photonics*, 8:737–743, 2014.

[35] Michele Saba, Michele Cadelano, Daniela Marongiu, Feipeng Chen, Valerio Sarritzu, Nicola Sestu, Cristiana Figus, Mauro Aresti, Roberto Piras, Alessandra Geddo Lehmann, Carla Cannas, Anna Musinu, Francesco Quochi, Andrea Mura, and Giovanni Bongiovanni. Correlated electron–hole plasma in organometal perovskites. *Nature Communications*, 5, 2014.

[36] Felix Deschler, Michael Price, Sandeep Pathak, Lina E. Klintberg, David-Dominik Jarausch, Ruben Higler, Sven Hüttner, Tomas Leijtens, Samuel D. Stranks, Henry J. Snaith, Mete Atatüre, Richard T. Phillips, and Richard H. Friend. High photoluminescence efficiency and optically pumped lasing in solution-processed mixed halide perovskite semiconductors. *J. Phys. Chem. Lett.*, 5:1421–1426, 2014.

[37] William Shockley and Hans J. Queisser. Detailed balance limit of efficiency of p-n junction solar cells. *Journal of Applied Physics*, 32(3):510–519, 1961.

[38] Jinsong Huang, Yongbo Yuan, Yuchuan Shao, and Yanfa Yan. Understanding the physical properties of hybrid perovskites for photovoltaic applications, 2017.

[39] R.J. Nelson and R.G. Sobers. Minority-carrier lifetimes and internal quantum efficiency of surface-free gaas. *Journal of Applied Physics*, 49, 1978.

[40] I. Schnitzer, E. Yablonovitch, C. Caneau, and T. J. Gmitter. Ultrahigh spontaneous emission quantum efficiency, 99.7% internally and 72% externally, from algaas/gaas/algaas double heterostructures. *Applied Physics Letters*, 62, 1993.

[41] Yanjun Fang, Haotong Wei, Qingfeng Dong, and Jinsong Huang. Quantification of re-absorption and re-emission processes to determine photon recycling efficiency in perovskite single crystals. *Nature Communications*, 8, 2017.

[42] Samuel D. Stranks, Giles E. Eperon, Giulia Grancini, Christopher Menelaou, Marcelo J. P. Alcocer, Tomas Leijtens, Laura M. Herz, Annamaria Petrozza, and Henry J. Snaith. Electron-hole diffusion lengths exceeding 1 micrometer in an organometal trihalide perovskite absorber. *Science*, 342:341–344, 2013.

[43] Dong Shi, Valerio Adinolfi, Riccardo Comin, Mingjian Yuan, Erkki Alarousu, Andrei Buin, Yin Chen, Sjoerd Hoogland, Alexander Rothenberger, Khabiboulakh Katsiev, Yaroslav Losovyj, Xin Zhang, Peter A. Dowben, Omar F. Mohammed, Edward H. Sargent, and Osman M. Bakr. Low trap-state density and long carrier diffusion in organolead trihalide perovskite single crystals. *Science*, 347, 2015.

[44] Chao Liang, Dandan Zhao, Pengwei Li, Bo Wu, Hao Gu, Jiacheng Zhang, Teck Wee Goh, Shi Chen, Yonghua Chen, Zhendong Sha, Guosheng Shao, Tze Chien Sum, and Guichuan Xing. Simultaneously boost diffusion length and stability of perovskite for high performance solar cells. *Nano Energy*, 59:721 – 729, 2019.

[45] Luis Pazos-Outon, Monika Szumilo, Robin Lamboll, M. Johannes Richter, Micaela Crespo-Quesada, Mojtaba Abdi-Jalebi, Happy J. Beeson, Milan Vrucinic, Mejd Alsari, Henry J. Snaith, Bruno Ehrler, H. Friend, Richard, and Felix Deschler. Photon recycling in lead iodide perovskite solar cells. *Science*, 351, 2016.

[46] Yasuhiro Yamada, Toru Nakamura, Masaru Endo, Atsushi Wakamiya, and Yoshihiko Kanemitsu. Photocarrier recombination dynamics in perovskite ch3nh3pbi3 for solar cell applications. *Journal of the American Chemical Society*, 136:11610–11613, 2014.

[47] Samuel D. Stranks, Victor M. Burlakov, Tomas Leijtens, James M. Ball, Alain Goriely, and Henry J. Snaith. Recombination Kinetics in Organic-Inorganic Perovskites: Excitons, Free Charge, and Subgap States. *Physical Review Applied*, 2(3), 2014.

[48] Dane W. DeQuilettes, Sarah M. Vorpahl, Samuel D. Stranks, Hirokazu Nagaoka, Giles E. Eperon, Mark E. Ziffer, Henry J. Snaith, and David S. Ginger. Impact of microstructure on local carrier lifetime in perovskite solar cells. *Science*, 2015.

[49] Nicholas Aristidou, Christopher Eames, Irene Sanchez-Molina, Xiangnan Bu, Jan Kosco, M. Saiful Islam, and A. Haque, Saif. Fast oxygen diffusion and iodide defects mediate oxygen-induced degradation of perovskite solar cells. *Nature Communications*, 8, 2017.

[50] Pengjun Zhao, Byeong Jo Kim, and Hyun Suk Jung. Passivation in perovskite solar cells: A review. *Materials Today Energy*, 7:267 – 286, 2018.

[51] Dane W. DeQuilettes, Wei Zhang, Victor M. Burlakov, Daniel J. Graham, Tomas Leijtens, Anna Osherov, Vladimir Bulović, Henry J. Snaith, David S. Ginger, and Samuel D. Stranks. Photo-induced halide redistribution in organic–inorganic perovskite films. *Nature Communications*, 2016.

[52] Yuxi Tian, Maximilian Peter, Eva Unger, Mohamed Abdellah, Kaibo Zheng, Tõnu Pullerits, Arkady Yartsev, Villy Sundström, and Ivan G. Scheblykin. Mechanistic insights into perovskite photoluminescence enhancement: light curing with oxygen can boost yield thousandfold. *Phys. Chem. Chem. Phys.*, 17(38):24978–24987, 2015.

[53] Teng Zhang, Sin Hang Cheung, Xiangyue Meng, Lei Zhu, Yang Bai, Carr Hoi Yi Ho, Shuang Xiao, Qingzhong Xue, Shu Kong So, and Shihe Yang. Pinning Down the Anomalous Light Soaking Effect toward High-Performance and Fast-Response Perovskite Solar Cells: The Ion-Migration-Induced Charge Accumulation. *Journal of Physical Chemistry Letters*, 8(20):5069–5076, 2017.

[54] Roberto Brenes, Christopher Eames, Vladimir Bulović, M. Saiful Islam, and Samuel D. Stranks. The Impact of Atmosphere on the Local Luminescence Properties of Metal Halide Perovskite Grains. *Advanced Materials*, 2018.

[55] Mojtaba Abdi-Jalebi, Zahra Andaji-Garmaroudi, Stefania Cacovich, Camille Stavrakas, Bertrand Philippe, Johannes M. Richter, Mejd Alsari, Edward P. Booker, Eline M. Hutter, Andrew J. Pearson, Samuele Lilliu, Tom J. Savenije, Håkan Rensmo, Giorgio Divitini, Caterina Ducati, Richard H. Friend, and Samuel D. Stranks. Maximizing and stabilizing luminescence from halide perovskites with potassium passivation. *Nature*, 555:497–501, 2018.

[56] Aurélien M. A. Leguy, Pooya Azarhoosh, M. Isabel Alonso, Mariano Campoy-Quiles, Oliver J. Weber, Jizhong Yao, Daniel Bryant, Mark T. Weller, Jenny Nelson, Aron Walsh, Mark van Schilfgaarde, and Piers R. F. Barnes. Experimental and theoretical optical properties of methylammonium lead halide perovskites. *Nanoscale*, 8(12):6317–6327, 2016.

[57] Rodney Loudon. *The Quantum Theory of Light*, volume 42. New York, NY (USA): Oxford University Press, 01 2000.

[58] I. Perez-Arjona, G. J. de Valcarcel, and Roldan. Two-photon absorption. *Revista Mexicana de Fisica*, 49:92–101, February 2003.

[59] Maria Göppert-Mayer. Über elementarakte mit zwei quantensprüngen. *Annalen der Physik*, 9:273–294, 1931.

[60] Ben Simons. Part ii: Advanced quantum mechanics - university of cambridge lecture series, 2009.

[61] Mariacristina Rumi and Joseph W. Perry. Two-photon absorption: an overview of measurements and principles. *Advances in Optics and Photonics*, 2010.

[62] Toshihiro Nakanishi, Hirokazu Kobayashi, Kazuhiko Sugiyama, and Masao Kitano. Full quantum analysis of two-photon absorption using two-photonwavefunction: Comparison with one-photon absorption. *Journal of the Physical Society of Japan*, 78:104401, 06 2009.

[63] Dan Browne, Sougato Bose, Florian Mintert, and M. S. Kim. From quantum optics to quantum technologies. *arXiv*, (1707.02925), 2017.

[64] Subhashish Banerjee and Arun Jayannavar. Current trends in quantum optics. *arXiv*, (1902.08576), 2019.

[65] Christian Hepp. *Electronic Structure of the Silicon-Vacancy Color Centre in Diamond*. PhD thesis, Universität des Saarlandes, 2014.

[66] Tina Muller, Christian Hepp, Benjamin Pingault, Elke Neu, Stefan Gsell, Matthias Schreck, Hadwig Sternschulte, Doris Steinmuller-Nethl, Christoph Becher, and Mete Atature. Optical signatures of silicon-vacancy spins in diamond. *Nature communications*, 5, 2014.

[67] Benjamin Pingault, Jonas N. Becker, Carsten H.H. Schulte, Carsten Arend, Christian Hepp, Tillmann Godde, Alexander I. Tartakovskii, Matthew Markham, Christoph Becher, and Mete Atature. All-Optical Formation of Coherent Dark States of Silicon-Vacancy Spins in Diamond. *Physical Review Letters*, 263601, 2014.

[68] E. Schrodinger. Die gegenwartige situation in der quantenmechanik. *Naturwissenschaften*, 23(48):807–812, Nov 1935.

[69] T D Ladd, F Jelezko, R Laflamme, Y Nakamura, C Monroe, and J L O'Brien. Quantum computers. *Nature*, 464(7285), 2010.

[70] Eleanor Rieffel and Wolfgang Polak. An introduction to quantum computing for non-physicists, 2000.

[71] F. Jelezko and J. Wrachtrup. Single defect centres in diamond: A review. *Physica Status Solidi (A) Applications and Materials Science*, 203, 2006.

[72] Igor Aharonovich, Andrew D. Greentree, and Steven Prawer. Diamond photonics. *Nature Photonics*, 5, 2011.

[73] Alp Sipahigil, Kay D. Jahnke, Lachlan J. Rogers, A Zibrov, Fedor Jelezko, and Mikhail D. Lukin. Indistinguishable photons from separated silicon-vacancy centers in diamond. *Physical review letters*, 113, 06 2014.

[74] B. J M Hausmann, B. J. Shields, Q. Quan, Y. Chu, N. P. De Leon, R. Evans, M. J. Burek, A. S. Zibrov, M. Markham, D. J. Twitchen, H. Park, M. D. Lukin, and M. Loncar. Coupling of NV centers to photonic crystal nanobeams in diamond. *Nano Letters*, 13, 2013.

[75] Lachlan J. Rogers, Kay D. Jahnke, Mathias H. Metsch, Alp Sipahigil, Jan M. Binder, Tokuyuki Teraji, Hitoshi Sumiya, Junichi Isoya, Mikhail D. Lukin, Philip Hemmer, and Fedor Jelezko. All-optical initialization, readout, and coherent preparation of single silicon-vacancy spins in diamond. *Phys. Rev. Lett.*, 113, 2014.

[76] Kay D Jahnke, Alp Sipahigil, Jan M Binder, Marcus W Doherty, Mathias Metsch, Lachlan J Rogers, Neil B Manson, Mikhail D Lukin, and Fedor Jelezko. Electron-phonon processes of the silicon-vacancy centre in diamond. *New Journal of Physics*, 17, 2015.

[77] Christian Hepp, Tina Muller, Victor Waselowski, Jonas N. Becker, Benjamin Pingault, Hadwig Sternschulte, Doris Steinmuller-Nethl, Adam Gali, Jeronimo R. Maze, Mete Atature, and Christoph Becher. Electronic structure of the silicon vacancy color center in diamond. *Physical Review Letters*, 112, 2014.

[78] Srujan Meesala, Young-Ik Sohn, Benjamin Pingault, Linbo Shao, Haig A. Atikian, Jeffrey Holzgrafe, Mustafa Gündoğan, Camille Stavrakas, Alp Sipahigil, Cleaven Chia, Ruffin Evans, Michael J. Burek, Mian Zhang, Lue Wu, Jose L. Pacheco, John Abraham, Edward Bielejec, Mikhail D. Lukin, Mete Atatüre, and Marko Lončar. Strain engineering of the silicon-vacancy center in diamond. *Phys. Rev. B*, 97:205444, May 2018.

[79] Young-Ik Sohn, Srujan Meesala, Benjamin Pingault, Haig A. Atikian, Jeffrey Holzgrafe, Mustafa Gündoğan, Camille Stavrakas, Megan J. Stanley, Alp Sipahigil, Joonhee Choi, Mian Zhang, Jose L. Pacheco, John Abraham, Edward Bielejec, Mikhail D. Lukin, Mete Atatr̈e, and Marko Lončar. Controlling the coherence of a diamond spin qubit through its strain environment. *Nature Communications*, 2018.

[80] David P. DiVincenzo. The physical implementation of quantum computation. *Fortschritte der Physik*, 48(9-11):771–783, 2000.

[81] Marvin Minsky. Double focussing stage scanning microscope - us patent number 3013467, 1957.

[82] Paul Davidovits and M. David Egger. Scanning laser microscope. *Nature*, 223:831, 1969.

[83] Paul Davidovits and M. David Egger. Photomicrography of corneal endothelial cells in vivo. *Nature*, 244:366–367, 1973.

[84] James Jonkman and Claire M. Brown. Any way you slice it—a comparison of confocal microscopy techniques. *J Biomol Tech.*, 26:54–65, 2015.

[85] Shyamsunder Erramilli. Confocal and two-photon microscopy—foundations, applications and advances. *Biomolecular Engineering*, 21:119–120, 11 2004.

[86] Alberto Diaspro, Paolo Bianchini, Giuseppe Vicidomini, Mario Faretta, Paola Ramoino, and Cesare Usai. Multi-photon excitation microscopy. *Biomed Eng Online*, 5, 2006.

[87] W. Amos and J. White. How the confocal laser scanning microscope entered biological research. *Biology of the Cell*, 95:335–342, 2003.

[88] JB Pawley. *Handbook of Biological Confocal Microscopy, 3rd edition*. Plenum Press, New York, 2006.

[89] B. V. R. Tata and Baldev Raj. Confocal laser scanning microscopy: Applications in material science and technology. *Bulletin of Materials Science*, 21(4):263–278, Aug 1998.

[90] C. Saldaña, V. Morales-Tlalpan, and V.M. Castaño. Confocal microscopy: from fundamental optics to innovative applications. *Microscopy: Science, Technology, Applications and Education, book by A.Méndez-Vilas and J. Díaz (Eds.)*, pages 1350–1355, 2010.

[91] Robert H Webb. Confocal optical microscopy. *Reports on Progress in Physics*, 59(3):427–471, mar 1996.

[92] G. B. Airy. On the Diffraction of an Object-glass with Circular Aperture. *Transactions of the Cambridge Philosophical Society*, 5:283, 1835.

[93] Gordon S. Kino and Timothy R. Corle. Confocal scanning optical microscopy. *Physics Today*, 42:55, 1989.

[94] T. Wilson. Optical sectioning in confocal fluorescent microscopes. *Journal of Microscopy*, 154:143–156, 1989.

[95] Incheon Song, Hongki Yoo, Jaebum Choo, and Dae-Gab Gweon. Measurement of point-spread function (psf) for confocal fluorescence microscopy. *Proceedings of SPIE - The International Society for Optical Engineering*, 5878, 08 2005.

[96] Michael Wahl PicoQuant. Time-correlated single photon counting.

[97] Anthony E. Siegman. *Lasers*. University Science Books, 1986.

[98] Theodore Maiman. Stimulated optical radiation in ruby. *Nature*, 187:493–494, 1960.

[99] P. F. Moulton. Spectroscopic and laser characteristics of ti:al2o3. *J. Opt. Soc. Am. B*, 3:125–133, 1986.

[100] T. Brabec, Ch. Spielmann, P. F. Curley, and F. Krausz. Kerr lens mode locking. *Opt. Lett.*, 17(18):1292–1294, 1992.

[101] Newport. Photonics technical note 1: Power meters and detectors.

[102] L. Brillouin. Diffusion of light and x-rays by a transparent homogeneous body. *Annales de Physique*, 17:88–122, 1922.

[103] J. Sapriel, S. Francis, and B. Kelly. *Acousto-Optics*. Wiley, 1979.

[104] McCarron D. J. A guide to acousto-optic modulators, 2007.

[105] Inrad Optics. Understanding electro-optic behavior.

[106] Schäfter+Kirchhoff. Optical modulators.

[107] ConOptics. Electro-optic components and systems.

[108] A.A Sa Opto-Electronic. Complete range of acousto-optic devices.

[109] ISOMET. Application note - an0510 - acousto-optic modulation.

[110] A.A Sa Opto-Electronic. Do you know acousto-optics? application notes.

[111] Newport. Technical note: Gaussian beam optics.

[112] A.A Sa Opto-Electronic and Pegasus Optik. Mt350 fast aom.

[113] Edward S. Barnard, Benedikt Ursprung, Eric Colegrove, Helio R. Moutinho, Nicholas J. Borys, Brian E. Hardin, Craig H. Peters, Wyatt K. Metzger, and P. James Schuck. 3D Lifetime Tomography Reveals How CdCl2Improves Recombination Throughout CdTe Solar Cells. *Advanced Materials*, 29(3), 2017.

[114] J.G. Fujimoto and D. Farkas. *Biomedical optical imaging*. Oxford University Press, 2009.

[115] Edward S. Barnard, Eric T. Hoke, Stephen T. Connor, James R. Groves, Tevye Kuykendall, Zewu Yan, Eric C. Samulon, Edith D. Bourret-Courchesne, Shaul Aloni, P. James Schuck, Craig H. Peters, and Brian E. Hardin. Probing carrier lifetimes in photovoltaic materials using subsurface two-photon microscopy. *Scientific Reports*, 3, 2013.

[116] Neil Everall. Modeling and measuring the effect of refraction on the depth resolution of confocal raman microscopy. *Applied Spectroscopy - APPL SPECTROSC*, 54:773–782, 06 2000.

[117] Bernard Wenger, Pabitra K. Nayak, Xiaoming Wen, Sameer V. Kesava, Nakita K. Noel, and Henry J. Snaith. Consolidation of the optoelectronic properties of ch3nh3pbbr3 perovskite single crystals. *Nature Communications*, 8(590), 2017.

[118] Sebastian Isbaner, Narain Karedla, Daja Ruhlandt, Simon C. Stein, Anna Chizhik, Ingo Gregor, and Jorg Enderlein. Dead-time correction of fluorescence lifetime measurements and fluorescence lifetime imaging. *Optics Express*, 24:9429–9445, 2016.

[119] Grant Walters, Brandon R. Sutherland, Sjoerd Hoogland, Dong Shi, Riccardo Comin, Daniel P. Sellan, Osman M. Bakr, and Edward. H. Sargent. Two-photon absorption in organometallic bromide perovskites. *ACS Nano*, 9(9):9340–9346, 2015. PMID: 26196162.

[120] Felix Saouma, Dae Young Park, Sung Hyuk Kim, mun seok Jeong, and Joon Jang. Multiphoton absorption coefficients of organic-inorganic lead halide perovskites ch 3 nh 3 pbx 3 (x = cl, br, i) single crystals. *Chemistry of Materials*, 29, 07 2017.

[121] Markku Makitalo and Alessandro Foi. Optimal inversion of the anscombe transformation in low-count poisson image denoising. *IEEE transactions*.

[122] Claudio Quarti, Edoardo Mosconi, James M. Ball, Valerio D'Innocenzo, Chen Tao, Sandeep Pathak, Henry J. Snaith, Annamaria Petrozza, and Filippo De Angelis. Structural and optical properties of methylammonium lead iodide across the tetragonal to cubic phase transition: implications for perovskite solar cells. *Energy Environ. Sci.*, 9:155–163, 2016.

[123] Camille Stavrakas, Szymon J. Zelewski, Kyle Frohna, Edward P. Booker, Krzysztof Galkowski, Kangyu Ji, Edoardo Ruggeri, Sebastian Mackowski, Robert Kudrawiec, Paulina Plochocka, and Samuel D. Stranks. Influence of grain size on phase transitions in halide perovskite films. *Advanced Energy Materials*, 9, 2019.

[124] Pierre Adrien Mante, Constantinos C. Stoumpos, Mercouri G. Kanatzidis, and Arkady Yartsev. Directional Negative Thermal Expansion and Large Poisson Ratio in CH3NH3PbI3 Perovskite Revealed by Strong Coherent Shear Phonon Generation. *Journal of Physical Chemistry Letters*, 2018.

[125] Antoine Létoublon, Serge Paofai, Benoît Rufflé, Philippe Bourges, Bernard Hehlen, Thierry Michel, Claude Ecolivet, Olivier Durand, Stéphane Cordier, Claudine Katan, and Jacky Even. Elastic Constants, Optical Phonons, and Molecular Relaxations in the High Temperature Plastic Phase of the CH3NH3PbBr3 Hybrid Perovskite. *Journal of Physical Chemistry Letters*, 2016.

[126] Yevgeny Rakita, Sidney R. Cohen, Nir Klein Kedem, Gary Hodes, and David Cahen. Mechanical properties of APbX3 (A = Cs or CH3NH3; X = i or Br) perovskite single crystals. *MRS Communications*, 2015.

[127] Massimo Spina, Ayat Karimi, Wanda Andreoni, Carlo A. Pignedoli, Bálint Náfrádi, László Forró, and Endre Horváth. Mechanical signatures of degradation of the photovoltaic perovskite CH3NH3PbI3upon water vapor exposure. *Applied Physics Letters*, 2017.

[128] W. N. Sharpe. Mechanical properties of MEMS materials. In *2001 International Semiconductor Device Research Symposium, ISDRS 2001 - Proceedings*, 2001.

[129] Kurt E. Petersen. Silicon as a mechanical material. In *Micromechanics and MEMS: Classic and Seminal Papers to 1990*. 1997.

[130] SM Sze. Wiley-Interscience.

[131] Tang-Yu Lai, Yu-Jen Hsiao, and Te-Hua Fang. Mechanical properties of CIGS film with different metallic composition by co-evaporation method. *Materials Research Express*, 4(11):115006, nov 2017.

[132] Shi Luo, Jiun Haw Lee, Chee Wee Liu, Jia Min Shieh, Chang Hong Shen, Tsung Ta Wu, Dongchan Jang, and Julia R. Greer. Strength, stiffness, and microstructure of Cu(In,Ga)Se2 thin films deposited via sputtering and co-evaporation. *Applied Physics Letters*, 2014.

[133] I. V. Kurilo, V. P. Alekhin, I. O. Rudyi, S. I. Bulychev, and L. I. Osypyshin. Mechanical properties of ZnTe, CdTe, CdHgTe and HgTe crystals from micromechanical investigation. *Physica Status Solidi (A) Applied Research*, 1997.

[134] Ana María Martínez, Rosario Soriano, Ricardo Faccio, and Alicia Beatríz Trigubó. Mechanical Properties Calculation of II-VI Semiconductors: Cd1-yZnyTe($0 \leq y \leq 1$). *Procedia Materials Science*, 8:656–664, 2015.

[135] Eric T. Hoke, Daniel J. Slotcavage, Emma R. Dohner, Andrea R. Bowring, Hemamala I. Karunadasa, and Michael D. McGehee. Reversible photo-induced trap formation in mixed-halide hybrid perovskites for photovoltaics. *Chemical Science*, 2015.

[136] Miguel Anaya, Juan F. Galisteo-López, Mauricio E. Calvo, Juan P. Espinós, and Hernán Míguez. Origin of Light-Induced Photophysical Effects in Organic Metal Halide Perovskites in the Presence of Oxygen. *Journal of Physical Chemistry Letters*, 2018.

[137] Xiaofan Deng, Xiaoming Wen, Cho Fai Jonathan Lau, Trevor Young, Jae Yun, Martin A. Green, Shujuan Huang, and Anita W.Y. Ho-Baillie. Electric field induced reversible and irreversible photoluminescence responses in methylammonium lead iodide perovskite. *Journal of Materials Chemistry C*, 2016.

[138] Priyanka Singh and N. M. Ravindra. Temperature dependence of solar cell performance - An analysis. *Solar Energy Materials and Solar Cells*, 2012.

[139] Anna Osherov, Eline M. Hutter, Krzysztof Galkowski, Roberto Brenes, Duncan K. Maude, Robin J. Nicholas, Paulina Plochocka, Vladimir Bulović, Tom J. Savenije, and Samuel D. Stranks. The Impact of Phase Retention on the Structural and Optoelectronic Properties of Metal Halide Perovskites. *Advanced Materials*, 2016.

[140] Weiguang Kong, Zhenyu Ye, Zhen Qi, Bingpo Zhang, Miao Wang, Arash Rahimi-Iman, and Huizhen Wu. Characterization of an abnormal photoluminescence behavior upon crystal-phase transition of perovskite CH3NH3PbI3. *Physical Chemistry Chemical Physics*, 2015.

[141] P. S. Whitfield, N. Herron, W. E. Guise, K. Page, Y. Q. Cheng, I. Milas, and M. K. Crawford. Structures, Phase Transitions and Tricritical Behavior of the Hybrid Perovskite Methyl Ammonium Lead Iodide. *Scientific Reports*, 2016.

[142] Sibel Y. Leblebici, Linn Leppert, Yanbo Li, Sebastian E. Reyes-Lillo, Sebastian Wickenburg, Ed Wong, Jiye Lee, Mauro Melli, Dominik Ziegler, Daniel K. Angell, D. Frank Ogletree, Paul D. Ashby, Francesca M. Toma, Jeffrey B. Neaton, Ian D. Sharp, and Alexander Weber-Bargioni. Facet-dependent photovoltaic efficiency variations in single grains of hybrid halide perovskite. *Nature Energy*, 2016.

[143] K. Galkowski, A. A. Mitioglu, A. Surrente, Z. Yang, D. K. Maude, P. Kossacki, G. E. Eperon, J. T.W. Wang, H. J. Snaith, P. Plochocka, and R. J. Nicholas. Spatially resolved studies of the phases and morphology of methylammonium and formamidinium lead tri-halide perovskites. *Nanoscale*, 2017.

[144] Milan Vrucinic, Clemens Matthiesen, Aditya Sadhanala, Giorgio Divitini, Stefania Cacovich, Sian E. Dutton, Caterina Ducati, Mete Atat??re, Henry Snaith, Richard H. Friend, Henning Sirringhaus, and Felix Deschler. Local Versus Long-Range Diffusion Effects of Photoexcited States on Radiative Recombination in Organic-Inorganic Lead Halide Perovskites. *Advanced Science*, 2015.

[145] Camille Stavrakas, Ayan A. Zhumekenov, Roberto Brenes, Mojtaba Abdi-Jalebi, Vladimir Bulović, Osman M. Bakr, Edward S. Barnard, and Samuel D. Stranks. Probing buried recombination pathways in perovskite structures using 3d photoluminescence tomography. *Energy Environ. Sci.*, 11:2846–2852, 2018.

[146] Xiaodong Ren, Zhou Yang, Dong Yang, Xu Zhang, Dong Cui, Yucheng Liu, Qingbo Wei, Haibo Fan, and Shengzhong Frank Liu. Modulating crystal grain size and optoelectronic properties of perovskite films for solar cells by reaction temperature. *Nanoscale*, 2016.

[147] Nadja Giesbrecht, Johannes Schlipf, Irene Grill, Philipp Rieder, Vladimir Dyakonov, Thomas Bein, Achim Hartschuh, Peter Müller-Buschbaum, and Pablo Docampo. Single-crystal-like optoelectronic-properties of MAPbI3 perovskite polycrystalline thin films. *Journal of Materials Chemistry A*, 6(11):4822–4828, 2018.

[148] Bo Chen, Tao Li, Qingfeng Dong, Edoardo Mosconi, Jingfeng Song, Zhaolai Chen, Yehao Deng, Ye Liu, Stephen Ducharme, Alexei Gruverman, Filippo De Angelis, and Jinsong Huang. Large electrostrictive response in lead halide perovskites. *Nature Materials*, 2018.

[149] Wei Zhang, Sandeep Pathak, Nobuya Sakai, Thomas Stergiopoulos, Pabitra K. Nayak, Nakita K. Noel, Amir A. Haghighirad, Victor M. Burlakov, Dane W. Dequilettes, Aditya Sadhanala, Wenzhe Li, Liduo Wang, David S. Ginger, Richard H. Friend, and Henry J. Snaith. Enhanced optoelectronic quality of perovskite thin films with hypophosphorous acid for planar heterojunction solar cells. *Nature Communications*, 2015.

[150] Jonathon S. Bechtel and Anton Van der Ven. Octahedral tilting instabilities in inorganic halide perovskites. *Physical Review Materials*, 2018.

[151] Timothy W. Jones, Anna Osherov, Mejd Alsari, Melany Sponseller, Benjamin C. Duck, Young-Kwang Jung, Charles Settens, Farnaz Niroui, Roberto Brenes, Camelia V. Stan, Yao Li, Mojtaba Abdi-Jalebi, Nobumichi Tamura, J. Emyr Macdonald, Manfred Burghammer, Richard H. Friend, Vladimir Bulović, Aron Walsh, Gregory J. Wilson, Samuele Lilliu, and Samuel D. Stranks. Local Strain Heterogeneity Influences the Optoelectronic Properties of Halide Perovskites. mar 2018.

[152] Samuel D. Stranks, Pabitra K. Nayak, Wei Zhang, Thomas Stergiopoulos, and Henry J. Snaith. Formation of thin films of organic-inorganic perovskites for high-efficiency solar cells. *Angewandte Chemie - International Edition*, 54(11):3240–3248, 2015.

[153] Alexander Kovalenko and Michal Hrabal. Printable Solar Cells. *Printable Solar Cells*, pages 163–202, 2017.

[154] Makhsud I. Saidaminov, Valerio Adinolfi, Riccardo Comin, Ahmed L. Abdelhady, Wei Peng, Ibrahim Dursun, Mingjian Yuan, Sjoerd Hoogland, Edward H. Sargent, and Osman M. Bakr. Planar-integrated single-crystalline perovskite photodetectors. *Nature Communications*, 6, 2015.

[155] Makhsud I. Saidaminov, Ahmed L. Abdelhady, Banavoth Murali, Erkki Alarousu, Victor M. Burlakov, Wei Peng, Ibrahim Dursun, Lingfei Wang, Yao He, Giacomo MacUlan, Alain Goriely, Tom Wu, Omar F. Mohammed, and Osman M. Bakr. High-quality bulk hybrid perovskite single crystals within minutes by inverse temperature crystallization. *Nature Communications*, 6, 2015.

[156] Samuel D. Stranks. Nonradiative Losses in Metal Halide Perovskites, 2017.

[157] Roberto Brenes, Dengyang Guo, Anna Osherov, Nakita K. Noel, Christopher Eames, Eline M. Hutter, Sandeep K. Pathak, Farnaz Niroui, Richard H. Friend, M. Saiful Islam, Henry J. Snaith, Vladimir Bulović, Tom J. Savenije, and Samuel D. Stranks. Metal Halide Perovskite Polycrystalline Films Exhibiting Properties of Single Crystals. *Joule*, 1(1):155–167, 2017.

[158] Connor G. Bischak, Erin M. Sanehira, Jake T. Precht, Joseph M. Luther, and Naomi S. Ginsberg. Heterogeneous Charge Carrier Dynamics in Organic-Inorganic Hybrid Materials: Nanoscale Lateral and Depth-Dependent Variation of Recombination Rates in Methylammonium Lead Halide Perovskite Thin Films. *Nano Letters*, 15(7):4799–4807, 2015.

[159] Dane W. DeQuilettes, Sarthak Jariwala, Sven Burke, Mark E. Ziffer, Jacob T.W. Wang, Henry J. Snaith, and David S. Ginger. Tracking Photoexcited Carriers in Hybrid Perovskite Semiconductors: Trap-Dominated Spatial Heterogeneity and Diffusion. *ACS Nano*, 11(11):11488–11496, 2017.

[160] Rafael Yuste. Fluorescence microscopy today, 2005.

[161] Fritjof Helmchen and Winfried Denk. Deep tissue two-photon microscopy, 2005.

[162] Weijian Yang and Rafael Yuste. In vivo imaging of neural activity, 2017.

[163] Jingzhou Li, Saifeng Zhang, Hongxing Dong, Xinqiang Yuan, Xiongwei Jiang, Jun Wang, and Long Zhang. Two-photon absorption and emission in CsPb(Br/I)3 cesium lead halide perovskite quantum dots. *CrystEngComm*, 18:7945–7949, 2016.

[164] Tingchao He, Junzi Li, Can Ren, Shuyu Xiao, Yiwen Li, and Rui Chen. Strong two-photon absorption of Mn-doped CsPbCl 3 perovskite nanocrystals. *Appl. Phys. Lett.*, 211105:1–5, 2017.

[165] Weiwei Liu, Jun Xing, Jiaxin Zhao, Xinglin Wen, Kai Wang, Peixiang Lu, and Qihua Xiong. Giant Two-Photon Absorption and Its Saturation in 2D Organic–Inorganic Perovskite. *Advanced Optical Materials*, 5(7), 2017.

[166] Khadga Jung Karki, Mohamed Abdellah, Wei Zhang, and Tõnu Pullerits. Different emissive states in the bulk and at the surface of methylammonium lead bromide perovskite revealed by two-photon micro-spectroscopy and lifetime measurements. *APL Photonics*, 1(4):046103, 2016.

[167] Supriya Ghosh, Suman Kalyan Pal, Khadga J. Karki, and Tönu Pullerits. Ion Migration Heals Trapping Centers in CH ₃ NH ₃ PbBr ₃ Perovskite. *ACS Energy Letters*, pages 2133–2139, 2017.

[168] Bo Wu, Huy Tiep Nguyen, Zhiliang Ku, Guifang Han, David Giovanni, Nripan Mathews, Hong Jin Fan, and Tze Chien Sum. Discerning the Surface and Bulk Recombination Kinetics of Organic–Inorganic Halide Perovskite Single Crystals. *Advanced Energy Materials*, 6(14), 2016.

[169] Banavoth Murali, Sukumar Dey, Ahmed L. Abdelhady, Wei Peng, Erkki Alarousu, Ahmad R. Kirmani, Namchul Cho, Smritakshi Phukan Sarmah, Manas R. Parida, Makhsud I. Saidaminov, Ayan A. Zhumekenov, Jingya Sun, Mohd S. Alias, Emre Yengel, Boon S. Ooi, Aram Amassian, Osman M. Bakr, and Omar F. Mohammed. Surface Restructuring of Hybrid Perovskite Crystals. *ACS Energy Letters*, 1(6):1119–1126, 2016.

[170] Junsheng Chen, Karel Žídek, Pavel Chábera, Dongzhou Liu, Pengfei Cheng, Lauri Nuuttila, Mohammed J. Al-Marri, Heli Lehtivuori, Maria E. Messing, Keli Han, Kaibo Zheng, and Tõnu Pullerits. Size-And Wavelength-Dependent Two-Photon Absorption Cross-Section of CsPbBr3 Perovskite Quantum Dots. *Journal of Physical Chemistry Letters*, 8(10):2316–2321, 2017.

[171] Qi Wei, Bin Du, Bo Wu, Jia Guo, Ming jie Li, Jianhui Fu, Zhipeng Zhang, Jianwei Yu, Tianyu Hou, Guichuan Xing, Tze Chien Sum, and Wei Huang. Two-Photon Optical Properties in Individual Organic–Inorganic Perovskite Microplates. *Advanced Optical Materials*, 5(24), 2017.

[172] Juan F. Galisteo-López, Yuelong Li, and Hernán Míguez. Three-Dimensional Optical Tomography and Correlated Elemental Analysis of Hybrid Perovskite Microstructures: An Insight into Defect-Related Lattice Distortion and Photoinduced Ion Migration. *Journal of Physical Chemistry Letters*, 7(24):5227–5234, 2016.

[173] Michael Saliba, Taisuke Matsui, Ji-Youn Seo, Konrad Domanski, Juan-Pablo Correa-Baena, Mohammad Khaja Nazeeruddin, Shaik M. Zakeeruddin, Wolfgang Tress, Antonio Abate, Anders Hagfeldt, and Michael Grätzel. Cesium-containing triple cation perovskite solar cells: improved stability, reproducibility and high efficiency. *Energy Environ. Sci.*, 9:1989–1997, 2016.

[174] Wei Zhang, Sandeep Pathak, Nobuya Sakai, Thomas Stergiopoulos, Pabitra K. Nayak, Nakita K. Noel, Amir A. Haghighirad, Victor M. Burlakov, Dane W. Dequilettes, Aditya Sadhanala, Wenzhe Li, Liduo Wang, David S. Ginger, Richard H. Friend, and Henry J. Snaith. Enhanced optoelectronic quality of perovskite thin films with hypophosphorous acid for planar heterojunction solar cells. *Nature Communications*, 6, 2015.

[175] Mojtaba Abdi-Jalebi, M. Ibrahim Dar, Aditya Sadhanala, Satyaprasad P. Senanayak, Fabrizio Giordano, Shaik Mohammed Zakeeruddin, Michael Grätzel, and Richard H. Friend. Impact of a Mesoporous Titania-Perovskite Interface on the Performance of Hybrid Organic-Inorganic Perovskite Solar Cells. *Journal of Physical Chemistry Letters*, 7(16):3264–3269, 2016.

[176] Adam D. Wright, Rebecca L. Milot, Giles E. Eperon, Henry J. Snaith, Michael B. Johnston, and Laura M. Herz. Band-Tail Recombination in Hybrid Lead Iodide Perovskite. *Advanced Functional Materials*, 27(29), 2017.

[177] Bernard Wenger, Pabitra K. Nayak, Xiaoming Wen, Sameer V. Kesava, Nakita K. Noel, and Henry J. Snaith. Consolidation of the optoelectronic properties of CH3NH3PbBr3 perovskite single crystals. *Nature Communications*, 8(1):590, 2017.

[178] Dong Shi, Valerio Adinolfi, Riccardo Comin, Mingjian Yuan, Erkki Alarousu, Andrei Buin, Yin Chen, Sjoerd Hoogland, Alexander Rothenberger, Khabiboulakh Katsiev, Yaroslav Losovyj, Xin Zhang, Peter A. Dowben, Omar F. Mohammed, Edward H. Sargent, and Osman M. Bakr. Low trap-state density and long carrier diffusion in organolead trihalide perovskite single crystals. *Science*, 2015.

[179] Valerio Adinolfi, Mingjian Yuan, Riccardo Comin, Emmanuel S. Thibau, Dong Shi, Makhsud I. Saidaminov, Pongsakorn Kanjanaboos, Damir Kopilovic, Sjoerd Hoogland, Zheng Hong Lu, Osman M. Bakr, and Edward H. Sargent. The In-Gap Electronic State Spectrum of Methylammonium Lead Iodide Single-Crystal Perovskites. *Advanced Materials*, 2016.

[180] Vishesh Manjunath, Ramya Krishna, Suresh Maniarasu, Easwaramoorthi Ramasamy, Sakthivel Shanmugasundaram, and Ganapathy Veerappan. Chapter 4 - perovskite solar cell architectures. In Sabu Thomas and Aparna Thankappan, editors, *Perovskite Photovoltaics*, pages 89 – 121. Academic Press, 2018.

[181] Krzysztof Galkowski, Anatolie Mitioglu, Atsuhiko Miyata, Paulina Plochocka, Oliver Portugall, Giles E. Eperon, Jacob Tse-Wei Wang, Thomas Stergiopoulos, Samuel D. Stranks, Henry J. Snaith, and Robin J. Nicholas. Determination of the exciton binding energy and effective masses for methylammonium and formamidinium lead tri-halide perovskite semiconductors. *The Royal Society of Chemistry*, 9(3):962–970, 2016.

[182] Hiba Diab, Gaëlle Trippé-Allard, Ferdinand Lédée, Khaoula Jemli, Christèle Vilar, Guillaume Bouchez, Vincent L.R. Jacques, Antonio Tejeda, Jacky Even, Jean-Sébastien Lauret, Emmanuelle Deleporte, and Damien Garrot. Narrow linewidth excitonic emission in organic–inorganic lead iodide perovskite single crystals. *The Journal of Physical Chemistry Letters*, 7(24):5093–5100, 2016. PMID: 27973876.

[183] Hiba Diab, Christophe Arnold, Ferdinand Lédée, Gaëlle Trippé-Allard, Géraud Delport, Christèle Vilar, Fabien Bretenaker, Julien Barjon, Jean-Sébastien Lauret, Emmanuelle Deleporte, and Damien Garrot. Impact of reabsorption on the emission spectra and recombination dynamics of hybrid perovskite single crystals. *The Journal of Physical Chemistry Letters*, 8(13):2977–2983, 2017. PMID: 28608691.

[184] Richard Ciesielski, Frank Schafer, Nicolai F. Hartmann, Nadja Giesbrecht, Thomas Bein, Pablo Docampo, and Achim Hartschuh. Grain boundaries act as solid walls for charge carrier diffusion in large crystal mapi thin films. *ACS Applied Materials and Interfaces*, 10:7974–7981, 02 2018.

[185] Qingfeng Dong, Yanjun Fang, Yuchuan Shao, Padhraic Mulligan, Jie Qiu, Lei Cao, and Jinsong Huang. Electron-hole diffusion lengths > 175 μm in solution-grown ch3nh3pbi3 single crystals. *Science*, 347, 2015.

[186] Bart Roose, Amita Ummadisingu, Juan-Pablo Correa-Baena, Michael Saliba, Anders Hagfeldt, Michael Graetzel, Ullrich Steiner, and Antonio Abate. Spontaneous crystal coalescence enables highly efficient perovskite solar cells. *Nano Energy*, 39:24 – 29, 2017.

[187] Yu Li, Weibo Yan, Yunlong Li, Shufeng Wang, Wei Wang, Zuqiang Bian, Lixin Xiao, and Qihuang Gong. Direct observation of long electron-hole diffusion distance in ch3nh3pbi3 perovskite thin film. *Scientific Reports*, 5(14485), 2015.

[188] Adrien Bercegol, Daniel Ory, Daniel Suchet, Stefania Cacovich, Olivier Fournier, Jean Rousset, and Laurent Lombez. Quantitative optical assessment of photonic and electronic properties in halide perovskite. *Nature Communications*, 10(1), 2019.

[189] Robert J. Stewart, Christopher Grieco, Alec V. Larsen, Joshua J. Maier, and John B. Asbury. Approaching bulk carrier dynamics in organo-halide perovskite nanocrystalline films by surface passivation. *The Journal of Physical Chemistry Letters*, 7(7):1148–1153, 2016. PMID: 26966792.

[190] Juan-Pablo Correa-Baena, Silver-Hamill Turren-Cruz, Wolfgang Tress, Anders Hagfeldt, Clara Aranda, Leyla Shooshtari, Juan Bisquert, and Antonio Guerrero. Changes from bulk to surface recombination mechanisms between pristine and cycled perovskite solar cells. *ACS Energy Letters*, 2(3):681–688, 2017.

[191] Markus Deserno. One-dimensional diffusion on a finite region, 2004.

[192] M. Abramowitz and I. A. Stegun. *Handbook of mathematical functions*. Dover Books, New York, 9th printing, 1970.

[193] MIT lecture series. Diffusion of an instantaneous, point release.

[194] Gleb Akselrod, Parag B Deotare, Nicholas J Thompson, Jiye Lee, William Tisdale, Marc A Baldo, Vinod Menon, and Vladimir Bulovic. Visualization of exciton transport in ordered and disordered molecular solids. *Nature communications*, 5:3646, 04 2014.

[195] Jean-Philippe Bouchaud and Antoine Georges. Anomalous diffusion in disordered media: Statistical mechanisms, models and physical applications. *Physics Reports*, 195(4):127 – 293, 1990.

[196] J. Crank. *The mathematics of diffusion*. Clarendon Press, Oxford, second edition, 1975.

[197] Rudy Slingerland and Lee Kump. *Mathematical Modeling of Earth's Dynamical Systems*. Princeton University Press, 2011.

[198] Bat-El Cohen, Malgorzata Wierzbowska, and Lioz Etgar. High efficiency quasi 2d lead bromide perovskite solar cells using various barrier molecules. *Sustainable Energy Fuels*, 1:1935–1943, 2017.

[199] Luis M. Pazos-Outón, Monika Szumilo, Robin Lamboll, Johannes M. Richter, Micaela Crespo-Quesada, Mojtaba Abdi-Jalebi, Harry J. Beeson, Milan Vrućinić, Mejd Alsari, Henry J. Snaith, Bruno Ehrler, Richard H. Friend, and Felix Deschler. Photon recycling in lead iodide perovskite solar cells. *Science*, 351(6280):1430–1433, 2016.

[200] M. A. Steiner, J. F. Geisz, I. García, D. J. Friedman, A. Duda, and S. R. Kurtz. Optical enhancement of the open-circuit voltage in high quality gaas solar cells. *Journal of Applied Physics*, 113(12):123109, 2013.

[201] Editorial. Quantum evolution. *Nature Photonics*, 3(12), 2009.

[202] M. Fox. *Quantum Optics: An Introduction*. Oxford University Press, 2006.

[203] T E Northup and R Blatt. Quantum information transfer using photons. *Nat Photon*, 8(5), 2014.

[204] J L O'Brien, G J Pryde, a G White, T C Ralph, and D Branning. Demonstration of an all-optical quantum controlled-NOT gate. *Nature*, 426(6964), 2003.

[205] K Muller, T Kaldewey, R Ripszam, J S Wildmann, a Bechtold, M Bichler, G Koblmuller, G Abstreiter, and J J Finley. All optical quantum control of a spin-quantum state and ultrafast transduction into an electric current. *Scientific reports*, 3, 2013.

[206] P. Zoller, Th Beth, D. Binosi, R. Blatt, H. Briegel, D. Bruss, T. Calarco, J. I. Cirac, D. Deutsch, J. Eisert, a. Ekert, C. Fabre, N. Gisin, P. Grangiere, M. Grassl, S. Haroche, a. Imamoglu, a. Karlson, J. Kempe, L. Kouwenhoven, S. Kroll, G. Leuchs, M. Lewenstein, D. Loss, N. Lutkenhaus, S. Massar, J. E. Mooij, M. B. Plenio, E. Polzik, S. Popescu, G. Rempe, a. Sergienko, D. Suter, J. Twamley, G. Wendin, R. Werner, a. Winter, J. Wrachtrup, and a. Zeilinger. Quantum information processing and communication: Strategic report on current status, visions and goals for research in Europe. *European Physical Journal D*, 36, 2005.

[207] H J Kimble. The quantum internet. *Nature*, 453, 2008.

[208] Dominik Maxein and Julien Laurat. Trapped ion to flying qubit. *Nature Photonics*, 7, 2013.

[209] Weng W. Chow and Frank Jahnke. On the physics of semiconductor quantum dots for applications in lasers and quantum optics. *Progress in Quantum Electronics*, 37, 2013.

[210] F. Jahnke. *Quantum Optics with Semiconductor Nanostructures*. Woodhead Publishing Series in Electronic and Optical Materials, 2012.

[211] Jorg Wrachtrup and Fedor Jelezko. Processing quantum information in diamond. *Journal of Physics: Condensed Matter*, 18, 2006.

[212] Marcus W. Doherty, Neil B. Manson, Paul Delaney, Fedor Jelezko, Jorg Wrachtrup, and Lloyd C L Hollenberg. The nitrogen-vacancy colour centre in diamond. *Physics Reports*, 528, 2013.

[213] Gopalakrishnan Balasubramanian, Philipp Neumann, Daniel Twitchen, Matthew Markham, Roman Kolesov, Norikazu Mizuochi, Junichi Isoya, Jocelyn Achard, Johannes Beck, Julia Tissler, Vincent Jacques, Philip R Hemmer, Fedor Jelezko, and Jorg Wrachtrup. Ultralong spin coherence time in isotopically engineered diamond. *Nature materials*, 8, 2009.

[214] Helena S Knowles, Dhiren M Kara, and Mete Atature. Observing bulk diamond spin coherence in high-purity nanodiamonds. *Nature materials*, 13, 2014.

[215] F. Dolde, I. Jakobi, B. Naydenov, N. Zhao, S. Pezzagna, C. Trautmann, J. Meijer, P. Neumann, F. Jelezko, and J. Wrachtrup. Room-temperature entanglement between single defect spins in diamond. *Nature Physics*, 9, 2013.

[216] E Togan, Y Chu, A S Trifonov, L Jiang, J Maze, L Childress, M V G Dutt, A S Sorensen, P R Hemmer, A S Zibrov, and M D Lukin. Quantum entanglement between an optical photon and a solid-state spin qubit. *Nature*, 466, 2010.

[217] D L Moehring, P Maunz, S Olmschenk, K C Younge, D N Matsukevich, L-M Duan, and C Monroe. Entanglement of single-atom quantum bits at a distance. *Nature*, 449, 2007.

[218] Dmitry Budker. Diamond nanosensors: The sense of colour centres, 2011.

[219] P. Maletinsky, S. Hong, M. S. Grinolds, B. Hausmann, M. D. Lukin, R. L. Walsworth, M. Loncar, and A. Yacoby. A robust scanning diamond sensor for nanoscale imaging with single nitrogen-vacancy centres. *Nature Nanotechnology*, 7, 2012.

[220] C. L. Degen. Scanning magnetic field microscope with a diamond single-spin sensor. *Applied Physics Letters*, 92(24), 2008.

[221] Gopalakrishnan Balasubramanian, I Y Chan, Roman Kolesov, Mohannad Al-Hmoud, Julia Tisler, Chang Shin, Changdong Kim, Aleksander Wojcik, Philip R Hemmer, Anke Krueger, Tobias Hanke, Alfred Leitenstorfer, Rudolf Bratschitsch, Fedor Jelezko, and Jorg Wrachtrup. Nanoscale imaging magnetometry with diamond spins under ambient conditions. *Nature*, 455, 2008.

[222] M S Grinolds, S Hong, P Maletinsky, L Luan, M D Lukin, R L Walsworth, and A Yacoby. Nanoscale magnetic imaging of a single electron spin under ambient conditions. *Nature Physics*, 9, 2013.

[223] P. Neumann, I. Jakobi, F. Dolde, C. Burk, R. Reuter, G. Waldherr, J. Honert, T. Wolf, A. Brunner, J. H. Shim, D. Suter, H. Sumiya, J. Isoya, and J. Wrachtrup. High-precision nanoscale temperature sensing using single defects in diamond. *Nano Letters*, 13, 2013.

[224] G. Kucsko, P. C. Maurer, N. Y. Yao, M. Kubo, H. J. Noh, P. K. Lo, H. Park, and M. D. Lukin. Nanometre-scale thermometry in a living cell. *Nature*, 500:54–58, 2013.

[225] Ashok Ajoy, Ulf Bissbort, Mikhail D. Lukin, Ronald L. Walsworth, and Paola Cappellaro. Atomic-scale nuclear spin imaging using quantum-assisted sensors in diamond. *ArXiv*, 2014.

[226] C Santori, P E Barclay, K-M C Fu, R G Beausoleil, S Spillane, and M Fisch. Nanophotonics for quantum optics using nitrogen-vacancy centers in diamond. *Nanotechnology*, 21, 2010.

[227] R. Albrecht, A. Bommer, C. Deutsch, J. Reichel, and C. Becher. Coupling of a single N-V center in diamond to a fiber-based microcavity. In *2013 Conference on Lasers and Electro-Optics Europe and International Quantum Electronics Conference, CLEO/Europe-IQEC 2013*, 2013.

[228] Roland Albrecht, Alexander Bommer, Christoph Pauly, Frank Mucklich, Andreas W. Schell, Philip Engel, Tim Schroder, Oliver Benson, Jakob Reichel, and Christoph Becher. Narrow-band single photon emission at room temperature based on a single Nitrogen-vacancy center coupled to an all-fiber-cavity. *Appl. Phys. Lett.*, 2014.

[229] Tom Feng and Bradley D. Schwartz. Characteristics and origin of the 1.681 eV luminescence center in chemical-vapor-deposited diamond films. *Journal of Applied Physics*, 73, 1993.

[230] Andreas Dietrich, Kay D. Jahnke, Jan M. Binder, Tokuyuki Teraji, Junichi Isoya, Lachlan J. Rogers, and Fedor Jelezko. Isotopically varying spectral features of silicon vacancy in diamond. *arXiv preprint arXiv: ...*, 2014.

[231] Elke Neu, David Steinmetz, Janine Riedrich-Moller, Stefan Gsell, Martin Fischer, Matthias Schreck, and Christoph Becher. Single photon emission from silicon-vacancy colour centres in chemical vapour deposition nano-diamonds on iridium. *New Journal of Physics*, 13, 2011.

[232] V. S. Vavilov, A. A. Gippius, A. M. Zaitsev, B. V. Deryaguin, B. V. Spitsyn, , and A. E. Aleksenko. *Sov. Phys. Semicond.*, 14, 1980.

[233] C.D. Clark and C.B. Dickerson. The 1.681 ev centre in polycrystalline diamond. *Surface and Coatings Technology*, 47(1), 1991.

[234] J P Goss, R Jones, S J Breuer, P R Briddon, and Sven Öberg. The twelve-line 1.682 ev luminescence center in diamond and the vacancy-silicon complex. *Physical Review Letters*, 77, 1996.

[235] A. M. Edmonds, M. E. Newton, P. M. Martineau, D. J. Twitchen, and S. D. Williams. Electron paramagnetic resonance studies of silicon-related defects in diamond. *Phys. Rev. B*, 77, 2008.

[236] Elke Neu, Martin Fischer, Stefan Gsell, Matthias Schreck, and Christoph Becher. Fluorescence and polarization spectroscopy of single silicon vacancy centers in heteroepitaxial nanodiamonds on iridium. *Phys. Rev. B*, 84, 2011.

[237] Michael Fleischhauer, Atac Imamoglu, and Jonathan P. Marangos. Electromagnetically induced transparency: Optics in coherent media. *Rev. Mod. Phys.*, 77, 2005.

[238] Benjamin Pingault, David-Dominik Jarausch, Christian Hepp, Lina Klintberg, Jonas N. Becker, Matthew Markham, Christoph Becher, and Mete Atature. Coherent control of the silicon-vacancy spin in diamond. *Nature Communications*, 8, 2017.

[239] G. Giedke, J. M. Taylor, D. D'Alessandro, M. D. Lukin, and Imamoglu A. Quantum measurement of a mesoscopic spin ensemble. *Phys. Rev. A*, 74, 2006.

[240] L. Robledo, L. Childress, H. Bernien, B. Hensen, Paul F.Q. Alkemade, and R. Hanson. High-fidelity projective read-out of a solid-state spin quantum register. *Nature*, 477:574–578, 2011.

[241] G. de Lange, Z. H. Wang, D. Riste, V. V. Dobrovitski, and R. Hanson. Universal dynamical decoupling of a single solid-state spin from a spin bath. *Science*, 330(6000), 2010.

[242] H. Bernien, B. Hensen, W. Pfaff, G. Koolstra, M. S. Blok, L. Robledo, T. H. Taminiau, M. Markham, D. J. Twitchen, L. Childress, and R. Hanson. Heralded entanglement between solid-state qubits separated by three meters. *Nature*, 497:86–90, 2013.

[243] Jiabao Zheng, Matthew Trusheim, Tim Schröder, Michael Walsh, Camille Stavrakas, Benjamin Pingault, Mustafa Gundogan, Christian Hepp, Jose Pacheco, Edward Bielejec, Mete Atature, and Dirk Englund. Circular gratings for efficient collection from implanted silicon vacancy centres in diamond. *CLEO conference 2016*, 2016.

[244] Pawel Latawiec, Michael J. Burek, Young-Ik Sohn, and Marko Loncar. Faraday cage angled-etching of nanostructures in bulk dielectrics. *Journal of Vacuum Science & Technology B*, 34, 2016.

[245] Michael J Burek, Yiwen Chu, Madelaine SZ Liddy, Parth Patel, Jake Rochman, Srujan Meesala, Wooyoung Hong, Qimin Quan, Mikhail D. Lukin, and Marko Loncar. High quality-factor optical nanocavities in bulk single-crystal diamond. *Nature communications*, 5, 2014.

[246] Michael J. Burek, Justin D. Cohen, Sean M. Meenehan, Thibaud Ruelle, Srujan Meesala, Jake Rochman, Haig A. Atikian, Matthew Markham, Daniel J. Twitchen, Mikhail D. Lukin, Oskar Painter, and Marko Loncar. Diamond optomechanical crystals. *arXiv:1512.04166*, 2015.

[247] Srujan Meesala, Young-Ik Sohn, Haig A. Atikian, Samuel Kim, Michael J. Burek, Jennifer T. Choy, and Marko Loncar. Enhanced strain coupling of nitrogen-vacancy spins to nanoscale diamond cantilevers. *Phys. Rev. Applied*, 5:034010, 2016.

[248] W. L. Barnes, G. Bjork, J. M. Gerard, P. Jonsson, J. a E Wasey, P. T. Worthing, and V. Zwiller. Solid-state single photon sources: Light collection strategies. *European Physical Journal D*, 18, 2002.

[249] Jiabao Zheng, Edward Chen, Luozhou Li, Florian Dolde, and Dirk R. Englund. Optimized scalable circular grating with efficient photon extraction for nitrogen vacancy centers in a bulk diamond. In *CLEO: 2015*. Optical Society of America, 2015.

[250] P. Siyushev, F. Kaiser, V. Jacques, I. Gerhardt, S. Bischof, H. Fedder, J. Dodson, M. Markham, D. Twitchen, F. Jelezko, and J. Wrachtrup. Monolithic diamond optics for single photon detection. *Applied Physics Letters*, 97, 2010.

[251] G. Alzetta, A. Gozzini, L. Moi, and G. Orriols. An experimental method for the observation of r.f. transitions and laser beat resonances in oriented na vapour. *Il Nuovo Cimento B (1971-1996)*, 36(1):5–20, Nov 1976.

[252] Mark Fox. *Quantum Optics*. Oxford Master Series in Atomic, Optical and Laser Physics. Oxford University Press, 2006.

[253] Claude Cohen-Tannoudji. Dark resonances from optical pumping to cold atoms and molecules, 2009.

[254] J Dalibard, S Reynaud, and C Cohen-Tannoudji. La cascade radiative de l'atome habille. In Luigi A. Radicati di Bronzolo, editor, *Interaction of radiation with matter: A volume in honour of A. Gozzini*. Scuola Normale Superiore, 1987.

[255] S. Gateva, E. Alipieva, and E. Taskova. Power dependence of the coherent-population-trapping resonances registered in fluorescence and transmission: Resonance-width narrowing effects. *Phys. Rev. A*, 72, 2005.

[256] P. C. Maurer, G. Kucsko, C. Latta, L. Jiang, N. Y. Yao, S. D. Bennett, F. Pastawski, D. Hunger, N. Chisholm, M. Markham, D. J. Twitchen, J. I. Cirac, and M. D. Lukin. Room-Temperature Quantum Bit Memory Exceeding One Second. *Science*, 336, 2012.

[257] M V Gurudev Dutt, L Childress, L Jiang, E Togan, J Maze, F Jelezko, A S Zibrov, P R Hemmer, and M D Lukin. Quantum register based on individual electronic and nuclear spin qubits in diamond. *Science (New York, N.Y.)*, 316, 2007.

[258] Philipp Neumann, Johannes Beck, Matthias Steiner, Florian Rempp, Helmut Fedder, Philip R. Hemmer, Jörg Wrachtrup, and Fedor Jelezko. Single-shot readout of a single nuclear spin. *Science*, 329, 2010.

[259] Charles Kittel. *Introduction to Solid State Physics, 8th Edition*. Wiley, 2005.

[260] A E Hughes and W A Runciman. Uniaxial stress splitting of doubly degenerate states of tetragonal and trigonal centres in cubic crystals. *Proceedings of the Physical Society*, 90(3), 1967.

[261] R. Paschotta, H. R. Telle, , and U. Keller. *Solid-State Lasers and Ap- plications*. CRC Press, 2007.

[262] Susan Clark. *Ultrafast optical control of semiconductor donor electron spin*. PhD thesis, Stanford University, 2010.

[263] C. Monroe. Quantum information processing with atoms and photons. *Nature*, 416:238–246, 2002.

[264] C. Monroe, D. M. Meekhof, B. E. King, W. M. Itano, and D. J. Wineland. Demonstration of a fundamental quantum logic gate. *Phys. Rev. Lett.*, 75:4714–4717, Dec 1995.

[265] E. Knill, R. Laflamme, and G. J. Milburn. A scheme for efficient quantum computation with linear optics. *Nature*, 409:46–52, 2001.

[266] Jeremy L. O'Brien. Optical quantum computing. *Science*, 318(5856):1567–1570, 2007.

[267] H.-J. Briegel, T. Calarco, D. Jaksch, J. I. Cirac, and P. Zoller. Quantum computing with neutral atoms. *Journal of Modern Optics*, 47(2-3):415–451, 2000.

[268] Gavin K. Brennen, Carlton M. Caves, Poul S. Jessen, and Ivan H. Deutsch. Quantum logic gates in optical lattices. *Phys. Rev. Lett.*, 82:1060–1063, Feb 1999.

[269] J. I. Cirac and P. Zoller. Quantum computations with cold trapped ions. *Phys. Rev. Lett.*, 74:4091–4094, May 1995.

[270] M. Sasura and V. Buzek. Cold trapped ions as quantum information processors. *Journal of Modern Optics*, 49(10):1593–1647, 2002.

[271] C. Langer, R. Ozeri, J. D. Jost, J. Chiaverini, B. DeMarco, A. Ben-Kish, R. B. Blakestad, J. Britton, D. B. Hume, W. M. Itano, D. Leibfried, R. Reichle, T. Rosenband, T. Schaetz, P. O. Schmidt, and D. J. Wineland. Long-lived qubit memory using atomic ions. *Phys. Rev. Lett.*, 95:060502, 2005.

[272] J. Benhelm, G. Kirchmair, C. F. Roos, and R. Blatt. Towards fault-tolerant quantum computing with trapped ions. *Nature Physics*, 2008.

[273] Kathy-Anne Brickman Soderberg, Nathan Gemelke, and Cheng Chin. Ultracold molecules: vehicles to scalable quantum information processing. *New Journal of Physics*, 11(5):055022, 2009.

[274] Daniel Loss and David P. DiVincenzo. Quantum computation with quantum dots. *Phys. Rev. A*, 57:120–126, 1998.

[275] B.E. Kane. A silicon-based nuclear spin quantum computer. *Nature*, 393:133–137, 1998.

[276] A. Imamoglu, D. D. Awschalom, G. Burkard, D. P. DiVincenzo, D. Loss, M. Sherwin, and A. Small. Quantum information processing using quantum dot spins and cavity qed. *Phys. Rev. Lett.*, 83:4204–4207, Nov 1999.

[277] Susan M. Clark, Kai-Mei C. Fu, Thaddeus D. Ladd, and Yoshihisa Yamamoto. Quantum computers based on electron spins controlled by ultrafast off-resonant single optical pulses. *Phys. Rev. Lett.*, 99:040501, Jul 2007.

[278] J. Q. You and Franco Nori. Quantum information processing with superconducting qubits in a microwave field. *Phys. Rev. B*, 68:064509, Aug 2003.

[279] J.Q. You and F. Nori. Superconducting circuits and quantum information. *Physics Today*, 2005.

[280] D. Kielpinski, C. Monroe, and D. J. Wineland. Architecture for a large-scale ion-trap quantum computer. *Nature*, 417:709–711, 2002.

[281] Timothy M. Sweeney, Carey Phelps, and Hailin Wang. Quantum control of electron spins in the two-dimensional electron gas of a cdte quantum well with a pair of raman-resonant phase-locked laser pulses. *Phys. Rev. B*, 84:075321, Aug 2011.

[282] Norman F. Ramsey. A molecular beam resonance method with separated oscillating fields. *Phys. Rev.*, 78:695–699, Jun 1950.

[283] The Royal Swedish Academy Of Sciences. Measuring and manipulating individual quantum systems, 2012.

[284] U. Gaubatz, P. Rudecki, S. Schiemann, and K. Bergmann. Population transfer between molecular vibrational levels by stimulated raman scattering with partially overlapping laser fields. a new concept and experimental results. *The Journal of Chemical Physics*, 92(5363), 1990.

[285] Klaas Bergmann, Nikolay V. Vitanov, and Bruce W. Shore. Perspective: Stimulated raman adiabatic passage: The status after 25 years. *The Journal of Chemical Physics*, 142(17), 2015.

[286] Christopher G. Yale, Bob B. Buckley, David J. Christle, Guido Burkard, F. Joseph Heremans, Lee C. Bassett, , and David D. Awschalom. All-optical control of a solid-state spin using coherent dark states. *PNAS*, 2013.

[287] D. Andrew Golter and Hailin Wang. Optically driven rabi oscillations and adiabatic passage of single electron spins in diamond. *Phys. Rev. Lett.*, 112:116403, Mar 2014.

[288] J. R. Kuklinski, U. Gaubatz, F. T. Hioe, and K. Bergmann. Adiabatic population transfer in a three-level system driven by delayed laser pulses. *Phys. Rev. A*, 40:6741–6744, 1989.

[289] M. A. Nielsen and I. L. Chuang. *Quantum Computation and Quantum Information.* Cambridge University Press, 2000.

[290] D. Press, T. D. Ladd, B. Zhang, and Y. Yamamoto. Complete quantum control of a single quantum dot spin using ultrafast optical pulses. *Nature*, 456:218–221, 2008.

[291] E. U. Condon and G. H. Shortley. *The Theory of Atomic Spectra.* Cambridge University Press, 1935.

[292] Kristiaan De Greve. *Towards Solid-State Quantum Repeaters: Ultrafast, Coherent Optical Control and Spin-Phonon Entanglement in Charged InAs Quantum Dots*. PhD thesis, Stanford University, 2012.

[293] C Cohen-Tannoudji and S Reynaud. Dressed-atom description of resonance fluorescence and absorption spectra of a multi-level atom in an intense laser beam. *Journal of Physics B: Atomic and Molecular Physics*, 10(3):345, 1977.

[294] Claude Cohen-Tannoudji and Jacques Dupont-Roc. Experimental study of zeeman light shifts in weak magnetic fields. *Phys. Rev. A*, 5:968–984, Feb 1972.

[295] J. A. Gupta, R. Knobel, N. Samarth, and D. D. Awschalom. Ultrafast manipulation of electron spin coherence. 292(5526):2458–2461, 2001.

[296] Sophia E. Economou, L. J. Sham, Yanwen Wu, and D. G. Steel. Proposal for optical u(1) rotations of electron spin trapped in a quantum dot. *Phys. Rev. B*, 74:205415, Nov 2006.

[297] A. Mysyrowicz, D. Hulin, A. Antonetti, A. Migus, W. T. Masselink, and H. Morkoc. "dressed excitons" in a multiple-quantum-well structure: Evidence for an optical stark effect with femtosecond response time. *Phys. Rev. Lett.*, 56:2748–2751, Jun 1986.

[298] J. A. Gupta, D. D. Awschalom, R. Knobel, and N. Samarth. Ultrafast manipulation of electron spin coherence in quantum wells. *International Journal of Modern Physics B*, 16(20n22):2930–2935, 2002.

[299] M.H. Mikkelsen, J. Berezovsky, and D.D. Awschalom. Ultrafast optical manipulation of single electron spins in quantum dots. *Solid State Communications*, 149:1451 – 1457, 2009. Fundamental Phenomena and Applications of Quantum Dots.

[300] Kristiaan De Greve, Peter L. McMahon, David Press, Thaddeus D. Ladd, Dirk Bisping, Christian Schneider, Martin Kamp, Lukas Worschech, Sven Hofling, Alfred Forchel, and Yoshihisa Yamamoto. Ultrafast coherent control and suppressed nuclear feedback of a single quantum dot hole qubit. *Nature Physics*, 7:872–878, 2011.

[301] Lim Jongseok, Lee Han-gyeol, Lee Sangkyung, Park Chang-Yong, and Ahn Jaewook. Ultrafast ramsey interferometry to implement cold atomic qubit gates. *Scientific Reports*, 4(5867), 2014.

[302] Jonas Nils Becker, Johannes Gorlitz, Carsten Arend, Matthew Markham, and Christoph Becher. Ultrafast, all-optical coherent control of single silicon vacancy colour centres in diamond. *Nature Communications*, 7:13512, Nov 2016.

[303] In Jean-Claude Diels and Wolfgang Rudolph, editors, *Ultrashort Laser Pulse Phenomena (Second Edition)*. Academic Press, Burlington, second edition edition, 2006.

[304] Coherent. *Operator's Manual - The Coherent Mira HP-F Laser*, 2015.

[305] Elke Neu, Mario Agio, and Christoph Becher. Photophysics of single silicon vacancy centers in diamond: implications for single photon emission. *Opt. Express*, 20(18):19956–19971, Aug 2012.

[306] Jonas N. Becker and Christophe Becher. Coherence properties and quantum control of silicon vacancy color centers in diamond. *Phys. Status Solidi A*, 2017.

[307] Thomas M. Brenner, David A. Egger, Andrew M. Rappe, Leeor Kronik, Gary Hodes, and David Cahen. Are mobilities in hybrid organic–inorganic halide perovskites actually "high"?, 2015.

[308] Thomas M. Brenner, David A. Egger, Leeor Kronik, Gary Hodes, and David Cahen. Hybrid organic—inorganic perovskites: low-cost semiconductors with intriguing charge-transport properties. *Nature Reviews Materials*, 1, 2016.

[309] Adam D. Wright, Carla Verdi, Rebecca L. Milot, Giles E. Eperon, Miguel A. Pérez-Osorio, Henry J. Snaith, Feliciano Giustino, Michael B. Johnston, and Laura M. Herz. Electron–phonon coupling in hybrid lead halide perovskites. *Nature Communications*, 7, 2016.

[310] Rinku Saran, Amelie Heuer-Jungemann, Antonios G. Kanaras, and Richard J. Curry. Giant bandgap renormalization and exciton–phonon scattering in perovskite nanocrystals. *Advanced Optical Materials*, 5(17):1700231, 2017.

[311] X.-Y. Zhu and V Podzorov. Charge carriers in hybrid organic–inorganic lead halide perovskites might be protected as large polarons. *J. Phys. Chem. Lett.*, 6, 2015.

[312] Carlo Motta and Stefano Sanvito. Electron–phonon coupling and polaron mobility in hybrid perovskites from first principles. *J. Phys. Chem. C*, 2018.

[313] Taishan Zhu and Elif Ertekin. Mixed phononic and non-phononic transport in hybrid lead halide perovskites: glass-crystal duality, dynamical disorder, and anharmonicity. *Energy Environ. Sci.*, 12:216–229, 2019.

[314] Battulga Munkhbat, Martin Wersäll, Denis G. Baranov, Tomasz J. Antosiewicz, and Timur Shegai. Suppression of photo-oxidation of organic chromophores by strong coupling to plasmonic nanoantennas. *Science Advances*, 4(7), 2018.

[315] Felipe Herrera and Frank C. Spano. Cavity-controlled chemistry in molecular ensembles. *Phys. Rev. Lett.*, 116:238301, Jun 2016.

[316] Ming-Hui Lu, Liang Feng, and Yan-Feng Chen. Phononic crystals and acoustic metamaterials. *Materials Today*, 12(12):34 – 42, 2009.

[317] Cheng Zhu, Xiuxiu Niu, Yuhao Fu, Nengxu Li, Chen Hu, Yihua Chen, Xin He Guangren Na, Pengfei Liu, Huachao Zai, Yang Ge, Yue Lu, Xiaoxing Ke, Yang Bai, Shihe Yang, Pengwan Chen, Yujing Li, Manling Sui, Lijun Zhang, Huanping Zhou, and Qi Chen. Strain engineering in perovskite solar cells and its impacts on carrier dynamics. *Nature Communications*, 10, 2019.

[318] Meagan V. Kelso, Naveen K. Mahenderkar, Qingzhi Chen, John Z. Tubbesing, and Jay A. Switzer. Spin coating epitaxial films. *Science*, 364(6436):166–169, 2019.

[319] Andreas Herklotz, Dongkyu Lee, Er-Jia Guo, Tricia L Meyer, Jonathan R Petrie, and Ho Nyung Lee. Strain coupling of oxygen non-stoichiometry in perovskite thin films. *Journal of Physics: Condensed Matter*, 29(49):493001, dec 2017.

[320] Thibaud Etienne, Edoardo Mosconi, and Filippo Angelis. Dynamical origin of the rashba effect in organohalide lead perovskites: A key to suppressed carrier recombination in perovskite solar cells? *The Journal of Physical Chemistry Letters*, 7, 04 2016.

[321] Yaxin Zhai, Sangita Baniya, Chuang Zhang, Junwen Li, Paul Haney, Chuan-Xiang Sheng, Eitan Ehrenfreund, and Zeev Valy Vardeny. Giant rashba splitting in 2d organic-inorganic halide perovskites measured by transient spectroscopies. *Science Advances*, 3(7), 2017.

[322] Maya Isaro, Liang Z. Tan, Maryna I. Bodnarchuk, Maksym V. Kovalenko, Andrew M. Rappe, and Efrat Lifshitz. Rashba effect in a single colloidal cspbbr3 perovskite nanocrystal detected by magneto-optical measurements. *Nano Lett.*, 17, 2017.

[323] Michael A. Becker, Roman Vaxenburg, Georgian Nedelcu, Peter C. Sercel, Andrew Shabaev, Michael J. Mehl, John G. Michopoulos, Samuel G. Lambrakos, Noam Bernstein, John L. Lyons, Thilo Stöferle, Rainer F. Mahrt, Maksym V. Kovalenko, David J. Norris, Gabriele Raino, and Alexander L. Efros. Bright triplet excitons in caesium lead halide perovskites. *Nature*, 553, 2018.

[324] Fan Zheng, Liang Z. Tan, Shi Liu, and Andrew M. Rappe. Rashba spin–orbit coupling enhanced carrier lifetime in ch3nh3pbi3. *Nano Lett.*, 15, 2015.

[325] Kyle Frohna, Tejas Deshpande, John Harter, Wei Peng, Bradford A. Barker, Jeffrey B. Neaton, Steven G. Louie, Osman M. Bakr, David Hsieh, and Bernardi; Marco. Inversion symmetry and bulk rashba effect in methylammonium lead iodide perovskite single crystals. *Nature Communications*, 9, 2018.

[326] Edoardo Mosconi, Thibaud Etienne, and Filippo De Angelis. Rashba band splitting in organohalide lead perovskites: Bulk and surface effects. *J. Phys. Chem. Lett.*, 8, 2017.

[327] Mikaël Kepenekian and Jacky Even. Rashba and dresselhaus couplings in halide perovskites: Accomplishments and opportunities for spintronics and spin–orbitronics. *J. Phys. Chem. Lett.*, 8, 2017.

[328] Minsung Kim, Jino Im, Arthur J. Freeman, Jisoon Ihm, and Hosub Jin. Switchable s = 1/2 and j = 1/2 rashba bands in ferroelectric halide perovskites. *Proceedings of the National Academy of Sciences*, 111(19):6900–6904, 2014.

[329] Samuel D. Stranks and Paulina Plochocka. The influence of the rashba effect. *Nature Materials*, 17, 2018.

[330] Yutong Wang, Wei-Hai Fang, Run Long, and Oleg V. Prezhdo. Symmetry breaking at mapbi3 perovskite grain boundaries suppresses charge recombination: Time-domain ab initio analysis. *J. Phys. Chem. Lett.*, 10, 2019.

[331] Ashley M. Cook, Benjamin M. Fregoso, Fernando de Juan, Sinisa Coh, and Joel E. Moore. Design principles for shift current photovoltaics. *Nature Communications*, 8, 2017.

[332] Liang Z Tan, Fan Zheng, Steve M Young, Fenggong Wang, Shi Liu, and Andrew M Rappe. Shift current bulk photovoltaic effect in polar materials—hybrid and oxide perovskites and beyond. *npj Computational Materials*, 2, 2016.

[333] Ming-Min Yang, Dong Jik Kim, and Marin Alexe. Flexo-photovoltaic effect. *Science*, 360(6391):904–907, 2018.

[334] Shankari Nadupalli, Jens Kreisel, and Torsten Granzow. Increasing bulk photovoltaic current by strain tuning. *Science Advances*, 5(3), 2019.

[335] Fan Zheng, Hiroyuki Takenaka, Fenggong Wang, Nathan Z. Koocher, and Andrew M. Rappe. First-principles calculation of the bulk photovoltaic effect in ch3nh3pbi3 and ch3nh3pbi3–xclx. *J. Phys. Chem. Lett.*, 6, 2015.

[336] Tejas Sherkar and L Koster. Can ferroelectric polarization explain the high performance of hybrid halide perovskite solar cells? *Physical Chemistry Chemical Physics*, 18:331–338, 11 2015.

[337] Wei-Jian Xu, Peng-Fei Li, Yuan-Yuan Tang, Wei-Xiong Zhang, Ren-Gen Xiong, and Xiao-Ming Chen. A molecular perovskite with switchable coordination bonds for high-temperature multiaxial ferroelectrics. *J. Am. Chem. Soc.*, 139, 2017.

[338] Qiang Pan, Zhi-Bo Liu, Yuan-Yuan Tang, Peng-Fei Li, Rong-Wei Ma, Ru-Yuan Wei, Yi Zhang, Yu-Meng You, Heng-Yun Ye, and Ren-Gen Xiong. A three-dimensional molecular perovskite ferroelectric: (3-ammoniopyrrolidinium)rbbr3. *J. Am. Chem. Soc.*, 139, 2017.

[339] P Jain, NS Dalal, BH Toby, HW Kroto, and AK. Cheetham. Order-disorder antiferroelectric phase transition in a hybrid inorganic-organic framework with the perovskite architecture. *J Am Chem Soc.*, 130, 2008.

[340] P Jain, V Ramachandran, RJ Clark, HD Zhou, BH Toby, NS Dalal, HW Kroto, and AK Cheetham. Multiferroic behavior associated with an order-disorder hydrogen bonding transition in metal-organic frameworks (mofs) with the perovskite abx(3) architecture. *J. Am. Chem. Soc*, 2009.

[341] Da-Wei Fu, Wen Zhang, Hong-Ling Cai, Yi Zhang, Jia-Zhen Ge, Ren-Gen Xiong, Songping D. Huang, and Takayoshi Nakamura. A multiferroic perdeutero metal–organic framework. *Angewandte Chemie International Edition*, 50(50):11947–11951, 2011.

[342] Lina Li, Zhihua Sun, Peng Wang, Weida Hu, Sasa Wang, Chengmin Ji, Maochun Hong, and Junhua Luo. Tailored engineering of an unusual (c4h9nh3)2(ch3nh3)2pb3br10 two-dimensional multilayered perovskite ferroelectric for a high-performance photodetector. *Angewandte Chemie International Edition*, 56(40):12150–12154, 2017.

[343] Heng-Yun Ye, Yuan-Yuan Tang, Peng-Fei Li, Wei-Qiang Liao, Ji-Xing Gao, Xiu-Ni Hua, Hu Cai, Ping-Ping Shi, Yu-Meng You, and Ren-Gen Xiong. Metal-free three-dimensional perovskite ferroelectrics. *Science*, 361(6398):151–155, 2018.

[344] Gavin B. Osterhoudt, Laura K. Diebel, Mason J. Gray, Xu Yang, John Stanco, Xiangwei Huang, Bing Shen, Ni Ni, Philip J. W. Moll, Ying Ran, and kenneth S. Burch. Colossal mid-infrared bulk photovoltaic effect in a type-i weyl semimetal. *Nature Materials*, 18, 2019.

[345] M. Aspelmeyer, S. Groblacher, K. Hammerer, and N. Kiesel. Quantum optomechanics: throwing a glance, 2010.

[346] Markus Aspelmeyer, Pierre Meystre, and Keith Schwab. Quantum optomechanics. *Physics Today*, 65, 2012.

[347] Philipp Treutlein. Optomechanics: a strained couple. *Nature nanotechnology*, 9, 2014.

[348] Laure Mercier de Lépinay, Benjamin Pigeau, Sven Rohr, Arnaud Gloppe, Aurélien Kuhn, Pierre Verlot, Eva Dupont-Ferrier, Benjamin Besga, and Olivier Arcizet. Nano-optomechanical measurement in the photon counting regime. *arXiv*, 03 2015.

[349] D Rugar, R Budakian, H J Mamin, and B W Chui. Single spin detection by magnetic resonance force microscopy. *Nature*, 430, 2004.

[350] a D O'Connell, M Hofheinz, M Ansmann, Radoslaw C Bialczak, M Lenander, Erik Lucero, M Neeley, D Sank, H Wang, M Weides, J Wenner, John M Martinis, and a N Cleland. Quantum ground state and single-phonon control of a mechanical resonator. *Nature*, 464, 2010.

[351] I Yeo, P-L de Assis, a Gloppe, E Dupont-Ferrier, P Verlot, N S Malik, E Dupuy, J Claudon, J-M Gerard, a Auffeves, G Nogues, S Seidelin, J-ph Poizat, O Arcizet, and M Richard. Strain-mediated coupling in a quantum dot-mechanical oscillator hybrid system. *Nature Nanotechnology*, 9(2), 2014.

[352] Markus Arndt and Klaus Hornberger. Testing the limits of quantum mechanical superpositions. *Nature Physics*, 10, 2014.

[353] Steven D. Bennett, Lynda Cockins, Yoichi Miyahara, Peter Grutter, and Aashish a. Clerk. Strong electromechanical coupling of an atomic force microscope cantilever to a quantum dot. *Physical Review Letters*, 104, 2010.

[354] David Hunger, Stephan Camerer, Theodor W. Hansch, Daniel Konig, Jorg P. Kotthaus, Jakob Reichel, and Philipp Treutlein. Resonant coupling of a bose-einstein condensate to a micromechanical oscillator. *Physical Review Letters*, 104, 2010.

[355] David Gevaux. Quantum resonators: At the limit, at last. *Nature Physics*, 6, 2010.

[356] A. Sipahigil, R. E. Evans, D. D. Sukachev, M. J. Burek, J. Borregaard, M. K. Bhaskar, C. T. Nguyen, J. L. Pacheco, H. A. Atikian, C. Meuwly, R. M. Camacho, F. Jelezko, E. Bielejec, H. Park, M. Lončar, and M. D. Lukin. An integrated diamond nanophotonics platform for quantum-optical networks. *Science*, 354(6314):847–850, 2016.

[357] Juan Yin, Yuan Cao, Yu-Huai Li, Sheng-Kai Liao, Liang Zhang, Ji-Gang Ren, Wen-Qi Cai, Wei-Yue Liu, Bo Li, Hui Dai, Guang-Bing Li, Qi-Ming Lu, Yun-Hong Gong, Yu Xu, Shuang-Lin Li, Feng-Zhi Li, Ya-Yun Yin, Zi-Qing Jiang, Ming Li, Jian-Jun Jia, Ge Ren, Dong He, Yi-Lin Zhou, Xiao-Xiang Zhang, Na Wang, Xiang Chang, Zhen-Cai Zhu, Nai-Le Liu, Yu-Ao Chen, Chao-Yang Lu, Rong Shu, Cheng-Zhi Peng, Jian-Yu Wang, and Jian-Wei Pan. Satellite-based entanglement distribution over 1200 kilometers. *Science*, 356(6343):1140–1144, 2017.